IMAGING OF THE VESTIBULAR SYSTEM

EDITED BY: Bryan Kevin Ward, Raymond Van De Berg, Marianne Dieterich
and Arnaud Attyé
PUBLISHED IN: Frontiers in Neurology

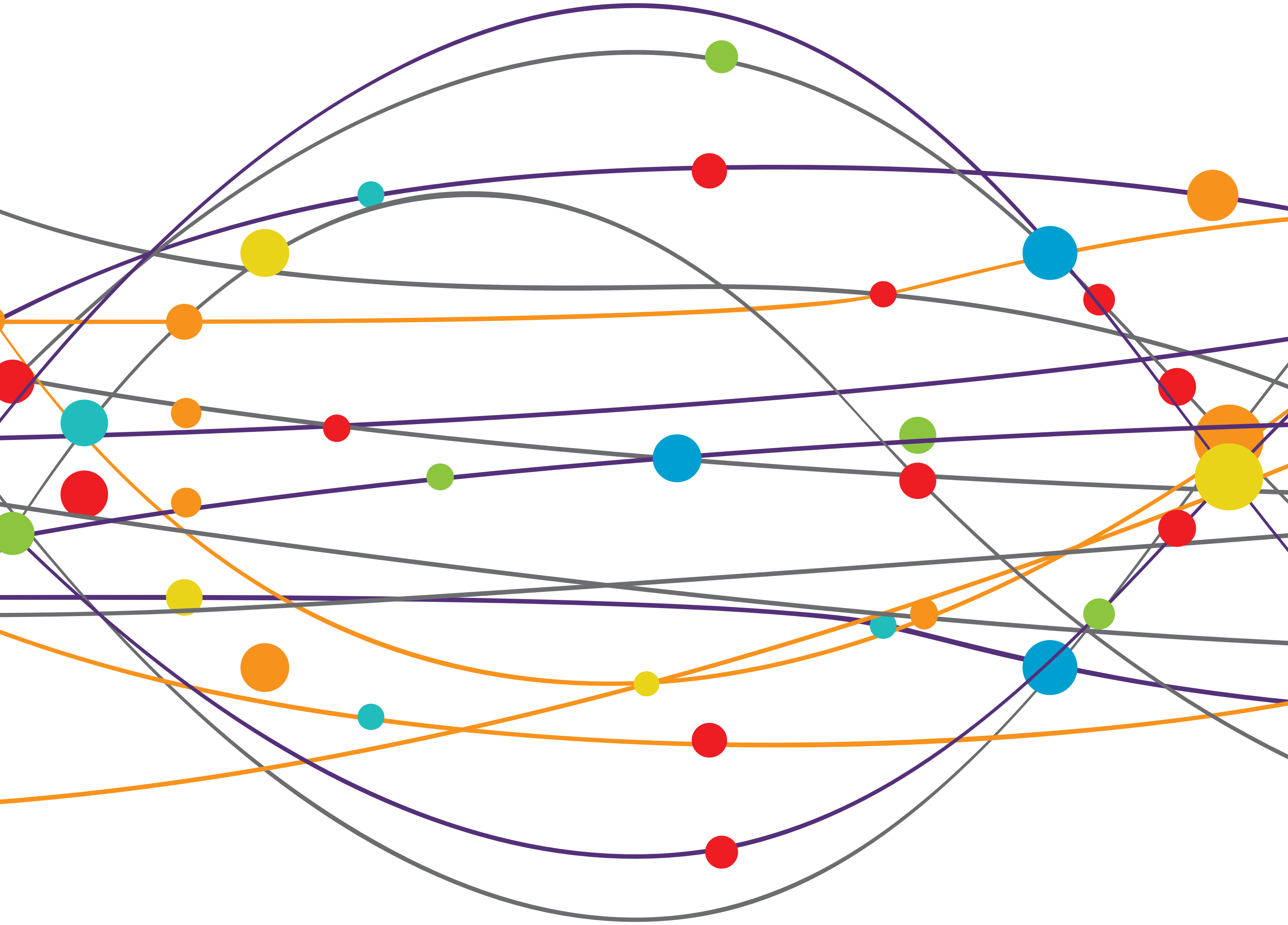

frontiers Research Topics

ISSN 1664-8714
ISBN 978-2-88976-589-8
DOI 10.3389/978-2-88976-589-8

About Frontiers

Frontiers is more than just an open-access publisher of scholarly articles: it is a pioneering approach to the world of academia, radically improving the way scholarly research is managed. The grand vision of Frontiers is a world where all people have an equal opportunity to seek, share and generate knowledge. Frontiers provides immediate and permanent online open access to all its publications, but this alone is not enough to realize our grand goals.

Frontiers Journal Series

The Frontiers Journal Series is a multi-tier and interdisciplinary set of open-access, online journals, promising a paradigm shift from the current review, selection and dissemination processes in academic publishing. All Frontiers journals are driven by researchers for researchers; therefore, they constitute a service to the scholarly community. At the same time, the Frontiers Journal Series operates on a revolutionary invention, the tiered publishing system, initially addressing specific communities of scholars, and gradually climbing up to broader public understanding, thus serving the interests of the lay society, too.

Dedication to Quality

Each Frontiers article is a landmark of the highest quality, thanks to genuinely collaborative interactions between authors and review editors, who include some of the world's best academicians. Research must be certified by peers before entering a stream of knowledge that may eventually reach the public - and shape society; therefore, Frontiers only applies the most rigorous and unbiased reviews.
Frontiers revolutionizes research publishing by freely delivering the most outstanding research, evaluated with no bias from both the academic and social point of view. By applying the most advanced information technologies, Frontiers is catapulting scholarly publishing into a new generation.

What are Frontiers Research Topics?

Frontiers Research Topics are very popular trademarks of the Frontiers Journals Series: they are collections of at least ten articles, all centered on a particular subject. With their unique mix of varied contributions from Original Research to Review Articles, Frontiers Research Topics unify the most influential researchers, the latest key findings and historical advances in a hot research area! Find out more on how to host your own Frontiers Research Topic or contribute to one as an author by contacting the Frontiers Editorial Office: frontiersin.org/about/contact

IMAGING OF THE VESTIBULAR SYSTEM

Topic Editors:
Bryan Kevin Ward, Johns Hopkins Medicine, United States
Raymond Van De Berg, Maastricht University Medical Centre, Netherlands
Marianne Dieterich, LMU Munich University Hospital, Germany
Arnaud Attyé, Université Grenoble Alpes, France

Citation: Ward, B. K., Van De Berg, R., Dieterich, M., Attyé, A., eds. (2022). Imaging of the Vestibular System. Lausanne: Frontiers Media SA.
doi: 10.3389/978-2-88976-589-8

Table of Contents

frontiers | Frontiers in Neurology

EDITORIAL
published: 23 June 2022
doi: 10.3389/fneur.2022.937955

Editorial: Imaging of the Vestibular System

*Marianne Dieterich**

Department of Neurology and German Center for Vertigo and Balance Disorders (DSGZ), University Hospital, Ludwig-Maximilians University, Munich, Germany

Keywords: vestibular system, labyrinth, brain network, imaging, MRI, PET, EEG, evoked potentials

OPEN ACCESS

Edited and reviewed by:
Michael Strupp,
Ludwig Maximilians University of
Munich, Germany

****Correspondence:***
Marianne Dieterich
marianne.dieterich@
med.uni-muenchen.de

Specialty section:
This article was submitted to
Neuro-Otology,
a section of the journal
Frontiers in Neurology

Received: *06 May 2022*
Accepted: *12 May 2022*
Published: *23 June 2022*

Citation:
Dieterich M (2022) Editorial: Imaging
of the Vestibular System.
Front. Neurol. 13:937955.
doi: 10.3389/fneur.2022.937955

Editorial on the Research Topic

Imaging of the Vestibular System

The articles submitted to the Research Topic with the overarching title "*Imaging of the Vestibular System*" can best be structured according to the following two categories:

- imaging of the peripheral system with the inner ear and eighth nerve, and
- imaging of the central circuitry from the vestibular nuclei in the pontomedullary brainstem to cerebellar midline structures and multiple cortical areas centered around the parieto-insular-opercular region.

Historically, imaging of peripheral structures within the inner ear was dominated in the 1990s by the otolaryngologist Harold Schuknecht (Pathology of the Ear. 2nd Edition, 1993, Lea and Febinger, Philadelphia) (1), who published the first experimental data on the pathophysiology of the most frequent labyrinthine disorders and proposed new creative hypotheses, which were subject to lively and sometimes controversial discussion, for example for benign peripheral positioning vertigo, vestibular neuritis, and Menière's disease. In contrast, the structure, function, and disorders of the human central vestibular system that is represented by a largely distributed, multisensory, and sensorimotor vestibular network, in particular its cortical hubs, were increasingly disclosed by imaging over the last 25 years [e.g., (2–9)]. Around a quarter of patients who present with the key symptoms of vertigo, dizziness, and imbalance are found to have central vestibular disorders.

The recent collection of articles here—with six original research articles, two systematic reviews, and one case report—focuses, on the one hand, on normal and pathological labyrinthine characteristics which may serve as indicators and reliable follow-up parameters for various forms of inner ear diseases such as endolymphatic hydrops. Precise measurement of the endolymphatic space by *in-vivo* non-invasive MRI with intravenous delayed contrast medium is increasingly becoming an essential clinical diagnostic tool to distinguish various causes of vestibulocochlear syndromes associated with endolymphatic hydrops. During the last years, different methodological approaches were used to investigate the endolymphatic space, either by intratympanal application of gadolinium or by non-invasive intravenous delayed contrast agent enhanced, high-resolution MR imaging (10–13) (Boegle et al.). The latter has the advantage of simultaneous imaging of both ears which allows a comparison of the volumetric parameters of both ears and can be helpful to differentiate Menière's disease from vestibular migraine. It turned out that an endolymphatic hydrops occurred more often in Menière's disease, and showed a higher grade and an asymmetry between both ears compared to vestibular migraine or a combined condition in which the patients fulfill the definition of both diseases (Oh et al.). To improve volumetric quantification methods further a novel open-source inner ear fluid segmentation approach was developed using a deep learning model (Ahmadi et al.). This segmentation method showed high accuracy, robustness toward domain shift, and rapid prediction times, and could speed up inner ear MRI analyses in the future. Another article deals with the relationship between imaging and electrocochleography (ECG) in 50 patients with Menière's disease (He et al.). A correlation was found between the endolymph hydrops in 3D-FLAIR MRI and ECG parameters, in particular between the area ratio of the summating potential to the action potential and the cochlear hydrops. This ECG parameter appeared sensitive and reliable for diagnosing the endolymph hydrops.

Other important structures of the inner ear are the capillaries that form a semi-permeable barrier, the blood-labyrinth barrier, less permeable than capillary barriers elsewhere. Also using MRI with intravenous contrast agents, here as a marker for the barrier's integrity, a dysfunction could probably be disclosed as a mechanism for several audio-vestibular disorders. A systematic review (Song et al.) on 14 animal studies and 53 studies in humans with different diseases found constant and reliable parameters in healthy ears of animals and humans, with a maximum contrast signal at 4 h in humans. Patients with idiopathic sudden sensorineural hearing loss and otosclerosis showed increased signal intensity before and shortly after contrast medium injection, whereas patients with Menière's disease and vestibular schwannoma showed an increased signal after 4 h. However, since sample size, control groups, and blinded analysts were heterogeneous, future studies with consistent methods are needed.

Another vascular dysfunction of the inner ear is presented in a case report of a patient with acute labyrinthine ischemia who subsequently developed a posterior semicircular canal fibrosis (Castellucci et al.).

On the other hand, three contributions deal with different aspects of the central vestibular system that is examined by MRI, PET, and vestibular-evoked potentials.

Vertigo, dizziness, double vision, and hearing loss may be symptoms of an acute ischemia or hemorrhage in the brain and/or labyrinth. About 4–10% of patients presenting with vertigo and balance disorders in the emergency room suffer from stroke and therefore need urgent diagnostics and therapy. However, symptomatology can be very similar in acute peripheral and central vestibular disorders, a reason why special neuro-otological examinations like the HINTS test (head impulse, nystagmus in different gaze positions, test for skew deviation) are performed in the acute situation for differentiation. In the acute situation, the first question is: Is it an acute unilateral peripheral or a central vestibular syndrome, and, if central, which lesion site is it? An acute peripheral vestibular syndrome can be mimicked by lesions of the medullary brainstem, cerebellar peduncle, and especially midline cerebellar structures such as the uvula, nodulus, tonsil, and the flocculus (7).

In a prospective trial examining these patients in the emergency room, symptoms and lesion topography were analyzed to characterize the lesion-symptom relationship in acute vestibular and ocular motor strokes (Zwergal et al.). An acute unilateral stroke was found in 47 of 351 patients (13%) with MRI lesions located in the cerebellar hemispheres in vertigo/dizziness, whereas strokes with double vision showed lesions in the upper brainstem. In another study, changes in the cortical networks were examined in healthy individuals who perceive self-motion after exposure to passive motion, a phenomenon named mal de debarquement syndrome (MdDS) (Jeon et al.). Here 28 fishermen, 15 of whom experienced transient symptoms of MdDS, were tested with neuropsychological assessment, vestibular testing, structural MRI, resting-state functional MRI, and FDG-PET. The detailed analyses disclosed activation of prefrontal and deactivation of cerebellar networks that correlated with neuropsychological assessment. The functional neuroimaging findings showed similarities with functional dizziness and anxiety disorders suggesting a shared mechanism of enhanced self-awareness.

In a review article on vestibular-evoked cerebral potentials (EP), results are summarized and compared from studies that have used a large range of vestibular stimulation, from natural vestibular stimulation on rotating chairs or motion platforms to artificial stimulation, for example, by sounds, galvanic stimulation or acceleration (Nakul et al.). Up to now EPs remain poorly standardized in vestibular neuroscience and neurotology.

With respect to imaging of the central vestibular system, new methods come into play such as segmentation techniques, functional connectivity, and dysconnectivity which will hopefully enable us to understand the pathophysiology of several central disorders affecting the vestibular system, e.g., vestibular migraine or cerebellar disorders. Furthermore, they can help us to understand the different types of compensatory mechanisms after an acute lesion within the network or in chronic vestibular disorders in which the other sensory and sensorimotor systems may substitute for the loss of vestibular function.

I don't want to end without noting that more recent articles on this topic of imaging the peripheral and central vestibular system can be found in specialized journals of neuroimaging and neuroscience.

AUTHOR CONTRIBUTIONS

The author confirms being the sole contributor of this work and has approved it for publication.

FUNDING

MD was partially supported by the German Foundation of Neurology (Deutsche Stiftung Neurologie, DSN) and the German Federal Ministry of Education and Research (BMBF) via the German Center for Vertigo and Balance Disorders (DSGZ, Grant No. 01 EO 0901).

REFERENCES

1. Schuknecht H. *Pathology of the Ear,* 2nd Edn. Philadelphia, PA: Lea and Febinger (1993).
2. Dieterich M, Brandt T. The bilateral central vestibular system: its pathways, functions, and disorders. *Ann N Y Acad Sci*. (2015) 1343:10–26. doi: 10.1111/nyas.12585
3. Dieterich M, Brandt T. Functional imaging of peripheral and central vestibular disorders. *Brain*. (2008) 131(Pt 10):2538–52. doi: 10.1093/brain/awn042
4. Lopez C, Blanke O, Mast FW. The human vestibular cortex revealed by coordinate-based activation likelihood estimation meta-analysis. *Neuroscience*. (2012) 212:159–79. doi: 10.1016/j.neuroscience.2012.03.028
5. Zu Eulenburg P, Caspers S, Roski C, Eickhoff SB. Meta-analytical definition and functional connectivity of the human vestibular cortex. *NeuroImage*. (2012) 60:162–9. doi: 10.1016/j.neuroimage.2011.12.032
6. Kirsch V, Keeser D, Hergenroeder T, Erat O, Ertl-Wagner B, Brandt T, et al. Structural and functional connectivity mapping of the vestibular circuitry from human brainstem to cortex. *Brain Struct Funct*. (2016) 221:1291–308. doi: 10.1007/s00429-014-0971-x
7. Brandt T, Dieterich M. The dizzy patient: don't forget disorders of the central vestibular system. *Nat Rev Neurol*. (2017) 13:252–62. doi: 10.1038/nrneurol.2017.58
8. Oh S-Y, Boegle R, Ertl M, Stephan T, Dieterich M. Multisensory vestibular, vestibular-auditory, and auditory network effects revealed by parametric sound pressure stimulation. *NeuroImage*. (2018) 176:354–63. doi: 10.1016/j.neuroimage.2018.04.057
9. Frank SM, Greenlee MW. The parieto-insular vestibular cortex in human: more than a single area? *J Neurophysiol*. (2018) 120:1438–50. doi: 10.1152/jn.00907.2017
10. Naganawa S, Yamazaki M, Kawai H, Bokura K, Sone M, Nakashima T. Imaging of endolymphatic and perilymphatic fluid after intravenous administration of single-dose gadodiamide. *Magn Reson Med Sci*. (2012) 11:145–50. doi: 10.2463/mrms.11.145
11. Naganawa S, Kawai H, Taoka T, and Sone M. Improved HYDROPS: imaging of endolymphatic hydrops after intravenous administration of gadolinium. *Magn Reson Med Sci*. (2017) 16:357–61. doi: 10.2463/mrms.tn.2016-0126
12. Naganawa S, Nakamichi R, Ichikawa K, Kawamura M, Kawai H, Yoshida T, et al. MR imaging of endolymphatic hydrops: utility of iHYDROPS-Mi2 combined with deep learning reconstruction denoising. *Magn Reson Med Sci*. (2020) 20:272–9. doi: 10.2463/mrms.mp.2020-0082
13. Gürkov R, Berman A, Dietrich O, Flatz W, Jerin C, Krause E, et al. MR volumetric assessment of endolymphatic hydrops. *Eur Radiol*. (2015) 25:585–95. doi: 10.1007/s00330-014-3414-4

Conflict of Interest: The author declares that the research was conducted in the absence of any commercial or financial relationships that could be construed as a potential conflict of interest.

frontiers in Neurology

ORIGINAL RESEARCH
published: 30 June 2020
doi: 10.3389/fneur.2020.00585

Neural Correlates of Transient Mal de Debarquement Syndrome: Activation of Prefrontal and Deactivation of Cerebellar Networks Correlate With Neuropsychological Assessment

Seung-Ho Jeon [1,2†], *Yeong-Hun Park* [3†], *Sun-Young Oh* [1,2*], *Jin-Ju Kang* [1,2], *Yeon-Hee Han* [4], *Hwan-Jeong Jeong* [2,4], *Jong-Min Lee* [3*], *Mijin Park* [3], *Ji-Soo Kim* [5] and *Marianne Dieterich* [6,7,8]

[1] Department of Neurology, Jeonbuk National University Hospital, Jeonju-si, South Korea, [2] Research Institute of Clinical Medicine of Jeonbuk National University, Jeonbuk National University Hospital, Jeonju-si, South Korea, [3] Department of Biomedical Engineering, Hanyang University, Seoul, South Korea, [4] Nuclear Medicine, School of Medicine, Jeonbuk National University Hospital, Jeonju-si, South Korea, [5] Department of Neurology, Seoul National University Bundang Hospital, Seoul National University School of Medicine, Seoul, South Korea, [6] Department of Neurology, Ludwig-Maximilians-University, Munich, Germany, [7] German Center for Vertigo and Balance Disorders (IFB^{LMU}), Ludwig-Maximilians-University, Munich, Germany, [8] Munich Cluster for Systems Neurology (SyNergy), Munich, Germany

OPEN ACCESS

Edited by:
Joel Alan Goebel,
Washington University School of Medicine in St. Louis, United States

Reviewed by:
Sergei B. Yakushin,
Icahn School of Medicine at Mount Sinai, United States
Giuseppe Chiarella,
University of Catanzaro, Italy

***Correspondence:**
Sun-Young Oh
ohsun@jbnu.ac.kr
Jong-Min Lee
ljm@hanyang.ac.kr

† These authors have contributed equally to this work

Specialty section:
This article was submitted to Neuro-Otology, a section of the journal Frontiers in Neurology

Received: *08 April 2020*
Accepted: *20 May 2020*
Published: *30 June 2020*

Citation:
Jeon S-H, Park Y-H, Oh S-Y, Kang J-J, Han Y-H, Jeong H-J, Lee J-M, Park M, Kim J-S and Dieterich M (2020) Neural Correlates of Transient Mal de Debarquement Syndrome: Activation of Prefrontal and Deactivation of Cerebellar Networks Correlate With Neuropsychological Assessment. Front. Neurol. 11:585. doi: 10.3389/fneur.2020.00585

Background: Mal de debarquement syndrome (MdDS) is characterized by a subjective perception of self-motion after exposure to passive motion, mostly after sea travel. A transient form of MdDS (t-MdDS) is common in healthy individuals without pathophysiological certainty. In the present cross-sectional study, the possible neuropsychiatric and functional neuroimaging changes in local fishermen with t-MdDS were evaluated.

Methods: The present study included 28 fishermen from Buan County in South Korea; 15 (15/28, 53.6%) participants experienced t-MdDS for 1–6 h, and 13 were asymptomatic (13/28, 46.4%). Vestibular function tests were performed using video-oculography, the video head impulse test, and ocular and cervical vestibular-evoked myogenic potentials. Visuospatial function was also assessed by the Corsi block test. Brain imaging comprised structural MRI, resting-state functional MRI, and [18F]FDG PET scans.

Results: The results of vestibular function tests did not differ between the fishermen with and those without t-MdDS. However, participants with t-MdDS showed better performance in visuospatial memory function than those without t-MdDS (6.40 vs. 5.31, p-value = 0.016) as determined by the Corsi block test. Structural brain MRIs were normal in both groups. [18F]FDG PET showed a relative hypermetabolism in the bilateral occipital and prefrontal cortices and hypometabolism in the vestibulocerebellum (nodulus and uvula) in participants with t-MdDS compared to those without t-MdDS. Resting-state functional connectivities were significantly decreased between the vestibular regions of the flocculus, superior temporal gyrus, and parietal operculum and the visual association areas of the middle occipital gyrus, fusiform gyrus, and cuneus in participants with t-MdDS. Analysis of functional connectivity of the significant regions in the PET scans revealed decreased connectivity between the prefrontal cortex and visual processing areas in the t-MdDS group.

Conclusion: Increased visuospatial memory, altered metabolism in the prefrontal cortex, visual cognition cortices, and the vestibulocerebellum, and decreased functional connectivity between these two functional areas might indicate reductions in the integration of vestibular input and enhancement of visuospatial attention in subjects with t-MdDS. Current functional neuroimaging similarities from transient MdDS via chronic MdDS to functional dizziness and anxiety disorders suggest a shared mechanism of enhanced self-awareness as a kind of continuum or as overlap disorders.

Keywords: Mal de Debarquement syndrome (MdDS), transient Mal de Debarquement (t-MdD), functional connectivity MRI, [18F]FDG PET, visuospatial memory, vestibular network, multisensory integration, emotional network

INTRODUCTION

Mal de Debarquement syndrome (MdDS) was recognized as a clinical entity for the first time in 1987 (1). The syndrome is characterized by a persistent rocking or swaying sensation occurring after prolonged passive movements, such as boat travel, that lasts for months or years, leading to balance problem, visuospatial and cognitive dysfunction (2). In contrast to typical MdDS, transient episodes of MdDS (t-MdDS) are fairly common even among healthy young individuals (3, 4). The post-motion-triggered rocking sensation is a common experience in healthy subjects with a prevalence of approximately 70% (4, 5) and is referred to "land-sickness."

The underlying mechanism of MdDS and t-MdDS is not yet clear. Traditionally, MdDS has been considered a dynamic and multi-sensorimotor form of central nervous system adaptive plasticity with delayed or defective readaptation of the vestibular system after cessation of motion. According to the neural mismatch theory, this delayed readaptation leads to intersensory conflict (6). For example, passengers are exposed to a series of contradictory vestibular, visual, and proprioceptive stimuli when at sea, which may cause adaptation to specific ship motions. After landing, the newly acquired visuovestibular perception are no longer appropriate, causing Mal de Debarquement which lasts until proper readaptation is achieved (7). Recent studies indicated that readaptation of the velocity storage for VOR pathway, i.e., the adaptive processes associated with roll-while-rotating, could be a source of body oscillations in MdDS (8, 9). Treatment based on the readaptation of the VOR also has led to a substantial improvement in 70% of the subjects with MdDS (8). Memory of an internal representation of external passive movement (i.e., release of stored vestibular information from the hippocampus) may underlie a mechanism of MdDS (6). In a recent neuroimaging study of 20 MdDS patients, an association was observed between resting-state metabolic activity and functional connectivity between the entorhinal cortex and amygdala (10). Gray matter volume alterations were also found in the visual-vestibular processing areas and in a structure involving default mode, salience and central executive networks (11). Due to the similar history and overlapping clinical features, t-MdDS and MdDS may likely share underlying brain mechanisms. We hypothesized that the transient motion illusion in subjects with t-MdDS is reflected by changes in brain metabolism and functional connectivity involving areas that process spatial information, similar to persistent pathological MdDS. In the current study, neuropsychological and functional neuroimaging studies were evaluated using [18F]FDG PET and functional connectivity magnetic resonance imaging (fcMRI) to determine alterations in visual-vestibular networks in participants with t-MdDS.

SUBJECTS AND METHODS

Subjects

A total of 28 fishermen living in Buan County in Korea were enrolled in this prospective study from May to June 2018. After a thorough clinical history focusing on vestibular disorders and MdDS symptoms had been performed, the individuals were divided into two groups: participants with t-MdDS and those without t-MdDS symptoms. No participant suffered from persistent MdDS for more than a month. The criteria for t-MdDS were as follows: (1) a perception of rocking and swaying after disembarking; (2) symptoms lasting $\leq$ 1 month; (3) no other causes of peripheral inner ear or central nervous system disorders after evaluation with appropriate neurotological testing.

All participants underwent neurological and neurotological evaluations, including video-oculography (VOG), video head impulse test (vHIT), cervical and ocular vestibular-evoked myogenic potentials (cVEMPs and oVEMPs, respectively), [18F]FDG PET/CT, structural MRI, and resting-state fcMRI. General cognitive function was assessed using the Korean Mini-Mental State Examination (K-MMSE). The Korean Beck Depression Inventory (K-BDI) and the Korean Beck Anxiety Inventory (K-BAI) were also carried out. In addition, the visuospatial function test, as part of the Wechsler Adult Intelligence Scale (WAIS)-IV, and the Corsi block test using the iPad's Path Span application were performed. Every evaluations were performed during the fishing ban period, i.e., symptom-free period.

All participants gave informed consent and received monetary compensation for participation. The study was approved by the Institutional Review Board at Jeonbuk National University Hospital (IRB No. 2017-09-022).

Vestibular Testing

Video-Oculography (VOG) (12)

Eye movements and gaze stability were examined using three-dimensional VOG (3D-VOG, SMI, The Netherlands). Eye movements and the ability to hold a steady gaze were evaluated during attempted fixation of visual targets located centrally or eccentrically (±30° horizontally, ±20° vertically). Spontaneous and gaze-evoked nystagmus, vibration and head-shaking nystagmus, positional tests, horizontal saccades, and smooth pursuit eye movements were evaluated. Digitized data were analyzed using MATLAB® software.

Video Head Impulse Test (vHIT)

VHIT was performed using a video-oculography system (SLMED, Seoul, Korea). Participants were examined at a distance of 1 m from the target at eye level. To ensure the reliability of examination, the goggles were fastened to the head with an elastic band to minimize slippage. Participants were seated in a height-adjustable chair, which allowed the examiner to adjust the height of the subject's head for optimal examination. Participants were instructed to look at a point on the wall 1 m ahead. The examination was conducted by an experienced examiner and manually performed more than 20 times (head rotation 15–20°, duration 150–200 ms, peak velocity $> 150°/s$) on both sides of each plane. Normal vHIT was defined as having a gain of ≤ 2 standard deviation (SD) of the age-matched normal gain reference range and no fixation catch-up saccades.

VEMPs

To record cervical VEMPs, subjects were in the supine position and asked to hold their head up 30° above the floor and rotate it contralaterally to ensure contraction of the sternocleidomastoid muscles (11). An active surface EMG electrode placed over the belly of the ipsilateral sternocleidomastoid and a reference self-adhesive Ag/AgCl electrode on the incisura jugularis of the sternum were used for the recording.

For the recording of ocular VEMPs, the active electrode was located on the infraorbital margin 1 cm below the center of the contralateral lower eyelid and the reference electrode was placed 1 cm below the active electrode. During monaural sound stimulation, participants were asked to fix their gaze on the target located 25° above eye level. Unilateral 500 Hz, 5 ms air-conducted sound tone bursts with a calibrated 100 dB intensity were used. Amplified EMG potentials were bandpass filtered at 10–3,000 Hz and then the data were averaged from the stimulus onset to 50 ms.

Neuropsychological Tests

All participants underwent the Visual Object and Space Perception Battery (VOSP) for visuospatial perception, the Corsi block test for visuospatial memory, and K-MMSE for general cognition.

VOSP

The VOSP battery consists of object perception and space perception tests. The spatial perception function was evaluated using dot count, position discrimination, number location, cube analysis, and the block design test. In addition, visuospatial memory was assessed using the Corsi block test.

i) Dot count: Participants were asked to count how many black dots are on a white card. There were 10 cards. One point was bestowed for every correct count and maximum score is 10.
ii) Position discrimination: Subjects were presented with 20 boards with two adjacent horizontal squares with a black dot (5 mm) at the center of each. One of the two squares had a dot in the center and the other was slightly off. The subject was asked to distinguish in which square the black dot was in the exact center. The examiner recorded the number of correct answers and maximum score is 20.
iii) Number location: Subjects were presented with 10 boards with two adjacent vertical squares. The upper square had numbers arranged in a random and the lower square had only one black dot. The subject was asked to identify which number in the top square corresponded to the dot in the bottom square (maximum score: 10).
iv) Cube analysis: Subjects were presented with 10 boards with three-dimensionally arranged cubes. Subjects were asked to identify how many cubes were on each board, including the hidden one (maximum score: 10). This test evaluated three-dimensional analysis presented on a two-dimensional plane.

Corsi Block Test

The examiner tapped cubes starting with a sequence of two blocks in front of the participant. Two trials were performed per block sequence length. The participant had to tap the cube sequence in the same order immediately after the examiner had finished. The number of cubes tapped ranged from 2 to 9. The subject had two chances to tap the cubes in the correct order; the subject only proceeded to the next step if he or she provided the correct answer.

Psychometric Testing

Korean Beck Depression Inventory (K-BDI)

The Korean version of BDI-II is a 21-item self-report inventory which is designed to determine the presence and severity in depressive symptoms. Based on the severity in the last 2 weeks, each item is rated on a 4-point Likert-type scale ranging from 0 to 3.

Korean Beck Anxiety Inventory (K-BAI)

The BAI is also a self-report assessment of anxiety symptoms, which consists of 21 items rated on a 4-point Likert scale from 0 (not at all) to 3.The total score ranges from 0 to 63 in each test, with higher scores inferring more severe depressive (BDI) and anxiety (BAI) symptoms.

Imaging Data Acquisition and Analysis

FDG PET

All participants fasted for at least 6 h prior to the intravenous injection of [18F]FDG, and blood glucose levels in all patients were < 126 mg/dL. Approximately 5.5 MBq of [18F]FDG per kilogram of body weight was administered intravenously. Scanning was performed approximately 60 min after [18F]FDG administration. Brain images were obtained using a Biograph TruePoint 40 PET/CT scanner (Siemens Medical Solutions, Knoxville, TN, USA). A CT scan was first obtained using a continuous spiral technique (120 kVp, 160 mA, 0.5 s rotation time). Next, a PET scan was taken in a three-dimensional mode for 10 min. The obtained PET data were iteratively reconstructed using an ordered-subset expectation maximization algorithm (128×128 matrix, 3.27 mm slice thickness, subset: 21, iterations: 2). The [18F]FDG PET/CT images were reviewed at a workstation (Syngo MI applications, Flexible Display 7.0.7.7; Siemens Medical Solutions, Erlangen, Germany).

Structural MRI and fMRI

Structural and functional images were acquired on a 3T MRI system (Magnetom Verio, Siemens Healthcare, Erlangen, Germany) with a 12-channel head coil. In a single session, 195 volumes (60 contiguous, axial, 2.5 mm-thick slices each; 1-mm gap) were acquired with a gradient echo, echo-planar imaging (EPI) T2*-sensitive sequence (repetition time: 2,000 ms; echo time: 30 ms; flip angle: 90°; matrix: 64×64; field of view: 192×192 mm). To reduce head movement and consequently artificial activation patterns, a foam pad was wrapped around the headphones. Anatomical images included a T1-weighted magnetization-prepared rapid gradient echo (MP-RAGE) sequence with a 256-mm field-of-view and $1.0 \times 1.0 \times 1.0$ mm^3 isotropic spatial resolution (TE, 4.37 ms; TR, 2,100 ms; 160 slices). Subjects were instructed to minimize movement and keep their eyes closed but not fall asleep.

Resting-state fMRI data were preprocessed with AFNI software (http://afni.nimh.nih.gov/) (13). After discarding the initial five volumes from each fMRI, images were de-spiked, slice timing was applied, and head motion was corrected. In the head motion correction, all functional scans were realigned to the first image with a 6-parameter, rigid body, spatial transformation, and differentiated head realignment parameters across frames yielded a six-dimensional time course representing instantaneous head motion. The anatomical image was co-registered to the functional image using affine registration with a Local Pearson Correlation cost function. The eroded white matter mask and eroded large ventricle (LV) mask were also transformed to EPI space. All images and masks in native space were normalized to a standard MNI 152 template and resampled with an isotropic voxel size of 2 mm. The normalized fMRI data were spatially smoothed with a 6-mm full width at half maximum (FWHM) Gaussian kernel (14). The normalized and smoothed fMRI data were corrected using a regression model with the nuisance signal removed with an anatomy-based correlation correction (ANATICOR) method (15). The anatomy-based regressors were extracted before spatial smoothing to avoid mixing signals from different tissues. The regressors of the ANATICOR method were as follows: (1) 6 parameters obtained by head motion correction, (2) the signal from the eroded LV mask, and (3) the signal from the eroded WM mask in the local neighborhood ($r = 15$ mm) of the voxel. The censoring was performed together in the nuisance regression model. The censoring was applied to fMRI data with the Euclidian norm of the first derivative of head motion > 0.25. The regressed and censored images were temporally bandpass-filtered ($0.009 < f < 0.08$) to reduce physiological noise.

Defining Regions of Interests (ROIs) and Seed-Based Functional Connectivity Analysis

The predefined established seed regions of known visual and vestibular processing areas were used to generate correlation maps ($p < 0.05$, FWE correction). The seeds included the bilateral posterior insula, inferior insula, superior temporal gyrus, parietal operculum, inferior parietal lobule (IPL), precuneus, thalamus, cerebellar flocculus and nodulus, vermis and vestibular nuclei in the brainstem. The structural boundaries of the whole seeds were delineated instead of defining spherical seeds within each region. The location of each seed was manually modified until it was within the boundary of each seed region in every subject. In order to analyze the functional connectivity of the significant regions in the PET analysis results, MNI coordinates of increased metabolic regions as well as widespread activation of the prefrontal cortex were used as follows: bilateral superior frontal cortex (SFC, x/y/z = 28/4/58 and −30/2/58), inferior prefrontal cortex (IPFC, x/y/z = 32/24/0 and −28/24/2), lateral orbital frontal cortex (LOFC, x/y/z = ±46, 34, 0) and bilateral dorsolateral prefrontal cortex (DLPFC, x/y/z = 30/46/20 and −34/52/14). These regions of interest (ROIs) were described as a 6-mm radius sphere at the peak using a voxel mask.

A region of interest (ROI)-based approach with *a priori* selected regions was used for resting-state functional connectivity analyses. For each seed, a resting-state time series was extracted separately for each subject by computing the mean BOLD intensity of all voxels within the seed boundary at each MR frame (time point). A correlation map of each seed was obtained *via* correlation analysis between the seed reference time series and the time series of the rest of the brain in a voxel-wise manner. The correlation map for each subject was converted to a z-value using Fisher's r-to-z transformation. The Mann-Whitney U-test was performed to compare functional connectivity between the subjects with and without t-MdDS. Monte Carlo simulation was conducted to control type I errors by calculating the significance level combination of cluster size and uncorrected individual voxel *p*-value (16). The simulation parameters were as follows: uncorrected individual voxel $p = 0.02$, simulation = 10,000 times, 8 mm FWHM Gaussian filter width with a whole brain mask. The Mann-Whitney U test was corrected by $P\alpha < 0.05$ level (uncorrected individual voxel height threshold of $p < 0.02$ with a minimum cluster size of 306 voxels).

Data Availability Statement

All of the individual participant data that underlie the results reported in this article, after deidentification (manuscript, tables, and figures) will be shared.

Statistical Analysis

All metrics were compared between groups using the non-parametric Mann-Whitney *U*-test. Fisher's exact test was used for univariate comparison regarding sex and motion sickness. The

Student's t-test was applied to test age and educational level as well as the Corsi block test. The Mann-Whitney U-test was used to compare the mean values of the two groups in MMSE, time at sea, and the visuospatial memory function test. A $p < 0.05$ was considered statistically significant. Analyses were performed using the Statistical Package for Social Sciences software (SPSS, Inc., Chicago, IL, USA).

RESULTS

Demographic and Clinical Data

Twenty-eight fishermen who resided in Buan County participated in and completed the present study. Fifteen of the participants experienced a transient sense of rocking and swaying motion immediately after landing (t-MdDS, 15/28, 53.6%) and 13 participants did not (13/28, 46.4%). The demographic and clinical characteristics of the participants with t-MdDS and those without are summarized in **Table 1**. No differences in age, sex, educational level, K-MMSE score, and total time spent at sea were observed between the two groups. A female predominance in MdDS has been noted in many studies varying from 75% to >95% and age of onset is typically in the 40 to 50 s. In the current study, however, t-MdDS appears to be consistent in both men and women in the 50 s. Symptoms described shortly after landing included rocking and swaying and the mean duration was 3.27 h (range, 2–6 h). No participant in the t-MdDS group became seasick while at sea and similarly, motion sickness with other transportation was experienced less in participants with t-MdDS than in those without (**Table 1**).

Vestibular Testing

Spontaneous or induced nystagmus was not observed in either group during VOG recordings. vHITs were normal for all six semicircular canals on both sides in all participants. There were no abnormalities in the cVEMP and oVEMP amplitudes and latencies in both groups.

Neuropsychological and Psychometric Tests

Visuospatial perception and general cognition did not differ between groups with and without t-MdDS (**Table 2**). However, in the Corsi block test, a predominant method for assessing spatial memory capacity, participants with t-MdDS performed significantly better than those without symptoms (6.40 ± 0.91 vs. 5.31 ± 1.24, $p = 0.016$, Mann-Whitney test; **Table 2**).

A comparison of the mean scores of the Korean version of BDI across two groups did not reveal significant differences between the t-MdDS group (mean = 22.69, SD = 28.9) and the group without t-MdDS (mean = 15.46, SD = 17.3, $p = 0.11$, **Table 1**). BAI also did not show differences between the two groups (mean = 7.92, SD = 3.67 vs. mean = 8.8, SD = 11.1, $p = 0.39$, **Table 1**). Correlation analysis with the BDI / BAI did not reveal any significant correlation in the brain structures with different metabolic activation or deactivation patterns.

TABLE 1 | Demographic and clinical characteristics of participants with MdDS and those without t-MdDS.

Characteristics	With t-MdDS (15/28, 53.6%)	Without t-MdDS (13/28, 46.4%)	*p*-value
Age	50.9 ± 6.0	56.7 ± 8.2	0.06†
Sex (male), *n* (%)	6 (40.0)	6 (46.2)	1.00*
Education (years)	10.2 ± 2.7	9.1 ± 2.7	0.30†
MMSE	28.8 ± 1.4	27.6 ± 1.7	0.06**
K-BDI[a]	22.7	15.5	0.11†
K-BAI[b]	7.92	8.8	0.39†
Handed (Right), *n* (%)	15 (100)	12 (100)	
Time at sea			
Total (years)	18.9 ± 7.7	20.1 ± 17.5	0.89**
Months per year (months)	7.6 ± 1.8	6.9 ± 1.7	0.13**
Hours per day (hours)	8.1 ± 2.1	6.7 ± 4.0	0.25**
Duration of symptoms (hours)			
Mean (SD)	3.27 (1.39)		
Median	3		
Range	2–6		
Motion sickness, n (%)	1 (6.7)	7 (58.3)	0.02*
Migraine	6 (40)	3 (23)	0.47
Aggravating factors	Bad sea conditions (windy with large waves)		
Relieving factors	Sufficient rest, lying down, or sleeping, during motion and driving		

**Fisher's exact test; †Student's t-test; **Mann-Whitney U-test; [a]K-BDI, Korean Beck Depression Inventory; [b]K-BAI, Korean Beck Anxiety Inventory.*

TABLE 2 | Results of visuospatial memory function tests in participants with and without t-MdDS.

	With t-MdDS (*n* = 15)	Without t-MdDS (*n* = 13)	*p*-value[a]
Visuospatial perception			
Position discrimination	18.9 ± 1.80	18.4 ± 4.0	0.94
Number location	7.7 ± 3.2	6.5 ± 2.6	0.20
Cube analysis	9.3 ± 1.5	8.3 ± 2.1	0.07
Block design	8.9 ± 2.2	8.4 ± 3.5	0.79
Visuospatial memory			
Corsi block test	6.4 ± 0.9	5.3 ± 1.2	0.016

[a]Mann-Whitney U-test.

FDG-PET Analysis

Subtraction analysis between groups with and without t-MdDS showed an increased metabolism in the left superior occipital, superior and inferior parietal lobules, and the right superior frontal gyrus including the dorsolateral prefrontal cortex (DLPFC) in subjects with t-MdDS compared to those

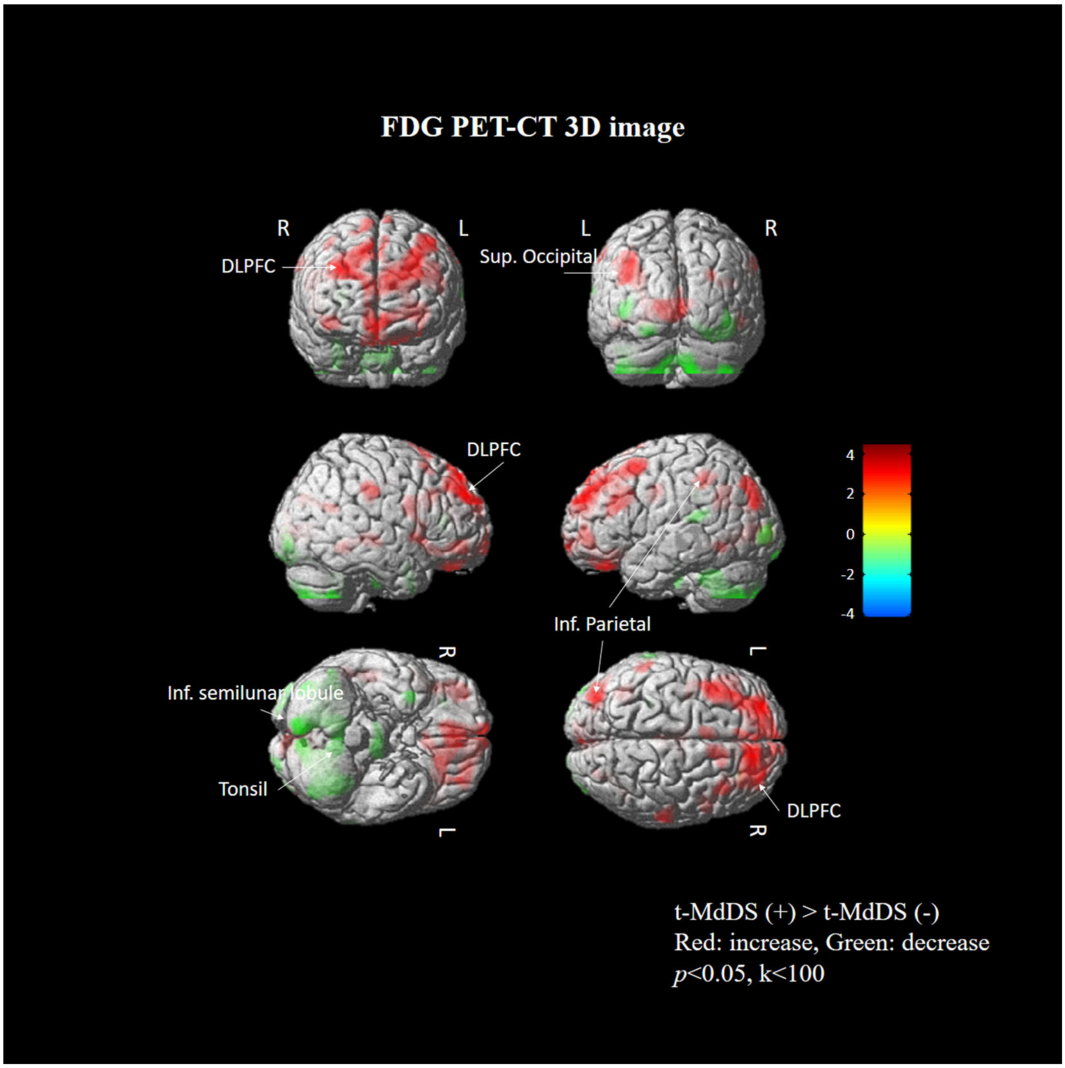

FIGURE 1 | Areas of relative hyper- and hypometabolism in participants with t-MdDS compared with those without. Image is presented at $z > 2.57$ for better visualization; extent voxels: 0.

without. In addition, hypometabolism was observed in t-MdDS participants bilaterally in the cerebellum including the right inferior semilunar lobule, nodulus, and the vermis especially the uvula ($p < 0.05$, uncorrected, **Figure 1** and **Table 3**).

Structural MRI

Volume changes in regional gray matter were not detected at a threshold of $p < 0.001$ uncorrected for the whole brain between groups with and without t-MdDS.

Resting-State fMRI

Different resting-state functional connectivities were observed at three ROIs (right flocculus, left posterior superior temporal gyrus, and left parietal operculum OP2) of the vestibular processing regions (**Figure 2** and **Table 4**, Mann-Whitney *U* test). Compared with participants without t-MdDS, subjects with t-MdDS showed decreased functional connectivity between the right flocculus and right middle occipital gyrus (z-value: −3.757, $P\alpha < 0.05$), between the left posterior superior temporal gyrus and right inferior parietal lobule (z-value: −3.66, $P\alpha < 0.05$) and the right fusiform gyrus (z-value: −3.757, $P\alpha < 0.05$), and between the left parietal operculum and left cuneus (z-value: −4.233. $P\alpha < 0.05$) and right fusiform gyrus (z-value: −3.611, $P\alpha < 0.05$). The inferior and posterior insula, which are considered core structures of vestibular processing and integration, did not differ in the resting-state functional connectivities between both groups with and without t-MdDS.

Sub-analysis of functional connectivity for the significant regions in the PET analysis, including widespread activation of the prefrontal cortex, revealed that the t-MdDS group showed decreased functional connectivity between the right superior frontal cortex and left cuneus, between the left inferior prefrontal cortex and right lingual and fusiform gyri, and between the right DLPFC and right cuneus compared to participants

TABLE 3 | Comparison of [18F]FDG PET/CT between participants with and without t-MdDS.

Brain Regions	Side	Coordinates (mm)			Z-score
		x	*y*	*z*	
Increased					
Superior occipital gyrus	L	−40	−84	34	2.74
Superior frontal gyrus	R	32	52	29	3.52
Superior parietal lobule	L	−38	−75	50	3.46
Inferior parietal lobule	L	−63	−39	44	2.81
Decreased					
Inferior semi-lunar lobule	R	10	−80	−38	−2.76
Nodule		10	−50	−28	−2.55
Uvula		−4	−81	−35	−2.52
Tonsil	L	−34	−58	−39	−2.38

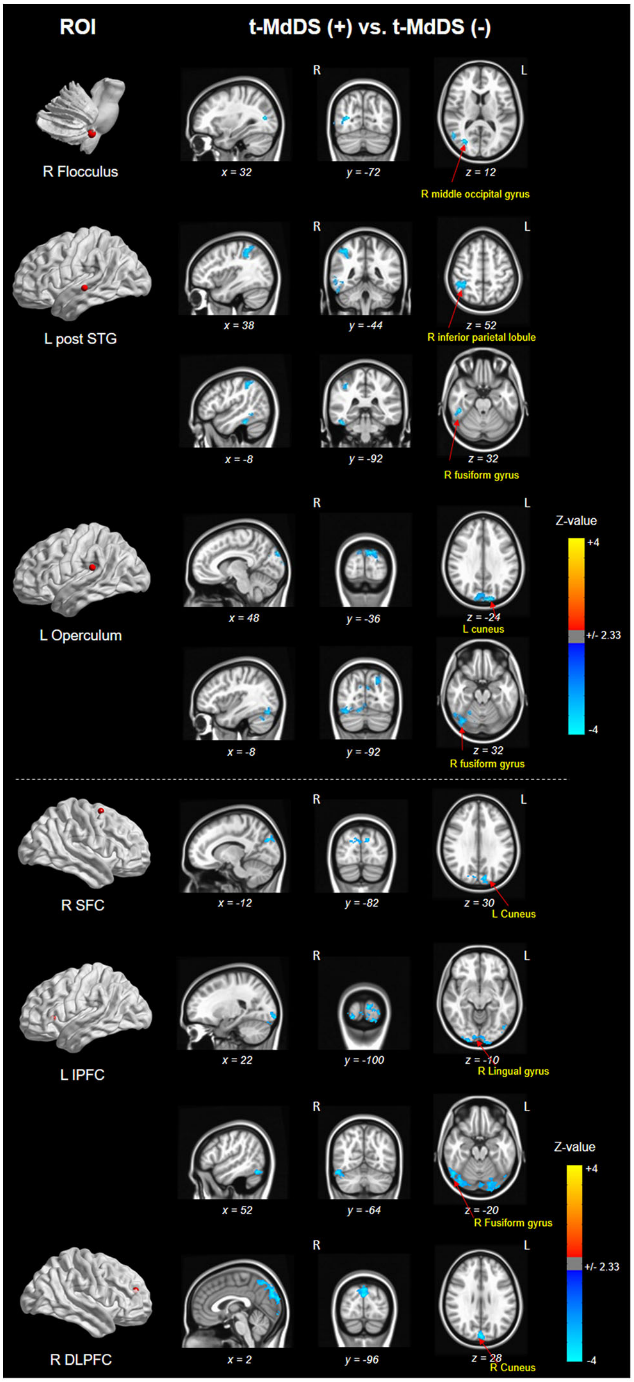

FIGURE 2 | Results of functional connectivity for three ROIs of the vestibular processing regions in both groups. Negative (cold color) *z*-value indicates that functional connectivity of subjects with t-MdDS is significantly lower than functional connectivity of subjects without symptoms ($P\alpha < 0.05$).

without t-MdDS (**Table 4**). Functional connectivity between the prefrontal cortex and the vestibular processing regions was increased between the left lateral orbital PFC and the left flocculus; it was decreased between the right vestibular nuclei and left inferior PFC and lateral orbital PFC (**Figure 3**).

DISCUSSION

Task-free resting-state fcMRI and FDG PET combined with neuropsychological tests were used in the present study to investigate the functional brain connectivity and metabolic signatures of t-MdDS in local fishermen. Visuospatial memory function was significantly higher, and changes in brain glucose metabolism and functional connectivity in the vestibular and visuospatial attention processing areas were observed in the t-MdDS group compared with the group without t-MdDS. FDG metabolism in t-MdDS participants was significantly increased in several regions, especially widespread bilaterally in the DLPFC and OFC that is involved in integration of different cognitive operations as well as in emotions. The prefrontal cortex plays a vital role in mood-regulating circuits, anxiety disorders, and fast responses to threats (17) and the OFC is involved in sensory integration and in representing the affective value and expectation (18). Metabolism increases were also seen in visual areas including the superior occipital gyrus responsive to visual orientation and to visuospatial attention. Further, an increase was found in the superior and inferior parietal lobules, which also contribute to spatial attention and reorientation (**Figure 1** and **Table 3**). This increased metabolism in the areas associated with visuospatial attention and orientation might reflect increased visuospatial memory function determined with the Corsi block test.

In addition, glucose metabolism was significantly reduced in the vestibulocerebellum, including the nodulus and uvula, in t-MdDS participants. This could indicate an adaptive mechanism that suppresses the enhanced visual-vestibular inputs during continuous movement on a boat. Alternatively, decreased function in the vestibulocerebellum may cause inadequate suppression of enhanced visuospatial memory induced by continuous oscillation of the visual environment. In combination with the bilateral enhanced metabolism of the prefrontal cortex, the reduced cerebellar metabolism may more likely represent

TABLE 4 | Different resting-state functional connectivities between participants with and without t-MdDS.

Seeds	Brain regions	Side	Coordinates (mm)			Minimum	Voxels
			x	*y*	*z*	z	
Flocculus, R	Middle occipital gyrus	R	32	−72	12	−3.757	426
Posterior superior temporal gyrus, L	Inferior parietal lobule fusiform gyrus	R R	38 48	−44 −36	52 −24	−3.66 −3.757	403 332
Parietal operculum 2, L	Cuneus fusiform gyrus	L R	−8 38	−92 −74	32 −20	−4.233 −3.611	929 657
Superior FC, R	Cuneus	L	−12	−82	30	−3.708	307
Inferior PFC, L	Lingual gyrus	R	22	−100	−10	−4.198	2160
	Fusiform gyrus	R	52	−64	−20	−4.031	609
DLPFC, R	Cuneus	R	2	−86	28	−3.939	975

FC, frontal cortex; PFC, prefrontal cortex; DLPFC, dorsolateral prefrontal cortex; R, right; L, left.

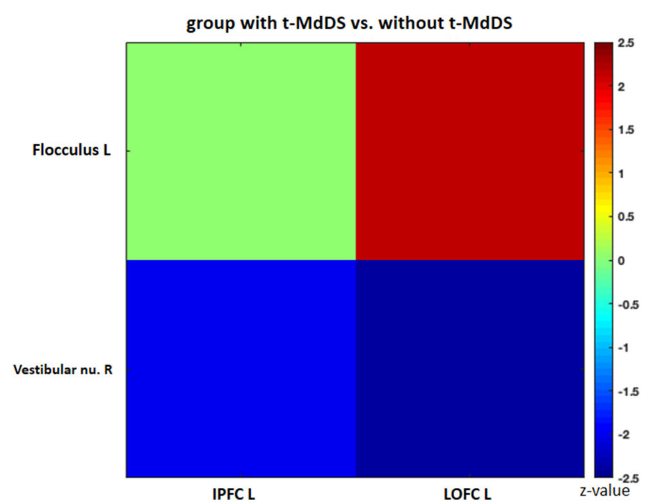

FIGURE 3 | Functional connectivity of the significant regions from the FDG-PET analysis. IPFC, inferior prefrontal cortex; LOPFC, lateral orbital prefrontal cortex; R, right; L, left.

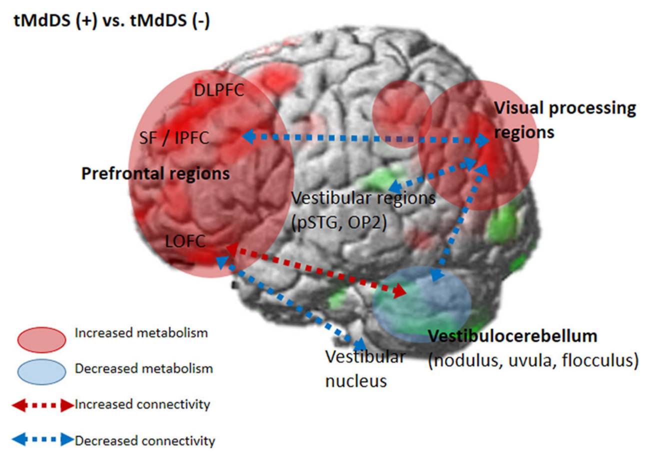

FIGURE 4 | Brain metabolic and functional connectivity changes in the t-MdDS group. Schematic descriptions are superimposed on the cortical [18F]FDG-PET results.

a reduction of automatic control, since the cerebellum is important for several aspects of sensorimotor integration such as subconscious automatic motor control (19).

We further assessed functional connectivity changes between the visual and vestibular sensory processing regions in the participants with t-MdDS compared to those without. During rest, fcMRI of the normal brain shows large-amplitude spontaneous low-frequency (<0.1 Hz) fluctuations that are temporally correlated across functionally related areas referred to as "resting-state functional connectivity" (rs-fc) (20). Connectivity between the vestibular regions and the visual association areas of the middle occipital gyrus, fusiform gyrus, and cuneus was significantly decreased in t-MdDS subjects based on rs-fc between the vestibular seed regions and whole-brain analysis (**Figure 2** and **Table 4**). Sub-analysis for fc of the significant regions in the PET analysis results showed decreased connectivities between the prefrontal cortices and visual processing areas of the cuneus as well as lingual and fusiform gyri in the t-MdDS group (**Figure 2** and **Table 4**). This could mean that the participants rely less on vestibular but more on visual input, i.e., they show a sensory shift from the vestibular to the visual system. Thus, the pattern of reduced connectivity between vestibular regions and visual cortex areas, reduced metabolism in the vestibulocerebellum, and increased metabolism in prefrontal and visual cortex areas reflects an enhanced conscious control of sensorimotor function under the lead of the visual system instead of an unconscious automatic control of stance and gait (**Figure 4**). A similar pattern was found in patients with functional dizziness, i.e., phobic postural vertigo (21), who are known to show a continuous co-contraction of antigravity muscles during normal stance that normalizes during distracting attention by dual task conditions (22). This co-contraction may be an expression of an irrational fear of imbalance which is observed also in specific phobias (23).

Clinically, the fishermen tended to have t-MdDS symptoms when they were exposed to a significant amount of motion in a boat on the sea during extreme weather with high winds and unpredictable large waves rather than when they spent a longer time on a calm sea (**Table 1**). Boat stability depends not only on the size of the boat but also on wind and wave conditions as well as the direction of the boat. Since fishing boats are usually small, substantial roll can occur depending on the size of the waves despite the ship's roll stabilizers. Modulation of roll motion mostly depends on the integrity of the cerebellar nodulus (24–26). In animal and human experiments, the nodulus and uvula exert powerful control on the velocity storage integrator. The lateral portions of the nodulus cause discharge activity in velocity storage during visual suppression as well as loss of stored activity in velocity storage during tilt-suppression (27–30). In addition, the central parts of the nodulus generate activities responsible for orienting the axis of eye, head, and body velocity to the spatial vertical (26, 28, 30, 31), and habituation of the time constant of the VOR (32). The majority of vestibular fibers in Scarpa's ganglion project directly to the Purkinje cells in the contralateral nodulus through the inferior olives that sense active or passive movements of the head and body (33). Thus, there is a strong projection to the nodulus continuously modulating the active or passive head and body movements. Vestibular neurons sense the (roll) position of the head and body and transmit this activity to the nodulus via the inferior olives. The nodulus also receives input from the inferior olive that originates in the nucleus of the optic tract which carries optokinetic-generated activity to the vestibular nuclei and the nodulus. Recently, the existence of visually driven Purkinje cells was revealed in the anterior part of the nodulus and ventral uvula near the midline (34). Studies of neural activity in the flocculus of alert monkeys showed that the main mossy fiber input to the flocculus originates in the vestibular nuclei and a second input of unknown origin conveys visual information from retinal slip (35). Thus, part of the flocculus may also be specialized to work visual-vestibular interactions. Convergence of vestibular and visual motion information is essential for accurate spatial orientation and navigation. Therefore, prolonged exposure to vestibular and moving visual inputs, when at sea, could condition the motion-related neurons or visually driven Purkinje cells in the nodulus and flocculus, subsequently contributing to changes or even maladaptation of the velocity storage integrator or visual-vestibular interaction in the vestibulocerebellum.

Another interesting finding was that participants in the t-MdDS group did not become seasick while at sea and experienced less motion sickness with other methods of transportation than those without t-MdDS (**Table 1**). The mechanism of this relative tolerance of motion sickness in the t-MdDS group remains unclear, but the properties of visuovestibular interaction also could be explained. As our data showed that the t-MdDS participants depend more on the visual than the vestibular system in the setting of consistently spontaneous motion, the participants may become more tolerant of slow changes in the visual surroundings because the visual system is usually used to stabilize low-frequency postural and visual sway. Indeed, a low-frequency oscillatory motion stimulation of 0.1 to 0.4 Hz as a roll and pitch rotation was found to be a typical experimental stimulus for t-MdDS in humans, especially when it was more unpredictable and along multiple dimensions (36). These low frequencies include both the frequency of natural stimuli n the boat (37) as well as the predominant frequency of 0.2–0.3 Hz of rocking sensations and body oscillations in individuals with MdDS (8, 9). During continuous activity within the visual system on a boat, reciprocal inhibitory activity of the visual and vestibular systems (38) leads to a suppression of vestibular processing areas in order to reduce the visuovestibular functional conflict. This tolerance to motion sickness with other transportation in subjects with t-MdDS is also consistent with Dai's readaptation hypotheses, which implies that if velocity storage path of the VOR cannot adapt, subjects experience motion sickness, and if VOR does adapt, then the subject may get MdDS (8).

Perception of motion and space information in the brain is processed in a widely distributed network involving the vestibular, visual, and somatosensory cortices because the interactions among these sensory systems are important for postural and spatial perception. In contrast to other sensory modalities of visual or auditory inputs, a unimodal primary sensory cortex for vestibular inputs does not exist. Instead, a multimodal vestibular cortical network contains neurons integrating information from vestibular, visual, auditory, and somatosensory stimuli. These multimodal sensory integrating neurons have been found not only in the vestibular brainstem nuclei but also in particular in several cortical regions centered around the posterior insula, retroinsular region, parietal operculum, and adjacent posterior perisylvian regions of the parietal and temporal cortices which superimpose the vestibular cortex and contribute to perception of spatial cognition and gravity (39, 40). Perception of self-motion is processed by the multimodal nature of the vestibular information in which visual signals as well as somatosensory and auditory inputs collectively provide information (41). However, detection of movement in space may often be more dependent on visual input than vestibular and somatosensory information, since it is necessary to stabilize the eyes on targets of interest. Significantly increased glucose metabolism in the visuospatial attention regions with reduced metabolism in the vestibulocerebellum and decreased resting-state functional connectivity between these two functional regions in the participants with t-MdDS indicate reductions in the integration of vestibular input and enhancement of visuospatial attention. The wide-spread increased glucose metabolism in the prefrontal and frontal cortex bilaterally and the visual processing areas associated with decreased functional connectivity between them also raise the question of whether these changes within the vestibular and visual networks could be due to an enhanced self-awareness, self-attention, and emotional processes (**Figure 4**). Increased functional connectivities were also found between the vestibulocerebellum (flocculus) and the orbitofrontal cortex in t-MdDS participants, i.e., within brain networks important for adaptive and goal-directed behavior (**Figure 3**). Similarly altered connectivities within the prefrontal and orbitofrontal cortex have been observed in patients with mood disorders (42, 43). The enhanced connectivity of these networks combined with decreased fc between the visual, vestibular and prefrontal networks in our study might explain the features of over-generalization and anxious response to certain stimuli, a disturbed self-awareness, and an overacted compensatory mechanism for evaluating the specific stimuli in the participants with t-MdDS (21). The dorsolateral prefrontal cortex influences multiple interconnected networks with effects on mood, cognition, and visuospatial processing (44–47). As mentioned above, similar patterns of increased metabolism or connectivity in the prefrontal cortex combined with a decrease in the vestibulocerebellum were also found in patients with functional dizziness (21). The patients with functional dizziness also shift their attention from the vestibular to the visual system. Based on such similarities, an overlap in a kind of continuum from transient MdDS via chronic MdDS to functional dizziness and anxiety disorders, all with enhanced self-awareness, can be suggested. Therefore, these networks may process the data differently under normal conditions such as when t-MdDS enhanced attention to the visual system and to more conscious balance control.

DATA AVAILABILITY STATEMENT

The raw data supporting the conclusions of this article will be made available by the authors, without undue reservation.

ETHICS STATEMENT

The studies involving human participants were reviewed and approved by the Institutional Review Board at Jeonbuk National University Hospital (IRB No. 2017-09-022). The patients/participants provided their written informed consent to participate in this study.

AUTHOR CONTRIBUTIONS

S-YO, J-SK, and MD contributed to the design and implementation of the research. S-HJ and J-JK contributed to gather and analyze the data and to the writing of the manuscript. Y-HP, Y-HH, H-JJ, J-ML, and MP contributed to the analysis of the imaging results and to the writing of the manuscript. All authors contributed to the article and approved the submitted version.

FUNDING

This work was supported by a National Research Foundation of Korea (NRF) grant funded by the Korean government (Ministry of Science and ICT) (No. 2019R1A2C1004796 and 2019R1H1A2101514).

REFERENCES

1. Brown JJ, Baloh RW. Persistent mal de debarquement syndrome: a motion-induced subjective disorder of balance. *Am J Otolaryngol*. (1987) 8:219–22. doi: 10.1016/S0196-0709(87)80007-8
2. Cha YH, Brodsky J, Ishiyama G, Sabatti C, Baloh RW. Clinical features and associated syndromes of mal de debarquement. *J Neurol*. (2008) 255:1038–44. doi: 10.1007/s00415-008-0837-3
3. Cha YH. Mal de debarquement syndrome: new insights. *Ann N Y Acad Sci*. (2015) 1343:63–8. doi: 10.1111/nyas.12701
4. Cohen H. Mild mal de debarquement after sailing. *Ann N Y Acad Sci*. (1996) 781:598–600. doi: 10.1111/j.1749-6632.1996.tb15734.x
5. Gordon CR, Doweck I, Nachum Z, Gonen A, Spitzer O, Shupak A. Clinical features of mal de debarquement: adaptation and habituation to sea conditions. *J Vestib Res*. (1995) 5:363–9.
6. Moeller L, Lempert T. Mal de debarquement: pseudo-hallucinations from vestibular memory? *J Neurol*. (2007) 254:813–5. doi: 10.1007/s00415-006-0440-4
7. Gordon CR, Doweck I, Nachum Z, Gonen A, Spitzer O, Shupak A. Survey of mal de debarquement. *BMJ*. (1992) 304:544. doi: 10.1136/bmj.304.6826.544
8. Dai M, Cohen B, Smouha E, Cho C. Readaptation of the vestibulo-ocular reflex relieves the mal de debarquement syndrome. *Front Neurol*. (2014) 5:124. doi: 10.3389/fneur.2014.00124
9. Cohen B, Yakushin SB, Cho C. Hypothesis: the vestibular and cerebellar basis of the Mal de debarquement syndrome. *Front Neurol*. (2018) 9:28. doi: 10.3389/fneur.2018.00028
10. Cha YH, Chakrapani S, Craig A, Baloh RW. Metabolic and functional connectivity changes in mal de debarquement syndrome. *PLoS ONE*. (2012) 7:e49560. doi: 10.1371/journal.pone.0049560
11. Cha YH, Chakrapani S. Voxel based morphometry alterations in Mal de debarquement syndrome. *PLoS ONE*. (2015) 10:e0135021. doi: 10.1371/journal.pone.0135021
12. Oh SY, Kim DH, Yang TH, Shin BS, Jeong SK. Clinical classification and neuro-vestibular evaluation in chronic dizziness. *Clin Neurophysiol*. (2015) 126:180–6. doi: 10.1016/j.clinph.2014.03.030
13. Cox RW. AFNI: software for analysis and visualization of functional magnetic resonance neuroimages. *Comput Biomed Res*. (1996) 29:162–73. doi: 10.1006/cbmr.1996.0014
14. Saad ZS, Glen DR, Chen G, Beauchamp MS, Desai R, Cox RW. A new method for improving functional-to-structural MRI alignment using local Pearson correlation. *Neuroimage*. (2009) 44:839–48. doi: 10.1016/j.neuroimage.2008.09.037
15. Jo HJ, Saad ZS, Simmons WK, Milbury LA, Cox RW. Mapping sources of correlation in resting state FMRI, with artifact detection and removal. *Neuroimage*. (2010) 52:571–82. doi: 10.1016/j.neuroimage.2010.04.246
16. Poline J-B, Worsley KJ, Evans AC, Friston KJ. Combining spatial extent and peak intensity to test for activations in functional imaging. *Neuroimage*. (1997) 5:83–96. doi: 10.1006/nimg.1996.0248
17. Duval ER, Javanbakht A, Liberzon I. Neural circuits in anxiety and stress disorders: a focused review. *Ther Clin Risk Manag*. (2015) 11:115–26. doi: 10.2147/TCRM.S48528
18. Kringelbach ML. The human orbitofrontal cortex: linking reward to hedonic experience. *Nat Rev Neurosci*. (2005) 6:691–702. doi: 10.1038/nrn1747
19. Morton SM, Bastian AJ. Cerebellar control of balance and locomotion. *Neuroscientist*. (2004) 10:247–59. doi: 10.1177/1073858404263517
20. Biswal B, Yetkin FZ, Haughton VM, Hyde JS. Functional connectivity in the motor cortex of resting human brain using echo-planar MRI. *Magn Reson Med*. (1995) 34:537–41. doi: 10.1002/mrm.1910340409
21. Popp P, Zu Eulenburg P, Stephan T, Bögle R, Habs M, Henningsen P, et al. Cortical alterations in phobic postural vertigo - a multimodal imaging approach. *Ann Clin Transl Neurol*. (2018) 5:717–29. doi: 10.1002/acn3.570
22. Wuehr M, Brandt T, Schniepp R. Distracting attention in phobic postural vertigo normalizes leg muscle activity and balance. *Neurology*. (2017) 88:284–8. doi: 10.1212/WNL.0000000000003516
23. Schniepp R, Wuehr M, Huth S, Pradhan C, Brandt T, Jahn K. Gait characteristics of patients with phobic postural vertigo: effects of fear of falling, attention, and visual input. *J Neurol*. (2014) 261:738–46. doi: 10.1007/s00415-014-7259-1
24. Barker AK, Duster M, Valentine S, Hess T, Archbald-Pannone L, Guerrant R, et al. The cerebellar nodulus and ventral uvula control the torsional vestibulo-ocular reflex. *J Neurophysiol*. (1994) 72:1443–7. doi: 10.1152/jn.1994.72.3.1443

25. Kornadt AE, Hess TM, Voss P, Rothermund K. Lesion of the nodulus and ventral uvula abolish steady-state off-vertical axis otolith response. *J Neurophysiol*. (1995) 73:1716–20. doi: 10.1152/jn.1995.73.4.1716
26. Wearne S, Raphan T, Cohen B. Control of spatial orientation of the angular vestibuloocular reflex by the nodulus and uvula. *J Neurophysiol*. (1998) 79:2690–715. doi: 10.1152/jn.1998.79.5.2690
27. Raphan T, Matsuo V, Cohen B. Velocity storage in the vestibulo-ocular reflex arc (VOR). *Exp Brain Res*. (1979) 35:229–48. doi: 10.1007/BF00236613
28. Raphan T, Cohen B. The vestibulo-ocular reflex in three dimensions. *Exp Brain Res*. (2002) 145:1–27. doi: 10.1007/s00221-002-1067-z
29. Waespe W, Cohen B, Raphan T. Dynamic modification of the vestibulo-ocular reflex by the nodulus and uvula. *Science*. (1985) 228:199–202. doi: 10.1126/science.3871968
30. Dai M, Kunin M, Raphan T, Cohen B. The relation of motion sickness to the spatial-temporal properties of velocity storage. *Exp Brain Res*. (2003) 151:173–89. doi: 10.1007/s00221-003-1479-4
31. Wearne S, Raphan T, Waespe W, Cohen B. Control of the three-dimensional dynamic characteristics of the angular vestibulo-ocular reflex by the nodulus and uvula. *Prog Brain Res*. (1997) 114:321–34. doi: 10.1016/S0079-6123(08)63372-5
32. Cohen H, Cohen B, Raphan T, Waespe W. Habituation and adaptation of the vestibuloocular reflex: a model of differential control by the vestibulocerebellum. *Exp Brain Res*. (1992) 90:526–38. doi: 10.1007/BF00230935
33. Barmack NH, Baughman RW, Errico P, Shojaku H. Vestibular primary afferent projection to the cerebellum of the rabbit. *J Comp Neurol*. (1993) 327:521–34. doi: 10.1002/cne.903270405
34. Yakusheva TA, Blazquez PM, Chen A, Angelaki DE. Spatiotemporal properties of optic flow and vestibular tuning in the cerebellar nodulus and uvula. *J Neurosci*. (2013) 33:15145–60. doi: 10.1523/JNEUROSCI.2118-13.2013
35. Waespe W, Henn V. Visual-vestibular interaction in the flocculus of the alert monkey. II. Purkinje cell activity. *Exp Brain Res*. (1981) 43:349–60. doi: 10.1007/BF00238377
36. Schepermann A, Bardins S, Penkava J, Brandt T, Huppert D, Wuehr M. Approach to an experimental model of Mal de Debarquement Syndrome. *J Neurol*. (2019) 266:74–9. doi: 10.1007/s00415-019-09345-6
37. Wawrzynski W, Krata P. On ship roll resonance frequency. *Ocean Eng*. (2016) 126:92–114. doi: 10.1016/j.oceaneng.2016.08.026
38. Brandt T, Bartenstein P, Janek A, Dieterich M. Reciprocal inhibitory visual-vestibular interaction - visual motion stimulation deactivates the parieto-insular vestibular cortex. *Brain*. (1998) 121:1749–58. doi: 10.1093/brain/121.9.1749
39. Indovina I, Maffei V, Pauwels K, Macaluso E, Orban GA, Lacquaniti F. Simulated self-motion in a visual gravity field: sensitivity to vertical and horizontal heading in the human brain. *Neuroimage*. (2013) 71:114–24. doi: 10.1016/j.neuroimage.2013.01.005
40. Lacquaniti F, Bosco G, Gravano S, Indovina I, La Scaleia B, Maffei V, et al. Multisensory integration and internal models for sensing gravity effects in primates. *Biomed Res Int*. (2014) 2014:615854. doi: 10.1155/2014/615854
41. Britten KH. Mechanisms of self-motion perception. *Annu Rev Neurosci*. (2008) 31:389–410. doi: 10.1146/annurev.neuro.29.051605.112953
42. Feldker K, Heitmann CY, Neumeister P, Bruchmann M, Vibrans L, Zwitserlood P, et al. Brain responses to disorder-related visual threat in panic disorder. *Hum Brain Mapp*. (2016) 37:4439–53. doi: 10.1002/hbm.23320
43. Schuck NW, Cai MB, Wilson RC, Niv Y. Human orbitofrontal cortex represents a cognitive map of state space. *Neuron*. (2016) 91:1402–12. doi: 10.1016/j.neuron.2016.08.019
44. Grimault S, Robitaille N, Grova C, Lina JM, Dubarry AS, Jolicoeur P. Oscillatory activity in parietal and dorsolateral prefrontal cortex during retention in visual short-term memory: additive effects of spatial attention and memory load. *Hum Brain Mapp*. (2009) 30:3378–92. doi: 10.1002/hbm.20759
45. Diwadkar VA, Carpenter PA, Just MA. Collaborative activity between parietal and dorso-lateral prefrontal cortex in dynamic spatial working memory revealed by fMRI. *Neuroimage*. (2000) 12:85–99. doi: 10.1006/nimg.2000.0586
46. Cha YH, Cui Y, Baloh RW. Repetitive transcranial magnetic stimulation for Mal de debarquement syndrome. *Otol Neurotol*. (2013) 34:175–9. doi: 10.1097/MAO.0b013e318278bf7c
47. Mucci V, Cha YH, Wuyts FL, Van Ombergen A. Perspective: stepping stones to unraveling the pathophysiology of Mal de debarquement syndrome with neuroimaging. *Front Neurol*. (2018) 9:42. doi: 10.3389/fneur.2018.00042

Conflict of Interest: The authors declare that the research was conducted in the absence of any commercial or financial relationships that could be construed as a potential conflict of interest.

frontiers in Neurology

ORIGINAL RESEARCH
published: 06 August 2020
doi: 10.3389/fneur.2020.00822

A Prospective Analysis of Lesion-Symptom Relationships in Acute Vestibular and Ocular Motor Stroke

Andreas Zwergal[1,2*†], Ken Möhwald[1,2†], Elvira Salazar López[1,2,3], Hristo Hadzhikolev[1,2], Thomas Brandt[2,4], Klaus Jahn[2,5] and Marianne Dieterich[1,2,6]

[1] Department of Neurology, University Hospital, LMU Munich, Munich, Germany, [2] German Center for Vertigo and Balance Disorders, DSGZ, LMU Munich, Munich, Germany, [3] Department of Human Movement Science, Technical University of Munich, Munich, Germany, [4] Clinical Neurosciences, LMU Munich, Munich, Germany, [5] Department of Neurology, Schön Klinik Bad Aibling, Bad Aibling, Germany, [6] Munich Cluster of Systems Neurology, SyNergy, Munich, Germany

OPEN ACCESS

Edited by:
Ji Soo Kim,
Seoul National University, South Korea

Reviewed by:
Ali S. Saber Tehrani,
The Johns Hopkins Hospital, Johns Hopkins Medicine, United States
Jorge Kattah,
College of Medicine, University of Illinois at Chicago, United States

Correspondence:
Andreas Zwergal
andreas.zwergal@med.uni-muenchen.de

† These authors have contributed equally to this work

Specialty section:
This article was submitted to Neuro-Otology, a section of the journal Frontiers in Neurology

Received: *14 April 2020*
Accepted: *30 June 2020*
Published: *06 August 2020*

Citation:
Zwergal A, Möhwald K, Salazar López E, Hadzhikolev H, Brandt T, Jahn K and Dieterich M (2020) A Prospective Analysis of Lesion-Symptom Relationships in Acute Vestibular and Ocular Motor Stroke. Front. Neurol. 11:822. doi: 10.3389/fneur.2020.00822

Background: Diagnosing stroke as a cause of acute vertigo, dizziness, or double vision remains a challenge, because symptom characteristics can be variable. The purpose of this study was to prospectively investigate lesion-symptom relationships in patients with acute vestibular or ocular motor stroke.

Methods: Three hundred and fifty one patients with acute and isolated vestibular or ocular motor symptoms of unclear etiology were enrolled in the EMVERT lesion trial. Symptom quality was assessed by the chief complaint (vertigo, dizziness, double vision), symptom intensity by the visual analog scale, functional impairment by EQ-5D-5L, and symptom duration by daily rating. Acute vestibular and ocular motor signs were registered by videooculography. A standardized MRI (DWI-/FLAIR-/T2-/T2*-/3D-T1-weighted sequences) was recorded within 7 days of symptom onset. MRIs with DWI lesions were further processed for voxel-based lesion-symptom mapping (VLSM).

Results: In 47 patients, MRI depicted an acute unilateral stroke (13.4%). The chief complaints were dizziness (42.5%), vertigo (40.4%) and double vision (17.0%). Lesions in patients with vertigo or dizziness showed a large overlap in the cerebellar hemisphere. VLSM indicated that strokes in the medial cerebellar layers 7b, 8, 9 were associated with vertigo, strokes in the lateral cerebellar layer 8, crus 1, 2 with dizziness, and pontomesencephalic strokes with double vision. Symptom intensity and duration varied largely between patients. Higher symptom intensity and longer duration were associated with medial cerebellar lesions. Hemispheric lesions of the cortex were rare and presented with milder symptoms of shorter duration.

Conclusions: Prospective evaluation of patients with acute vestibular or ocular motor stroke revealed that symptom quality, intensity and duration were not suited to differentiating peripheral from central etiologies. Lesions in the lateral cerebellum, thalamus, or cortex presented with unspecific, mild and transient symptoms prone to being misdiagnosed.

Keywords: vertigo, dizziness, double vision, acute vestibular syndrome, stroke

INTRODUCTION

Vertigo, dizziness or double vision may be symptoms of an acute cerebral ischemia or hemorrhage (1). Overall, 4–10% of patients in the emergency department (ED) presenting with vertigo and balance disorders suffer from stroke (2). Sixteen percentage of diplopia-related ED visits result from stroke or TIA (3). Patients with vestibular or ocular motor stroke often have no additional focal neurological deficits and therefore are at greater risk of being misdiagnosed (4, 5).

Cerebral lesions presenting with vertigo, dizziness, or double vision mostly involve vestibular and ocular motor circuits in the brainstem and cerebellum, whereas thalamo-cortical networks are affected only occasionally (6, 7). The reason for this lesion distribution can be found in the functional anatomy of the bilaterally organized central vestibular system, which converts direction-specific signals of each labyrinth into more global position-in-space signals along the ascending vestibular projections (8). Consequently, the vestibular syndromes of the lower brainstem present with severe vertigo and ipsilesional falling tendency, while lesions of the parieto-insular vestibular cortex may cause "higher vestibular symptoms" such as altered spatial perception or neglect (9). However, previous knowledge about the topography and symptoms of pure vestibular or ocular motor strokes is mostly based on retrospective analyses, which lack detail in the description of the quality, intensity, and time course of clinical symptoms.

Therefore, in the prospective EMVERT (EMergency VERTigo) lesion trial, symptoms and lesion topography were characterized in consecutive patients, who presented to the ED of a tertiary referral center with acute vertigo, dizziness or double vision due to stroke (10). This approach focuses on the clinical triage practice in the ED, which initially is based on the description of symptoms by the patient rather than on vestibular and ocular motor signs. The major question was whether symptom characteristics could be sufficient to differentiate peripheral from central disorders. A further aim was the evaluation of the distribution of lesion sites in pure vestibular and ocular motor stroke in relation to the quality, intensity, and time course of the accompanying chief complaint.

METHODS

Patient Characteristics

Eight hundred and forty consecutive patients with an acute presentation of vertigo, dizziness or double vision were prospectively screened for inclusion in the EMVERT lesion trial at the ED of the University Hospital, Ludwig-Maximilians-University, Munich. Four hundred and eighty-nine patients were excluded, because of the following reasons: definite peripheral vestibular or ocular motor disorders (like nystagmus typical for BPPV during repositioning maneuvers, recurrent attacks of definite Menière's disease, definite peripheral N III, N IV, N VI palsy without central ocular motor signs, vertigo/dizziness, or SVV deviation on the non-paretic eye) ($n = 203$); strokes with accompanying non-vestibular symptoms (like hemiparesis, hemihypesthesia, hemiataxia) ($n = 15$); decline to participate ($n = 186$); incapability to be included for other reasons (e.g., communications problem, psychiatric co-morbidity, cognitive deficits, critical illness, symptoms <10 min) ($n = 85$). Three hundred and fifty-one patients (60.1 ± 16.7 years, 46.6% female) with isolated vertigo, dizziness or double vision of unclear etiology were included (**Figure 1**). Two hundred and sixty patients had persistent symptoms at the time of inclusion. Fifty eight percentage of symptomatic patients had spontaneous nystagmus (SPN) at acute examination.

Protocol Approval and Patient Consent

The study was approved by the Ethics Committee of the University of Munich on 02/23/2015 (57-15). The study was conducted according to the Guideline for Good Clinical Practice, the Federal Data Protecting Act and the Helsinki Declaration of the World Medical Association (revision of Fortaleza, Brazil, October 2013). All subjects gave their informed, written consent to participate in the study.

Trial Flow

Adult patients with an acute onset of vertigo, dizziness, or double vision within the last 24 h and a duration of at least 10 min were screened prospectively for inclusion in this single center trial (10). A structured medical history and standardized clinical examination with an emphasis on vestibular and ocular motor function tests was performed in the ED. Patients with a clinically proven peripheral etiology (e.g., typical signs of BPPV, recurrent attacks of definite Menière's disease, peripheral N III, N IV, N VI palsy), and central etiology (e.g., signs of acute hemiparesis, hemihypesthesia, hemiataxia) were excluded. The remaining patients with unclear etiology of isolated vertigo, dizziness or double vision were defined as the subpopulation of interest for the EMVERT trial. Patients, who consented to participate, were included and received a comprehensive assessment of vestibular, ocular motor and postural signs by videooculography (VOG, EyeSeeCam®), mobile posturography, measurement of SVV, as well as scores and scales in the ED. A standardized magnetic resonance imaging (MRI) protocol was applied within 7 days after symptom onset to identify acute stroke (time to MRI: 2 ± 2.8 days, 93% of cases > 1 day) (**Figure 1**).

Scoring and Scaling of Chief Complaint, Symptom Duration, and Functional Impairment

At admission, the patients were asked to categorize their chief complaint as either vertigo (sensation of apparent self-motion), dizziness (unspecific sensation without self-motion), or double

---

Abbreviations: AICA, Anterior Inferior Cerebellar Artery; BPPV, Benign Peripheral Positional Vertigo; CT, Computed Tomography; DHI, Dizziness Handicap Inventory; DWI, Diffusion-Weighted Image; EMVERT, EMergency VERTigo and balance disorders; EQ-5D-5L, European Quality of life scale–5 Dimensions–5 Levels; EQ-VAS, European Quality of life scale—Visual Analog Scale; FLAIR, Fluid Attenuated Inversion Recovery; FSPGR, Fast Spoiled Gradient Echo; INO, internuclear ophthalmoplegia; MNI, Montreal Neurological Institute; MRI, Magnetic Resonance Imaging; mRS, modified Rankin Scale; PICA, posterior inferior cerebellar artery; SCA, superior cerebellar artery; T, Tesla; VAS, Visual Analog Scale; VLSM, Voxel-based Lesion-Symptom Mapping; VOR, Vestibulo-Ocular Reflex.

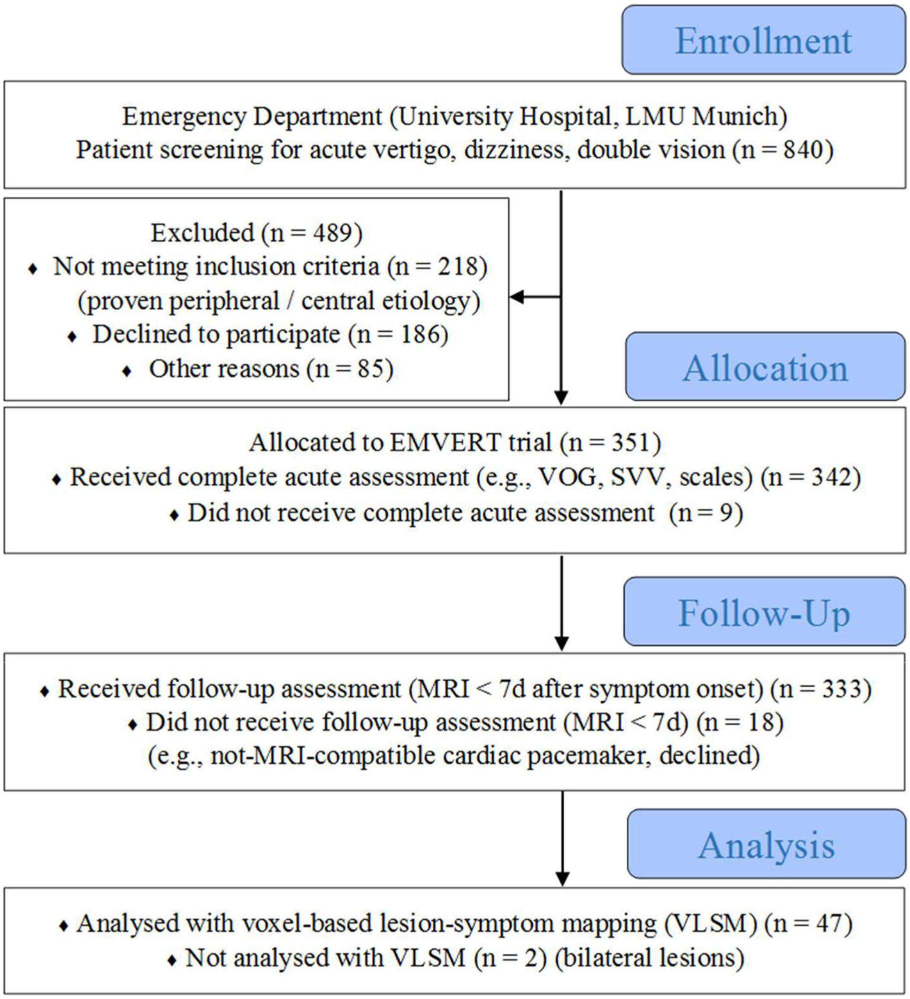

FIGURE 1 | Flow diagram of the EMVERT lesion trial. Eight hundred and forty consecutive patients with an acute presentation of vertigo, dizziness, or double vision were prospectively screened for inclusion in the EMVERT lesion trial at the Emergency Department (ED) of the University Hospital, Ludwig-Maximilians-University, Munich. Four hundred and eighty nine patients were excluded, because of the following reasons: definite peripheral vestibular or ocular motor disorder (like definite BPPV, recurrent attacks of definite Menière's disease, definite peripheral N III, N IV, N VI palsy) ($n = 203$); stroke with accompanying non-vestibular symptoms (like hemiparesis, hemihypesthesia, hemiataxia) ($n = 15$); decline to participate ($n = 186$); incapability to be included for other reasons (e.g., communications problem, psychiatric co-morbidity, cognitive deficits, critical illness, symptoms < 10 min) ($n = 85$). Three hundred and fifty one patients (60.1 ± 16.7 years, 46.6% female) with isolated vertigo, dizziness or double vision of unclear etiology were included. Three hundred and forty two patients received complete acute assessment in the ED, 333 patients a follow-up MRI within 7 days after symptom onset. Forty-seven of 49 patients with a stroke on MRI were included in the voxel-based lesion-symptom mapping analysis (2 excluded because of bilateral lesions). MRI, magnetic resonance imaging; SVV, subjective visual vertical; VLSM, voxel-based lesion-symptom mapping; VOG, videooculography.

vision. If mixed phenotypes (e.g., vertigo/double vision) were reported, the patient had to choose the predominant one. Accompanying vegetative symptoms like nausea or vomiting were documented. The maximum intensity of the chief complaint was measured using a visual analog scale (VAS, range 0–10). Decline of symptoms intensity was estimated by repeated testing of VAS for the chief complaint. Duration of vestibular or ocular motor symptoms was categorized in <1 days, 1–4 days, and >4 days based on daily reports of the patients. The Dizziness Handicap Inventory (DHI) and European Quality of Life scale-5 dimensions-5 levels (EQ-5D-5L) were performed as additional scores for graduation of symptom severity, quality of life (QoL) and functioning at admission (11). The Modified Ranking Scale (mRS) was documented at the time of discharge from the hospital.

Assessment of Vestibular and Ocular Motor Signs

The following vestibular and ocular motor signs were documented by VOG in the ED: nystagmus in straight ahead position (slow-phase velocity with/without fixation), gaze holding (lateral/vertical gaze positions), smooth pursuit (horizontal/vertical direction), saccades (horizontal/vertical direction), horizontal vestibulo-ocular reflex (VOR) (gain threshold: 0.7, presence of compensatory saccades), horizontal VOR-suppression, skew deviation and ocular motility deficits (cover test in lateral, vertical and straight ahead gaze position). The main criterion of skew deviation (in contrast to vertical misalignment due to N III or N IV palsy) was that the amount of vertical deviation from both eyes was the same in different eye positions on alternating cover test. VOG recording was done at the non-paretic eye, if monocular motility was restricted. Binocular subjective visual vertical (SVV) was measured in general, using the bucket test. SVV was determined via the non-affected eye in case of monocular paretic eye movements. Ten repetitions were performed (5 clockwise, 5 counterclockwise) and the mean SVV deviation was calculated (normal range: $0 \pm 2.5^\circ$) (12).

MRI Protocol

The standardized protocol included whole brain and brainstem fine slice (3 mm) DWI, FLAIR-, T2-, T2*-weighted images, 3D-T1-weighted sequences (FSPGR 1 mm) and time-of-flight angiography. All images were evaluated for the presence of ischemic stroke or bleeding by two specialized neuro-radiologists.

Voxel-Based Lesion-Symptom Mapping

Lesions were directly manually delineated on DWI sequences (MRI < 3 days post stroke) or T2-weighted sequences (MRI > 3 days post stroke) by an experienced imaging scientist, blinded for the clinical information, on a slice-by-slice basis using MRIcron (13). DWI or T2-images were co-registered with 3D-T1 images to enrich the normalization process. Normalization quality of lesion maps was visually checked by a second operator. Right-sided lesions were flipped to the left for the purpose of analysis. Patients presenting with bilateral lesions ($n = 2$) were discarded for analysis. Patients with simultaneous lesions in the medial and lateral cerebellum, in the medulla and cerebellum and in multiple unilateral locations were included in the analysis. None of the patient had critical ischemic edema. Images were normalized to Montreal Neurological Institute space (MNI) by Statistical Parametric Mapping Software (SPM 8) employing an established template. For descriptive analysis, the lesion site was assigned to the respective vascular territory/territories [posterior inferior cerebellar artery (PICA), anterior inferior cerebellar artery (AICA), superior cerebellar artery (SCA), brainstem perforators, middle cerebral artery (MCA), posterior cerebral artery (PCA)] and the affected anatomical structure(s) (cerebellar midline: nodulus, uvula, pyramis, tonsil, lingula, central lobule; cerebellar hemispheres: flocculus, biventer, inferior/superior semilunar, posterior/anterior quadrangulate lobule; brainstem: medulla, pons, midbrain; thalamus: dorsolateral, anteromedial; cortex: parieto-insular cortex, occipital cortex).

Voxel-based lesion-symptom mapping (VLSM) was performed using the statistical package Non-Parametric Mapping (NPM) implemented in MRIcron. For lesion analysis a custom-made mask was applied (**Supplement 1**), which included all relevant hubs of the cerebral vestibular network (e.g., brainstem, cerebellum, thalamus and insula). *T*-test (numerical variables) or *Liebermeister*-test (dichotomous variables) corrected for multiple comparison with false discovery rate (FDR) were calculated to assess whether behavioral scores differed significantly between the patients' pattern for lesioned and non-lesioned voxels (14). Since NPM toolbox interprets that a lower value in the behavioral scoring refers to a poorer performance, the different behavioral scores were computed reversed when necessary for statistical purposes. Only voxels affected in 15% of the sample were computed in each analysis to avoid inflated *z*-scores. Areas with significant differences in VLSM were labeled using the Automated Anatomical Labeling template (AAL-Atlas) (15).

Statistics

ANOVA with *post-hoc* testing was used to compare the scoring and scaling data (e.g., lesion volume, VAS) between subgroups (e.g., stroke/non-stroke, left-/right-sided lesions, vertigo/dizziness) using SPSS®24 (IBM). Pearson's correction coefficient was calculated for the correlation of lesion volume and VAS in the total group and subgroups (vertigo, dizziness, double vision).

Data Availability

Data reported in this article will be shared with any appropriately qualified investigator on request after pseudonymization.

RESULTS

Patient Characteristics

MRI indicated acute unilateral stroke in 47 patients (13.4% of enrolled patients, 5.6% of screened patients, 29 men). The mean age of stroke patients was 64.7 ± 13.0 years. The most frequent chief complaint in stroke patients was dizziness (42.5%), followed by vertigo (40.4%) and double vision (17.0%). Fifty percentage of patients with the chief complaint double vision reported accompanying vertigo or dizziness. 40.4% of stroke patients had nausea or vomiting, none had hiccups. Age did not differ significantly between the subgroups dizziness (66.7 ± 14.2 years), vertigo (63.5 ± 13.2 years), and double vision (61.9 ± 8.0 years). Forty four patients with vestibular or ocular motor stroke were symptomatic at the time of acute VOG assessment. In these patients spontaneous nystagmus (SPN) was detected in 45%. In total 74% of patients with vertigo and 30% of patients with dizziness had SPN (**Table 1**). In these cases, HINTS had a central pattern in 93% vs. 83% of patients (vertigo vs. dizziness). The head impulse test (HIT) was normal in 95, 85, and 63% of cases (vertigo, dizziness and double vision). Skew deviation appeared in 26% of patients with vertigo, 20% of patients with dizziness and 25% of patients with double vision. SVV was pathological in 68, 65, and 88% of patients with vertigo, dizziness, and double vision. The etiologies of double vision were internuclear ophthalmoplegia (37%), skew deviation (25%) and N III, N IV, N VI nuclear/fascicular palsy (13%, each) (**Table 1**).

Lesion Topography and Chief Complaint

In the total group, the most common lesion sites were in the cerebellum (PICA > SCA territory), followed by the brainstem (pontomedullary > mesencephalic tegmentum), thalamus and

TABLE 1 | Vestibular and ocular motor signs in patients with stroke.

	Vertigo (%)	Dizziness (%)		Double Vision (%)
SPN	74	30	Oculomotor palsy	13
HINTS central*	68	25	Trochlear palsy	13
HIT normal	95	85	Abducens palsy	13
Skew deviation	26	20	INO	37
SVV	68	65	Skew deviation	25

*An acute vestibular syndrome with SPN was more frequent in patients with vertigo compared to dizziness. HINTS had a high diagnostic sensitivity, if SPN was present, irrespective of the chief complaint. Data are shown as % of all patients with the respective chief complaint. HINTS, head impulse, nystagmus, test of skew; HIT, head impulse test; INO, internuclear ophthalmoplegia; SPN, spontaneous nystagmus; SVV, subjective visual vertical. *HINTS is supposed to be applied only in patients with SPN. The reported HINTS sensitivity in the table is irrespective of the presence of SPN.*

cortex. Lesion volume did not differ in patients with right-sided (mean: 8.0 cc, range 0.01–33.6 cc) and left-sided lesions (mean: 8.6 cc, range 0.01–102.2 cc) ($p = 0.89$). Patients with vertigo most frequently had lesions in the medial PICA territory (biventer lobule 58%, inferior semilunar lobule 37%, nodulus 37%, uvula 32%, tonsil 32%) and the pontomedullary brainstem (medulla 16%, pons 21%) (**Figure 2A**, **Supplement 2**). In patients with dizziness the lesions were found mostly in the lateral PICA territory (biventer lobule 25%, superior semilunar lobule 25%), SCA territory (posterior/anterior quadrangulate lobule 15%, each), the pontomesencephalic brainstem tegmentum (midbrain 25%, pons 20%) and the thalamus (dorsolateral/anteromedial 5%, each) (**Figure 2B**, **Supplement 2**). Lesions of patients with vertigo and dizziness showed a considerable overlap in the PICA territory (biventer, inferior semilunar lobule). Patients with double vision had pontomesencephalic and mesodiencephalic lesions (**Figure 2C**). Lesion volume was different in patients with vertigo (13.2 ± 24.3 cc), dizziness (7.4 ± 7.7 cc) and double vision (0.5 ± 0.6 cc) ($p = 0.04$). Patients with strokes in the medial cerebellum (PICA territory) had nausea or vomiting in 91%, in the lateral cerebellum, pontomesencephalic brainstem and thalamus in only 17%, respectively. Symptomatic stroke patients without SPN ($n = 24$) had lesions in the lateral PICA territory (30%), medial PICA territory (8%), SCA territory (8%), pontomesencephalic brainstem (38%), thalamus (8%), and insular cortex (8%).

VLSM in vestibular networks revealed that lesions in the medial cerebellar layers 7b, 8, 9 were significantly associated with the vertigo [*Liebermeister*-test, $p = 0.05$ (FDR-corrected), $Z = 1.66$] (**Figure 3A**). For the chief complaint dizziness, a lesion core area was found in the lateral cerebellar layer 8 and Crus 1, 2 using VLSM [*Liebermeister*-test, $p < 0.05$ (uncorrected), $Z = 0.65$] (**Figure 3B**). VLSM analysis conducted in patients with double vision did not reveal a significant association to a certain brain area (data not shown).

Lesion Topography and Symptom Intensity

The maximum symptom intensity (measured by VAS) was higher in the dizziness group (8.4 ± 1.8) and vertigo group (8.3 ± 2.3) and lower in the double vision group (6.2 ± 1.6) ($p = 0.015$ compared to the dizziness group and $p = 0.04$ compared to the vertigo group). Patients with nausea or vomiting had a higher VAS during the attack (9.5 ± 1.2), compared to patients without (7.0 ± 2.1) ($p < 0.0001$). VAS at symptom onset did not differ between patients with right-sided (7.7 ± 2.8) and left-sided lesions (8.2 ± 2.0) ($p = 0.99$). The mean decline of VAS per day was not significantly different between groups (dizziness group, 3.0 ± 1.7; vertigo group, 3.7 ± 1.7; double vision group, 1.9 ± 2.2). Lesions in patients with a high symptom intensity (VAS > 8) were larger and located in the cerebellar hemispheres (PICA > SCA territory) and pontomedullary brainstem (**Figure 4A**), while patients with a lower symptom intensity (VAS < 8) had smaller lesions in the cerebellar cortex (PICA/SCA territory), pontomesencephalic brainstem, thalamus and parieto-insular cortex (**Figure 4B**).

VLSM conducted with VAS at symptom onset showed significant voxels in the cerebellar layers 7b, 8, 9 in all patients with higher symptom intensity (*t*-test, $p = 0.05$ (FDR-corrected), $Z = 1.75$) (**Figure 4C**). In patients with cerebellar stroke, lesion volume was higher if symptoms were more severe ($r = -0.42$, $p = 0.03$), while in patients with cortical and thalamic lesions no correlation was found ($r = -0.15$, $p = 0.85$). Analysis of lesion volume and VAS at symptom onset by subgroups indicated no correlation for patients with vertigo ($r = -0.1$, $p = 0.97$), dizziness ($r = -0.14$, $p = 0.63$), or double vision ($r = -0.14$, $p = 0.91$).

Lesion Topography and Symptom Duration

In 6 patients symptom duration was <1 day, in 12 patients 1–4 days and in 29 patients >4 days. Duration of symptoms was not significantly different between the subgroups with vertigo, dizziness or double vision. In the total group, patients with a shorter symptom duration (<4 days) had lesions mostly in the lateral and distal cerebellar hemisphere (PICA territory), pontomesencephalic brainstem and parieto-insular cortex (**Figures 5A,B**), while patients with symptoms lasting >4 days had larger lesions involving the medial and lateral cerebellar hemispheres (PICA > SCA territory), the mesencephalon and thalamus (**Figure 5C**). Comparison of patients with a symptom duration of less and more than 4 days using VLSM showed that areas in the cerebellar layer 7b, 8, 9, and Crus 1, 2 were associated with longer symptom duration [*Liebermeister*-test, $p = 0.05$ (FDR-corrected), $Z = 1.72$] (**Figure 5D**).

Lesion Distribution, QoL, and Functioning Parameters

The health-related QoL measured by the EQ-5D-5L questionnaire was worse in the vertigo (12.2 ± 4.0) compared to the dizziness group (9.4 ± 3.6; $p = 0.02$). In the vertigo group higher scores were found in the EQ-5D-5L subtests for mobility ($p = 0.047$), overall activity ($p = 0.042$), and anxiety ($p = 0.024$). Similarly, DHI was higher in the vertigo (52.0 ± 22.1) compared to the dizziness group (34.4 ± 20.2, $p = 0.01$) and lowest in patients with double vision (42.3 ± 27.9).

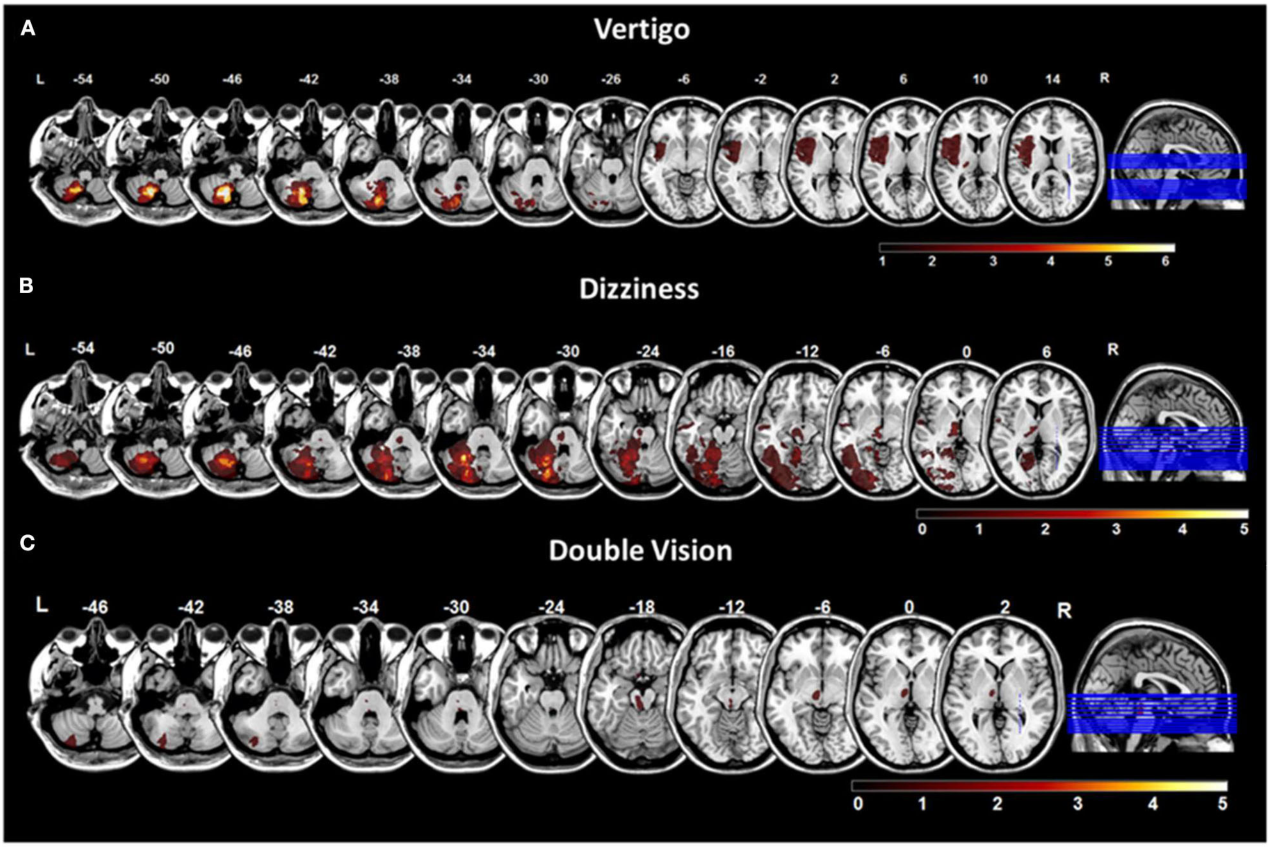

FIGURE 2 | Overlap lesion plots for chief complaints. Overlap lesion plots for the chief complaints vertigo **(A)**, dizziness **(B)**, and double vision **(C)**. The number of overlapping lesions is illustrated by the color bar from dark red ($n = 0$) to bright yellow (maximum number). Coordinates are given in MNI space. MNI, Montreal Neurological Institute; L, left; R, right.

VLSM in vestibular networks indicated that areas in cerebellar layers 8, 9, and Crus 2 were associated with higher EQ-5D-5L scores in the total group (t-test, $p = 0.05$ (FDR-corrected), $Z = 1.69$). VLSM for the subtest anxiety/depression showed a significant specific engagement of cerebellar layer 8 [t-test, $p = 0.05$ (FDR-corrected), $Z = 1.79$]. The analysis within patient subgroups revealed that the cerebellar layer 6 and Crus 1 correlated with worse QoL in patients with vertigo (**Figure 6A**), while the cerebellar layer 8 was related to higher EQ-5D-5L scores in patients reporting dizziness (**Figure 6B**). When VLSM was performed for DHI, areas in cerebellar layer 8 were significantly associated with higher DHI scores.

DISCUSSION

In the prospective EMVERT lesion trial, symptoms of patients with acute vestibular or ocular motor stroke were systematically documented and correlated to lesion topography. The major findings were the following: (1) Vertigo and dizziness were equally frequent in vestibular stroke and underlying lesions showed a large overlap in the cerebellar hemisphere. Vertigo was more likely associated with medial cerebellar lesions (biventer lobule, nodulus, uvula), while dizziness appeared more frequently in lateral and superior cerebellar lesions. (2) Symptom intensity and duration varied largely in vestibular and ocular motor stroke patients. Higher symptom intensity and longer symptom duration were associated with medial cerebellar lesions. Cortical lesions presented with milder symptoms of shorter duration. (3) QoL and functioning was worst in patients with vertigo and lesions in the medial cerebellar structures.

Symptom Characteristics and Diagnostic Classification of Vestibular Stroke

The diffuse lesion-symptom topography in vestibular and ocular motor stroke has direct practical implications for the processing of patients. The symptom quality does not allow differentiation of peripheral and central etiologies of vestibular syndromes. Therefore, the traditional approach of assessment by the symptoms vertigo, dizziness, postural instability or disequilibrium has major limitations in acute vestibular disorders (16, 17). Similar conclusions have been drawn in previous studies, where symptom quality was imprecise even in peripheral vestibular disorders (18).

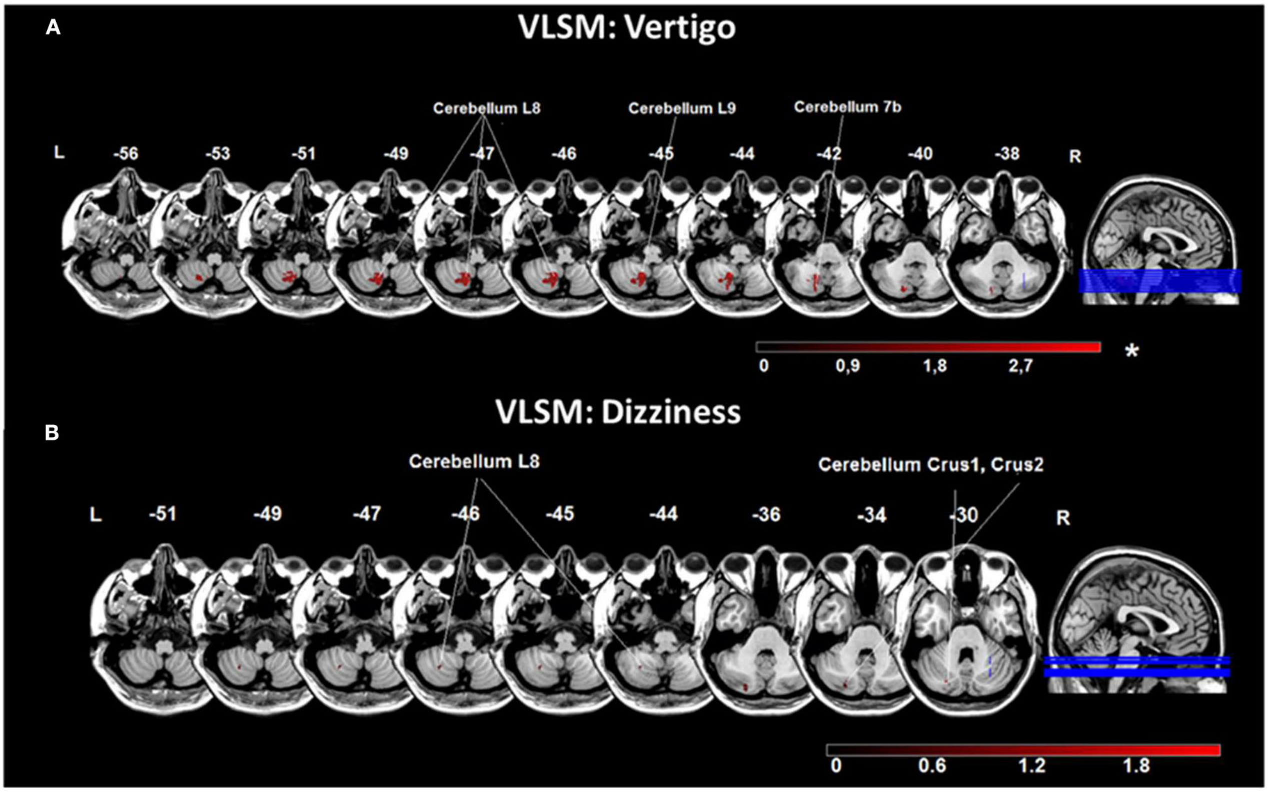

FIGURE 3 | Voxel-based lesion-symptom mapping (VLSM) analysis for the chief complaints vertigo and dizziness. **(A)** VLSM for the presence of the chief complaint vertigo showed an association with areas in the medial cerebellar hemisphere (cerebellar layers 7b, 8, 9). **(B)** VLSM analysis for the chief complaint dizziness indicated related voxels more laterally in the cerebellar hemisphere (cerebellar layer 8, Crus 1, 2). Presented are voxels that exceed a $p < 0.05$ (*FDR-corrected for vertigo; uncorrected for dizziness). The color bar from dark to light red indicates the z-scores. Coordinates are given in MNI space. MNI, Montreal Neurological Institute; L, left; R, right.

In the current study, symptom duration and intensity varied largely and consequently could not be taken as an indicator or criterion for exclusion of stroke. A recent study showed that functional impairment in acute central vestibulopathies is lower than in acute unilateral peripheral vestibulopathies, which may increase the risk of a false-benign diagnosis in vestibular stroke (19). Furthermore, previous studies described that suspected ischemic attacks with vestibular symptoms may present with short-lasting and transient symptoms (50% lasting <1 h) (20–22). Consequently, modern concepts of symptom-based differentiation of vestibular disorders rely more on the presence of triggers preceding vestibular symptoms and the time course of symptom onset and evolution (e.g., TiTrATE algorithm, including timing, trigger, and targeted examination) (23, 24).

Symptom Characteristics and the Risk of Misdiagnosis of Vestibular Stroke

Based on a recent meta-analysis, unspecific presentations of dizziness, short duration, and subtle intensity of symptoms may increase the risk for a misdiagnosis in patients with acute vestibular stroke (5). In these scenarios, the probability for missing stroke was about 10-fold compared to other focal neurological presentations. In total about 10% of strokes were missed at first contact in the ED (25). This problem is also reflected in a 50-fold increased risk of being readmitted to a hospital with a secondary stroke diagnosis in the first week, and a 9.3-times higher stroke risk after 30 days in patients discharged from the ED with a suspected benign diagnosis of acute vertigo or dizziness compared to matched controls (26). Lesion-symptom relationships from the current EMVERT lesion trial point out that especially patients with lesions in the lateral cerebellar hemispheres, mesencephalon and parieto-insular cortex may be at risk of being falsely processed. In these localizations patients do complain about more unspecific symptoms (such as dizziness, unsteadiness), transient symptoms (<1 day), lower symptom intensity (VAS < 8), and less vegetative symptoms (like nausea or vomiting) (**Figures 2**, **3**, **5**). Furthermore, patients with lesions in the lateral cerebellum, upper midbrain and cortex do not show clinical signs of an acute vestibular syndrome (e.g., SPN), which further complicates the diagnosis. HINTS is not applicable in the majority of these cases. In contrast, lesions in the pontomedullary tegmentum and medial cerebellar

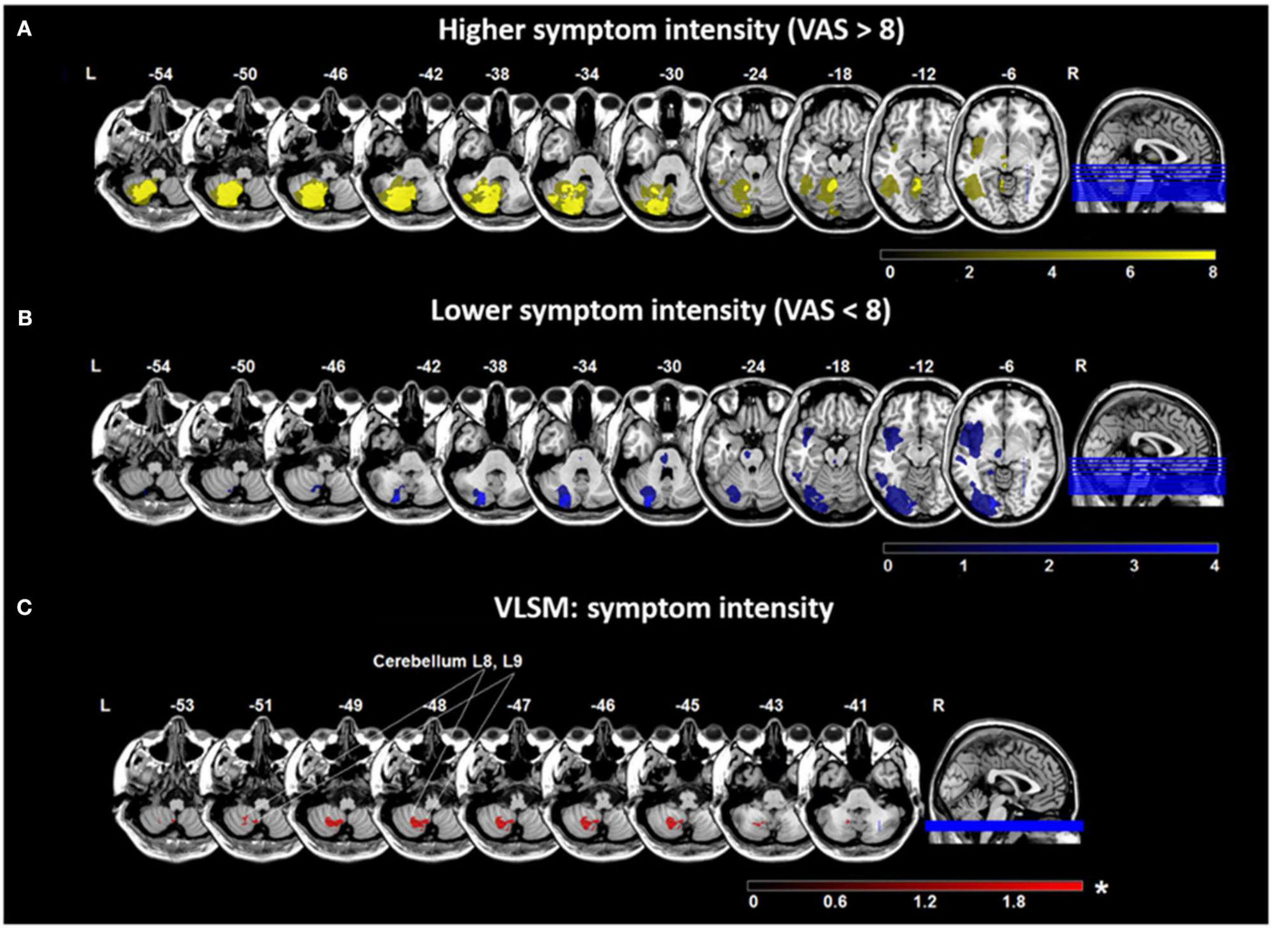

FIGURE 4 | Overlap lesion plots and voxel-based lesion-symptom mapping (VLSM) for symptom intensity. Maximum intensity of the chief complaint was measured by the visual analog scale (VAS) (range 0–10). Overlap lesion plots for patients with higher symptom intensity (VAS $>$ 8) ($n = 34$) **(A)** and lower symptom intensity (VAS $<$ 8) ($n = 13$) **(B)**. The degree of lesion overlap is illustrated by color bars from dark to bright yellow or blue. **(C)** VLSM analysis in 47 patients based on VAS indicated an area in the medial cerebellar hemisphere (cerebellar layer 8, 9) related to more severe symptoms. Presented are voxels that exceed a $p < 0.05$ (*FDR-corrected). The color bar from dark to light red indicates the z-scores. Coordinates are given in MNI space. MNI, Montreal Neurological Institute; L, left; R, right.

hemispheres may be more apparent, because patients report more intense and longer-lasting symptoms and show more prominent clinical signs (such as SPN, ocular tilt reaction, and HINTS central pattern) (27–29). Lesion size may be another relevant factor, because patients with smaller lesions had less intense vertigo. For lesions <10 mm, MRI has a high false-positive rate (about 50%) in the first 1–2 days after symptom onset, which questions the rationale of a purely imaging-based diagnosis of acute vestibular or ocular motor stroke (30). Patients in our study received MRI in 93% of cases later than 1 day post symptom onset to increase the sensitivity to capture small DWI lesions.

Pathophysiological Principles Behind Lesion-Symptom Relationships in Vestibular Stroke

Despite the variety of symptomatic presentations across lesion sites, some general principles seem to exist: (1) Lesions in the nodulus, uvula, and medial cerebellar hemisphere are associated with vertigo symptoms of the highest intensity and a high rate of nausea or vomiting. The most likely explanation is that these regions are directly involved in processing of vestibular and ocular motor signals. The nodulus has been implicated in integration of otolith and semicircular canals signals, tilt suppression of post-rotatory vertigo and the judgement of verticality perception (7, 31–33). Nodular lesions often present with SPN and ocular tilt reaction (34). Anatomically, the nodulus has inhibitory ipsilateral projections to the vestibular nucleus (31). Functionally, medial cerebellar lesions cause an excitation of the ipsilesional vestibular nucleus (via disinhibition) and resemble the clinical picture of a vestibular nucleus lesion on the other side. The lateral and superior cerebellar hemispheres are not specifically dedicated to vestibular processing but rather to sensorimotor and posture control. Therefore, lesions may cause less specific dizziness, as a sign of disturbed multisensory integration or balance control, and only rarely

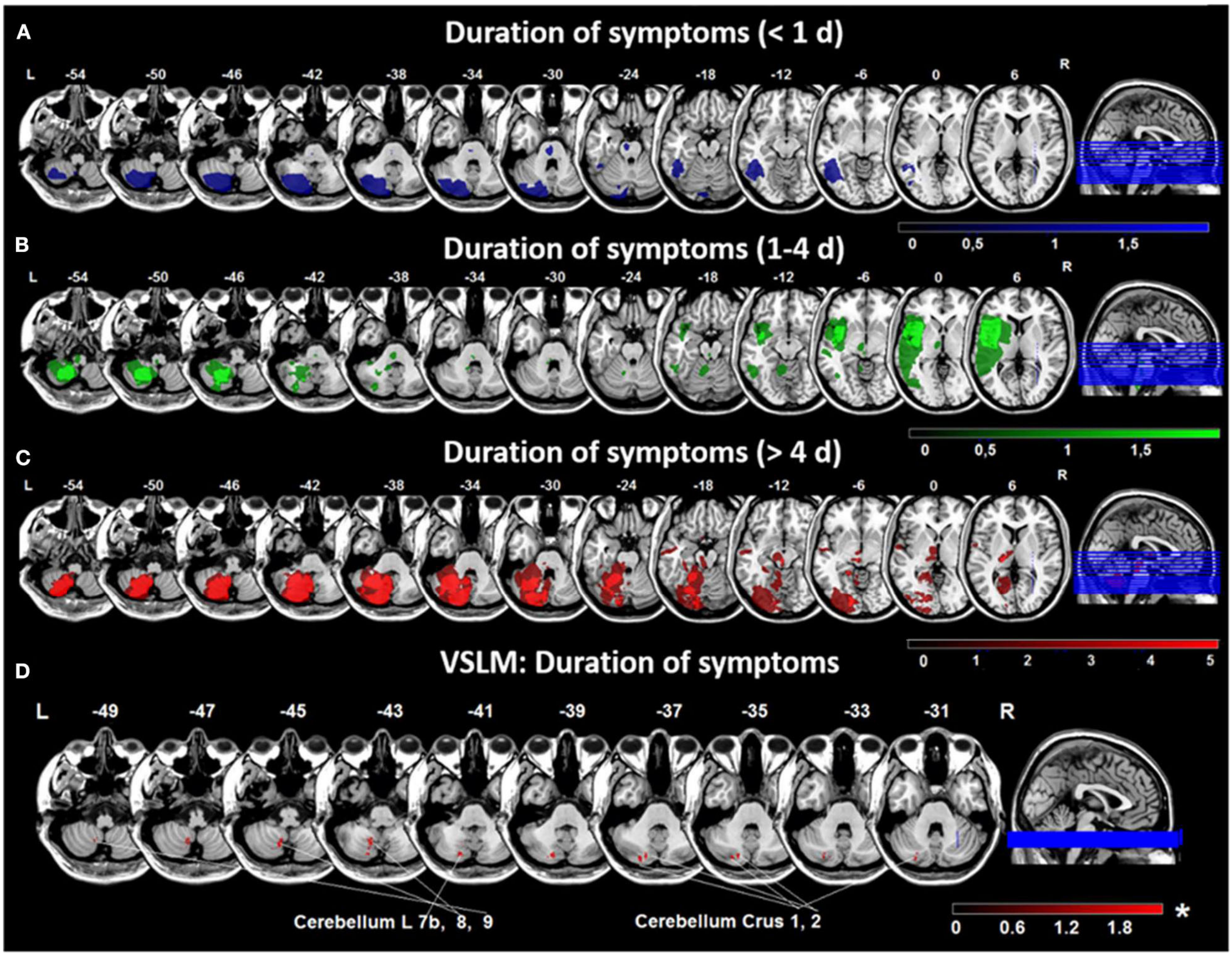

FIGURE 5 | Overlap lesion plots and voxel-based lesion-symptom mapping (VLSM) for duration of symptoms. Overlap lesion plots are shown for patients with a duration of symptoms <1 day ($n = 6$) **(A)**, 1–4 days ($n = 12$) **(B)** and > 4 days ($n = 29$) **(C)**. The degree of lesion overlap is illustrated by color bars from dark to bright blue, green or red. **(D)** VLSM analysis in 47 patients based on symptom duration in days showed an area in the medial cerebellar hemisphere (cerebellar layer 7b, 8, 9, and Crus 1, 2) associated with longer duration of symptoms. Presented are voxels that exceed a $p < 0.05$ (*FDR-corrected). The color bar from dark to light red indicates the z-scores. Coordinates are given in MNI space. D, day; MNI, Montreal Neurological Institute; L. left; R, right.

nausea or vomiting. (2) Perceived impairment of QoL and functioning follows the degree of vestibular asymmetry. Patients with vertigo had a higher EQ-5D-5L anxiety score than dizzy patients. VLSM found an association of higher EQ-5D-5L scores in the medial cerebellar hemisphere. In accordance, a recent study found that the degree of horizontal SPN is the most important factor for worse health-related quality of life in acute vestibulopathies (19). In another previous study, patients with unilateral vestibular disorders had more anxiety than patients with bilateral vestibulopathy (35). (3) Symptom duration was higher in medial compared to lateral cerebellar and thalamo-cortical lesions. This finding could be explained either by the different peak levels of initial symptoms in these subgroups or by a less effective central compensation of strategic lesions in vestibular cerebellar networks. The latter hypothesis may be substantiated by the finding that patients with medial cerebellar lesions had a prolonged course of compensation (36). Furthermore, symptoms from unilateral parieto-insular cortex lesions may be compensated by the intact cerebral hemisphere (6). (4) Symptom quality changed along the brainstem-thalamic axis from more direction-specific symptoms (i.e., vertigo) in the lower brainstem to more position-specific symptoms (i.e., dizziness) in the midbrain and thalamus. The reason for this topography may be the specific computation of vestibular signs at different brain levels. Vestibular signs at the lower brainstem level drive direction-specific ocular motor and postural responses. Along the ascending vestibular projections head direction signals from both sides are integrated to head position in space signals (37, 38). In the thalamo-cortical networks, a global percept of the environment is built by integration of multisensory information. In consequence, lesions at the midbrain level and above will rather give dizziness as a

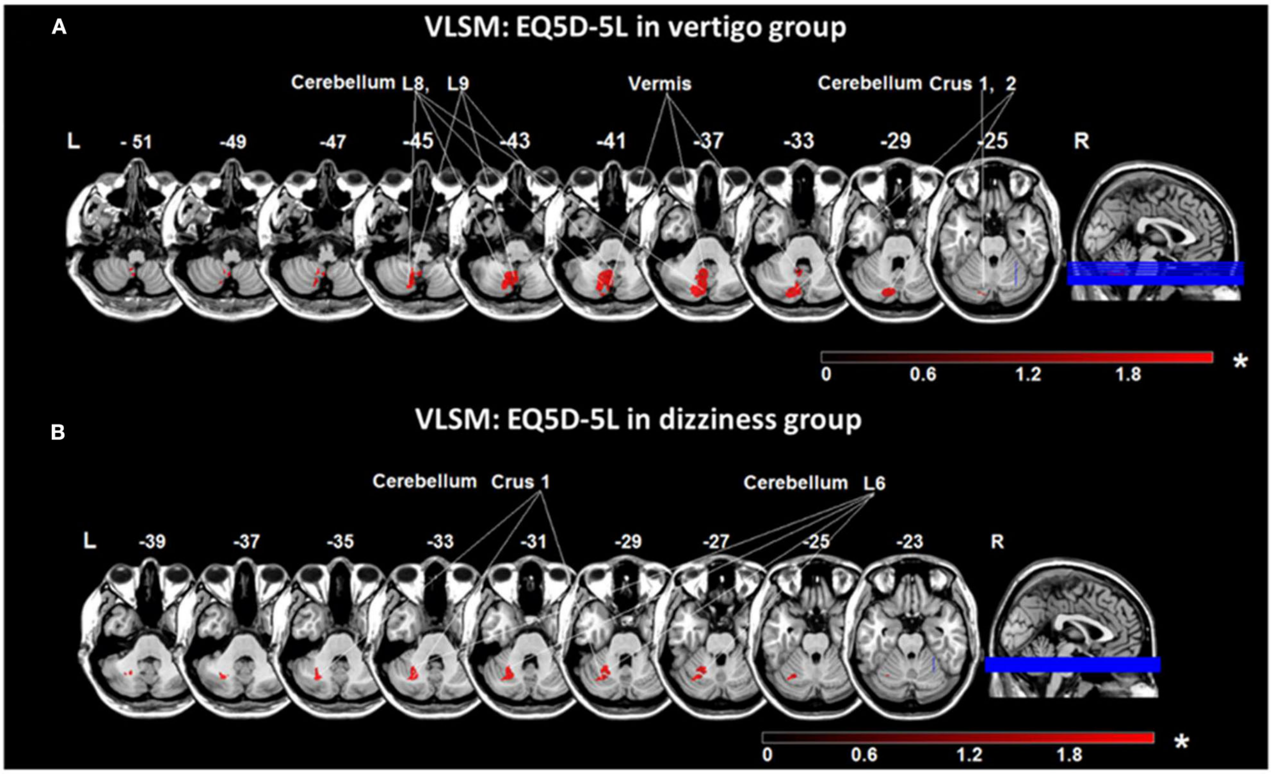

FIGURE 6 | Voxel-based lesion-symptom mapping (VLSM) analyses based on the QoL scale EQ5D-5L. **(A)** VLSM based on EQ5D-5L in the vertigo subgroup showed an association of voxels in the medial cerebellar hemisphere (cerebellar layers 8, 9, vermis, and crus 1, 2) with worse QoL scores. **(B)** VLSM analysis using EQ5D-5L in the dizziness subgroup indicated a more lateral area (cerebellar layer 6, and Crus 1) engaged in higher EQ5D-5L scores. Presented are voxels that exceed a $p < 0.05$ (*FDR-corrected). The color bar from dark to light red indicates the z-scores. Coordinates are given in MNI space. EQ5D-5L: European Quality of Life scale −5 dimensions −5 levels, MNI, Montreal Neurological Institute; L, left; R, right.

disturbed perception of the environment without the feeling of self-motion (6).

CONCLUSIONS

A simple symptom-lesion topography in acute vestibular and ocular motor stroke is an inappropriate clinical approach. Symptom quality, intensity, and duration are not suited to differentiate peripheral from central etiologies of vestibular presentations. Clinicians should be aware that rare lesion sites in the lateral cerebellum, thalamus, or cortex may present with rather unspecific, mild, and transient symptoms and therefore are at risk of being categorized as false-benign. Symptom intensity and perceived impairment are highest in lesions, which directly affect pontomedullary and medial cerebellar vestibular hubs. Lesions in ascending vestibular projections above the VOR brainstem circuit, rarely present with direction-specific vestibular symptoms (namely vertigo). Detailed neuro-ophthalmological and -ototological examinations are required in all patients with monosymptomatic vertigo, dizziness, or double vision.

DATA AVAILABILITY STATEMENT

The raw data supporting the conclusions of this article will be made available by the authors, without undue reservation.

ETHICS STATEMENT

The studies involving human participants were reviewed and approved by Ethics Committee of the University of Munich on 02/23/2015 (57-15). The patients/participants provided their written informed consent to participate in this study.

AUTHOR CONTRIBUTIONS

AZ: drafting/revising the manuscript, study concept and design, acquisition of data, analysis and interpretation of data, and statistical analysis. KM: drafting/revising the manuscript, study concept and design, acquisition of data, and analysis and interpretation of data. ES: drafting/revising the manuscript, analysis and interpretation of data, and statistical analysis. HH: drafting/revising the manuscript and acquisition of data. TB and MD: revising the manuscript, study concept and design, and analysis and interpretation of data. KJ: drafting/revising the manuscript, study concept and design, and analysis and interpretation of data. All authors contributed to the article and approved the submitted version.

FUNDING

We acknowledge funding from the German Federal Ministry of Education and Research (BMBF) in the context of the foundation of the German Center for Vertigo and Balance Disorders (DSGZ) (grant number 01 EO 1401) and from the Hertie Foundation (to TB).

ACKNOWLEDGMENTS

We thank Katie Göttlinger for copyediting the manuscript.

SUPPLEMENTARY MATERIAL

The Supplementary Material for this article can be found online at: https://www.frontiersin.org/articles/10.3389/fneur.2020.00822/full#supplementary-material

REFERENCES

1. Kim SH, Kim HJ, Kim JS. Isolated vestibular syndromes due to brainstem and cerebellar lesions. *J Neurol.* (2017) 264:S63–69. doi: 10.1007/s00415-017-8455-6
2. Newman-Toker DE, Hsieh YH, Camargo CA Jr, Pelletier AJ, Butchy GT, Edlow JA. Spectrum of dizziness visits to US emergency departments: cross-sectional analysis from a nationally representative sample. *Mayo Clin Proc.* (2008) 83:765–75. doi: 10.4065/83.7.765
3. De Lott LB, Kerber KA, Lee PP, Brown DL, Burke JF. Diplopia-related ambulatory and emergency department visits in the United States, 2003-2012. *JAMA Ophthalmol.* (2017) 135:1339–44. doi: 10.1001/jamaophthalmol.2017.4508
4. Lee H, Sohn SI, Cho YW, Lee SR, Ahn BH, Park BR, et al. Cerebellar infarction presenting isolated vertigo: frequency and vascular topographical patterns. *Neurology.* (2006) 67:1178–83. doi: 10.1212/01.wnl.0000238500.02302.b4
5. Tarnutzer AA, Lee SH, Robinson KA, Wang Z, Edlow JA, Newman-Toker DE. ED misdiagnosis of cerebrovascular events in the era of modern neuroimaging: a meta-analysis. *Neurology.* (2017) 88:1468–77. doi: 10.1212/WNL.0000000000003814
6. Dieterich M, Brandt T. Why acute unilateral vestibular cortex lesions mostly manifest without vertigo. *Neurology.* (2015) 84:1680–4. doi: 10.1212/WNL.0000000000001501
7. Choi KD, Kim JS. Vascular vertigo: updates. *J Neurol.* (2019) 266:1835–43. doi: 10.1007/s00415-018-9040-3
8. Dieterich M, Glasauer S, Brandt T. Why acute unilateral vestibular midbrain lesions rarely manifest with rotational vertigo: a clinical and modelling approach to head direction cell function. *J Neurol.* (2018) 265:1184–98. doi: 10.1007/s00415-018-8828-5
9. Brandt T, Dieterich M. The dizzy patient: don't forget disorders of the central vestibular system. *Nat Rev Neurol.* (2017) 13:352–62. doi: 10.1038/nrneurol.2017.58
10. Möhwald K, Bardins S, Müller HH, Jahn K, Zwergal A. Protocol for a prospective interventional trial to develop a diagnostic index test for stroke as a cause of vertigo, dizziness and imbalance in the emergency room (EMVERT study). *BMJ Open.* (2017) 7:e019073. doi: 10.1136/bmjopen-2017-019073
11. Herdman M, Gudex C, Lloyd A, Janssen M, Kind P, Parkin D, et al. Development and preliminary testing of the new five-level version of EQ-5D (EQ-5D-5L). *Qual Life Res.* (2011) 20:1727–36. doi: 10.1007/s11136-011-9903-x
12. Zwergal A, Rettinger N, Frenzel C, Dieterich M, Brandt T, Strupp M. A bucket of static vestibular function. *Neurology.* (2009) 72:1689–92. doi: 10.1212/WNL.0b013e3181a55ecf
13. Rorden C, Brett M. Stereotaxic display of brain lesions. *Behav Neurol.* (2000) 12:191–200. doi: 10.1155/2000/421719
14. Rorden C, Karnath HO, Bonilha L. Improving lesion-symptom mapping. *J Cogn Neurosci.* (2007) 19:1081–8. doi: 10.1162/jocn.2007.19.7.1081
15. Tzourio-Mazoyer N, Landeau B, Papathanassiou D, Crivello F, Etard O, Delcroix N, et al. Automated anatomical labeling of activations in SPM using a macroscopic anatomical parcellation of the MNI MRI single-subject brain. *Neuroimage.* (2002) 15:273–89. doi: 10.1006/nimg.2001.0978
16. Bisdorff A, Von Brevern M, Lempert T, Newman-Toker DE. Classification of vestibular symptoms: towards an international classification of vestibular disorders. *J Vestib Res.* (2009) 19:1–13. doi: 10.3233/VES-2009-0343
17. Saber Tehrani AS, Kattah JC, Kerber KA, Gold DR, Zee DS, Urrutia VC, et al. Diagnosing stroke in acute dizziness and vertigo: pitfalls and pearls. *Stroke.* (2018) 49:788–95. doi: 10.1161/STROKEAHA.117.016979
18. Kerber KA, Callaghan BC, Telian SA, Meurer WJ, Skolarus LE, Carender W, et al. Dizziness symptom type prevalence and overlap: a US nationally representative survey. *Am J Med.* (2017) 130:1465.e1-9. doi: 10.1016/j.amjmed.2017.05.048
19. Möhwald K, Hadzhikolev H, Bardins S, Becker-Bense S, Brandt T, Grill E, et al. Health-related quality of life and functional impairment in acute vestibular disorders. *Eur J Neurol.* (2020). doi: 10.1111/ene.14318. [Epub ahead of print].
20. Paul NL, Simoni M, Rothwell PM, Oxford Vascular Study. Transient isolated brainstem symptoms preceding posterior circulation stroke: a population-based study. *Lancet Neurol.* (2013) 12:65–71. doi: 10.1016/S1474-4422(12)70299-5
21. Hoshino T, Nagao T, Mizuno S, Shimizu S, Uchiyama S. Transient neurological attack before vertebrobasilar stroke. *J Neurol Sci.* (2013) 325:39–42. doi: 10.1016/j.jns.2012.11.012
22. Choi JH, Park MG, Choi SY, Park KP, Baik SK, Kim JS, et al. Acute transient vestibular syndrome: prevalence of stroke and efficacy of bedside evaluation. *Stroke.* (2017) 48:556–62. doi: 10.1161/STROKEAHA.116.015507
23. Newman-Toker DE, Edlow JA. TiTrATE: a novel, evidence-based approach to diagnosing acute dizziness and vertigo. *Neurol Clin.* (2015) 33:577–99. doi: 10.1016/j.ncl.2015.04.011
24. Kuroda R, Nakada T, Ojima T, Serizawa M, Imai N, Yagi N, et al. The TriAGe + score for vertigo or dizziness: a diagnostic model for stroke in the emergency department. *J Stroke Cerebrovasc Dis.* (2017) 26:1144–53. doi: 10.1016/j.jstrokecerebrovasdis.2017.01.009
25. Newman-Toker DE, Moy E, Valente E, Coffey R, Hines AL. Missed diagnosis of stroke in the emergency department: a cross-sectional analysis of a large population-based sample. *Diagnosis.* (2014) 1:155–66. doi: 10.1515/dx-2013-0038
26. Atzema CL, Grewal K, Lu H, Kapral MK, Kulkarni G, Austin PC. Outcomes among patients discharged from the emergency department with a diagnosis of peripheral vertigo. *Ann Neurol.* (2016) 79:32–41. doi: 10.1002/ana.24521
27. Cnyrim CD, Newman-Toker D, Karch C, Brandt T, Strupp M. Bedside differentiation of vestibular neuritis from central "vestibular pseudoneuritis". *J Neurol Neurosurg Psychiatry.* (2008) 79:458–60. doi: 10.1136/jnnp.2007.123596
28. Kattah JC, Talkad AV, Wang DZ, Hsieh YH, Newman-Toker DE. HINTS to diagnose stroke in the acute vestibular syndrome: three-step bedside oculomotor examination more sensitive than early MRI diffusion-weighted imaging. *Stroke.* (2009) 40:3504–10. doi: 10.1161/STROKEAHA.109.551234

29. Ahmadi SA, Vivar G, Navab N, Möhwald K, Maier A, Hadzhikolev H, et al. Modern machine-learning can support diagnostic differentiation of central and peripheral acute vestibular disorders. *J Neurol.* (2020). doi: 10.1007/s00415-020-09931-z. [Epub ahead of print].
30. Saber Tehrani AS, Kattah JC, Mantokoudis G, Pula JH, Nair D, Blitz A, et al. Small strokes causing severe vertigo: frequency of false-negative MRIs and nonlacunar mechanisms. *Neurology.* (2014) 83:169–73. doi: 10.1212/WNL.0000000000000573
31. Baier B, Bense S, Dieterich M. Are signs of ocular tilt reaction in patients with cerebellar lesions mediated by the dentate nucleus? *Brain.* (2008) 131:1445–54. doi: 10.1093/brain/awn086
32. Choi JY, Glasauer S, Kim JH, Zee DS, Kim JS. Characteristics and mechanism of apogeotropic central positional nystagmus. *Brain.* (2018) 141:762–75. doi: 10.1093/brain/awx381
33. Zwergal A, Dieterich. Vertigo and dizziness in the emergency room. *Curr Opin Neurol.* (2020) 33:117–25. doi: 10.1097/WCO.0000000000000769
34. Moon IS, Kim JS, Choi KD, Kim MJ, Oh SY, Lee H, et al. Isolated nodular infarction. *Stroke.* (2009) 40:487–91. doi: 10.1161/STROKEAHA.108.527762
35. Decker J, Limburg K, Henningsen P, Lahmann C, Brandt T, Dieterich M. Intact vestibular function is relevant for anxiety related to vertigo. *J Neurol.* (2019) 266:89–92. doi: 10.1007/s00415-019-09351-8
36. Baier B, Müller N, Rhode F, Dieterich M. Vestibular compensation in cerebellar stroke patients. *Eur J Neurol.* (2015) 22:416–8. doi: 10.1111/ene.12475
37. Kirsch V, Keeser D, Hergenroeder T, Erat O, Ertl-Wagner B, Brandt T, et al. Structural and functional connectivity mapping of the vestibular circuitry from human brainstem to cortex. *Brain Struct Funct.* (2016) 221:1291–308. doi: 10.1007/s00429-014-0971-x
38. Glasauer S, Dieterich M, Brandt T. Neuronal network-based mathematical modeling of perceived verticality in acute unilateral vestibular lesions: from nerve to thalamus and cortex. *J Neurol.* (2018) 265:101–12. doi: 10.1007/s00415-018-8909-5

Conflict of Interest: The authors declare that the research was conducted in the absence of any commercial or financial relationships that could be construed as a potential conflict of interest.

frontiers in Neurology

CASE REPORT
published: 13 January 2021
doi: 10.3389/fneur.2020.608838

Case Report: Filling Defect in Posterior Semicircular Canal on MRI With Balanced Steady-State Gradient-Echo Sequences After Labyrinthine Ischemia in the Common Cochlear Artery Territory as an Early Sign of Fibrosis

Andrea Castellucci[1], Emanuela Pepponi[1], Annalisa Bertellini[2], Caterina Senesi[3], Margherita Bettini[4], Cecilia Botti[1,5], Salvatore Martellucci[6], Pasquale Malara[7], Silvia Delmonte[4], Francesco Maria Crocetta[1], Martina Fornaciari[1], Francesca Lusetti[1], Giovanni Bianchin[4] and Angelo Ghidini[1]*

[1] ENT Unit, Department of Surgery, Azienda USL – IRCCS di Reggio Emilia, Reggio Emilia, Italy, [2] Department of Radiology, Azienda USL – IRCCS di Reggio Emilia, Reggio Emilia, Italy, [3] Department of Neurology, Azienda USL – IRCCS di Reggio Emilia, Reggio Emilia, Italy, [4] Audiology and Ear Surgery Unit, Azienda USL – IRCCS di Reggio Emilia, Reggio Emilia, Italy, [5] Clinical and Experimental Medicine, University of Modena and Reggio Emilia, Modena, Italy, [6] ENT Unit, Santa Maria Goretti Hospital, Azienda USL Latina, Latina, Italy, [7] Audiology and Vestibology Service, Centromedico Bellinzona, Bellinzona, Switzerland

We describe a rare case of posterior semicircular canal (PSC) fibrosis following acute labyrinthine ischemia in the territory supplied by the common cochlear artery (CCA) and review the relevant literature. A 71-year-old man with multiple vascular risk factors presented 12 days after the onset of acute vertigo and profound left-sided hearing loss. Right-beating spontaneous nystagmus with downbeat components elicited by mastoid vibrations and headshaking was detected. The video head impulse test (vHIT) revealed an isolated hypofunction of the left PSC, whereas vestibular evoked myogenic potentials (VEMPs) showed ipsilateral saccular loss. The clinical presentation and instrumental picture were consistent with acute ischemia in the territory supplied by left CCA. Compared to previous imaging, a new MRI of the brain with 3D-FIESTA sequences highlighted a filling defect in the left PSC, consistent with fibrosis. Hearing function exhibited mild improvement after steroid therapy and hyperbaric oxygen sessions, whereas vHIT abnormalities persisted over time. To the best of our knowledge, this is the only case in the literature reporting a filling defect on MRI, consistent with semicircular canal fibrosis following acute labyrinthine ischemia. Moreover, PSC fibrosis was related with poor functional outcome. We therefore suggest using balanced steady-state gradient-echo sequences a few weeks following an acute lesion of inner ear sensors to detect signal loss within membranous labyrinth consistent with post-ischemic fibrosis. Besides addressing the underlying etiology, signal loss might also offer clues on the functional behavior of the involved sensor over time. In cases of acute loss of inner

Edited by:
Raymond Van De Berg,
Maastricht University Medical Centre, Netherlands

Reviewed by:
Michael C. Schubert,
Johns Hopkins University, United States
Nese Celebisoy,
Ege University, Turkey
Luke Chen,
Monash University, Australia

****Correspondence:***
Andrea Castellucci
andrea.castellucci@ausl.re.it

Specialty section:
This article was submitted to Neuro-Otology, a section of the journal Frontiers in Neurology

Received: *21 September 2020*
Accepted: *02 December 2020*
Published: *13 January 2021*

Citation:
Castellucci A, Pepponi E, Bertellini A, Senesi C, Bettini M, Botti C, Martellucci S, Malara P, Delmonte S, Crocetta FM, Fornaciari M, Lusetti F, Bianchin G and Ghidini A (2021) Case Report: Filling Defect in Posterior Semicircular Canal on MRI With Balanced Steady-State Gradient-Echo Sequences After Labyrinthine Ischemia in the Common Cochlear Artery Territory as an Early Sign of Fibrosis. Front. Neurol. 11:608838. doi: 10.3389/fneur.2020.608838

ear function, a careful bedside examination supplemented by instrumental assessments, including vHIT and VEMPs, of vestibular receptors and afferents may be completed by MRI with balanced steady-state gradient-echo sequences at a later time to confirm the diagnosis and address both etiology and functional outcome.

Keywords: common cochlear artery, labyrinthine ischemia, posterior semicircular canal, labyrinthine fibrosis, video-head impulse test, vestibular-evoked myogenic potentials, inner ear MRI

INTRODUCTION

Inner ear fibrosis and ossification result from fibrous tissue deposits and new bone formation, respectively, in labyrinthine structures. These conditions represent subsequent final steps of several inner ear pathologies, including infections, genetic and autoimmune diseases, trauma, and ischemia (1). Animal studies on labyrinthine arterial obstruction have demonstrated that ischemia may result in end-organ fibrosis within 2 weeks and ossification within a few months (2, 3). Similarly, inner ear fibrosis has been observed in post-mortem examination of patients who had suffered an acute labyrinthine ischemia (4, 5).

Magnetic resonance imaging (MRI) with balanced steady-state gradient-echo sequences has demonstrated higher sensitivity in detecting signs of early fibrosis compared to high-resolution CT (HRCT) scans (6). In particular, steady-state gradient-echo MRI such as FIESTA (fast imaging employing steady-state acquisition) and constructive interference in steady state (CISS) sequences with multiplanar reconstructions can offer a high-contrast evaluation of the signal loss within the fluid-filled spaces on the membranous labyrinth due to fibrotic tissue deposits (7).

The development of modern tools for vestibular testing, such as video head impulse test (vHIT) and vestibular evoked myogenic potentials (VEMPs), has allowed fast measurements of the activity of each semicircular canal (SC) and otolith receptors/afferents in clinical settings (8, 9). Thanks to the interpretation of data obtained from matching results from assessments of all five inner ear sensors, it has become possible to identify specific lesion patterns and offer reliable hypothesis on underlying etiopathological mechanisms affecting inner ear receptors or vestibular nerve branches.

Here we describe the onset of posterior semicircular canal (PSC) fibrosis on MRI in a patient with a clinical presentation and instrumental findings consistent with acute stroke in the territory supplied by the common cochlear artery (CCA). We also review the relevant literature.

CASE DESCRIPTION

A 71-year-old man was admitted to our institution for evaluation of sudden onset of left-sided hearing loss (HL), vertigo, and severe unsteadiness persisting for over 12 days. His clinical history was consistent with arterial hypertension, atrial fibrillation (in treatment with oral anticoagulants), and myelodysplastic syndrome (regular hematologic follow-ups). He reported a transient ischemic attack 4 years earlier but denied any previous inner ear symptoms. Corresponding brain MRI images were reviewed, showing signs of periventricular leukoaraiosis and normal posterior fossa structures, including normally fluid-filled SCs on FIESTA sequences (**Figures 1A–C**).

Vestibular examination with video Frenzel goggles detected sustained spontaneous right-beating nystagmus exhibiting downbeat/right-torsional components after mastoid vibrations and headshaking. Oculomotor testing and a neurological examination ruled out central nervous system involvement, as did a brain CT scan. Tympanic membranes were unremarkable on micro-otoscopy. Pure-tone audiometry showed right-sided high-frequency sensorineural HL consistent with the patient's age and profound left-sided hearing impairment (**Figure 2A**). An ICS Impulse device (Otometrics, Natus Medical Inc, Denmark) was used to measure the vestibulo-ocular reflex (VOR) gain for all six semicircular canals. Gains were considered normal if >0.8 for lateral canals and >0.7 for vertical canals (8). Selective mild reduction of left posterior SC (PSC) activity was detected on vHIT (**Figure 2B**). A 2-channel evoked potential acquisition system (Viking, Nicolet EDX, CareFusion, Germany) was used for cervical and ocular VEMPs testing. Potentials were measured by delivering tone bursts (frequency: 500 Hz, duration: 8 ms, stimulation rate 5 Hz) *via* headphones. The recording system used an EMG-based biofeedback monitoring method to minimize variations in muscle contractions and VEMPs amplitudes. Each stimulus was retested to assess reproducibility of responses, and the stimulus intensity was reduced by 10 dB until the threshold for each side was reached. Although no cervical responses could be detected on the pathologic side consistent with left-sided isolated saccular loss, symmetrical potentials were evoked for ocular testing (**Figures 2C,D**). Clinical presentation and instrumental findings suggested a labyrinthine ischemia in the territory supplied by the left CCA.

The patient immediately began steroid therapy (1 week intravenous 1 mg/Kg dexamethasone followed by oral tapering for 1 additional week) and oral treatment with 48 mg/day betahistine for 2 weeks, in accordance with recommendations available in the literature (10). Simultaneously, he received 15 sessions of hyperbaric oxygen therapy, and a cardiologic evaluation with transcranial Doppler assessment was requested to adjust anticoagulant and antihypertensive therapy, if necessary. Since stenosis or blood flow abnormalities within the main intracranial arteries were excluded, current therapy was continued.

Due to related cardiovascular risk factors, a new brain MRI was also scheduled in the following days. Acute brainstem infarction in diffusion-weighted and T2-weighted

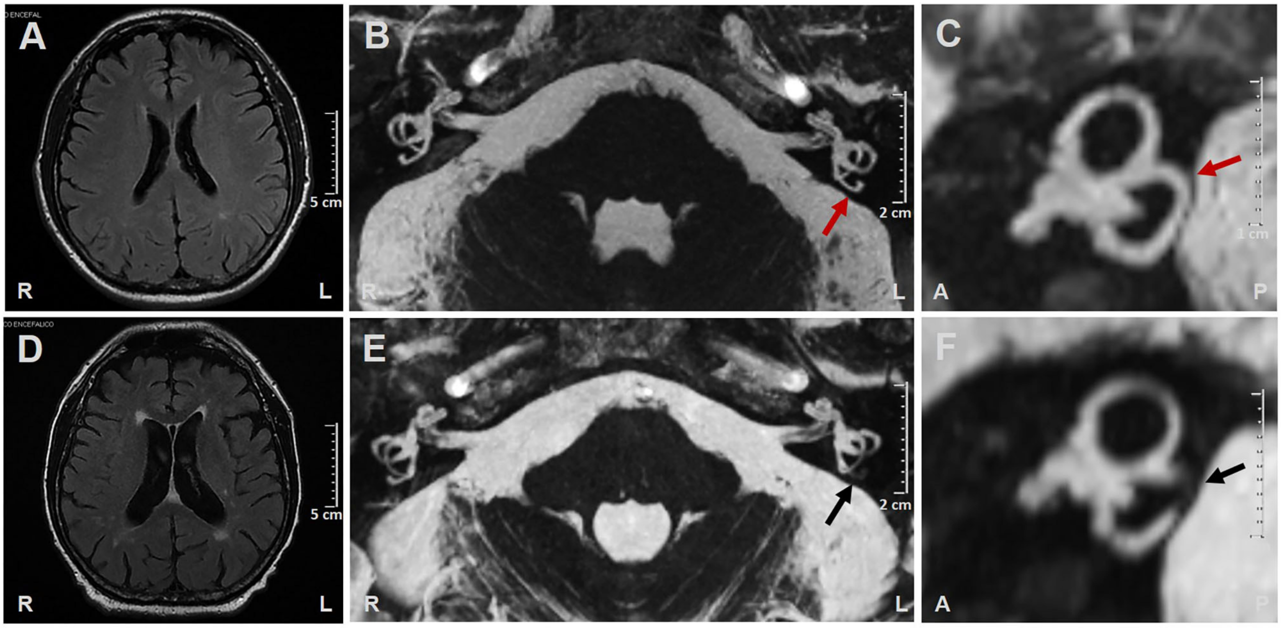

FIGURE 1 | (A–C) Brain MRI performed 4 years prior to left-sided labyrinthine ischemia exhibiting **(A)** Slight signs of periventricular leukoaraiosis on axial T2-weighted FLAIR (fluid-attenuated inversion recovery) images. **(B)** Axial and **(C)** sagittal MRI with 3D-FIESTA (fast imaging employing steady-state acquisition) sequences showing normally fluid filled semicircular canals on both sides (red arrows indicate left posterior semicircular canal). **(D–F)** Brain MRI performed 14 days after left-sided labyrinthine ischemia showing **(D)** Increased areas of periventricular leukoaraiosis and widened cerebrospinal fluid spaces on atrophic basis on axial T2-weighted FLAIR images. **(E)** Axial and **(F)** sagittal MRI with 3D-FIESTA sequences showing filling defect within the left posterior semicircular canal (black arrows). A, anterior; L, left; P, posterior; R, right.

fluid-attenuated inversion recovery (FLAIR) images were excluded, whereas widened cerebrospinal-fluid spaces on atrophic basis and increased areas of leukoaraiosis compared with previous neuroimaging were detected (**Figure 1D**). 3D-FIESTA sequences detected signal loss within left-sided PSC consistent with fibrous tissue deposits (**Figures 1E,F**).

At 3-week evaluation with video Frenzel goggles, slight spontaneous right-beating nystagmus enhanced by mastoid vibrations and headshaking could still be detected. Hearing evaluation with pure-tone audiometry showed a moderate to severe down-sloping sensorineural HL on the left side, consistent with mild recovery of cochlear function (**Figure 3A**). Nevertheless, word recognition on the left side was poor on speech audiometry, while the speech discrimination score was optimal on the healthy side (**Figure 3B**). However, the patient refused additional therapy with intratympanic steroids.

Although vHIT showed further reduction in left-sided PSC activity (**Figure 3C**), the patient reported that his vestibular symptoms were substantially relieved. Rehabilitation was therefore not pursued, and the patient refused to undergo additional testing, including VEMPs reassessment and caloric testing. Temporal bone HRCT performed 2 weeks later finally excluded signs of labyrinthine ossifications (**Figures 3D,E**).

Written informed consent was obtained from the patient for the publication of this case report, including all data and images.

DISCUSSION

The inner ear is supplied by the internal auditory artery, which branches from the anterior-inferior cerebellar artery (AICA) and divides into two main terminal branches: the anterior vestibular artery and CCA. Whereas, the first mostly supplies the utricle and the horizontal and superior SCs, the latter mainly serves the cochlear turns, saccule, and PSC (11, 12) (**Figure 4**).

In recent years, thanks to the introduction in clinical practice of fast modern devices such as vHIT and VEMPs, which provide a precise assessment for each SC and the otolith end organs in the high-frequency domain, instrumental testing has demonstrated its pivotal role in the topographical diagnosis of selective dysfunction of inner ear structures, including in the acute stage (8, 9). Nevertheless, underlying etiologic mechanisms may remain unclear. In fact, whereas ischemic damage should always be suspected when symptoms consistent with peripheral vestibular loss are accompanied by sudden HL, in cases of isolated vertigo of peripheral origin, clinical and instrumental assessments may not clarify whether an inflammatory or vascular lesion represents the underlying mechanism (13–16). For example, a partial vestibular hypofunction sparing saccular and PSC activity may be due either to neuritis involving the superior nerve division or to anterior vestibular artery stroke (15, 17). Conversely, a selective ischemia in the territory supplied by CCA seems to represent the most likely disorder

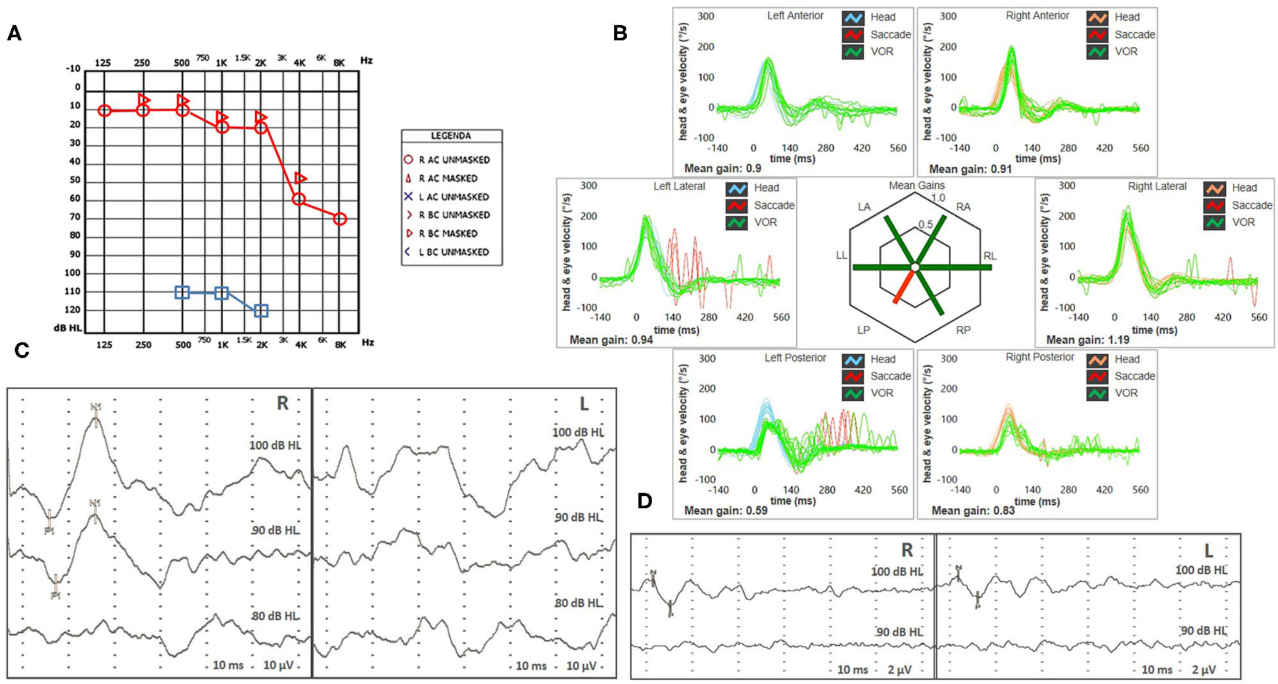

FIGURE 2 | (A,B) Presenting scenario including **(A)** Pure-tone audiometry exhibiting right-sided high-frequency sensorineural hearing impairment and profound left-sided hearing loss. **(B)** vHIT. Blue lines represent head impulses exciting left canals, orange lines correspond to impulses for right canals, green lines represent eye movements induced by the activation of VOR following each impulse and red lines correspond to corrective saccades. Mean value of VOR-gain (eye velocity/head velocity) is reported for each canal. The hexagonal plot in the center of the figure summarizes mean VOR-gains for each canal; normal gains are shown in green and deficient gains are in red. A selective deficient VOR-gain for the left posterior semicircular canal (0.59) with overt saccades can be observed. Cervical VEMPs **(C)** and ocular VEMPs **(D)** for air-conducted sounds. For cervical VEMPs, right and left lines correspond to myogenic responses (p1–n1) recorded on the right and left SCM muscle (i.e., right and left saccular responses), respectively. For ocular VEMPs, being crossed responses, right and left lines represent potentials (n–p) recorded under the left and right eye (i.e., right and left utricular responses), respectively. VEMPs testing revealed normal responses on the right side (83 µV at 100 dB HL stimuli) and absent potentials on the left, whereas symmetrical amplitudes for ocular VEMPs (R: 6 µV and L: 5 µV at 100 dB HL stimuli) could be detected. L, left; LA, left anterior; LL, left lateral; LP, left posterior; R, right; RA, right anterior; RL, right lateral; RP, right posterior; SCM, sternocleidomastoid; vHIT, video head impulse test; VEMPs, vestibular evoked myogenic potentials; VOR, vestibulo-ocular reflex.

accounting for an acute functional loss of cochlear epithelium, saccular macula and PSC ampulla (13, 18, 19). The same lesion pattern was detected in our patient exhibiting profound left-sided HL, abnormal cervical VEMPs on the same side and selective VOR-gain reduction for ipsilateral PSC. Furthermore, asymmetrical stimulation of vertical SCs resulting from an acute selective loss for left-sided PSC activity may likely account for right-torsional/downbeat components elicited by mastoid vibrations and headshaking in the acute stage (20, 21). On the other hand, different levels of vestibular compensation or hypothetical involvement of hair cells encoding low-frequency stimuli for left horizontal SC may explain horizontal paretic nystagmus detected at the follow-up evaluation. Unfortunately, the patient refused to undergo the caloric test, which assesses horizontal VOR in the low-frequency domain, so we could not test type II hair cells within the horizontal SC and regular afferents running along the superior division of the vestibular nerve.

Steady-state gradient-echo MRI such as FIESTA and CISS sequences offer a high signal-to-noise ratio that allows submillimeter imaging and high-quality multiplanar reconstructions. These images are widely used when a high-contrast evaluation of the fluid-filled spaces on the membranous labyrinth is required to check for cochlear patency and inner ear malformations in patients scheduled for cochlear implant surgery (22, 23). The same algorithms are generally included in MRI protocols to evaluate the internal auditory canal content for VIII cranial nerve tumors due to the high contrast between fluids and solid structures (24–26). Conversely, in cases of suspected posterior fossa stroke, other sequences, such as diffusion-weighted MRI, are routinely used to rule out acute infarct lesions (27). Nevertheless, an accurate bedside examination with a 3-step bedside oculomotor testing called the HINTS protocol (head impulse, observation of nystagmus in different gaze positions and test of skew) has demonstrated its ability to detect an acute stroke of the posterior fossa within the first 48 h with higher sensitivity compared to early MRI (27). More recently, further studies have concluded that including hearing evaluation in the protocol (HINTS plus) can add a substantial contribution to detecting AICA strokes (28).

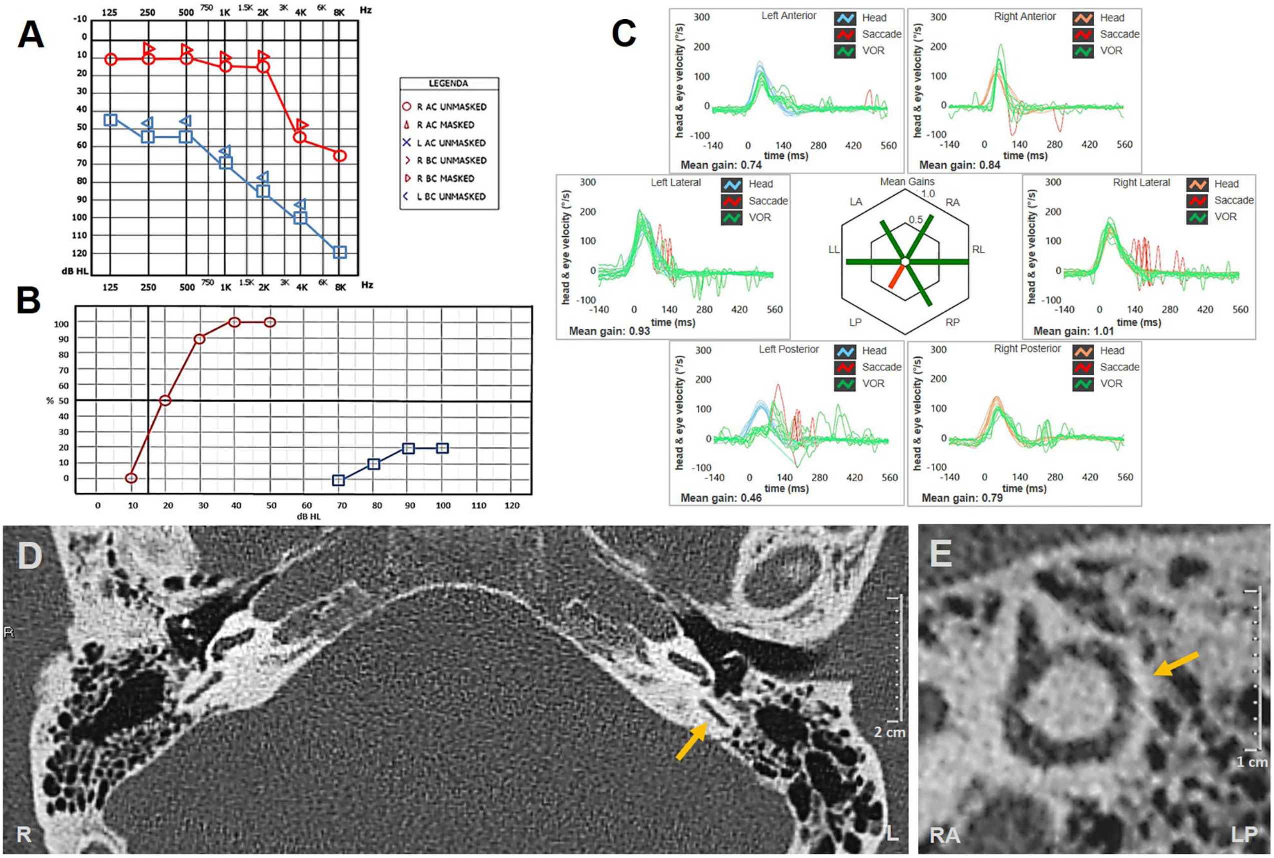

FIGURE 3 | (A–C) Instrumental picture following steroids and hyperbaric oxygen therapy. **(A)** Pure-tone audiometry exhibiting partial recovery for right-side hearing function with a pure-tone average (500 Hz−4 kHz) of 77.5 dB. **(B)** Standard speech audiometry in silent setting showing optimal (100%) and poor (20%) speech discrimination score on the right and left sides, respectively. **(C)** vHIT showing persistent selective loss for left posterior canal VOR-gain (0.46) with both overt and covert saccades. Affected canal VOR-gain is further impaired compared to presenting values. **(D,E)** Temporal bones HRCT scans with axial **(D)** and parasagittal reconstructed image along the Stenver plane **(E)** excluding signs of posterior semicircular canal ossification on the left side (yellow arrows). HRCT, high-resolution computed tomography; L, left; LA, left anterior; LL, left lateral; LP, left posterior; R, right; RA, right anterior; RL, right lateral; RP, right posterior; vHIT, video head impulse test; VOR, vestibulo-ocular reflex.

Therefore, patients presenting with acute cochleovestibular symptoms and high vascular risk factors should always be scheduled for a brain MRI at 48 h to rule out associated brainstem infarction. Conversely, in cases where symptoms are likely due to peripheral disorders, bedside examination complemented by instrumental inner ear assessment should adequately guide the detection of the lesion site; neuroimaging can be postponed to rule out VIII cranial nerve lesions and/or labyrinthine abnormalities.

To the best of our knowledge, this is the first report showing newly formed inner ear fibrosis based on MRI findings before and after a CCA ischemic lesion. Besides clinical and instrumental findings supporting this etiopathogenetic hypothesis, labyrinthine ischemia is also consistent with the high cardiovascular risk factors exhibited by the patient. Additional MRI data, including pronounced periventricular leukoaraiosis and wide cerebrospinal fluid spaces, are also in accordance with atrophic sequelae following chronic hypoxic insult to the brain tissue. The aforementioned findings strengthen the assumed mechanism underlying the presenting scenario involving ischemic mechanisms. It might be postulated that the lack of concurrent cochlear and saccular abnormalities on imaging may reflect possible variable susceptibility to steroid and oxygen therapy among different hair cells or different inter-individual patterns of venous drainage among inferior labyrinthine structures, making PSC more vulnerable to hypoxia in this case (11). The asymmetrical extent of damage among inner ear receptors sharing the same vascular supply from CCA can likely account for the different behavior exhibited by each sensor over time. In fact, whereas cochlear function mildly improved following treatment, though not achieving a serviceable hearing level, left-sided PSC activity was found further impaired on follow-up. This aspect seems to be in agreement with recent studies correlating loss of vestibular function with filling defect within the inner ear on MRI (6, 23). Unfortunately,

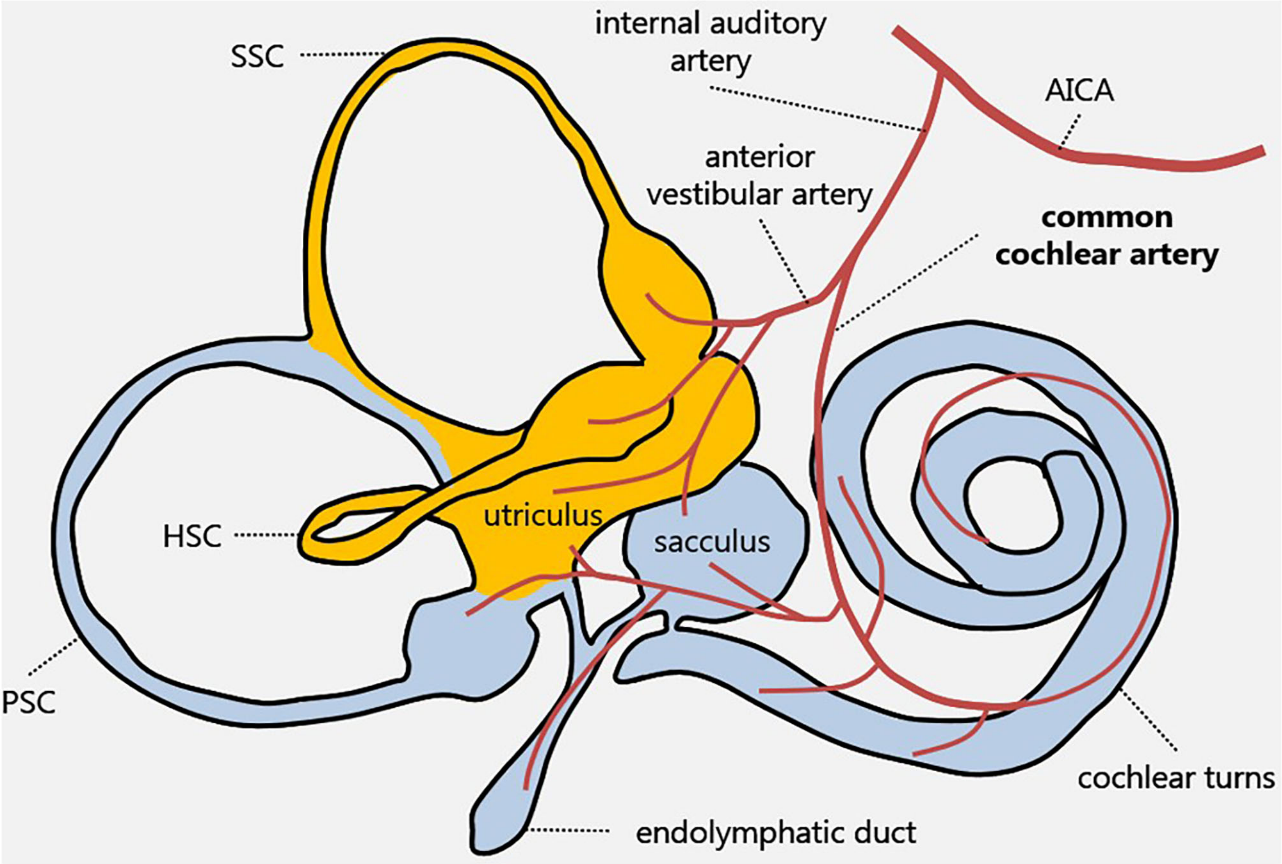

FIGURE 4 | Inner ear vascular supply. Labyrinthine receptors mainly supplied by the anterior vestibular artery and the common cochlear artery are in yellow and in light blue, respectively. AICA, anterior-inferior cerebellar artery; HSC, horizontal semicircular canal; PSC, posterior semicircular canal; SSC, superior semicircular canal.

VEMPs could not be reassessed to check whether saccular function recovered as expected in accordance with the lack of corresponding radiological abnormalities, despite the fact that patients exhibiting chronic white matter lesions on MRI seem to develop worse VEMPs outcomes after acute vestibular loss (29).

Temporal bone HRCT scans performed almost 2 months after symptom onset showed normally patent inner ear structures, excluding progression of damage toward ossification. Nevertheless, due to the short-term follow-up, we cannot exclude a possible late onset of PSC ossification in our patient.

Since balanced steady-state gradient echo sequences represent a reliable tool to detect inner ear fibrosis irrespective of the patients' age (7, 30), it seems reasonable to recommend considering CCA ischemia in cases of filling defects for PSC in patients with acute onset of HL and vertigo. Clinicians should be aware of the eventuality of a labyrinthine stroke, as it has been demonstrated how peripheral ischemic lesions may precede a major stroke involving posterior fossa structures (31, 32). Furthermore, as already suggested, clinicians are encouraged to seek causes of dizziness other than the sole chronic white matter lesions, given that small vessel disease is often associated to other peripheral vestibular disorders, as has already been described (33).

Though this report likely represents a unique case with obvious limitations related to single-case reports without histopathological support, it might be assumed that post-ischemic fibrosis of inner ear receptors could not represent an exceptional finding, particularly when we consider that steady-state gradient-echo MRI sequences are not routinely included in the imaging protocol adopted for acute HL and vertigo. Therefore, in the case of acute cochleovestibular symptoms where a careful clinical/instrumental assessment orients the diagnosis toward a peripheral lesion, along with recommending a global vestibular assessment with vHIT and VEMPs, we would also suggest postponing neuroimaging and routinely using the 3D-FIESTA MRI sequences to detect possible signs of post-ischemic fibrosis. This finding may be extremely helpful especially in those cases where underlying etiopathological mechanisms are not adequately addressed by clinical and instrumental assessments, which was not the case for our patient.

CONCLUSION

The patient described in this report exhibited on MRI an unusual filling defect consistent with fibrosis in the PSC following acute labyrinthine ischemia. This finding seems also to be related to poor functional outcome for the affected end organ. Therefore, it may be reasonable to suggest using balanced steady-state gradient-echo sequences a few weeks following an acute lesion of the inner ear sensors, as they might detect signal loss within the membranous labyrinth suggesting post-ischemic fibrosis. This finding, besides addressing the diagnosis in cases where the underlying etiopathological mechanisms are unclear, might hypothetically provide clues on the functional behavior of the involved inner ear sensors over time. However, additional reports reproducing similar findings with longer follow-up are needed before any conclusion can be reached on the clinical value of filling defects within inner ear on MRI in patients with acute cochleovestibular symptoms.

DATA AVAILABILITY STATEMENT

The raw data supporting the conclusions of this article will be made available by the authors, without undue reservation.

ETHICS STATEMENT

Written informed consent was obtained from the patient for the publication of any potentially identifiable images or data included in this article.

AUTHOR CONTRIBUTIONS

AC, EP, and AB: conceptualization, investigation, data acquisition and interpretation, and original draft preparation. AC: images and artwork. CS, MB, CB, SD, FC, MF, and FL: investigation, data collection, and original draft preparation. SM and PM: substantial role in data interpretation and manuscript revision. GB and AG: supervision and manuscript review. All authors approved the final version of the manuscript.

ACKNOWLEDGMENTS

The authors would like to thank Jacqueline M. Costa for providing English language editing.

REFERENCES

1. Jackler RK, Brackmann DE. *Neurotology*. 2nd ed. Philadelphia: Mosby (2005).
2. Kimura RS, Perlman HB. Arterial obstruction of the labyrinth: part I, cochlear changes. *Ann Otol Rhinol Laryngol.* (1958) 67:5–24. doi: 10.1177/000348945806700101
3. Kimura RS, Perlman HB. Arterial obstruction of the labyrinth: part I, cochlear changes; part II, vestibular changes. *Ann Otol Rhinol Laryngol.* (1958) 67:25–40. doi: 10.1177/000348945806700102
4. Gussen R. Sudden deafness of vascular origin: a human temporal bone study. *Ann Otol Rhinol Laryngol.* (1976) 85:94–100. doi: 10.1177/000348947608500117
5. Kim JS, Lopez I, DiPatre PL, Liu F, Ishiyama A, Baloh RW. Internal auditory artery infarction: clinicopathologic correlation. *Neurology.* (1999) 52:40–4. doi: 10.1212/wnl.52.1.40
6. Van Rompaey V, De Belder F, Parizel P, Van de Heyning P. Semicircular canal fibrosis as a biomarker for lateral semicircular canal function loss. *Front Neurol.* (2016) 7:43. doi: 10.3389/fneur.2016.00043
7. Held P, Fellner C, Fellner F, Graf S, Seitz J, Strutz J. 3D MRI of the membranous labyrinth. An age related comparison of MR findings in patients with labyrinthine fibrosis and in persons without inner ear symptoms. *J Neuroradiol.* (1998) 25:268–74.
8. Halmagyi GM, Chen L, MacDougall HG, Weber KP, Mc Garvie LA, Curthoys IS. The video head impulse test. *Front Neurol.* (2017) 8:258. doi: 10.3389/fneur.2017.00258
9. Rosengren SM, Welgampola MS, Colebatch JG. Vestibular evoked myogenic potentials: past, present and future. *Clin Neurophysiol.* (2010) 121:636–51. doi: 10.1016/j.clinph.2009.10.016
10. Stachler RJ, Chandrasekhar SS, Archer SM, Rosenfeld RM, Schwartz SR, Barrs DM, et al. Clinical practice guideline: sudden hearing loss. *Otolaryngol Head Neck Surg.* (2012) 146(Suppl. 3):S1–35. doi: 10.1177/0194599812436449
11. Belal A, Jr. The effects of vascular occlusion on the human inner ear. *J Laryngol Otol.* (1979) 93:955–68. doi: 10.1017/s0022215100087958
12. Mazzoni A. The vascular anatomy of the vestibular labyrinth in man. *Acta Otolaryngol.* (1990) 472:1–83. doi: 10.3109/00016489009121137
13. Rambold H, Boenki J, Stritzke G, Wisst F, Neppert B, Helmchen C. Differential vestibular dysfunction in sudden unilateral hearing loss. *Neurology.* (2005) 64:148–51. doi: 10.1212/01.WNL.0000148599.18397.D2
14. Iwasaki S, Takai Y, Ozeki H, Ito K, Karino S, Murofushi T. Extent of lesions in idiopathic sudden hearing loss with vertigo: study using click and galvanic vestibular evoked myogenic potentials. *Arch Otolaryngol Head Neck Surg.* (2005) 131:857–62. doi: 10.1001/archotol.131.10.857
15. Kim JS, Lee H. Inner ear dysfunction due to vertebrobasilar ischemic stroke. *Semin Neurol.* (2009) 29:534–40. doi: 10.1055/s-0029-1241037
16. Lee H, Kim JS, Chung EJ, Yi HA, Chung IS, Lee SR, et al. Infarction in the territory of anterior inferior cerebellar artery: spectrum of audiovestibular loss. *Stroke.* (2009) 40:3745–51. doi: 10.1161/STROKEAHA.109.564682
17. Jeong SH, Kim HJ, Kim JS. Vestibular neuritis. *Semin Neurol.* (2013) 33:185–94. doi: 10.1055/s-0033-1354598
18. Pogson JM, Taylor RL, Young AS, McGarvie LA, Flanagan S, Halmagyi GM, et al. Vertigo with sudden hearing loss: audio-vestibular characteristics. *J Neurol.* (2016) 263:2086–96. doi: 10.1007/s00415-016-8214-0
19. Eliezer M, Toupet M, Guichard JP, Kania R, Houdart E, Hautefort C. Cochleovestibular artery syndrome: consideration based on VHIT, VEMP, and inner ear MRI. *J Neurol.* (2019) 266:2327–9. doi: 10.1007/s00415-019-09407-9
20. Halmagyi GM, Aw ST, Karlberg M, Curthoys IS, Todd MJ. Inferior vestibular neuritis. *Ann NY Acad Sci.* (2002) 956:306–13. doi: 10.1111/j.1749-6632.2002.tb02829.x
21. Kim JS, Kim HJ. Inferior vestibular neuritis. *J Neurol.* (2012) 259:1553–60. doi: 10.1007/s00415-011-6375-4
22. Trimble K, Blaser S, James AL, Papsin BC. Computed tomography and/or magnetic resonance imaging before pediatric cochlear implantation? Developing an investigative strategy. *Otol Neurotol.* (2007) 28:317–24. doi: 10.1097/01.mao.0000253285.40995.91
23. West N, Sass H, Klokker M, Cayé-Thomasen P. Functional loss after meningitis-evaluation of vestibular function in patients with postmeningitic hearing loss. *Front Neurol.* (2020) 11:681. doi: 10.3389/fneur.2020.00681
24. Oh JH, Chung JH, Min HJ, Cho SH, Park CW, Lee SH. Clinical application of 3D-FIESTA image in patients with unilateral inner ear symptom. *Korean J Audiol.* (2013) 17:111–7. doi: 10.7874/kja.2013.17.3.111
25. Ishikawa K, Haneda J, Okamoto K. Decreased vestibular signal intensity on 3D-FIESTA in vestibular schwannomas differentiating from meningiomas. *Neuroradiology.* (2013) 55:261–70. doi: 10.1007/s00234-012-1100-2
26. Abele TA, Besachio DA, Quigley EP, Gurgel RK, Shelton C, Harnsberger HR, et al. Diagnostic accuracy of screening MR imaging using unenhanced

axial CISS and coronal T2WI for detection of small internal auditory canal lesions. *AJNR Am J Neuroradiol.* (2014) 35:2366–70. doi: 10.3174/ajnr.A4041

27. Kattah JC, Talkad AV, Wang DZ, Hsieh YH, Newman-Toker DE. HINTS to diagnose stroke in the acute vestibular syndrome: three-step bedside oculomotor examination more sensitive than early MRI diffusion-weighted imaging. *Stroke.* (2009) 40:3504–10. doi: 10.1161/STROKEAHA.109.551234
28. Newman-Toker DE, Kerber KA, Hsieh YH, Pula JH, Omron R, Saber Tehrani AS, et al. HINTS outperforms ABCD2 to screen for stroke in acute continuous vertigo and dizziness. *Acad Emerg Med.* (2013) 20:986–96. doi: 10.1111/acem.12223
29. Adamec I, Skorić MK, HandŽić J, Barušić AK, Bach I, Gabelić T, et al. The role of cervical and ocular vestibular-evoked myogenic potentials in the follow-up of vestibular neuritis. *Clin EEG Neurosci.* (2014) 45:129–36. doi: 10.1177/1550059413483452
30. Melhem ER, Shakir H, Bakthavachalam S, MacDonald CB, Gira J, Caruthers SD, et al. Inner ear volumetric measurements using high-resolution 3D T2-weighted fast spin-echo MR imaging: initial experience in healthy subjects. *AJNR Am J Neuroradiol.* (1998) 19:1819–22.
31. Kim JS, Cho KH, Lee H. Isolated labyrinthine infarction as a harbinger of anterior inferior cerebellar artery territory infarction with normal diffusion-weighted brain MRI. *J Neurol Sci.* (2009) 278:82–4. doi: 10.1016/j.jns.2008.12.002
32. Lee H. Audiovestibular loss in anterior inferior cerebellar artery territory infarction: a window to early detection? *J Neurol Sci.* (2012) 313:153–9. doi: 10.1016/j.jns.2011.08.039
33. Cerchiai N, Mancuso M, Navari E, Giannini N, Casani AP. Aging with cerebral small vessel disease and dizziness: the importance of undiagnosed peripheral vestibular disorders. *Front Neurol.* (2017) 8:241. doi: 10.3389/fneur.2017.00241

Conflict of Interest: The authors declare that the research was conducted in the absence of any commercial or financial relationships that could be construed as a potential conflict of interest.

frontiers in Neurology

ORIGINAL RESEARCH
published: 20 January 2021
doi: 10.3389/fneur.2020.595038

The Correlation of a 2D Volume-Referencing Endolymphatic-Hydrops Grading System With Extra-Tympanic Electrocochleography in Patients With Definite Ménière's Disease

Baihui He [1,2,3†], ***Fan Zhang*** [1,2,3†], ***Hui Zheng*** [4†], ***Xiayu Sun*** [1,2,3], ***Junmin Chen*** [1,2,3], ***Jianyong Chen*** [1,2,3], ***Yupeng Liu*** [1,2,3], ***Lu Wang*** [1,2,3], ***Wei Wang*** [1,2,3], ***Shuna Li*** [1,2,3], ***Jun Yang*** [1,2,3*] ***and Maoli Duan*** [5,6*]

[1] Department of Otolaryngology Head and Neck Surgery, Xinhua Hospital, Shanghai Jiaotong University School of Medicine, Shanghai, China, [2] Ear Institute, Shanghai Jiaotong University School of Medicine, Shanghai, China, [3] Shanghai Key Laboratory of Translational Medicine on Ear and Nose Diseases, Shanghai, China, [4] Department of Radiology, Xinhua Hospital, Shanghai Jiaotong University School of Medicine, Shanghai, China, [5] Department of Otolaryngology Head and Neck and Neurotology and Audiology, Karolinska Institute, Karolinska University Hospital, Stockholm, Sweden, [6] Department of Clinical Science, Intervention and Technology, Karolinska Institute, Stockholm, Sweden

Edited by:
Bryan Kevin Ward,
Johns Hopkins University,
United States

Reviewed by:
Valerie Kirsch,
LMU Munich, Germany
Haibo Shi,
Shanghai Jiao Tong University
Affiliated Sixth People's
Hospital, China

****Correspondence:***
Jun Yang
yangjun@xinhuamed.com.cn
Maoli Duan
maoli.duan@ki.se

† These authors have contributed equally to this work

Specialty section:
This article was submitted to
Neuro-Otology,
a section of the journal
Frontiers in Neurology

Received: *14 August 2020*
Accepted: *16 December 2020*
Published: *20 January 2021*

Citation:
He B, Zhang F, Zheng H, Sun X, Chen J, Chen J, Liu Y, Wang L, Wang W, Li S, Yang J and Duan M (2021) The Correlation of a 2D Volume-Referencing Endolymphatic-Hydrops Grading System With Extra-Tympanic Electrocochleography in Patients With Definite Ménière's Disease. Front. Neurol. 11:595038. doi: 10.3389/fneur.2020.595038

Background: Although magnetic resonance imaging (MRI) of the membranous labyrinth and electrocochleography (ECochG) have been used to diagnose endolymphatic hydrops (ELH) in patients with Ménière's disease (MD), the relationship between imaging and ECochG is not well-documented.

Objectives: This study evaluates the ELH using 3D-FLAIR MRI and extra-tympanic ECochG (ET-ECochG) and correlates the results from 3D-FLAIR MRI to those from ET-ECochG.

Materials and Methods: 3D-FLAIR MRI images of 50 patients were assessed using a 2D volume-referencing grading system (VR scores, relative scores according to the known volumes of the cochlea, vestibule, and semicircular canals). Forty healthy subjects were included and compared to 51 definite MD ears of 50 patients while analyzing the ET-ECochG, which used a self-made bronze foil electrode. The amplitude ratio of the summating potential (SP) to the action potential (AP) (SP/AP) and the area ratio of SP to AP (Asp/Aap) were collected. Relative ELH grade scores were then correlated to ET-ECochG (SP/AP, Asp/Aap).

Results: The VR scores showed a better correlation ($r = 0.88$) with the pure tone average (PTA), disease duration, and vertigo frequency of MD than the Bernaerts scores (grading the cochlea and vestibule separately) ($r = 0.22$). The SP/AP and Asp/Aap of the unilateral MD patients were statistically comparable to those measured in contralateral ears and the results between the definite MD ears with healthy ears were statistically comparable ($p < 0.05$). In a ROC analysis Asp/Aap (area under curve, AUC 0.98) significantly ($p = 0.01$) outperformed SP/AP (AUC 0.91).

The total score of ELH, vestibular ELH, and cochlear ELH were also correlated with SP/AP and Asp/Aap. The strongest correlation was found between the Asp/Aap and cochlear ELH ($r = 0.60$).

Conclusion: The 2D volume-referencing grading system was more meaningful than the Bernaerts scores. A correlation was found between ELH revealed by 3D-FLAIR MRI and the SP/AP of ET-ECochG in evaluating definite MD patients. The Asp/Aap appeared a more sensitive and reliable parameter than SP/AP for diagnosing the ELH of the membranous labyrinth.

Keywords: endolymphatic hydrops, magnetic resonance imaging, Ménière's disease, electrocochleography, diagnosis

INTRODUCTION

Menière's disease (MD) is a multifactorial inner ear disorder characterized by fluctuating sensorineural hearing loss, spontaneous vertigo attacks, tinnitus, and aural fullness (1). The pathophysiology of MD is still unclear and may be related to a combination of genetic effect and environmental factors (1, 2), while the histopathological association of MD and endolymph hydrops (ELH) in the cochlear and the vestibular organs is definite (3, 4). The development and progress in magnetic resonance imaging (MRI) techniques has enabled the visualization of ELH separately in cochlea and vestibule using a 3.0 Tesla (T) scanner and a gadolinium-based contrast agent (5–7). Recently, volume quantification methods of the inner ear, especially the endolymph, have been introduced. However, these methods require specific scan sequences, 3D workstations (8–10), or probabilistic atlas (11) that require imaging processing capabilities and therefore may be difficult to establish in a clinical setting. Relatively, clinicians prefer a 2D semi-quantitative grading system that is easily and quickly applicable without having to invest further time or resources, for example, the grading standard stated by Nakashima (12). Additional 2D grading methods have been proposed to grade the ELH in the cochlea and vestibule. However, 2D ELH grading methods grade ELH in the cochlea and vestibule separately (13–15) without considering the volume ratio between cochlea and the vestibule and excluded the semicircular canals. The volume ratio and the semicircular canals should be taken into consideration to better represent the total ELH of inner ears. Therefore, an adjusted grading standard was used in this study, according to the literature about the volume ratio (10) to evaluate the ELH of MD patients.

The diagnosis of MD is based on clinical manifestations and the pure tone audiogram according to the 2015 consensus statement of the Barany Society (1). Other auditory and vestibular tests like electrocochleogram (ECochG), vestibular-evoked myogenic potential (VEMP), and glycerol test are applied to provide supportive information (2, 16). Besides, MRI can support the diagnosis of MD by identifying ELH (16). The high expense and complex procedure limit the wide usage of MRI among early diagnosed patients. Therefore, a low-cost non-MRI-dependent diagnostic proxy for ELH is needed. ECochG is a method of directly recording the electrical activity of the cochlea and the acoustic nerve in response to acoustic stimuli (17, 18). It has been recognized that ECochG is a valuable tool in the diagnosis of MD due to its sensitivity to the hydrops in the membranous labyrinth (18, 19). However, the diagnostic value of ECochG for MD diagnosis was under debate (18, 20). Extra-tympanic ECochG (ET-ECochG) is a non-invasive protocol using an external auditory canal electrode. An elevation of the amplitude ratio of the summating potential (SP) to the action potential (AP) (SP/AP) of ECochG has been used as an adjunct to diagnose MD (18). It is likely that the analysis of the area ratio of SP to AP (Asp/Aap) increases the sensitivity of the test (19). However, the relationship between ET-ECochG and the grading of ELH is not well-documented. The purpose of this study was to establish a 2D volume-referencing ELH grading system and further explore the relationship between the degree of ELH with ET-ECochG in definite MD patients.

MATERIALS AND METHODS

Ethics

This study was approved by the Ethics Committee of Xinhua Hospital, Shanghai Jiaotong University School of Medicine (Approval Number: XHEC-D-2020-119). Written informed consent was obtained from each participant.

Subjects

In this retrospective study, clinically diagnosed MD patients were enrolled between August 2018 and June 2020 at the Department of Otolaryngology-Head and Neck Surgery, Xinhua Hospital, Shanghai Jiaotong University School of Medicine. The inclusion criteria were as follows: (a) patients with a clinical diagnosis of the definite MD according to the 2015 consensus statement of the Barany Society (1); (b) complete medical history record with ET-ECochG and MRI. The exclusion criteria were as follows: (a) chronic otitis media or a history of other middle or inner ear diseases; (b) history of middle or inner ear surgery; (c) lesions of the central nervous system and the inner ear or cerebellopontine angle; (d) history of vasodilators, diuretics or intratympanic gentamicin or dexamethasone treatment in the previous 2 weeks; (e) patients with claustrophobia, pregnancy, or allergy to Gadolinium-based contrast agents. Fifty patients met the inclusion criteria (51 definite MD ears; 28 females and 22 males; age range = 27–75 years; mean age = 53 years, SD = 12.2 years). All of their clinical history and examination results were collected from the medical history system.

Forty healthy subjects (80 ears; 23 females and 17 males; age range = 24–42 years; medium age = 27; quartile: 25–29 years) served as healthy controls for the ET-ECochG test using the bronze foil electrodes. Inclusion criteria for healthy subjects were as follows: normal otoscopy, pure tone thresholds better than 25 dBnHL from 0.25 to 8 kHz, normal tympanometry.

MRI

Intratympanic Gd Injection

Gadopentetate dimeglumine (Xudonghaipu Pharmaceutical Co. Ltd., Shanghai, China) was diluted eight-fold with saline (v/v = 1:7) and injected intra-tympanically (0.5 ml) through the inferior-posterior quadrant of the tympanic membrane bilaterally using a 1 ml syringe connected to a 23 G needle under the microscope. The subjects were then kept in the supine position for 60 min.

Acquisition of MRI

MRI was performed 24 h after the application of the contrast agent on a 3.0 Tesla MR scanner (Umr 770, united-imaging, Shanghai, China), using a 24-channel head coil. Three-dimensional heavily T2-weighted spectral attenuated inversion recovery (3D-T2-SPAIR, T2) and 3D T2 fluid-attenuated inversion recovery (3D-FLAIR) imaging were subsequently performed. The scan parameters for the 3D-FLAIR sequence were as follows: voxel size = 0.78 ∗ 0.78 ∗ 1.1 mm, scan time = 6 min and 11 s, time of repetition (TR) = 6500 ms, time of echo (TE) = 286.1 ms, time of inversion = 1950 ms, flip angle = 67°, echo train length = 160 points, slice thickness = 0.6 mm, field of view = 200 ∗ 200 mm, and matrix size = 256 ∗ 256. We used a heavily T2-weighted SPAIR sequence with the detailed scan parameters as follows: voxel size = 0.65 ∗ 0.52 ∗ 0.76 mm, scan time = 4 min and 30 s, TR = 1,300 ms, TE = 254.7 ms, flip angle = 110°, slice thickness = 0.4 mm, field of view = 200 ∗ 200 mm, and matrix size = 384 ∗ 384.

Image Processing of MRI

The images were evaluated separately by two experienced radiologists with 7-year and 25-year working experience. The radiologists were blinded to the patient's information according to an adjusted 2D volume-referencing semi-quantification grading system (VR scores, **Figure 1**). We preferred 2D semi-quantification analysis and made an adjusted criteria according to the inner ear fluid volume (21) and the normal endolymph ratio (10) described by Inui et al. and Ito et al. (**Table 1**). In brief, the degree of ELH in the vestibule and cochlea was assessed by visual comparison of the relative areas of the non-enhanced endolymphatic space vs. the contrast-enhanced perilymph space in several axial planes. The maximum hydrops' volumes for the vestibule and semicircular canals of the inner ear were estimated as the maximum inner ear fluid's volume of each part. However, in the cochlea, the endolymphatic hydrops seldom herniated into the scala tympani due to the bony spiral plate according to the images previously published (12, 22, 23). The volume ratio of the scala tympani vs. scala vestibuli (including the scala media) according to the area data describe by Wysocki et al. (24) is about 1.04. Therefore, the estimated maximum hydrops volume for cochlear ELH accounts for about 1/(1 + 1.04) of the total cochlear inner ear fluid volume or approximately 55.6 μl. To mark the hydrops of each part of the inner ear, we defined the same expansile volume represent for 1 point in each part. Since three semicircular canals have five crura and three canals, we supposed each semicircular canal or crus had a similar volume according to the reported guinea pigs data (25) and human segmentation pictures showed by Inui et al. (21). We also supposed ELH was distributed evenly in each part for easier calculation for the volume scores, and each part was marked as 1 point if the perilymph became narrow (mild hydrops) and 2 points if it became dark (severe hydrops). Therefore, the maximum hydrops' score for semicircular canals was 16 points, which represented the maximum expansile volume of ELH in semicircular canals (78.2 μl, each point = 4.89 μl). Accordingly, the cochlea was counted 9 points considering the relative expand volume while the vestibule was counted 12 points for the maximum hydrops' scores (**Table 1**). Then we adopted the semi-quantification grading system described by Bernaerts et al. (13) to separate vestibular hydrops into four degrees (Bernaerts scores). However, as for the cochlear hydrops, the cochlear endolymphatic expand volume was more than twice the volume of the scala media according to the human cochlear anatomy showed by Raufer et al. (26) and according to the calculated results (**Table 1**). So we separated the hydrops of cochlea into four degrees (**Figure 1**-cochlea) by adding a degree between normal cochlea and Grade I described by Bernaerts et al. because we discovered that for some patients the scala media could expand a bit without forming a round dark circle (**Figure 1b**). No grading system was proposed for semicircular canals before this study because researchers seldom viewed hydrops in semicircular canals. However, some reported vestibular herniation into the crura of the semicircular canals (23, 27). Among these studies, Sugimoto et al. defined that visible black area exceeded 1/3 or more as ELH herniation in the lateral and posterior semicircular canals. Furthermore, a small dark area can be found in asymptomatic contralateral ears frequently (**Figure 1i**). Given the convenient 2D semi-quantification in both vestibule and cochlea, the grading for semicircular canals was simplified by mainly evaluating and separating the hydrops in the lateral semicircular canal into four degrees. Therefore, we defined a small visible herniation which was 1/3 less than the semicircular canal with perilymph surrounding as no hydrops (None), a larger herniation (>1/3) with hydrops as Grade I and the total invisibility of crura, which often accompany the stenosis of canals as Grade II. If all semicircular canals were invisible, we defined as Grade III (**Figure 1**-semicircular canals). Finally, we analyzed the scores of each part of the inner ear separately (**Table 1**) and also in sum with the clinical history and ET-ECochG results. As reported in our previous study, patients with a long history of MD and severe hearing loss in the definite MD ears are more likely to exhibit endolymphatic hydrops in the asymptomatic contralateral ear (28), we thereby excluded

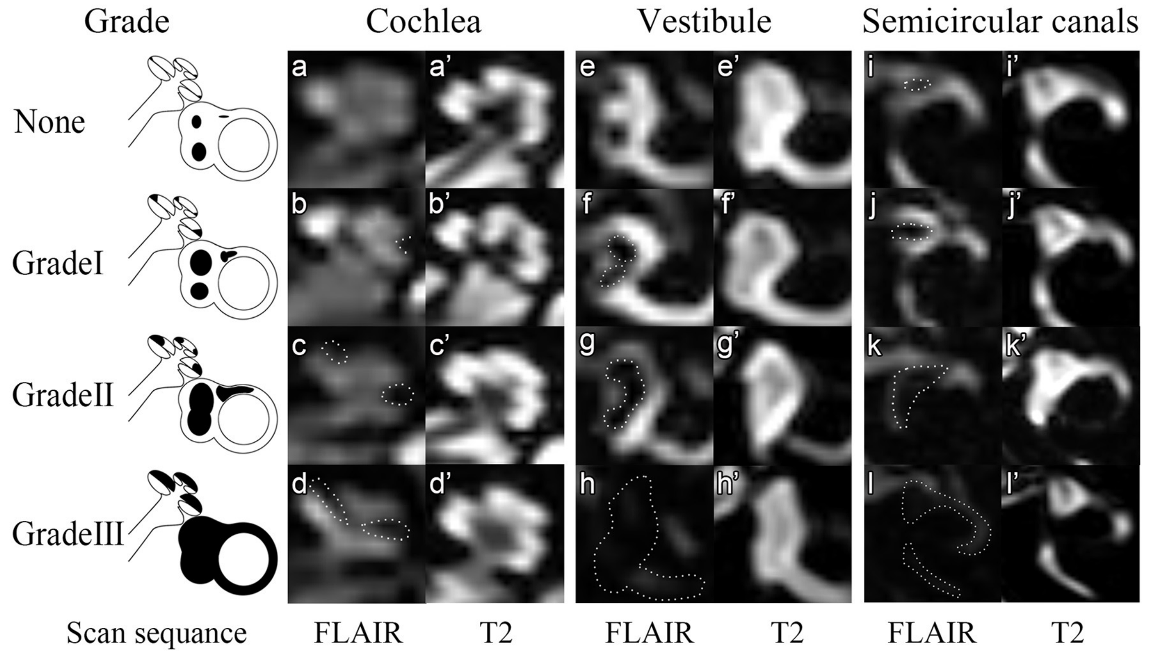

FIGURE 1 | Four grades of the inner ear ELH. In this figure, 3D-FLAIR pictures **(a–l)** are shown adjacent to T2 weighted image for each grade **(a'–l')**. None = Normal inner ear. In the normal inner ear, one can recognize no enlargement in the scala media **(a,a')**. The saccule and utricle are separate and saccule is smaller than the utricle **(e,e')**. The semicircular canals and a narrow dark area (<1/3 of the ampulla) are visible **(i,i')**. Grade I = Mild hydrops. In mild hydrops cochlea, an enlarged scala media can be observed with the scala vestibuli around **(b,b')**. In mild hydrops vestibule, saccule becomes larger than utricle but not yet confluent with utricle **(f,f')**. In mild hydrops semicircular canals, a dark area occupying over 1/3 of the ampulla is observed **(j,j')**. Grade II = Moderate hydrops. In moderate hydrops cochlea, the scala media expands into circle **(c,c')**. In the vestibule, a confluence of the saccule and utricle appears with visible perilymph surrounding **(g,g')**. In semicircular canals, the crura become dark and some of the canals become invisible. Grade III = Severe hydrops. The scala vestibuli, saccule and utricle and semicircular canals are filled with endolymph so that no signals could be viewed in these areas.

asymptomatic contralateral ears of patients with unilateral MD and only include ears with definite MD. The ELH of each definite MD ear was assessed by both the VR scores and the Bernaerts scores. We calculated the sum scores of the ELH to provide a semi-quantitative assessment of total inner ear hydrops. The Sum score of the ELH of a definite MD ear equaled the sum of the score of the cochlea, the score of the vestibule, and the score of the semicircular canals according to our VR scores. The sum score of the Bernaerts scores included only the sum of the grade of the cochlea and vestibule. We also calculated the sum score of the vestibule with the semicircular canals for the herniation hypothesis and presented this sum as the entire vestibular ELH.

ET-ECochG

Recording Procedure of ECochG

Bio-logic® Navigator Pro auditory evoked system 7.0.0 (Natus Medical Inc., San Carlos, CA, USA) was used for electrocochleography. The extra-tympanic electrode connecting a bronze foil was self-made. The bronze foil was chosen due to its availability and lower price than the gold one in order to reduce the cost of routine clinical expenses. Besides, bronze has better electric conductivity, which may improve the acquisition of small signals of the ET electrode compared with the tympanic electrode (29). Furthermore, the placement of a TM electrode on the tympanic membrane must be completed under an otoscope, which is a little difficult and time-consuming for audiologists. ET electrode could reduce the discomfort and made this test more acceptable for patients as well. The reference electrode was placed on the mastoid of the non-tested ear, whereas the ground electrode was placed on the forehead. Prior to electrode placement, all electrode sites were treated with an alcohol wipe and a lightly abrasive skin prepping gel using a cotton swab to ensure maximum adhesion and conductivity. Prior to placing the earphone into the ear canal, the ET electrode was covered with the Ten 20 conductive electrode paste and then surrounding the ER-3A insert earphone. The impedance of the ET electrode was kept below 5 kΩ. The other electrode impedances were kept below 1 kΩ. Alternating click stimuli of 100 µs duration at a rate of 11.3/s at 90 dBnHL of hearing level were presented monaurally. Intensity delay of 0.8 ms and the filter setting of 0.1–3 kHz were used. For ensuring the good quality of the responses, the stimuli were presented with 2,000 sweeps. For adequate visualization, the acquired responses were amplified 100,000 times. The SP and AP data were obtained, and each waveform was replicated at least two times for each subject. During the testing, the examinee lay comfortably on the bed in a soundproof room in the Diagnosis and Treatment Center of Hearing Impairment and Vertigo in Xinhua Hospital.

TABLE 1 | Relative maximum volume referencing scores (VR scores) of different parts in the inner ear and the relative points of four gradings of each part.

Content	Cochlea	Vestibule	Semicircular canal
Volume of inner ear fluid (μl) (21)*	113.5	69.0	91.8
ELH space (%) (10)	10.2	17.7	14.8
ELH volume (μl) = Volume of inner ear fluid* ELH space	11.6	12.2	13.6
Hydrops volume$_{max}$ (μl)**	55.6	69.0	91.8
Expansile volume$_{max}$ (μl)*** = Hydrops volume$_{max}$ – ELH volume	44.0	56.8	78.2
Relative hydrops scores (points)	9	12	16
GRADINGS OF ELH**			
None: no hydrops	0	0	0
GradeI: mild hydrops	3	4	5
GradeII: medium hydrops	6	8	10
GradeIII: severe hydrops	9	12	16

**Inner ear volume: The calculated inner ear volume for different parts of the human inner ear, taken from Inui et al. (21) as the mean of bilateral ears in both genders.*

***Hydrops volume$_{max}$: The maximum volume for endolymphatic hydrops, calculated according to the percentage showed by Ito et al. (7). In the cochlea, hydrops seldom herniates into the scala tympani, thus the volume of scala vestibuli was used as the maximum volume.*

****Expansile volume$_{max}$: The estimated maximum volume for maximum endolymph expansion of each parts of the inner ear.*

*****Gradings of ELH: The scores of each part of the inner ear were rounded to the nearest integer according to the relative expand volume of the semicircular canals which contained 16 points. Sixteen came from the assumptions that three semicircular canals and five crura had similar volume and ELH was distributed evenly in each part, in which we marked 1 point if the perilymph became narrow (mild hydrops) and 2 points if became dark (severe hydrops). Then each part had four points for four grades which were divided equally and rounded to integers. However, for Grade II of the semicircular canals, we rounded the points down to 10 rather than 11 because we noticed that most canals and crura were narrow but still visible compared to the severe hydrops' ones.*

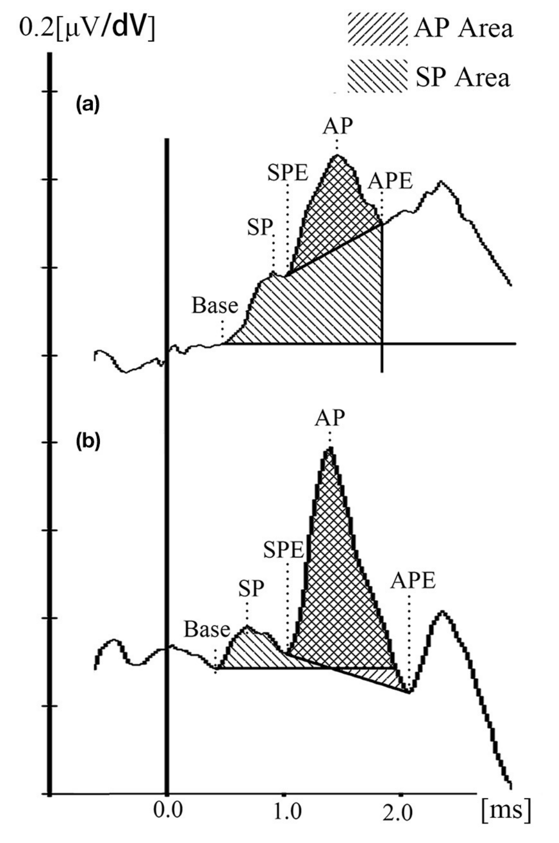

FIGURE 2 | ET-ECochG waveforms and the calculation method. **(a)** Waveform of an definite MD ear. **(b)** Waveform of a healthy ear. SP duration = SPE — Base; AP duration = APE — SPE.

Measurement of the Amplitude Ratio and Area Ratio

In the current study, the Auditory Evoked Potential system attached to the Bio-logic system was used to analyze first, and the waveforms were inverted before analyzed. For further figure analysis, such as area calculation, photoshop CC 2018 (Adobe, San Jose, CA, USA) and Image J 1.52 p (NIH, USA) were used. The baseline was defined as a horizontal line crossing the base point, which was the onset of the initial peak of SP of the waveform (determined by at least two repeat tracings) (30). The AP amplitude was determined from the baseline to the first large peak (represent the N1 of AP) between 1.0 and 2.0 ms after the SP peak. The latencies of the SP, AP, and their duration were collected. It has been reported that the SP/AP area ratio could improve the sensitivity and specificity of MD diagnosis (31, 32). However, this conclusion was argued by later researches (33, 34). Ferraro et al. firstly mentioned the area ratio because a widening of the SP/AP complex in patients with MD and the notice of the trailing edge of the AP-N1 does not return to baseline (35). Ferraro and Devaiah et al. thereby defined the SP area as the space under the curve from baseline to the next point where the waveform returned to baseline, and the AP area was defined from the onset of the AP to its first negative peak following N1 (32, 35). However, we found that few MD patients ECochG waveforms returned to the baseline, and the SP area would be infinite (**Figure 2A**). Therefore, we set a vertical line crossing the endpoint of N1 to make the SP area countable for those waveforms. The different methods and measurement standards might result in various debates for the clinical meaning of the ECochG and normal values for each center was recommended (36). Due to the new calculating method and the bronze foil ET electrode used in the current study, we collected 40 healthy subjects to establish the normative data for SP/AP amplitude ratio and area ratio (**Figure 2B**).

Pure-Tone Audiometry

Pure-tone audiometry was performed in a soundproof room with the use of an audiometer (Type Madsen, Astera, Denmark). The Pure-tone average (PTA) was calculated as the mean of 0.5, 1 k, 2 k, and 4 k Hz air conduction thresholds (37, 38). Stage criteria were not mentioned in the 2015 consensus, so the clinical MD stage was classified according to the 1995 AAO-HNS guidelines by dividing PTA into four stages: I 0–25 dBnHL, II 26–40 dBnHL, III 41–70 dBnHL, IV > 70 dBnHL.

Statistical Analysis

The data were analyzed using SPSS 26.0 for Windows (IBM, Chicago, IL, USA). Descriptive statistics were done for age, gender, clinical MD stage, disease duration (years), and vertigo attack frequency (vertigo episodes per month) in MD patients. The normal distribution test was done before the analysis of continuous variables. The paired *t*-test and independent *t*-test were used to analyze the differences between normatively distributed groups. The Mann-Whitney U-test was used for non-normal data. As for degrees of ELH and its correlation with clinical features (PTA, clinical course, vertigo frequency), the Pearson, Spearman, and Kendall correlation coefficient were used for different paired variables. The ordinal variables like the ELH points were analyzed again with the graded variables of all clinical features. Each variable was calculated several times in the same correlation comparison, so the Bonferroni correction was done. Furthermore, the canonical correlation was done for the correction of the normative linear data. To interpret correlation coefficients Cohen's standard classification ranges were used (weak 0.10–0.29, moderate 0.30–0.49, strong $\geq$ 0.50, Jacob Cohen, 1987). F test was used for the normative distributed data among several groups. ROC curve was analyzed using SPSS and Medcalc 19.3.1 (MedCalc Software Ltd., Ostend, Belgium) for the area under the curve (AUC), best cut-point, and difference analysis. The difference was considered to be statistically significant when $p < 0.05$.

RESULTS

Clinical Characteristic of MD Patients

Fifty patients were enrolled in this study, 28 females (56%) and 22 males (44%), with a mean age of 53 ± 12.2 years. All patients had unilateral MD except one who had bilateral MD (51 definite MD ears). All patients presented with episodic vertigo (at least more than twice) and fluctuating low-frequency sensorineural hearing loss. Each vertigo attack lasted 20 min−12 h. The distribution of clinical stages of MD, disease duration, and frequency of vertigo episodes per month were shown in **Table 2**. Tinnitus was reported more frequently than ear fullness in definite MD ears in these patients.

TABLE 2 | Clinical characteristic of definite MD ears.

Characteristic	Number of ears (%, $n = 51$)
GENDER	
Male	22 (43.14)
Female	29 (56.86)
SIDE	
Left	22 (43.14)
Right	29 (56.86)
CLINICAL STAGE	
I	5 (9.80)
II	11 (21.57)
III	29 (56.86)
IV	6 (11.76)
Tinnitus	49 (96.08)
Ear fullness	44 (86.27)
DISEASE DURATION*	
D1: <1 year	10 (19.61)
D2: 1–3 years	14 (27.45)
D3: 3-6 years	14 (27.45)
D4: >= 6 years	13 (25.49)
VERTIGO FREQUENCY (IN LAST MONTH)**	
V1: <1 time (<1 per month)	11 (21.57)
V2: 1–4 times (<1 per week)	13 (25.49)
V3: 4–15 times (< 1 every 2 days)	7 (13.73)
V4: >= 15 times (>1 every 2 days)	15 (29.41)
GRADING OF COCHLEA (POINTS)	
None (0)	1 (1.96)
Grade I (3)	17 (33.33)
Grade II (6)	27 (52.94)
Grade III (9)	6 (11.76)
GRADING OF VESTIBULE (POINTS)	
None (0)	0 (0.00)
Grade I (4)	15 (29.41)
Grade II (8)	23 (45.10)
Grade III (12)	13 (25.49)
GRADING OF SEMICIRCULAR CANALS (POINTS)	
None (0)	35 (68.63)
Grade I (5)	12 (23.53)
Grade II (10)	3 (5.89)
Grade III (16)	1 (1.96)

**Disease duration: the total disease duration from the onset of vertigo. The four levels (D1–D4) were divided according to the quartiles of our data.*

***Vertigo frequency (in last month): the times of vertigo in the last month according to the recorded history. The four levels (V1–V4) were divided according to the quartiles of our data.*

ELH Evaluation and MRI Association With Clinical Characteristics

ELH was detected in 51 definite MD ears (100%) and 19 asymptomatic contralateral ears (38.76%) of the 49 unilateral MD patients. No adverse effects or complications were observed after the intratympanic administration of gadolinium. The degree of ELH evaluated by the VR scores was found to have different degrees of ELH in the vestibule, cochlea, or semicircular canals shown in 3D-FLAIR MR images (e.g., **Figure 3**). Cochlear ELH and vestibular ELH were more detectable than ELH in semicircular canals in most patients (**Table 2**). Spearman correlation analysis showed the cochlear ELH was correlated with the vestibular ELH ($r_s = 0.44, p < 0.01$) and the entire vestibular ELH ($r_s = 0.43$, $p < 0.01$). The sum score of the total inner ear ELH in different clinical stages was revealed significantly different by the *F*-test ($F = 7.81$, $p < 0.01$). There was no correlation between vestibular ELH and the semicircular canals' ELH. The individual multiple correlation analysis revealed the significant correlation between cochlear ELH with the disease duration ($r_s = 0.35$, $p = 0.01$) and the vertigo frequency ($r_s = 0.36$, $p = 0.01$) ($p < 0.017$). The sum ELH of VR system correlated significantly with the disease duration ($r_s = 0.47$, $p < 0.01$). However, no statistically sufficient relationship was shown between the PTA ($r_s = 0.20$, $p = 0.15$) and the vertigo frequency ($r_s = 0.29$, $p = 0.04$) with the sum ELH ($p < 0.017$). The difference was considered to be statistically significant when $p < 0.017$ for this part according to Bonferroni correction

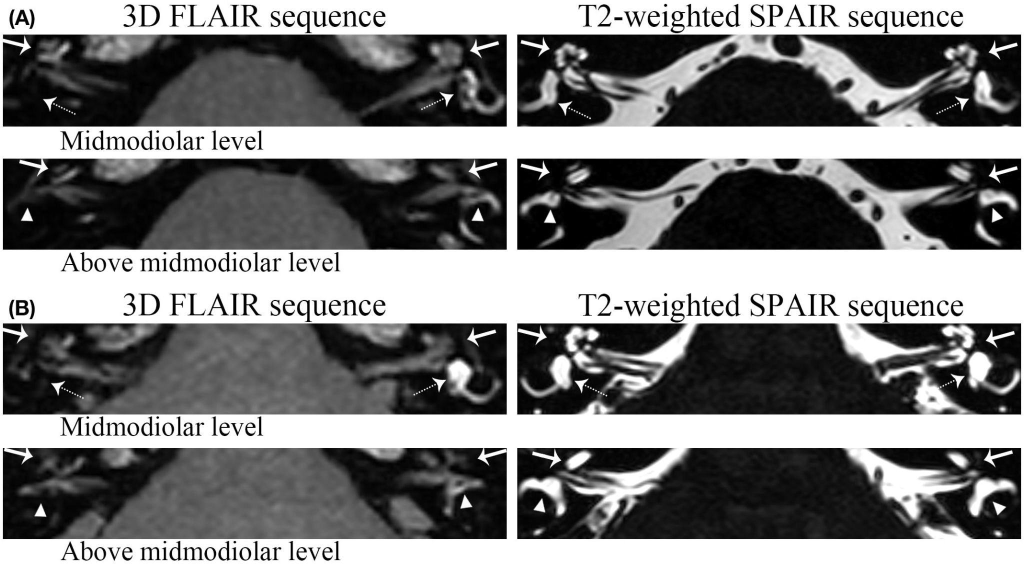

FIGURE 3 | Grading examples of the ELH. **(a)** Patient I. For this patient, volume-referencing scores for each ear was marked as follows: Left ear: cochlea (arrow)-0, vestibule (dashed arrow)-0, semicircular canals (triangle) (**Figure 1i**)-0; Right ear: cochlea-9; vestibule-12; semicircular canals: 16. **(b)** Patient II: These pictures belong to the bilateral MD patient involved. Volume-referencing scores for each ear was marked as follows: Left ear: cochlea-3, vestibule-0, semicircular canals-5; Right ear: cochlea-6; vestibule-12; semicircular canals: 10. The right semicircular canals were graded 10 because some parts of the canals were still visible.

because all the data were cited three times for analysis. To better compare the VR scores with the Bernaerts scores, the adjusted Canonical correlation was calculated between the clinical features (include PTA, disease duration, and vertigo frequency) and the ELH (include the VR scores and the Bernaerts scores) to reduce the possible errors caused by multiple comparisons. The correlation of the VR sum scores was closer with all clinical features ($r = 0.88$) than the Bernaerts sum scores ($r = 0.22$) according to the correlation formula between clinical features to two different scores (**Table 3-u1**). Disease duration presented a closer correlation ($r = 0.74$) to the ELH (**Table 3-v1**).

ET-ECochG Analysis

The results of ET-ECochG were calculated in all definite MD ears (51 ears) and the asymptomatic contralateral ears (49 ears) in these MD patients. Given that the possibility of MD development of the asymptomatic contralateral ears, ECochG waveforms were also collected and calculated in 40 healthy subjects (80 ears) to make a contrast and better evaluate the diagnosis value. Forty-three of fifty-one definite MD ears (84.31%) had recordable ECochG waveforms. The 8 ears with unrecordable ECochG waveforms were composed of 1 Stage II MD ear, 6 Stage III MD ears, and 1 Stage IV MD ear (clinical MD stages according to PTA). Among patients with unrecordable ECochG, auditory thresholds were elevated in the high frequencies (68.75 ± 13.82 dB HL at 4 kHz; 78.13 ± 17.31 dB HL at 8 kHz). Affected and unaffected ears were first compared for the 49 unilateral MD patients. The paired-sample *t*-test revealed a significant difference of the SP/AP ratio (SP/AP) between the definite MD ears and the contralateral ears ($t = 7.91$, $p < 0.01$) (**Table 4**). There was a significant difference between the area ratio of SP/AP (Asp/Aap) of the definite MD ears and the contralateral ears by the Wilcoxon Man-Whitney-test ($p < 0.01$). The SP duration of the definite MD ears varied significantly from the contralateral ears ($p < 0.01$). AP latencies of definite MD ears were significantly longer than the contralateral ears ($p = 0.04$).

TABLE 3 | The correlation of ELH with clinical features by the two different grading systems.

Contents	Sum VR*	Sum B	S_V	S_C
PTA [rs(*p*)**]	0.20 (0.15)	0.51 (<0.01)	0.20 (0.15)	0.15 (0.30)
Disease duration (DD)	0.47 (<0.01)	0.12 (0.39)	0.47 (<0.01)	0.35 (0.01)
Vertigo frequency (VF)	0.29 (0.04)	0.14 (0.32)	0.22 (0.12)	0.36 (0.01)
Clinical stage	0.17 (0.24)	0.51 (<0.01)	0.17 (0.24)	0.12 (0.40)
D1–D4	0.44 (<0.01)	0.07 (0.61)	0.35 (<0.01)	0.25 (0.05)
V1–V4	0.25 (0.07)	0.02 (0.90)	0.16 (<0.01)	0.31 (0.01)
St ANDARDIZED CANONICAL CORRELATION COEFFICIENTS* **				
u1 = −0.88 * Sum VR −0.22 * Sum B				
v1 = −0.73 * DD −0.44 * ln(PTA) −0.29 * VF				

**Sum VR: the total ELH score (sum of three inner ear parts) according to the VR scores; Sum B: the sum of grades of cochlea and vestibule according to the Bernaerts scores;* S_V*: the score of ELH in vestibule according to the VR scores; Sc: the score of ELH in cochlea according to the VR scores.*

****r_S *(p): Results were presented as coefficient of the spearman analysis with the p-value. Bonferroni's correction for multiple correlations:* $p < 0.017$.

****The normative linear variables were calculated, in which ln(PTA) were used.*

For setting a diagnostic point for the ET-ECochG using bronze foil electrode, all definite MD ears (51 ears) and healthy ears (80 ears) were included for the ROC curves. We also drew the ROC curve for the combined assessment of two methods (**Figure 4**).

TABLE 4 | Significantly varied data of the ECochG in unilateral MD patients.

	SP/AP		Sp duration (ms)	
	Symptomatic ears	Contralateral ears	Symptomatic ears	Contralateral ears
Mean ± SD	0.49 ± 0.16	0.28 ± 0.16	0.66 ± 0.18	0.54 ± 0.14
t-value	7.91		3.84	
p-value	<0.01		<0.01	
	Asp/Aap		**Ap latency (ms)**	
Quartile	3.12, 5.39	1.55, 2.38	1.52, 1.73	1.47, 1.66
p-value	<0.01		0.04	

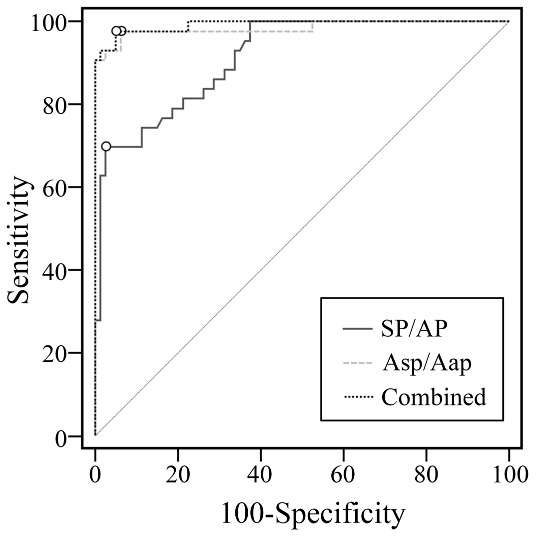

FIGURE 4 | ROC curves of SP/AP, Asp/Aap and the two indexes combined.

TABLE 5 | Roc curve index and analysis.

Contents	SP/AP	Asp/Aap	Combined
Cut off value	0.38	2.41	$P = 0.20$
AUC	0.91	0.98	0.99
95%CI	0.85–0.96	0.94–1.00	0.96–1.00
P-value (vs. SP/AP)	/	0.01	<0.01

The AUC of ROC curves can intuitively display the efficiency of the test index. The AUC of the Asp/Aap was 0.98, which was larger than the AUC of SP/AP (0.91). There was a significant difference of the ROC AUC between SP/AP with Asp/Aap ($p = 0.01$) and the combined assessment ($p < 0.01$) (**Table 5**). The cutoff point value of SP/AP was 0.38 (sensitivity = 69.77%, specificity = 97.50%), and the cutoff point value of Asp/Aap was 2.41 (sensitivity = 97.67%, specificity = 93.75%).

TABLE 6 | Correlative analysis between ECochG and MRI.

Indicaters	Sv [r_S (p)*]	Sc	Sv + scc**	Sum VR
SP/AP	0.46 (<0.01)	0.41 (0.01)	0.46 (<0.01)	0.51 (<0.01)
Asp/Aap	0.41 (<0.01)	0.60 (<0.01)*	0.46 (<0.01)	0.55 (<0.01)

**Asp/Aap had largest coefficient with cochlear ELH.*

***Sv + scc: the sum score of vestibular and semicircular canals ELH. Bonferroni correction for multiple correlations: $p < 0.0125$.*

Correlation Between ET-ECochG and MRI

Pearson or spearman analysis was done between the results of ET-ECochG and MRI of the definite MD ears (**Table 6**). Both SP/AP and Asp/Aap were significantly correlated with cochlear and vestibular ELH, the sum score of vestibular ELH, and the total score of inner ear ELH after the Bonferroni correction was done.

DISCUSSION

ELH, an excessive accumulation of endolymph in the cochlea (which is involved in hearing) and the vestibule (which is involved in balance), is a characteristic feature often observed in MD patients (2, 16). Foster et al. reported that MD patients had a near-certain probability of having endolymphatic hydrops in at least one ear (4). The relationship between the degree of ELH and clinical features was proved by researchers. Cochlear or vestibular ELH was correlated with the low-frequency hearing threshold according to Shi et al. (39). Yang et al. demonstrated a significant correlation between hearing loss and both the cochlear ELH and vestibular ELH (40). Bernaerts et al. reported a correlation between disease duration and the ELH of cochlea and vestibule (13). Gurkov et al. showed a correlation between cochlear ELH with both hearing loss and disease duration (23). Recently, the volumetric quantification was proposed to establish a methodological basis for further investigations into the pathophysiology and therapeutic monitoring of Menière's disease (8). The evaluation of the ELH volume required 3D volume analysis (9, 11). However, these 3D analyses are time intensive and impractical for routine work. Therefore, we proposed a convenient semi-quantification volume-referencing grading system according to the reported inner ear fluid volume results (9, 10). The VR scores showed a better correlation with the MD clinical features than the Bernaerts scores described by Bernaerts et al. (13). Thus, we believed that the sum score of hydrops of the entire inner ear according to the volume-referencing grading system had more diagnostic value than the Bernaerts scores, which graded the vestibule and cochlea separately.

MR imaging demonstrating inner ear fluid following intratympanic injection was reported in our previous research in 2004 (41) in guinea pigs and was first proposed in MD patients in 2007 (42). The first semi-quantification grading of ELH was raised in 2009 (12). Various improvements in MR protocols have been made afterward for higher quality images (43–46). However, the ELH grading system remained at the original level, which only evaluated the cochlea and vestibule without considering the relative volume. We referred to the four-grade semi-quantification vestibular grading system and the cochlear grading system mentioned by Bernaerts et al. (13) while analyzing. Gurkov et al. evaluated the cochlea into four grades but did not include the definition of how to divide four grades (23). Yang et al. then described the definition (40). Kirsch et al. (47) and Van et al. (48) then evaluated ELH of the total inner ear into four grades. We graded each part of the inner ear separately and differed from what Yang et al. mentioned. So we explained our grading carefully in the method part and showed in **Figure 1**. Since the pressure of perilymph and endolymph changed a little after ELH, according to the previous researches (49, 50), the total endolymph volume of the inner ear is much more important as measurement. Therefore, we recommend the volume-referencing grading system proposed in this study as it could easily and precisely estimate the ELH for the MRI images.

On the other hand, researchers hoped to explore more value of auditory and vestibular examinations, which would be easier for outpatients and provide diagnostic support for MD. This was because we observed that the high expense and complex procedure limited the wide usage of MRI among early diagnosed patients. ECochG was reported as a valuable tool in the diagnosis of MD due to its sensitivity to the ELH (18, 19). Cho et al. reported that the vestibular ELH was larger in patients with abnormal SP/AP than those with normal results (51). Yang et al. showed a correlation between SP/AP with vestibular ELH, but not with cochlear ELH (40). Our results revealed that ECochG was a valuable test for its correlation with the degree of ELH. Furthermore, the Asp/Aap had the largest coefficient to the cochlear ELH. The results supported the theory that ECochG reveals the potentials derived from the cochlea (17). It has been suggested that AP is derived from the afferent fibers in the cochlear nerve, and SP is a direct current potential arising in response to a current alternative stimulus (17). Our results showed that the duration of AP (nerve fibers) was not influenced by ELH while the duration of SP (summating response) was larger and had a high coefficient with the degree of ELH in the cochlea where the main response occurred. The underlying hypothesis of the enlarged SP is that hydrops-related inflation of the scala media leads to a static bias of the resting position of the organ of Corti and of outer-hair-cell stereocilia bundles and modified the electrical and mechanical properties of the cells (52).

However, according to the literature published, the diagnostic value of ECochG has been controversial (53) and some suggested that it had limited value as a clinical tool in the diagnosis of MD (34). The different reports might be due to the varied diagnostic value of ECochG, different electrodes, and multiple settings, which might influence the sensitivity and specificity of ECochG. Take SP/AP as an example, Quatre et al. (54) took >0.43 as abnormal, while Lamounier et al. (55) took >0.5. The absence of a shared ECochG procedure (electrode, stimuli type, and rate) made a great difference between the SP/AP and Asp/Aap (56). Therefore, the major debated point was the SP/AP cutoff value (between 0.32 and 0.5 in researches, reasonably no higher than 0.4) and the Asp/Aap cutoff value (53). Besides, the waveform varied a lot due to the different electrodes and stimuli (18, 56). ET-ECochG was chosen in this study due to its convenience and better acceptance in patients and inspection technicians in our center compare to the complex procedure like local anesthesia of the tympanic electrode (57). So as recommended (36), we calculated the specific diagnostic cutoff point for our laboratory. The best diagnostic cutoff point for our ET-ECochG protocol was calculated in 43 MD ears, and 80 healthy ears enrolled. The diagnostic value is 0.38 for SP/AP and 2.41 for Asp/Aap according to our results. The AUC of the ROC curve evidently represents a higher clinical significance of the index Asp/Aap and its combination with SP/AP than SP/AP only. Therefore, we recommended the ET-ECochG as a supportive examination for MD diagnosis with adding Asp/Aap as a diagnostic index, especially for outpatients.

These methodical limitations should be taken into consideration: First, the reliability of the statistical analyses would profit from a greater number of patients that were evenly distributed in all four clinical MD stages. Second, the control group varied considerably in age and gender from the investigated MD patients. Third, the MR image quality could be improved by different sequences. Fourth, there is a lack of verification through 3D quantification. For example, it had been proved that one slice of the vestibule could represent the total ELH of the vestibule, however, no literature proved that the ELH in lateral semicircular canals could represent the total ELH of semicircular and the supposed even distribution of ELH among eight parts of the semicircular canals should also be proved. Thus, further research should be conducted to assess the accuracy of the volume-referencing grading system. Furthermore, more studies with radiological and clinical follow-ups should be done to confirm the cutoff value of the point of ET-ECochG and the value of the volume-referencing grading system.

DATA AVAILABILITY STATEMENT

The raw data supporting the conclusions of this article will be made available by the authors, without undue reservation.

ETHICS STATEMENT

The studies involving human participants were reviewed and approved by Ethics Committee of Xinhua Hospital. The patients/participants provided their written informed consent to participate in this study.

AUTHOR CONTRIBUTIONS

JY and MD contributed to study design, critically reviewed, and approved the final manuscript. BH and FZ contributed to the detailed study design and performed data acquisition, statistical analysis, and interpretation of results, drafting of the manuscript, and revised the manuscript. HZ contributed to the radiological supports and worked out the new grading system together with

BH. XS and JC contributed to the study design, data acquisition, and statistical analysis. JC, YL, and SL contributed to the methods of statistical analysis and critically reviewed the manuscript. WW and LW contributed to ECochG data acquisition. All authors agree to be accountable for the content of the work, integrity, and accuracy of the data. All authors contributed to the article and approved the submitted version.

FUNDING

This work was funded by Cross-key Projects in Medical and Engineering Fields of Shanghai Jiaotong University (No. ZH2018ZDA11), Clinical Research Cultivation Fund of Xinhua Hospital (Nos. 17CSK03 and 18JXO04).

ACKNOWLEDGMENTS

The authors wish to thank all the coworkers at The Department of Otolaryngology-Head and Neck Surgery and the Hearing Impairment and Vertigo Diagnosis and Treatment Center for their valuable support of the detailed history collection and accurate hearing and vertigo examinations even under high-intensity working environment. Also, thanks to the supports from the director and other coworkers of the Department of Radiology in Xinhua Hospital, Shanghai, China. We thank Professor Ren Tianying from Oregon Hearing Research Center, Department of Otolaryngology, Oregon Health and Science University, Portland, the United States for editing English.

REFERENCES

1. Lopez-Escamez JA, Carey J, Chung W-H, Goebel JA, Magnusson M, Mandalà M, et al. Diagnostic criteria for Menière's disease. *J Vestib Res*. (2015) 25:1–7. doi: 10.3233/ves-150549
2. Nakashima T, Pyykko I, Arroll MA, Casselbrant ML, Foster CA, Manzoor NF, et al. Meniere's disease. *Nat Rev Dis Primers*. (2016) 2:16028. doi: 10.1038/nrdp.2016.28
3. Gürkov R, Pyykö I, Zou J, Kentala E. What is Menière's disease? A contemporary re-evaluation of endolymphatic hydrops. *J Neurol*. (2016) 263:71–81. doi: 10.1007/s00415-015-7930-1
4. Foster CA, Breeze RE. Endolymphatic hydrops in Ménière's disease: cause, consequence, or epiphenomenon? *Otol Neurotol*. (2013) 34:1210–4. doi: 10.1097/MAO.0b013e31829e83df
5. Zou J, Pyykkö I, Bretlau P, Klason T, Bjelke B. *In vivo* visualization of endolymphatic hydrops in guinea pigs: magnetic resonance imaging evaluation at 4.7 tesla. *Ann Otol Rhinol Laryngol*. (2003) 112:1059–65. doi: 10.1177/000348940311201212
6. Naganawa S, Sugiura M, Kawamura M, Fukatsu H, Sone M, Nakashima T. Imaging of endolymphatic and perilymphatic fluid at 3T after intratympanic administration of gadolinium-diethylene-triamine pentaacetic acid. *Am J Neuroradiol*. (2008) 29:724–6. doi: 10.3174/ajnr.A0894
7. Naganawa S, Satake H, Kawamura M, Fukatsu H, Sone M, Nakashima T. Separate visualization of endolymphatic space, perilymphatic space and bone by a single pulse sequence; 3D-inversion recovery imaging utilizing real reconstruction after intratympanic Gd-DTPA administration at 3 Tesla. *Eur J Radiol*. (2008) 18:920–4. doi: 10.1007/s00330-008-0854-8
8. Gurkov R, Berman A, Dietrich O, Flatz W, Jerin C, Krause E, et al. MR volumetric assessment of endolymphatic hydrops. *Eur Radiol*. (2015) 25:585–95. doi: 10.1007/s00330-014-3414-4
9. Inui H, Sakamoto T, Ito T, Kitahara T. Magnetic resonance volumetric measurement of endolymphatic space in patients without vertiginous or cochlear symptoms. *Acta Otolaryngol*. (2016) 136:1206–12. doi: 10.1080/00016489.2016.1204663
10. Ito T, Inui H, Miyasaka T, Shiozaki T, Hasukawa A, Yamanaka T, et al. Endolymphatic volume in patients with meniere's disease and healthy controls: three-dimensional analysis with magnetic resonance imaging. *Laryngoscope Investig Otolaryngol*. (2019) 4:653–8. doi: 10.1002/lio2.313
11. Kirsch V, Nejatbakhshesfahani F, Ahmadi SA, Dieterich M, Ertl-Wagner B. A probabilistic atlas of the human inner ear's bony labyrinth enables reliable atlas-based segmentation of the total fluid space. *J Neurol*. (2019) 266(Suppl. 1):52–61. doi: 10.1007/s00415-019-09488-6
12. Nakashima T, Naganawa S, Pyykko I, Gibson WP, Sone M, Nakata S, et al. Grading of endolymphatic hydrops using magnetic resonance imaging. *Acta Otolaryngol Suppl*. (2009) 129:5–8 doi: 10.1080/00016480902729827
13. Bernaerts A, Vanspauwen R, Blaivie C, van Dinther J, Zarowski A, Wuyts FL, et al. The value of four stage vestibular hydrops grading and asymmetric perilymphatic enhancement in the diagnosis of Meniere's disease on MRI. *Neuroradiology*. (2019) 61:421–9. doi: 10.1007/s00234-019-02155-7
14. Naganawa S, Kanou M, Ohashi T, Kuno K, Sone M. Simple estimation of the endolymphatic volume ratio after intravenous administration of a single-dose of gadolinium contrast. *Magn Reson Med Sci*. (2016) 15:379–85. doi: 10.2463/mrms.mp.2015-0175
15. Attyé A, Eliezer M, Boudiaf N, Tropres I, Chechin D, Schmerber S, et al. MRI of endolymphatic hydrops in patients with Meniere's disease: a case-controlled study with a simplified classification based on saccular morphology. *Eur Radiol*. (2016) 27:3138–46. doi: 10.1007/s00330-016-4701-z
16. Liu Y, Yang J, Duan M. Current status on researches of Meniere's disease: a review. *Acta Otolaryngol*. (2020) 140:808–12. doi: 10.1080/00016489.2020.1776385
17. Gibson WP. The clinical uses of electrocochleography. *Front Neurosci*. (2017) 11:274. doi: 10.3389/fnins.2017.00274
18. Eggermont JJ. Ups and downs in 75 years of electrocochleography. *Front Syst Neurosci*. (2017) 11:2. doi: 10.3389/fnsys.2017.00002
19. Lamounier P, Gobbo DA, Souza TS, Oliveira CA, Bahmad F, Jr. Electrocochleography for Meniere's disease: is it reliable? *Braz J Otorhinolaryngol*. (2014) 80:527–32. doi: 10.1016/j.bjorl.2014.08.010
20. Nguyen LT, Harris JP, Nguyen QT. Clinical utility of electrocochleography in the diagnosis and management of Meniere's disease: AOS and ANS membership survey data. *Otol Neurotol*. (2010) 31:455–9. doi: 10.1097/MAO.0b013e3181d2779c
21. Inui H, Sakamoto T, Ito T, Kitahara T. Volumetric measurements of the inner ear in patients with Meniere's disease using three-dimensional magnetic resonance imaging. *Acta Otolaryngol*. (2016) 136:888–93. doi: 10.3109/00016489.2016.1168940
22. Barath K, Schuknecht B, Naldi AM, Schrepfer T, Bockisch CJ, Hegemann SC. Detection and grading of endolymphatic hydrops in Meniere disease using MR imaging. *Am J Neuroradiol*. (2014) 35:1387–92. doi: 10.3174/ajnr.A3856
23. Gurkov R, Flatz W, Louza J, Strupp M, Ertl-Wagner B, Krause E. *In vivo* visualized endolymphatic hydrops and inner ear functions in patients with electrocochleographically confirmed Meniere's disease. *Otol Neurotol*. (2012) 33:1040–5. doi: 10.1097/MAO.0b013e31825d9a95
24. Wysocki J. Dimensions of the human vestibular and tympanic scalae. *Hear Res*. (1999) 135:39–46. doi: 10.1016/s0378-5955(99)00088-x
25. Wu C, Yang L, Hua C, Wang K, Zhang T, Dai P. Geometrical and volume changes of the membranous vestibular labyrinth in guinea pigs with endolymphatic hydrops. *ORL J Otorhinolaryngol Relat Spec*. (2013) 75:108–16. doi: 10.1159/000350569
26. Raufer S, Guinan JJ, Jr., Nakajima HH. Cochlear partition anatomy and motion in humans differ from the classic view of mammals. *Proc Natl Acad Sci USA*. (2019) 116:13977–82. doi: 10.1073/pnas.1900787116
27. Sugimoto S, Yoshida T, Teranishi M, Kobayashi M, Shimono M, Naganawa S, et al. Significance of endolymphatic hydrops herniation into the semicircular canals detected on MRI. *Otol Neurotol*. (2018) 39:1229–34. doi: 10.1097/MAO.0000000000002022

28. Liu Y, Jia H, Shi J, Zheng H, Li Y, Yang J, et al. Endolymphatic hydrops detected by 3-dimensional fluid-attenuated inversion recovery MRI following intratympanic injection of gadolinium in the asymptomatic contralateral ears of patients with unilateral Meniere's disease. *Med Sci Monit*. (2015) 21:701–7. doi: 10.12659/MSM.892383
29. Hornibrook J. Tone burst electrocochleography for the diagnosis of clinically certain Meniere's disease. *Front Neurosci*. (2017) 11:301. doi: 10.3389/fnins.2017.00301
30. Ferraro JA, Durrant JD. Electrocochleography in the evaluation of patients with Meniere's disease/endolymphatic hydrops. *J Am Acad Audiol*. (2006) 17:45–68. doi: 10.3766/jaaa.17.1.6
31. Al-momani MO, Ferraro JA, Gajewski BJ, Ator G. Improved sensitivity of electrocochleography in the diagnosis of Meniere's disease. *Int J Audiol*. (2009) 48:811–9. doi: 10.3109/14992020903019338
32. Devaiah AK, Dawson KL, Ferraro JA, Ator GA. Utility of area curve ratio electrocochleography in early Meniere disease. *Arch Otolaryngol Head Neck Surg*. (2003) 129:547–51. doi: 10.1001/archotol.129.5.547
33. Baba A, Takasaki K, Tanaka F, Tsukasaki N, Kumagami H, Takahashi H. Amplitude and area ratios of summating potential/action potential (SP/AP) in Meniere's disease. *Acta Otolaryngol*. (2009) 129:25–9. doi: 10.1080/00016480701724888
34. Oh KH, Kim K-W, Chang J, Jun H-S, Kwon EH, Choi J-Y, et al. Can we use electrocochleography as a clinical tool in the diagnosis of Meniere's disease during the early symptomatic period? *Acta Otolaryngol*. (2014) 134:771–5. doi: 10.3109/00016489.2014.907500
35. Ferraro JA, Tibbils RP. SP/AP area ratio in the diagnosis of Méniére's disease. *Am J Audio*. (1999) 8:21–8. doi: 10.1044/1059-0889(1999/001)
36. Redondo-Martínez J, Morant-Ventura A, Robledo-Aguayo D, Ayas-Montero A, Mencheta-Benet E, Marco-Algarra J. Extra-tympanic electrocochleography in a normal population. A descriptive study. *Acta Otorrinolaringol Esp*. (2016) 67:254–60. doi: 10.1016/j.otoeng.2015.10.001
37. Sykopetrites V, Giannuzzi AL, Lauda L, Di Rubbo V, Bassi M, Sanna M. Surgical labyrinthectomy and cochlear implantation in Meniere's disease. *Otol Neurotol*. (2020) 41:775–81. doi: 10.1097/MAO.0000000000002646
38. Daneshi A, Hosseinzadeh F, Mohebbi S, Mohseni M, Mohammadi SS, Asghari A. New marsupialization technique in endolymphatic sac surgery. *Laryngoscope Investig Otolaryngol*. (2020) 5:546–51. doi: 10.1002/lio2.403
39. Shi S, Guo P, Li W, Wang W. Clinical features and endolymphatic hydrops in patients with MRI evidence of hydrops. *Ann Otol Rhinol Laryngol*. (2019) 128:286–92. doi: 10.1177/0003489418819551
40. Yang S, Zhu H, Zhu B, Wang H, Chen Z, Wu Y, et al. Correlations between the degree of endolymphatic hydrops and symptoms and audiological test results in patients with Meniere's disease: a reevaluation. *Otol Neurotol*. (2018) 39:351–6. doi: 10.1097/MAO.0000000000001675
41. Duan M, Bjelke B, Fridberger A, Counter SA, Klason T, Skjonsberg A, et al. Imaging of the guinea pig cochlea following round window gadolinium application. *Neuroreport*. (2004) 15:1927–30. doi: 10.1097/00001756-200408260-00019
42. Nakashima T, Naganawa S, Sugiura M, Teranishi M, Sone M, Hayashi H, et al. Visualization of endolymphatic hydrops in patients with Meniere's disease. *Laryngoscope*. (2007) 117:415–20. doi: 10.1097/MLG.0b013e31802c300c
43. Naganawa S, Yamazaki M, Kawai H, Bokura K, Iida T, Sone M, et al. MR imaging of Meniere's disease after combined intratympanic and intravenous injection of gadolinium using HYDROPS2. *Magn Reson Med Sci*. (2014) 13:133–7. doi: 10.2463/mrms.2013-0061
44. Naganawa S, Yamazaki M, Kawai H, Bokura K, Sone M, Nakashima T. Imaging of Meniere's disease after intravenous administration of single-dose gadodiamide: utility of multiplication of MR cisternography and HYDROPS image. *Magn Reson Med Sci*. (2013) 12:63–8. doi: 10.2463/mrms.2012-0027
45. Naganawa S, Yamazaki M, Kawai H, Bokura K, Sone M, Nakashima T. Imaging of Meniere's disease after intravenous administration of single-dose gadodiamide: utility of subtraction images with different inversion time. *Magn Reson Med Sci*. (2012) 11:213–9. doi: 10.2463/mrms.11.213
46. Naganawa S, Yamazaki M, Kawai H, Bokura K, Sone M, Nakashima T. Visualization of endolymphatic hydrops in Meniere's disease with single-dose intravenous gadolinium-based contrast media using heavily T(2)-weighted 3D-FLAIR. *Magn Reson Med Sci*. (2010) 9:237–42. doi: 10.2463/mrms.9.237
47. Kirsch V, Becker-Bense S, Berman A, Kierig E, Ertl-Wagner B, Dieterich M. Transient endolymphatic hydrops after an attack of vestibular migraine: a longitudinal single case study. *J Neurol*. (2018) 265(Suppl. 1):51–3. doi: 10.1007/s00415-018-8870-3
48. van Steekelenburg JM, van Weijnen A, de Pont LMH, Vijlbrief OD, Bommelje CC, Koopman JP, et al. Value of endolymphatic hydrops and perilymph signal intensity in suspected meniere disease. *Am J Neuroradiol*. (2020) 41:529–34. doi: 10.3174/ajnr.A6410
49. Mateijsen DJ, Rosingh HJ, Wit HP, Albers FW. Perilymphatic pressure measurement in patients with Meniere's disease. *Eur Arch Otorhinolaryngol*. (2001) 258:1–4. doi: 10.1007/pl00007515
50. Long CH, III, Morizono T. Hydrostatic pressure measurements of endolymph and perilymph in a guinea pig model of endolymphatic hydrops. *Otolaryngol Head Neck Surg*. (1987) 96:83–95. doi: 10.1177/019459988709600115
51. Cho YS, Ahn JM, Choi JE, Park HW, Kim YK, Kim HJ, et al. Usefulness of intravenous gadolinium inner ear MR imaging in diagnosis of Meniere's disease. *Sci Rep*. (2018) 8:17562. doi: 10.1038/s41598-018-35709-5
52. Gerenton G, Giraudet F, Djennaoui I, Pavier Y, Gilain L, Mom T, et al. Abnormal fast fluctuations of electrocochleography and otoacoustic emissions in Meniere's disease. *Hear Res*. (2015) 327:199–208. doi: 10.1016/j.heares.2015.07.016
53. Mammarella F, Zelli M, Varakliotis T, Eibenstein A, Pianura CM, Bellocchi G. Is electrocochleography still helpful in early diagnosis of Meniere disease? *J Audiol Otol*. (2017) 21:72–6. doi: 10.7874/jao.2017.21.2.72
54. Quatre R, Attye A, Karkas A, Job A, Dumas G, Schmerber S. Relationship between audio-vestibular functional tests and inner ear MRI in Meniere's disease. *Ear Hear*. (2019) 40:168–76. doi: 10.1097/AUD.0000000000000584
55. Lamounier P, de Souza TSA, Gobbo DA, Bahmad F, Jr. Evaluation of vestibular evoked myogenic potentials (VEMP) and electrocochleography for the diagnosis of Meniere's disease. *Braz J Otorhinolaryngol*. (2017) 83:394–403. doi: 10.1016/j.bjorl.2016.04.021
56. Lake AB, Stuart A. The effect of test, electrode, and rate on electrocochleography measures. *J Am Acad Audiol*. (2019) 30:41–53. doi: 10.3766/jaaa.17081
57. Grasel SS, Beck RMdO, Loureiro RSC, Rossi AC, de Almeida ER, Ferraro J. Normative data for TM electrocochleography measures. *J Otol*. (2017) 12:68–73. doi: 10.1016/j.joto.2017.04.005

Conflict of Interest: The authors declare that the research was conducted in the absence of any commercial or financial relationships that could be construed as a potential conflict of interest.

frontiers in Neurology

ORIGINAL RESEARCH
published: 11 March 2021
doi: 10.3389/fneur.2021.594481

Endolymphatic Hydrops in Patients With Vestibular Migraine and Concurrent Meniere's Disease

Sun-Young Oh[1,2†], Marianne Dieterich[3,4,5†], Bit Na Lee[1], Rainer Boegle[3,4], Jin-Ju Kang[1], Na-Ri Lee[2,6], Johannes Gerb[3,4], Seung-Bae Hwang[2,7*] and Valerie Kirsch[3,4]*

[1] Department of Neurology, School of Medicine, Jeonbuk National University, Jeonju, South Korea, [2] Research Institute of Clinical Medicine, Jeonbuk National University Hospital-Biomedical Research Institute, Jeonbuk National University, Jeonju, South Korea, [3] Department of Neurology, University Hospital, Ludwig-Maximilians-Universität, Munich, Germany, [4] German Center for Vertigo and Balance Disorders-IFB, University Hospital, Ludwig-Maximilians-Universität, Munich, Germany, [5] Munich Cluster for Systems Neurology (SyNergy), Munich, Germany, [6] Division of Oncology and Hematology, Department of Internal Medicine, Jeonbuk National University Hospital and School of Medicine, Jeonju, South Korea, [7] Department of Radiology, Jeonbuk National University Hospital and School of Medicine, Jeonju, South Korea

Edited by:
Sergio Carmona,
INEBA Institute of Neurosciences
Buenos Aires, Argentina

Reviewed by:
Nicolas Perez-Fernandez,
University Clinic of Navarra, Spain
Yasuhiro Chihara,
Raffles Japanese Clinic, Singapore

***Correspondence:**
Sun-Young Oh
ohsun@jbnu.ac.kr
Seung-Bae Hwang
sbh1010@jbnu.ac.kr

† These authors have contributed equally to this work

Specialty section:
This article was submitted to Neuro-Otology, a section of the journal Frontiers in Neurology

Received: *13 August 2020*
Accepted: *09 February 2021*
Published: *11 March 2021*

Citation:
Oh S-Y, Dieterich M, Lee BN, Boegle R, Kang J-J, Lee N-R, Gerb J, Hwang S-B and Kirsch V (2021) Endolymphatic Hydrops in Patients With Vestibular Migraine and Concurrent Meniere's Disease. Front. Neurol. 12:594481. doi: 10.3389/fneur.2021.594481

Objective: Intravenous contrast agent enhanced, high-resolution magnetic resonance imaging of the inner ear (iMRI) confirmed that patients with Menière's disease (MD) and vestibular migraine (VM) could present with endolymphatic hydrops (EH). The present study aimed to investigate EH characteristics and their interrelation to neurotologic testing in patients with VM, MD, or VM with concurrent MD (VM-MD).

Methods: Sixty–two patients (45 females, aged 23–81 years) with definite or probable VM ($n = 25$, 19 definite), MD ($n = 29$, 17 definite), or showing characteristics of both diseases ($n = 8$) were included in this study. Diagnostic workup included neurotologic assessments including video-oculography (VOG) during caloric stimulation and head-impulse test (HIT), ocular and cervical vestibular evoked myogenic potentials (o/cVEMP), pure tone audiometry (PTA), as well as iMRI. EH's degree was assessed visually and via volumetric quantification using a probabilistic atlas-based segmentation of the bony labyrinth and volumetric local thresholding (VOLT).

Results: Although a relevant number of VM patients reported varying auditory symptoms (13 of 25, 52.0%), EH in VM was only observed twice. In contrast, EH in VM-MD was prevalent (2/8, 25%) and in MD frequent [23/29, 79.3%; $\chi^2(2) = 29.1$, $p < 0.001$, $\varphi = 0.7$]. Location and laterality of EH and neurophysiological testing classifications were highly associated (Fisher exact test, $p < 0.005$). In MD, visual semi-quantitative grading and volumetric quantification correlated highly to each other ($r_S = 0.8$, $p < 0.005$, two-sided) and to side differences in VOG during caloric irrigation (vestibular EH ipsilateral: $r_S = 0.6$, $p < 0.05$, two-sided). In VM, correlations were less pronounced. VM-MD assumed an intermediate position between VM and MD.

Conclusion: Cochlear and vestibular hydrops can occur in MD and VM patients with auditory symptoms; this suggests inner ear damage irrespective of the diagnosis of MD or

VM. The EH grades often correlated with auditory symptoms such as hearing impairment and tinnitus. Further research is required to uncover whether migraine is one causative factor of EH or whether EH in VM patients with auditory symptoms suggests an additional pathology due to MD.

Keywords: vestibular migraine, Meniere's disease, endolymphatic hydrops, magnetic resonance imaging, intravenous gadolinium, image analysis

INTRODUCTION

The Bárány Society recently published diagnostic criteria for vestibular migraine (VM) and Menière's disease (MD) (1, 2). However, their critical clinical symptoms overlap, and no specific diagnostic test can reliably distinguish them: Up to 40% of VM patients present with auditory symptoms such as aural pressure, tinnitus, and sudden sensorineural hearing loss (3, 4). Half of the MD patients present with migrainous features, such as a headache with photophobia or positive family history for migraine (5, 6). Moreover, about a quarter of VM and MD patients meet both diagnostic criteria (3, 7). Therefore, establishing the correct diagnosis remains challenging (3).

So far, the MD's pathophysiology remains unknown. Nevertheless, based on post-mortem temporal bones analyses, endolymphatic hydrops (EH) was considered a potential MD marker (8). However, EH is also known as an endpoint of different etiologies such as trauma, electrolyte imbalance (9), cellular channelopathies (10), viral infection, and autoimmune processes (11). Furthermore, fluctuating EH dependent on the time interval after a VM attack was reported recently by longitudinal MRI (12). It remains to be seen whether the EH is a bystander phenomenon or pathophysiological relevant in VM. Consequently, the EH's mere verification did not prove the desired clear-cut discriminatory diagnostic criteria between VM and MD.

The present study uses intravenous, delayed, contrast agent enhanced, high-resolution magnetic resonance imaging of the inner ear (iMRI) to investigate EH characteristics and its interrelation to neurotologic testing in patients with VM, MD, and VM with concurrent MD (VM-MD).

MATERIALS AND METHODS

Setting and Institutional Review Board Approval

Jeonbuk National University Hospital between 2018 and 2019. Institutional review board (IRB) approval was obtained before the study's initiation (IRB No. 2017-09-022). All participants provided informed oral and written consent following the declaration of Helsinki before inclusion into the study and received monetary compensation for participation.

Study Population

Sixty-two patients with either probable or definite VM, MD, or both disease characteristics (VM-MD) participated in this study. Diagnosis for VM was based on the consensus document of the Bárány Society and the International Headache Society (1). Diagnosis for MD was based on the classification of the Bárány Society, 2015 (2).

The classification was done based on the history (with particular attention to ear symptoms, symptoms in the head, headache, and other neurological symptoms) and the neurotological data. For example, profound hearing loss, aural fullness of one ear, or significant unilateral vestibular dysfunction (>30–35% side difference of caloric nystagmus) during or immediately after an attack pointed to MD. Migraine headache with phono- and photophobia, nausea, and vomiting indicated VM. Unfortunately, it was not always possible to differentiate between preexisting chronic auditory or vestibular signs and symptoms and acute ones during the attack.

After detailed history taking, all patients underwent neurological and neurotological testing, including 3D-video-oculography (VOG) with caloric stimulation (cVOG), video head impulse test (vHIT), cervical and ocular vestibular-evoked myogenic potentials (cVEMPs and oVEMPs, respectively), pure tone audiometry (PTA), and inner ear MRI with delayed intravenous gadolinium enhancement (iMRI).

Nomenclature

In the following, "ipsilateral" refers to the clinically leading side and "contralateral" to the opposite side. In the case of patients presenting without a leading clinical side, a pseudorandom number generator ("Marsenne Twister" algorithm, uniform distribution) was used to generate a random number between 1 (= minimum value) and 9 (= maximum value). Even numbers

---

Abbreviations: 3D, Three-dimensional; 3D mean, ELS volume mean of the right and left inner ear; AAO-HNS, American Academy of Otolaryngology-Head and Neck Surgery; AC, Air conducted; AR, Asymmetry ratio; cELS, ELS of the cochlea; cTFS, TFS of the cochlea; cVEMP, cervical vestibular-evoked myogenic potential; dB, Decibel; Diff, The difference in volume between the left and right side; DOF, Degrees of freedom; EH, Endolymphatic hydrops; ELS, Endolymphatic space; FA, Flip angle; FLAIR, Fluid-attenuated inversion recovery; FOV, Field of view; GRAPPA, Generalized auto-calibrating partially parallel acquisition; IRB, Institutional Review Board; HYDROPS, HYbriD of Reversed image Of Positive endolymph signal and native image of positive perilymph Signal; hT2W, heavily T2-weighted; iMRI, Intravenous contrast agent enhanced MRI of the inner ear; L, Left; MD, Meniere's Disease; MRC, MR cisternography; MRI, Magnetic resonance imaging; NEX, Number of excitations; No, Number; oVEMP, ocular vestibular-evoked myogenic potential; PEI, Positive endolymphatic image; PLS, Perilymphatic space; PPI, Positive perilymph image; PTA, Pure tone audiometry; R, Right; SD, Standard deviation; SF, Supplementary figure; SPACE, Sampling perfection with application-optimized contrasts by using different flip angle evolutions; TE, Echo time; TFS, Total fluid space; TR, Repetition time; vHIT, Video head impulse test; VM, Vestibular Migraine; VEMP, Vestibular evoked myogenic potential; VOG, Video-oculography; VOLT, Volumetric Local Thresholding; vELS, ELS of the vestibulum; vTFS, TFS of the vestibulum.

meant left clinically leading side (13), and uneven numbers indicated right clinically leading side.

"Headache" pertains to the attack-associated migrainous head and neck pain or pressure, both uni- and bilateral, that fit the criteria of VM. "Auditory symptoms" comprehends attack-associated tinnitus, ear fullness, hearing loss, and or hearing fluctuation that fit the criteria for MD.

Vestibular and Auditory Testing

Video-Oculography (VOG)

Eye movements and gaze stability were examined using three-dimensional VOG (3D-VOG, SMI, The Netherlands) (14). Eye movements and the ability to hold a steady gaze were evaluated during attempted fixation of visual targets located centrally or eccentrically (± 30° horizontally, ± 20° vertically). Spontaneous and gaze-evoked nystagmus, vibration-induced and head-shaking nystagmus, positional tests, horizontal saccades, and smooth pursuit eye movements were evaluated. Digitized data were analyzed using MATLAB® software.

VOG During Caloric Irrigation

Caloric testing with VOG was performed for both ears with 30° Celsius (C) cold and 44° C warm water. Vestibular paresis was defined as >35% asymmetry between the right- and left-sided responses; this was calculated with the formula of (15) based on the slow-phase velocity of caloric nystagmus (16):

$$\{\left[(R33^\circ C + R44^\circ C) - (L30^\circ C + L44^\circ C)\right] / \left[(R33^\circ C + R44^\circ C) + (L30^\circ C + L44^\circ C)\right]\} \times 100.$$

Video Head Impulse Test (vHIT)

vHIT was performed using a video-oculography system (SLMED, Seoul, Korea). Patients were examined at a distance of 1 m from the target at eye level. The slippage of the goggles was minimized by fastening them to the head with an elastic band. Patients were seated in a height-adjustable chair, which allowed the examiner to adjust the subject's head for optimal examination. Patients were instructed to look at a point on the wall 1 m ahead. An experienced examiner conducted the examination and manually performed it more than 20 times (head rotation 15–20°, duration 150–200 ms, peak velocity $> 150^\circ$/s) on both sides of each plane. Normal vHIT was defined as having a gain of ≤ 2 standard deviations (SD) of the age-matched normal gain reference range and no fixation catch-up saccades.

Cervical and Ocular Vestibular Evoked Myogenic Potentials

Vestibular evoked myogenic potentials (VEMPs) were evoked by air conducted (AC) 500-Hz short tone bursts (100 dB nHL; rise/fall time = 2 ms; plateau time = 1 ms; 100 trials at 5 Hz) using customized software (Cadwell Laboratories, Kennewick, WA, USA) and delivered by calibrated headphones of the same firm. Patients lay supine with surface EMG electrodes placed according to the evoked potentials [for details see (17, 18)].

For cVEMP (cervical VEMP) recordings, the recording electrode was placed over the belly of the ipsilateral sternocleidomastoid muscle, the reference electrode on the medial clavicle with self-adhesive Ag/AgCl electrodes and with the ground electrode fixed on the sternums' incisura jugularis. During unilateral stimulation, patients were asked to raise their head from the horizontal by 30° and rotate it to the contralateral side. The electromyographic (EMG) signal was amplified (bandwidth 20Hz−3kHz), sampled at 5 kHz, and then averaged for a 50 ms time window (starting from stimulus onset), for each side, respectively, and sequentially.

For oVEMP (ocular VEMP) recordings, responses obtained from the contralateral eye to the stimulated ear (the initial negative peak with short latencies around 10 ms and the following positive peak) were analyzed. The recording electrode was placed on the infraorbital ridge 1 cm below the center of each lower eyelid, the reference electrode was placed 2 cm below, and the ground electrode was on the forehead (19). During stimulation, patients were asked to fix their gaze on the target located 25° above eye level in about 60 cm distance. The EMG signal was amplified (bandwidth 10Hz−2kHz), sampled at 10 kHz, and then averaged for a 60 ms time window (starting from 2 ms before stimulus onset) for each side simultaneously.

To avoid bias due to different examiners, asymmetry ratios (AR) of VEMP amplitudes and latencies (cVEMP = p13, n23; oVEMP = n10, p15) were chosen as outcome parameters. The AR was calculated using the following formula:

$$AR = [(larger\ response - smaller\ response)/(larger\ response + smaller\ response) \times 100].$$

Pure Tone Audiometry Test

Pure tone audiometry (PTA) was assessed based on the hearing levels recorded at which the subjects exhibited their worst 4-tone average during a month before Gd enhanced MRI. Medical history of acute or chronic otitis media, sudden sensorineural hearing loss, vestibular neuritis, or benign paroxysmal positional vertigo was excluded.

Delayed Intravenous Gadolinium-Enhanced MRI of the Inner Ear (iMRI)

Data Acquisition

All MR imaging was acquired on a 3.0 Tesla MR scanner (Magnetom Skyra; Siemens, Erlangen, Germany) using a 64-channel phased-array head coil. All patients underwent MR imaging 4 h after administering a standard dose (0.2 ml/kg body weight, i.e., 0.1 mmol/kg body weight) of gadoterate meglumine (Gd-DOPTA, Dotarem; Guerbet). We used improved HYDROPS (HYbriD of Reversed image Of Positive endolymph signal and native image of positive perilymph Signal) imaging protocol for the evaluation of endolymphatic space previously proposed by Naganawa et al. (20) to reduce scan time. The following imaging sequences were obtained from all patients: heavily T2-weighted (hT2W) MR cisternography (MRC) for an anatomical total lymph space reference, hT2W three-dimensional (3D) fluid-attenuated inversion recovery (FLAIR) with an inversion time of 2,900 ms (positive perilymph image, PPI) and hT2W 3D FLAIR with an inversion time of

2,500 ms (positive endolymphatic image, PEI) for evaluating endolymphatic hydrops.

Detailed scan parameters were as follows. MRC acquisition parameters were: variable flip angle 3D turbo spin-echo (sampling perfection with application-optimized contrasts by using different flip angle evolutions [SPACE]); repetition time (TR), 4,400 ms; echo time (TE), 542 ms; flip angle (FA), initial refocusing FA of 180 degrees rapidly decreased to constant FA of 120 degrees for the turbo-spin-echo refocusing echo train; matrix size, 384 × 324; slices per slab, 104; slice thickness, 1 mm; field of view (FOV), 162 × 192 mm; generalized auto-calibrating partially parallel acquisition (GRAPPA) parallel imaging technique; acceleration factor, 2; number of excitations (NEX), 1.8; and scan time, 3 min 15 s. The parameters of PPI were: SPACE sequence; TR, 16,000 ms; TE, 542 ms; inversion time, 2,900 ms; FA, initial refocusing FA of 180 degree rapidly decreased to constant FA of 120 degrees for the turbo-spin-echo refocusing echo train; matrix size, 384 × 324; slices per slab, 104; slice thickness, 1 mm; FOV, 162 × 192 mm; GRAPPA parallel imaging technique with an acceleration factor of 2; NEX, 1.4; and scan time, 7 min 14 s. The PEI parameters were the same as those of PPI except for the inversion time of 2,500 ms.

HYDROPS images were generated on the scanner console by subtracting the PEI from the PPI for the visualization of endolymphatic hydrops. For the image analysis, HYDROPS-Mi2 images providing a higher contrast-to-noise ratio than HYDROPS images were also generated on a MATLAB (MATrix LABoratory) software by multiplication of HYDROPS and MRC images. Identical FOV, matrix size, and slice thickness were applied to MRC, PPI, and PEI for facilitating comparison and subtraction.

Semi-quantitative Visual Grading of the Endolymphatic Space

An experienced neuroradiologist who was blinded to the clinical patient data classified the degree of EH in the vestibulum and cochlea according to the methods proposed by Nakashima et al. (21). The degree of EH was visually classified as none (grade 0), mild (grade 1), or severe (grade 2) in the cochlea and vestibulum separately. A detailed description with an image example of the cochlea classification and the vestibulum can be found in **Figure 1**. For the cochlear EH grading (**Figures 1A–C**), the slice with the most substantial height of the cochlear modiolus was selected. For the vestibular EH grading (**Figures 1D–F**), the lowest slice where the lateral semicircular canal is almost visible was chosen. The ampulla and semicircular canals were excluded from the classification process. The endolymphatic space and total fluid space (sum of the endolymphatic and perilymphatic space) of the vestibulum were outlined manually to determine the grading of vestibular EH using ImageJ software (http://rsb.info.nih.gov). The total fluid space was drawn on the MRC image, and the endolymphatic space with a negative (dark) signal was drawn on the HYDROPS-Mi2 image. The ratio of the endolymphatic space area to that of the total fluid space determined EH grading and is shown in **Figures 1D–F**.

Volumetric Quantification of the Endolymphatic Space

After two patients were discarded due to missing sequences (one patient with probable VM, one patient with probable MD), the data of sixty patients underwent volumetric quantification of the ELS. The method used were atlas-based segmentation of the bony labyrinth of the inner ear (22) and Volumetric Local Thresholding or VOLT (23) of the total fluid space (TFS). The following open-source software was used: 3D Slicer version 4.11 toolbox (24), ImageJ Fiji (25), and the "MorphoLibJ Toolbox" (26). An overview of the volumetric pipeline can be seen in **Figure 2**.

VOLT operates on a pre-segmented region-of-interest (ROI) of the inner ear, which requires a series of data pre-processing steps: *(i)* A side-independent version of the probabilistic atlas of the bony labyrinth of the inner ear (22) was created. *(ii)* A cuboid containing the subjects' inner ears (30 × 30 × 52 mm) was cropped from the MRC and HYDROPSMi2 image stacks using FiJi (27). Volumes were then converted into 8-bit and re-scaled (factor 2) using Quintic B-spline interpolation Transform-plugin (28). Also, histogram-based noise reduction was performed on the MRC-volumes to simplify atlas registration. *(iii)* Atlas registration was done through the BRAINSFIT-algorithm (29) with the following parameters: fixed image: MRC volume, moving image: atlas, mode: affine (12 DOF; degrees of freedom), percentage of samples: 0.5, maximum step length 0.5. *(iv)* MRC-images underwent segmentation into the inner ear and background. Subsequently, MRC volumes labeled as inner ear were volumetrically thresholded in three dimensions to create a binary hull. Since MRC, PPI, and PEI were precisely aligned according to the HYDROPSMi2-protocol, a dilated version of this hull could be directly applied to the HYDROPSMi2 image, creating a fusion image that could be used for direct intensity-based analysis.

Data processing with VOLT (23) on the HYDROPSMi2-fusion volumes included the following steps: First, 3D-reconstructions of the source image in three different orthogonal orientations. Second, the calculation of multiple binarized versions [two thresholding algorithms: Niblack (30), Mean; two spatial resolutions: 6, 10]. Third, aggregation into one final volume resulted in a 3D probability map, where low intensities classify as endolymph, and high intensities classify as perilymph. Fourth, the selection of cut-off 11 for endolymphatic VOLT-classifications and analysis of the resulting volumes using MorphoLibJ-Suite (26). After VOLT-processing, manual 3D cropping was performed using FiJi to differentiate between cochlear and vestibular ELS.

Parameters Derived From Endolymphatic Space Measures

The extent of the ELS was estimated as the mean between the ipsilateral and contralateral side in mm^3, as well as the ratio of the ELS regarding the TFS [in %] for the complete inner ear, the cochlea (c), and the vestibulum (v). The asymmetry between the two sides was assessed using the difference (Diff) between the ipsilateral and contralateral side, the ratio regarding the TFS (Diff/TFS-Ratio in %) as well as using an asymmetry index

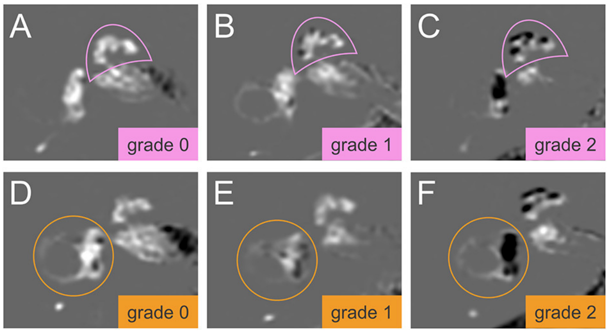

FIGURE 1 | Grading of the cochlear and vestibular endolymphatic hydrops (EH). The degree of EH in cochlea (pink semicircle, top row, **A–C**) and vestibulum (orange circle, lower row, **D–F**) was classified according to Nakashima et al. (21). In HYDROPS-Mi2 images, the presence of EH as enlarged endolymphatic space (ELS) can be observed as hypointense (= dark) signal spaces surrounded by the hyperintense (= bright white) signal Gadolinium-enhanced perilymphatic space (PLS) and bony labyrinth. Grading of the cochlear EH **(A–C)** is done at the slice of the mid-modiolar level. EH in the cochlea can be categorized as grade 0 = no EH, no displacement of Reissner's membrane, contrast-enhanced PLS with no enlarged endolymphatic spaces **(A)**; grade 1 = mild, mild displacement of Reissner's membrane, ELS area (dark) of the cochlear duct is as large as the area of the scala vestibuli **(B)**; grade 2 = severe displacement of Reissner's membrane, the area of cochlear duct markedly enlarged and is larger than the area of the scala vestibuli **(C)**. Grading of the vestibular EH **(D–F)** is done at the lowest slice of the vestibulum when the lower part of the lateral semicircular canal is still visible. EH in the vestibulum can be graded as follows: Grade 0 = no vestibular EH is defined as the area ratio of the endolymphatic space to the total fluid space is not < 33.3% **(D)**; grade 1 = mild vestibular EH is defined as the area ratio exceeds 33.3% but is below 50% **(E)**; grade 2 = severe vestibular EH is defined as the area ratio exceeds 50% **(F)**. HYDROPSMi2, Hybrid of the reversed image of positive endolymph signal and native image of positive perilymph signal multiplied by T2.

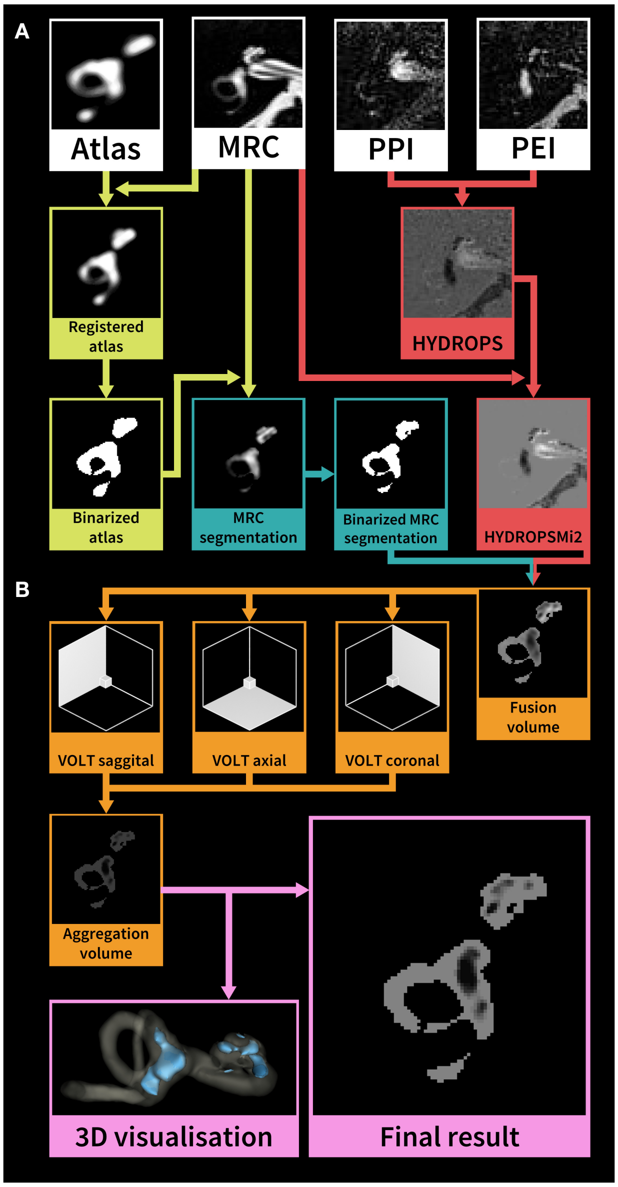

FIGURE 2 | Overview of the HYDROPSMi2 volumetric quantification pipeline. The flowchart shows a step-by-step overview of an example of an exemplary single subject's right inner ear. Each color corresponds to a different processing step. The pipeline is divided into **(A)** pre-processing and **(B)** volumetric local thresholding (VOLT) processing steps: First, a probabilistic atlas of the bony labyrinth (22) is co-registered to the MRC image, binarized using 3D-thresholding and then used to segment the MRC image (green steps). Second, the HYDROPSMi2-image is created by subtracting the PEI from the PPI and multiplying the result with the MRC image (red steps). Third, a fusion volume is created from the binarized MRC-segmentation and the HYDROPSMi2-image (red and blue arrows). VOLT (23) is then performed with two algorithms and two spatial resolutions on each of the reconstructions. All VOLT-results are reconstructed into one direction and aggregated into one volume (orange steps). This aggregation volume can be used to visualize the endolymphatic space (ELS) in 3D or as a quantification of the ELS in mathematical analysis (pink steps). HYDROPSMi2, Hybrid of the reversed image of positive endolymph signal and native image of positive perilymph signal multiplied by T2; MRC, Magnetic resonance cisternography; PPI, Positive perilymph image; PEI, Positive endolymph image.

$[(EH_R - EH_L.) / (EH_R + EH_L.)]$ in %, again for the complete inner ear, the cochlea, and the vestibulum. **Figure 2** depicts a step-by-step overview of the volumetric quantification pipeline on an exemplary single-subject level.

Data Availability Statement

All of the individual participant data that underlie the results reported in this article will be shared after deidentification (manuscript, tables, and figures).

Statistical Analysis

Analyses were performed using the Statistical Package for Social Sciences software (SPSS, Inc., Chicago, IL, USA). A chi-square test was used to compare univariate categorical variables, such as gender, the presence of clinical symptoms, or pathological results in diagnostic testing. Fisher's exact test was used to examine the significance of the association (contingency) between EH and neurophysiological classifications. One-way analysis of variance (ANOVA) for multiple comparisons, which was *post-hoc* Bonferroni-corrected for multiple testing, was used for scalar (volumetric quantification result, clinical diagnostic raw data) and ordinal (Semi-quantitative visual scoring result) values. Group differences were assessed between all VM vs. all MD vs.

all VM-MD (A), definite VM vs. definite MD vs. all VM-MD (D), and probable VM vs. probable MD vs. all VM-MD (P). Linear agreement between parameter pairs was calculated for each method separately using the two-sided Spearman's correlation coefficient. Results were reported at a significance level of $p < 0.05$ and $p < 0.005$. Categorical values are reported as the number of cases that fit the category/number of patients in the examined group (%); ordinal or scalar values are presented as means ± standard deviations.

RESULTS

Demographic and Neurotological Findings

A result overview of demographic and neurotological findings can be viewed in **Table 1**. Sixty-two patients were included in the current study. Twenty-five patients met the diagnostic criteria for definite or probable VM (all (a) VM: 18 females, mean age ± SD, 51.3 ± 16.0 years, range 24–84 years; 19 definite (d) VM: 14 females, 51.3 ± 16.2 years, range 23–84 years; 6 probable (p) VM: 4 females, mean age ± SD, 51.3 ± 17.1 years, range 24–70 years) and 29 patients for definite or probable MD (aMD: 19 females, 61.1 ± 9.5 years, range 38–78 years; 15 dMD: 4 females, 60.3 ± 10.0 years, range 44–78 years; 14 pMD: 11 females, 62.0 ± 9.2 years, range 38–72 years). The remaining eight patients (8 of 62 = 12.9%, 6 females, mean age ± SD, 49.0 ± 17.4 years, range 23–72 years) fulfilled the criteria for VM and MD (VM-MD; 2 fulfilling criteria for definite VM and definite MD, 4 for definite VM and probable MD, 2 for probable VM and MD) at the same time or separately in succession. VM symptoms included visual aura, photophobia with a unilateral throbbing headache; MD symptoms included vertigo with typical fluctuating aural fullness and tinnitus with documented low tone hearing impairment.

Age between VM, MD and VM-MD group differed significantly (A: $F = 4.6$, D: $F = 14.4$, $p < 0.05$, Bonferoni-corrected) and the female proportion was higher in VM (aVM = 18/25, 72%, dVM = 14/19, 73.7%, pVM = 4/6, 66.7%) when compared to MD (aMD = 19/29, 55.5%, dMD = 8/15, 53.3%, pMD = 11/14, 78.6%) and VM-MD (6/8, 75%). The migrainous headaches in VM patients began at about 43.5 years, while their vertigo attacks began around 45 years (on average 1.5 years later). Headaches were significantly more frequent [A (=aVM vs. aMD vs. VM-MD): $\chi^2(2) = 32.1$, $p < 0.001$, $\varphi = 0.7$; D (=dVM vs. dMD vs. VM-MD):$\chi^2(2) = 20.4$, $p < 0.001$, $\varphi = 0.7$, P (= pVM vs. pMD vs. VM-MD): $\chi^2(2) = 11.1$, $p < 0.005$, $\varphi = 0.6$] in VM (aVM = 25/25; dVM = 19/19; pVM 6/6, 100%) when compared to MD (aMD = 7/29, 24.1%; dMD = 4/15, 26.7%; pMD = 5/14, 35.7%) or VM-MD (5/8, 62.5%). A relevant number of patients with VM (aVM = 9 of 25, 36%; dVM = 7/19, 36.8%; pVM = 2/6, 33.3%) reported fluctuating degrees of hearing disturbances, tinnitus, or aural fullness. However, whereas ipsilateral auditory symptoms, such as tinnitus [A: $\chi^2(4) = 16.3$, $p < 0.05$, $\varphi = 0.5$; D: $\chi^2(4) = 15.2$, $p < 0.05$, $\varphi = 0.6$], aural fullness [A: $\chi^2(4) = 21.6$, $p < 0.005$, $\varphi = 0.4$; D:$\chi^2(4) = 18.2$, $p < 0.005$, $\varphi = 0.7$], aural fluctuation [A: $\chi^2(4) = 21.2$, $p < 0.005$, $\varphi = 0.6$; D:$\chi^2(4) = 23.7$, $p < 0.005$, $\varphi = 0.8$], and hearing impairment [A: $\chi^2(4) = 23.5$, $p < 0.005$, $\varphi = 0.6$; D:$\chi^2(6) = 21.5$, $p < 0.005$, $\varphi = 0.7$] were mostly observed in the MD (aMD = 21/29, 72.4%; dMD = 13/15, 86.7%; pMD = 8/14, 57.1%) and VM-MD (3/8, 37.5%) groups, the VM group (aVM = 4/25, 16%; aVM 3/15 = 15.8%; pVM = 1/6, 16.7%) presented more with bilateral auditory symptoms [A: $\chi^2(2) = 12.9$, $p < 0.001$, $\varphi = 0.5$; D:$\chi^2(2) = 9.9$, $p < 0.001$, $\varphi = 0.5$; P: $\chi^2(2) = 13.29$, $p < 0.005$, $\varphi = 0.7$]. Unilateral auditory symptoms in MD were accompanied with ipsilateral audio-vestibular dysfunction such as low tone hearing loss patterns, abnormal caloric asymmetry, and decreased vHIT gain with corrective saccades. Latencies and the abnormal asymmetry ratio (AR) of cervical and ocular VEMPs did not differ between groups ($p > 0.05$).

Endolymphatic Hydrops (Visual Grading) and Its Correlation to Neurophysiological Data

An overview of the EH visual grading scores and their correlation to neurophysiological results can be viewed in **Tables 2**, **3**, respectively. EH was significantly [A (= aVM vs. aMD vs. VM-MD):$\chi^2(2) = 29.1$, $p < 0.001$, $\varphi = 0.7$, D (= dVM vs. dMD vs. VM-MD):$\chi^2(2) = 20.9$, $p < 0.001$, $\varphi = 0.7$; P (= pVM vs. pMD vs. VM-MD): $\chi^2(2) = 9.2$, $p < 0.05$, $\varphi = 0.6$] more frequent in MD (all: 79.3%, definite: 80.0%, probable 71.4%) than in VM-MD (2/8, 25%) or VM (all: 8%, definite: 5.3%, probable: 16.7%). EH was observed in only two of the patients with VM (2 of 25, 8.0%); one showed mild [grade 1, following Nakashima et al. (21)], and one showed a severe [grade 2, following Nakashima et al. (21)] bilateral hydrops, either only in the cochlea or also including the vestibulum (**Table 2**). Both patients presented with bilateral tinnitus and aural fullness. In contrast, EH was more frequently observed ipsilaterally [A: $\chi^2(4) = 15.3$, $p < 0.005$, $\varphi = 0.5$; D:$\chi^2(4) = 18.1$, $p < 0.005$, $\varphi = 0.7$] in MD (23 of 29, 79.3%) with grade 1 (11/29, 37.9%) or grade 2 (12/29, 41.4%). VM-MD took an interim position in this respect (2/8, 25%). In addition, visual grading on the ipsilateral side differed significantly for inner ear (A: $F = 12.8$, $p < 0.05$, D: $F = 14.9$, $p < 0.05$, Bonferroni-corrected), cochlea (A: $F = 15.8$, D: $F = 16.6$, $p < 0.05$, Bonferroni-corrected), and vestibulum (A: $F = 7.6$, $p < 0.005$, D: $F = 10.7$, $p < 0.05$, Bonferroni-corrected) between VM, MD, and VM-MD (**Table 2**).

The main common feature seemed to be auditory symptoms that correlated with initial PTA > 25 dB ($r_S = 0.3$, $p < 0.05$, two-sided) and low tone hearing loss pattern ($r_S = 0.4$, $p < 0.005$, two-sided). Matching this, the visual EH grading of the ipsilateral cochlea significantly correlated with the level of PTA thresholds ($r_S = 0.4$, $p < 0.005$, two-sided) and VOG during caloric irrigation (A: $r_S = 0.5$, $p < 0.005$, two-sided) on the ipsilateral side, as well as side difference (SD) during caloric irrigation (D: $r_S = 0.7$, $p < 0.05$, two-sided). The EH's anatomical location (cochlea, vestibulum, both) and how they correlated with the respective dysfunction (e.g., PTA for cochlea, caloric asymmetry, vHIT) is presented in **Table 3**.

Overall pathologies, patients with cochlear deficits had cochlear EH, and those with vestibular deficits had vestibular EH (Fisher's exact test, $p < 0.005$, **Table 3A**). Furthermore, the laterality of EH correlated positively with the lesion side of

TABLE 1 | Demographics and clinical features in VM, MD and VM-MD patients.

		VM			**MD**		**VM-MD**	
	All $n = 25$	**Definite** $n = 19$	**Probable** $n = 6$	**All** $n = 29$	**Definite** $n = 15$	**Probable** $n = 14$	**All** $n = 8$	**Statistical model**
Age [yrs]	51.3 ± 16.0 ▲	51.3 ± 16.2✦	51.3 ± 17.1	61.1 ± 9.5 ▲	60.3 ± 10.0✦	62.0 ± 9.2	49.0 ± 17.4 ▲,✦	[2]
Gender [females]	18/25 (72.0%)▲▲	14/19 (73.7%)✦	4/6 (66.7%)✧	19/29 (55.5%)▲▲	8/15 (53.3%)✦	11/14 (78.6%)✧	6/8 (75%)▲▲,✦,✧	[1]
Onset age of vertigo [yrs]	45.0 ± 15.6 ▲	42.9 ± 14.2✦	51.6 ± 19.3	55.0 ± 8.3 ▲	55.2 ± 9.5✦	54.8 ± 7.1	40.7 ± 15.3 ▲,✦	[2]
Duration since start of vertigo [yrs]	6.3 ± 5.5	6.7 ± 4.9	5.1 ± 7.6	6.1 ± 6.5	5.2 ± 5.3	7.2 ± 7.6	8.3 ± 7.7	
Vertigo attacks in the last 6 months	24.0 ± 37.4	28.6 ± 41.8	9.3 ± 9.8	9.6 ± 17.9	8.6 ± 16.7	10.6 ± 19.6	16.3 ± 37.1	
Headache symptoms	25/25 (100%)▲▲	19/19 (100%)✦✦	6/6 (100%)✧✧	7/29 (24.1%)▲▲	4/15 (26.7%)✦✦	5/14 (35.7%)✧✧	5/8 (62.5%)▲▲,✦✦,✧✧	[1]
Onset age of headache [yrs]	43.5 ± 16.1	41.3 ± 14.7	50.6 ± 19.6	47.8 ± 7.5	49.0 ± 9.8	47.1 ± 7.0	40.6 ± 15.2	
Duration since start of headache [yrs]	7.8 ± 6.0	8.3 ± 5.3	6.0 ± 8.1	9.2 ± 7.0	9.3 ± 4.4	9.1 ± 8.7	8.4 ± 7.7	
Auditory symptoms	9/25 (36%)	7/19 (36.8%)	2/6 (33.3%)	29/29 (100%)	15/15 (100%)	14/14 (100%)	8/8 (100%)	[1]
Tinnitus	11/25 (44%)▲	9/19 (47.4%)	2/6 (33.3%)	24/29 (82.8%)▲	14/15 (93.3%)	10/14 (71.4%)	6/8 (75.0%)▲	[1]
Bilateral	7/25 (28%)	6/19 (31.6%)	1/6 (16.7%)	4/29 (13.8%)	2/15 (13.3%)	2/14 (14.3%)	1/8 (12.5%)	
Ipsilateral	4/25 (16%)	3/19 (15.8%)	1/6 (16.7%)	20/29 (69%)	12/15 (80%)	8/14 (57.1%)	5/8 (62.5%)	
Contralateral	–	–	0/6 (0%)	0/29 (0%)	0/15 (0%)	0/14 (0%)	0/8 (0%)	
Aural fullness	3/25 (12%)▲▲	2/19 (10.5%)✦✦	1/6 (16.7%)✧✧	17/29 (58.6%)▲▲	10/15 (66.7%)✦✦	7/14 (50.0%)✧✧	6/8 (75.0%)▲▲,✦✦,✧✧	[1]
Bilateral	3/25 (12%)	2/19 (10.5%)	1/6 (16.7%)	2/29 (6.9%)	1/15 (6.7%)	1/14 (7.1%)	1/8 (12.5%)	
Ipsilateral	–	–	0/6 (0%)✧✧	14/29 (48.3%)	9/15 (60%)	5/14 (35.7%)	5/8 (62.5%)	
Contralateral	–	–	0/6 (0%)	1/29 (3.4%)	0/15 (0%)	1/14 (7.1%)	0/8 (0%)	
Aural fluctuation	3/25 (12%)▲▲	2/19 (10.5%)✦✦	1/6 (16.7%)✧✧	20/29 (69%)▲▲	14/15 (93.3%)✦✦	6/14 (42.9%)✧✧	3/8 (37.5%)▲▲,✦✦,✧✧	[1]
Bilateral	3/25 (12%)	2/19 (10.5%)	1/6 (16.7%)	–	–	–	–	
Ipsilateral	–	–	–	12/29 (41.4%)	10/15 (66.7%)	2/14 (14.3%)	2/8 (25%)	
Contralateral	–	–	–	8/29 (27.6%)	4/15 (26.7%)	4/14 (28.6%)	1/8 (12.5%)	
Hearing impairment	5/25 (20.0%)▲▲	4/19 (21.1%)✦✦	1/6 (16.7%)✧✧	25/29 (86.2%)▲▲	14/15 (93.3%)✦✦	10/14 (71.4%)✧✧	3/8 (37.5%)▲▲,✦✦,✧✧	[1]
Bilateral	–	–	–	2/29 (6.9%)	1/15 (6.7%)	1/14 (7.1%)	–	
Ipsilateral	4/25 (16%)	3/19 (15.8%)	1/6 (16.7%)	21/29 (72.4%)	13/15 (86.7%)	8/14 (57.1%)	3/8 (37.5%)	
Contralateral	1/25 (4%)	1/19 (5.3%)	–	1/29 (3.4%)	–	1/14 (7.1%)	–	
Headache and auditory symptoms	9/25 (36%)	7/19 (36.8%)	2/6 (33.3%)	9/29 (31%)	4/15 (26.7%)	5/14 (35.7%)	5/8 (62.5%)	[1]
PTA mean [dB]	21.1 ± 18.0	22.4 ± 19.0	17.5 ± 15.8	29.0 ± 18.0	34.5 ± 19.2	23.6 ± 15.5	31.6 ± 23.5	
Ipsilateral	21.0 ± 19.9	21.0 ± 19.9	15.3 ± 9.4	31.6 ± 25.2	34.8 ± 25.4	28.5 ± 25.7	17.1 ± 11.2	
Contralateral	21.2 ± 20.8	21.2 ± 20.8	19.7 ± 23.0	24.5 ± 23.5	30.2 ± 30.9	18.8 ± 11.2	46.0 ± 41.2	
Initial PTA ≥ 25 dB	6/25 (24.0%)	4/19 (21.1%)	2/6 (33.3%)	20/29 (69%)	14/15 (93.3%)	6/14 (42.9%)	2/8 (25.0%)	[1]

(Continued)

TABLE 1 | Continued

		VM			MD		VM-MD	
	All *n* = **25**	**Definite** *n* = **19**	**Probable** *n* = **6**	**All** *n* = **29**	**Definite** *n* = **15**	**Probable** *n* = **14**	**All** *n* = **8**	**Statistical model**
Low tone hearing loss pattern	3/25 (12.0%)▲▲	2/19 (10.5%)✦✦	–✧✧	9/29 (31%)▲▲	7/15 (46.7%)✦✦	2/14 (14.3%)✧✧	1/8 (12.5%)▲▲,✦✦,✧✧	
vHIT hVOR mean gain	0.96 ± 0.07	0.95 ± 0.06	0.99 ± 0.08	0.93 ± 0.08	0.94 ± 0.08	0.91 ± 0.07	0.98 ± 0.06	
Ipsilateral	0.96 ± 0.07	0.95 ± 0.07	0.98 ± 0.08	0.91 ± 0.11	0.93 ± 0.10	0.89 ± 0.12	0.98 ± 0.07	
Contralateral	0.96 ± 0.08	0.94 ± 0.07	1.0 ± 0.09✧	0.94 ± 0.07	0.96 ± 0.09	0.93 ± 0.04✧	0.98 ± 0.06	[2]
Abnormal vHIT hVOR gain	1/25 (4%)	1/19 (5.3%)	0/6 (0%)	5/29 (17.2%)	3/15 (20%)	2/14 (14.3%)	0/8 (0%)	
Presence of vHIT corrective saccades	–▲▲	–✦✦	–✧✧	6/29 (20.7%)▲▲	4/15 (26.7%)✦✦	2/14 (14.3%)✧✧	–▲▲,✦✦,✧✧	[1]
Caloric response mean [°/s]	18.6 ± 8.1	19.7 ± 8.6✦	13.8 ± 3.0	12.7 ± 7.3	11.2 ± 7.4✦	14.3 ± 7.2	13.3 ± 8.9✦	[2]
Ipsilateral	19.2 ± 10.2	20.7 ± 10.7	12.7 ± 4.5	14.8 ± 8.4	13.1 ± 8.1	16.6 ± 8.6	14.3 ± 8.8	
Contralateral	18.0 ± 8.2▲	18.7 ± 9.0✦	14.9 ± 2.0	10.5 ± 9.2▲	9.2 ± 7.9✦	11.9 ± 10.6	12.4 ± 9.7✦	[2]
Caloric response AR	18.2%	19.5%	14.3%	47.2%	47.5%	46.7%	15%	
Abnormal caloric AR ≥ 35%	1/25 (4.0%)▲▲	1/19 (5.3%)✦✦	–✧	17/29 (58.6%)▲▲	8/15 (53.3%)✦✦	9/14 (64.3%)✧	1/8 (12.5%)▲▲.✦✦,✧	[1]
cVEMP p13 amplitude AR ≥ 40%	1/25 (4%)	1/19 (5.3%)	–	5/29 (17.2%)	3/15 (20%)	2/14 (14.3%)	1/8 (12.5%)	
cVEMP p13 amplitude AR [%]	16.8 ± 15.0	17.7 ± 16.1	14.3 ± 12.7	16.5 ± 15.5	16.1 ± 17.2	17.1 ± 14.0	14.4 ± 18.7	
cVEMP p13 mean latency [ms]	13.8 ± 0.6	13.7 ± 0.6	14.1 ± 0.5	14.6 ± 2.6	15.0 ± 2.5	14.2 ± 2.6	14.4 ± 2.3	
Ipsilateral	13.8 ± 0.7	13.6 ± 0.7	14.1 ± 0.7	14.3 ± 2.1	14.3 ± 1.9	14.3 ± 2.4	14.3 ± 2.4	
Contralateral	13.9 ± 0.6	13.7 ± 0.7	14.1 ± 0.4	14.9 ± 3.3	15.7 ± 3.6	14.0 ± 2.9	14.5 ± 2.3	
oVEMP n10 amplitude AR ≥ 40%	4/25 (16%)	4/19 (21.1%)	–	6/29 (20.7%)	5/15 (30.3%)	1/14 (7.1%)	–	
oVEMP n10 amplitude AR [%]	25.7 ± 18.5	27.5 ± 19.9	21.3 ± 15.5	22.2 ± 18.8	27.4 ± 21.3	16.5 ± 14.5	28.8 ± 23.8	
oVEMP n10 mean latency [ms]	11.2 ± 2.1	11.4 ± 2.4	10.5 ± 0.4	11.0 ± 1.0	11.1 ± 1.0	11.0 ± 1.2	10.5 ± 0.3	
Ipsilateral	11.4 ± 2.1	11.7 ± 2.4	10.6 ± 0.4	10.7 ± 2.2	10.4 ± 2.9	11.1 ± 1.2	10.5 ± 0.4	
Contralateral	11.1 ± 2.1	11.3 ± 2.5	10.4 ± 0.5	11.0 ± 1.3	11.2 ± 1.3	10.8 ± 1.4	10.6 ± 0.4	

▲ *Chi-Square test [1], or ANOVA [2] for VM (all) vs. MD (all) vs. VM-MD (all), where* $p < 0.05$*, or* ▲▲ *if* $p < 0.005$*.*

✦ *Chi-Square test [1], or ANOVA [2] for VM (definite) vs. MD (definite) vs. VM-MD (all), where* $p < 0.05$*, or* ✦✦ *if* $p < 0.005$*.*

✧ *Chi-Square test [1], or ANOVA [2] for VM (probable) vs. MD (probable) vs. VM-MD (all), where* $p < 0.05$*, or* ✧✧ *if* $p < 0.005$*.*

TABLE 2 | Semi-quantitative visual scoring of endolymphatic hydrops (EH) in VM, MD, and VM-MD patients.

	VM			**MD**			**VM-MD**	
	All ***n* = 25**	**Definite** ***n* = 19**	**Probable** ***n* = 6**	**All** ***n* = 29**	**Definite** ***n* = 15**	**Probable** ***n* = 14**	**All** ***n* = 8**	**Statistical model**
Presence of EH	2/25 (8.0%)▲▲	1/19 (5.3%)✦✦	1/6 (16.7%)✧	23/29 (79.3%)▲▲	12/15 (80%) ✦✦	10/14 (71.4%)✧	2/8 (25.0%)▲▲, ✦✦,✧	[1]
A) Grading								
Grade 1 (mild)	1/25 (4.0%)	–	1/6 (16.7%)	11/29 (37.9%)	2/15 (13.3%)	8/14 (57.1%)	–	
Grade 2 (severe)	1/25 (4.0%)	1/19 (5.3%)	–	12/29 (41.4%)	10/15 (66.7%)	2/14 (14.3%)	2/8 (25.0%)	
B) Anatomical location								
Cochlea	2/25 (8.0%)	1/19 (5.3%)	1/6 (16.7%)	22/29 (75.9%)	9/15 (60%)	10/12 (71.4%)	2/8 (25.0%)	[1]
Ipsilateral [°]	0.08 ± 0.28▲	0.05 ± 0.23✦	0.08 ± 0.20	1.03 ± 0.87▲	1.27 ± 0.96✦	0.79 ± 0.70✧	0.25 ± 0.46▲,✦	[2]
Contralateral [°]	0.12 ± 0.40	0.11 ± 0.46	0.08 ± 0.20	0.21 ± 0.41	0.20 ± 0.41	0.21 ± 0.43	–	
Vestibulum	1/25 (4.0%)▲▲	1/19 (5.3%)✦	0/6 (0%)✧✧	13/29 (44.8%)▲▲	12/15 (80%)✦	4/14 (21.4%)✧✧	1/8 (12.5%)▲▲,✦,✧✧	[1]
Ipsilateral [°]	0.08 ± 0.40 ▲	0.11 ± 0.46✦	0.17 ± 0.41	0.79 ± 0.94 ▲	1.13 ± 0.99✦	0.43 ± 0.76	0.13 ± 0.35 ▲,✦	[2]
Contralateral [°]	0.08 ± 0.40	0.11 ± 0.46	0.17 ± 0.41	–	–	–	–	
Inner ear (cochlea & vestibulum)	1/25 (4.0%)	1/19 (5.3%)	–	12/29 (41.4%)	9/15 (60%)	3/14 (21.4%)	1/8 (12.5%)	[1]
Ipsilateral [°]	0.08 ± 0.31 ▲	0.08 ± 0.34✦	–	0.91 ± 0.85▲	1.20 ± 0.92✦	0.61 ± 0.66	0.19 ± 0.37▲,✦	[2]
Contralateral [°]	0.10 ± 0.41	0.11 ± 0.46	–	0.10 ± 0.21	0.10 ± 0.21	0.11 ± 0.21	–	
C) Laterality of EH								
Bilateral	2/25 (8.0%)▲▲	1/19 (5.3%)✦✦	1/6 (16.7%)	3/29 (10.3%)▲▲	1/15 (16.7%)✦✦	2/14 (14.3%)	–▲▲,✦✦	[1]
Unilateral	–▲▲	–✦✦	–	19/29 (65.5%)▲▲	11/15 (73.7%)✦✦	8/14 (57.1%)	2/8 (25.0%)▲▲,✦✦	
Ipsilateral	–▲▲	–✦✦	–	16/29 (55.2%)▲▲	9/15 (60%)✦✦	7/14 (50%)	–▲▲,✦✦	
Contralateral	–▲▲	–✦✦	–	3/29 (10.3%)▲▲	2/15 (13.3%)✦✦	1/14 (7.1%)	–▲▲,✦✦	

▲ *Chi-Square test [1], or ANOVA [2] for VM (all) vs. MD (all) vs. VM-MD (all), where $p < 0.05$, or ▲▲ if $p < 0.005$.*

✦ *Chi-Square test [1], or ANOVA [2] for VM (definite) vs. MD (definite) vs. VM-MD (all), where $p < 0.05$, or ✦✦ if $p < 0.005$.*

✧ *Chi-Square test [1], or ANOVA [2] for VM (probable) vs. MD (probable) vs. VM-MD (all), where $p < 0.05$.*

TABLE 3 | Interrelation between EH characteristics and neurophysiological testing results.

	Neurophysiological testing results					
Location of EH	**Normal** ***n* = 24**	**Vestibular deficits** ***n* = 13**	**Cochlear deficits** ***n* = 12**	**Vestibulocochlear deficits** ***n* = 13**	**Total** ***n* = 62**	***Fisher's exact test***
A) Anatomical location of EH and correlation to neurophysiological data based on visual grading						
No EH	19 (79.2%)	8 (61.5%)	6 (50.0%)	2 (15.4%)	35	
Vestibular EH	0 (0%)	1 (7.7%)	0 (0%)	0 (0%)	1	*p* < *0.005*
Cochlear EH	4 (16.7%)	2 (15.4%)	2 (16.7%)	4 (30.8%)	12	
Vestibular and cochlear EH	1 (4.2%)	2 (15.4%)	4 (33.3%)	7 (53.8%)	14	

	Neurophysiological testing results					
Laterality of EH	**Normal** ***n* = 28**	**Right-sided deficits** ***n* = 12**	**Left-sided deficits** ***n* = 16**	**Bilateral deficits** ***n* = 6**	**Total** ***n* = 62**	***Fisher's exact test***
B) Laterality of EH and correlation to neurophysiological data based on visual grading						
No EH	22 (78.6%)	3 (25.0%)	5 (31.3%)	4 (66.7%)	34	
Right-sided EH	4 (14.3%)	8 (66.7%)	1 (6.3%)	1 (16.7%)	14	*p* < *0.005*
Left-sided EH	0 (0%)	0 (0%)	9 (56.3%)	1 (16.7%)	10	
Bilateral EH	2 (7.1%)	1 (8.3%)	1 (6.3%)	0 (0%)	4	

vestibular and/or cochlear deficits (Fisher's exact test, $p < 0.005$, **Table 3B**).

Volumetric Quantification of the ELS and Its Correlation to Neurophysiological Data

An overview of the results can be seen in **Table 4**. Overall, the patient groups' characteristics were most pronounced for definite diagnoses, followed by all (definite and probable) and least pronounced between patients with probable diagnoses. Two interrelations were analyzed: Parameters referring to the sheer size of the ELS (mean ELS, ELS/TFS-Ratio) and parameters referring to the symmetry between ipsilateral and contralateral inner ear (difference of the ELS between the sides (Diff), Diff/TFS-Ratio, as well as the asymmetry-index or AI).

Mean ELS were most prominent on the ipsilateral side in definite MD (inner ear: 16.7 ± 9.7 mm^3, cochlea: 4.8 ± 4.0 mm^3, vestibulum: 12.0 ± 6.0 mm^3), while definite VM (inner ear: 10.4 ± 4.9 mm^3, cochlea: 2.5 ± 1.3 mm^3, vestibulum: 7.9 ± 4.5 mm^3), and VM-MD (inner ear: 9.5 ± 3.8 mm^3, cochlea: 1.9 ± 1.9 mm^3, vestibulum: 7.3 ± 3.7 mm^3) were less pronounced ($F = 4.1$, $p < 0.05$, Bonferroni-corrected). In addition, ELS/TFS-Ratio on the ipsilateral side differed significantly ($F = 4.9$, $p < 0.05$, Bonferroni-corrected) for definite VM (4.2 ± 1.8%) vs. definite MD (6.8 ± 3.8%) vs. VM-MD (3.8 ± 2.1%). Nonetheless, differences between groups were most pronounced in the parameters referring to the asymmetry of the ipsilateral and contralateral ELS, such as the asymmetry index (AI: $F = 3.7$, cAI: $F = 4.1$, vAI: $F = 4.1$, $p < 0.05$, Bonferroni-corrected) and difference (Diff: $F = 8.0$, cDiff: $F = 3.6$, vDiff $F = 9.3$, $p < 0.05$, Bonferroni-corrected) between VM (Diff: 1.8 ± 6.3 mm^3, cDiff: 0.9 ± 0.9 mm^3, vDiff: 1.7 ± 1.3 mm^3) and MD (Diff: 8.6 ± 8.1 mm^3, cDiff: 4.7 ± 2.9 mm^3, vDiff: 6.3 ± 5.1 mm^3), and less when compared to VM-MD (Diff: 2.6 ± 2.4 mm^3, cDiff: 1.2 ± 1.4 mm^3, vDiff: 1.9 ± 1.0 mm^3).

In MD, volumetric quantification parameters correlated highly with the semi-quantitative visual grading of the EH. In particular, the parameters referring to the absolute size of the ELS (mean, ipsilateral) correlated highly with the visual grade of the cochlea (mean: $r_S = 0.9$, ipsilateral: $r_S = 0.8$, $p < 0.005$, two-sided), vestibulum (ipsilateral: $r_S = 0.8$, $p < 0.005$, two-sided), and the whole inner ear (mean: $r_S = 0.7$, ipsilateral: $r_S = 0.8$, $p < 0.005$, two-sided). The highest correlations were seen with parameters referring to the "ELS side relation" in the cochlea (AI: $r_S = 0.7$, Diff: $r_S = 0.8$, Diff/TFS-Ratio: $r_S = 0.8$, $p < 0.005$, two-sided) vestibulum (AI: $r_S = 0.8$, Diff: $r_S = 0.9$, Diff/TFS-Ratio: $r_S = 0.9$, $p < 0.005$, two-sided), or inner ear (AI: $r_S = 0.7$, Diff: $r_S = 0.8$, Diff/TFS-Ratio: $r_S = 0.8$, $p < 0.005$, two-sided). Parameters referring to the "ELS side relation" were the ELS difference between the ipsilateral and contralateral side, the ELS/TFS-Ratio of said difference, as well as the asymmetry index. In addition, quantitative ELS measurements in definite MD correlated with the side difference in VOG during caloric irrigation (ELS mean: $r_S = 0.7$, ELS/TFS: $r_S = 0.6$, ELS ipsilateral: $r_S = 0.7$, cELS mean: $r_S = 0.8$, cELS ipsilateral: $r_S = 0.7$, cELS/cTFS: $r_S = 0.9$, vELS mean: $r_S = 0.6$, vELS ipsilateral: $r_S = 0.6$, vELS/vTFS: $r_S = 0.5$, $p < 0.05$, two-sided), as well as with low tone hearing loss patterns in PTA (ELS mean: $r_S = 0.6$, ELS ipsilateral: $r_S = 0.7$, ELS/TFS: $r_S = 0.7$, AI: $r_S = 0.7$, Diff: $r_S = 0.6$, Diff/TFS-Ratio: $r_S = 0.7$, vELS ipsilateral: $r_S = 0.8$, vELS/vTFS: $r_S = 0.8$, vAI: $r_S = 0.7$, vDiff: $r_S = 0.7$, vDiff/vTFS-Ratio: $r_S = 0.7$, $p < 0.05$, two-sided).

In VM, correlations were less pronounced when considering the semi-quantitative visual grading parameters (cochlea, inner ear) and most prominent for the vestibulum (vELS/vTFS-Ratio:

TABLE 4 | Volumetric quantification results for VM, MD, and VM-MD patients.

		VM			MD		VM-MD
	All *n* = 24	**Definite** *n* = 19	**Probable** *n* = 5	**All** *n* = 28	**Definite** *n* = 15	**Probable** *n* = 13	**All** *n* = 8
Inner ear							
ELS mean [mm^3]	10.1 ± 4.3 (3.8–21.3)	10.3 ± 4.8 (3.8–21.3)	9.6 ± 1.9 (7.8–12.2)	10.8 ± 5.2 (3.8–25.0)	12.7 ± 5.8 (4.3–25.0)	8.7 ± 3.5 (3.8–15.2)	9.5 ± 3.8 (3.8–15.3)
Ipsilateral	10.2 ± 4.4 (3.6–21.4)	10.4 ± 4.9 (3.6–21.4)✦	9.6 ± 2.3 (5.8–11.7)	13.1 ± 8.3 (3.7–36.5)	16.7 ± 9.7 (3.7–36.5)✦	9.1 ± 3.4 (4.3–13.9)	9.2 ± 5.2 (3.4–19.2)✦
Contralateral	10.1 ± 4.6 (1.5–21.3)	10.2 ± 5.0 (1.5–21.3)	9.5 ± 2.3 (6.6–12.8)	8.5 ± 3.6 (1.9–16.9)	8.7 ± 3.2 (4.9–15.6)	8.4 ± 4.1 (1.9–16.9)	9.8 ± 2.9 (4.2–14.2)
ELS/TFS–Ratio [%]	4.1 ± 1.5 (1.7–7.8)	4.1 ± 1.7 (1.7–7.8)	3.9 ± 0.6 (3.3–4.8)	4.4 ± 2.0 (1.7–9.5)	5.2 ± 2.2 (1.9–9.5)	3.5 ± 1.4 (1.7–6.1)	3.9 ± 1.5 (1.6–6.3)
Ipsilateral	4.1 ± 1.6 (1.6–7.9)	4.2 ± 1.8 (1.6–7.9)✦	3.9 ± 0.9 (2.6–4.7)	5.3 ± 3.3 (1.7–15.0)	6.8 ± 3.8 (1.7–15.0)✦	3.6 ± 1.3 (1.9–5.5)	3.8 ± 2.1 (1.5–7.9)✦
Contralateral	4.0 ± 1.6 (0.6–7.7)	4.1 ± 1.8 (0.6–7.7)	3.8 ± 0.8 (2.8–4.9)	3.5 ± 1.4 (0.8–6.7)	3.6 ± 1.3 (2.1–6.0)	3.3 ± 1.6 (0.8–6.7)	4.0 ± 1.1 (1.8–5.7)
Diff [mm^3]	1.9 ± 1.6 (0.1–6.8)▲	1.8 ± 1.7 (0.1–6.8)✦	2.2 ± 1.2 (0.9–4.0)	5.7 ± 6.8 (0.2–27.9)▲	8.6 ± 8.1 (0.2–27.9)✦	2.3 ± 1.6 (0.3–4.8)	2.6 ± 2.4 (0.6–36.2)✦
Diff–Ratio [%]	0.8 ± 0.7 (0–3.0)▲	0.7 ± 0.7 (0–3.0)✦	0.9 ± 0.6 (0.3–1.7)	2.3 ± 2.8 (0.1–12.0)▲	3.5 ± 3.4 (0.1–12.0)✦	0.9 ± 0.7 (0.1–1.9)	1.1 ± 1.0 (0.2–3.2)▲,✦
Asymmetry–Index [%]	11.6 ± 12.5 (0.4–61.0)▲	11.3 ± 13.5 (0.4–61.0)✦	12.7 ± 8.7 (4.4–25.5)	22.8 ± 18.3 (0.9–62.1)▲	29.0 ± 19.2 (0.9–62.1)✦	15.8 ± 15.0 (1.5–51.2)	14.2 ± 10.2 (2.7–26.1)✦
TFS	245.5 ± 21.8 (212.2–290.6)	245.0 ± 21.2 (212.2–281.8)	247.5 ± 26.8 (222.6–290.6)	245.4 ± 15.1 (202.0–269.9)	241.2 ± 12.7 (229.4–265.4)	250.1 ± 13.3 (229.7–269.9)	244.3 ± 9.5 (232.7–261.6)
Cochlea							
cELS mean [mm^3]	2.4 ± 1.0 (0.8–4.5)	2.4 ± 1.0 (0.8–4.5)✦	2.2 ± 0.6 (1.7–3.0)	2.7 ± 2.1 (0.1–7.9)	3.5 ± 2.4 (0.6–7.9)✦	1.7 ± 1.1 (0.1–3.8)	1.6 ± 1.7 (0.1–4.0)✦
Ipsilateral	2.4 ± 1.2 (0.5–5.2)	2.5 ± 1.3 (0.5–5.2)✦	2.0 ± 0.6 (1.5–3.1)	3.4 ± 3.4 (0.1–12.2)	4.8 ± 4.0 (0.2–12.2)✦	1.8 ± 1.3 (0.1–4.3)	1.9 ± 1.9 (0.2–6.2)✦
Contralateral	2.4 ± 1.1 (0.1–4.5)	2.4 ± 1.1 (0.1–4.5)	2.4 ± 1.1 (1.6–4.1)	2.0 ± 1.2 (0.03–5.5)	2.3 ± 1.1 (0.7–5.5)	1.5 ± 1.1 (0.03–4.0)	1.4 ± 0.9 (0–2.4)
cELS/cTFS–Ratio [%]	3.2 ± 1.2 (1.1–6.1)	3.2 ± 1.3 (1.1–6.1)✦	2.9 ± 0.8 (2.1–3.8)	3.5 ± 2.6 (0.1–10.2)	4.7 ± 2.9 (0.9–10.2)✦	2.2 ± 1.4 (0.1–4.9)	2.2 ± 1.5 (0.1–4.9)✦
Ipsilateral	3.1 ± 1.5 (0.8–7.1)	3.3 ± 1.7 (0.8–7.1)✦	2.6 ± 0.8 (1.9–3.8)	4.4 ± 4.2 (0.1–15.5)	6.2 ± 5.0 (0.3–15.5)✦	2.4 ± 1.6 (0.1–5.1)	2.6 ± 2.3 (0.2–7.5)✦
Contralateral	3.2 ± 1.5 (0.1–18.2)	3.2 ± 1.5 (0.1–6.3)	3.1 ± 1.6 (1.9–5.7)	2.6 ± 1.5 (0.04–7.1)	3.1 ± 1.4 (1.1–7.1)	2.0 ± 1.5 (0.04–5.1)	1.9 ± 1.2 (0–3.4)
cDiff [mm^3]	0.9 ± 0.9 (0.3–2.8)	0.9 ± 0.8 (0–2.8)✦	0.7 ± 1.1 (0.1–2.6)	1.8 ± 2.6 (0–10.2)	2.8 ± 3.2 (0.1–10.2)✦	0.6 ± 0.7 (0–2.4)	1.2 ± 1.4 (0.2–4.3)✦
cDiff–Ratio [%]	1.2 ± 1.1 (0–3.9)	1.2 ± 1.1 (0–3.9)✦	1.0 ± 1.5 (0.1–3.6)	2.3 ± 3.4 (0–13.2)	3.7 ± 4.2 (0.1–13.2)✦	0.7 ± 0.8 (0–2.9)	1.6 ± 1.7 (0.2–5.3)✦
cAsymmetry–Index [%]	21.9 ± 21.9 (0–89.3)	23.0 ± 22.6 (0–89.3)	14.3 ± 19.6 (1.0–25.2)	27.5 ± 21.7 (0.6–70.8)	33.0 ± 25.2 (2.1–70.8)	21.2 ± 15.0 (0.6–52.6)	41.1 ± 30.0 (13.1–100.0)
cTFS	75.1 ± 5.3 (67.1–86.9)	74.0 ± 4.4 (67.1–80.4)	79.2 ± 7.2 (70.0–87.0)	74.8 ± 5.7 (62.2–84.2)	73.5 ± 6.2 (62.2–83.6)	76.3 ± 5.0 (69.7–84.2)	72.6 ± 5.7 (65.2–81.0)
Vestibulum							
vELS mean [mm^3]	7.8 ± 4.0 (2.2–19.3)	7.9 ± 4.3 (2.2–19.3)	7.3 ± 2.4 (4.9–10.6)	8.2 ± 3.6 (2.4–17.4)	9.2 ± 3.8 (2.4–17.4)	7.0 ± 3.1 (2.6–12.6)	7.9 ± 3.1 (2.6–11.5)
Ipsilateral	7.8 ± 4.1 (2.3–20.3)	7.9 ± 4.5 (2.3–20.3)✦	7.6 ± 2.3 (4.4–9.9)	9.8 ± 5.3 (2.5–24.2)	12.0 ± 6.0 (2.5–24.2)✦	7.2 ± 2.9 (3.9–12.6)	7.3 ± 3.7 (2.1–13.0)✦
Contralateral	7.7 ± 4.1 (1.4–18.2)	7.8 ± 4.4 (1.4–18.2)	7.1 ± 2.8 (3.6–11.2)	8.5 ± 3.6 (1.9–16.9)	6.3 ± 3.2 (2.4–12.3)	6.8 ± 3.7 (1.3–14.3)	8.4 ± 2.7 (3.2–11.8)
vELS/vTFS–Ratio [%]	4.5 ± 2.0 (1.4–10.0)	4.5 ± 2.2 (1.4–10.0)	4.3 ±1.2 (3.1–6.1)	4.8 ± 2.1 (1.5–9.7)	5.4 ± 2.2 (1.5–9.7)	4.0 ± 1.7 (1.7–7.2)	4.6 ± 1.8 (1.5–7.0)
Ipsilateral	4.6 ± 2.1 (1.6–10.8)	4.6 ± 2.4 (1.6–10.8)✦	4.6 ± 1.2 (2.9–5.7)	5.7 ± 3.1 (1.6–14.8)	7.0 ± 3.4 (1.6–14.8)✦	4.2 ± 1.6 (2.5–7.3)	4.3 ± 2.3 (1.3–8.2)✦
Contralateral	4.4 ± 2.1 (0.9–9.2)	4.5 ± 2.3 (0.9–9.2)	4.2 ± 1.5 (2.4–6.5)	3.5 ± 1.4 (0.8–6.7)	3.8 ± 1.9 (1.4–7.1)	3.9 ± 2.1 (0.8–8.1)	4.9 ± 1.6 (1.8–7.0)
vDiff [mm^3]	1.7 ± 1.2 (0.3–5.5)▲	1.7 ± 1.3 (0.3–5.5)✦	1.6 ± 0.5 (1.1–2.5)	4.4 ± 4.3 (0–17.8)▲	6.3 ± 5.1 (0.1–17.8)✦	2.3 ± 1.6 (0–5.7)	1.9 ± 1.7 (0.2–4.1)✦
vDiff–Ratio [%]	1.0 ± 0.8 (0.2–3.6)▲	1.0 ± 0.8 (0.2–3.6)✦	1.0 ± 0.4 (0.5–1.6)	2.6 ± 2.6 (0–11.4)▲	3.7 ± 3.1 (0–11.4)✦	1.3 ± 0.9 (0–3.2)	1.1 ± 1.0 (0.1–2.5)✦
vAsymmetry–Index [%]	13.0 ± 11.5 (2.6–53.3)▲	13.1 ± 12.4 (2.6–53.3)✦	12.5 ± 7.9 (0.9–4.0)	25.0 ± 19.3 (0–59.8)▲	31.1 ± 20.8 (1.2–59.8)✦	17.9 ± 15.1 (0–50.6)	14.2 ± 12.4 (0.9–36.2)✦
vTFS	170.4 ± 3.9 (212.2–290.6)	171.0 ± 18.2 (145.2–203.3)	168.3 ± 21.4 (152.7–203.6)	170.6 ± 11.0 (139.8–186.2)	167.8 ± 10.7 (139.8–183.8)	173.8 ± 10.8 (152.7–186.2)	171.7 ± 8.3 (161.3–185.3)

▲ *ANOVA Bonferroni-corrected for multiple comparisons for VM (all) vs. MD (all) vs. VM-MD (all), where $p < 0.05$.*

✦ *ANOVA Bonferroni-corrected for multiple comparisons for VM (definite) vs. MD (definite) vs. VM-MD (all), where $p < 0.05$, or ✦✦ if $p < 0.005$.*

✧ *ANOVA Bonferroni-corrected for multiple comparisons for VM (probable) vs. MD (probable) vs. VM-MD (all) showed no significant differences.*

$r_S = 0.5, p < 0.05$, two-sided). Here, age (ELS mean: $r_S = 0.6$, ELS ipsilateral: $r_S = 0.6$, ELS/TFS ipsilateral: $r_S = 0.7$, ELS/TFS: $r_S = 0.7$, vELS mean: $r_S = 0.7$, vELS ipsilateral: $r_S = 0.6$, vELS/vTFS: $r_S = 0.7$, vAI: $r_S = 0.5$, cDiff: $r_S = 0.5$, cDiff/cTFS-Ratio: $r_S = 0.5$, $p < 0.05$, two-sided) and age when dizziness started (ELS/TFS: $r_S = 0.5$, AI: $r_S = 0.7$, Diff: $r_S = 0.6$, Diff/TFS-Ratio: $r_S = 0.5$, vELS/vTFS: $r_S = 0.5$, vELS/vTFS ipsilateral: $r_S = 0.5$, vAI: $r_S = 0.6$, $p < 0.05$, two-sided) correlated with quantitative ELS measurements. ELS parameters of the cochlea correlated with mean PTA threshold (cELS/cTFS-Ratio, $r_S = 0.6, p < 0.05$, two-sided). In definite VM, ELS parameters also correlated to the mean value of VOG during caloric irrigation (cAI: $r_S = 0.6$, cDiff: $r_S = 0.6, p < 0.05$ two-sided) and mean HIT (vAI: $r_S = 0.6$, vDiff: $r_S = 0.6$, vDiff/vTFS: $r_S = 0.6, p < 0.05$, two-sided).

In VM-MD, cochlear volumetric symmetry proxies (cDiff; cDiff/cTFS) mostly correlated with visual grading asymmetry-indices (AI: $r_S = 0.5$, cAI: $r_S = 0.5$, $p < 0.05$, two-sided) and grades (cochlea: $p < 0.05$; inner ear: $p < 0.05$). Cochlear AI correlated with PTA variables (mean: $r_S = 0.7$, ipsilateral: $r_S = 0.8$, when initial PTA > 25 dB: $r_S = 0.9$, $p < 0.05$, two-sided). Furthermore, ELS quantification parameters correlated with ipsilateral HIT gain (AI: $r_S = 0.8, p < 0.05$, two-sided).

Figure 3 shows each a typical VM, MD, and VM-MD case, including their imaging (**Figure 3**) results. Neurophysiological results (PTA, vHIT waveforms, cVOG data, o/cVEMP waveforms) of all three cases are shown in the **Supplementary Material**.

DISCUSSION

The current study focused on EH characteristics (extent and location) and its relationship with neurophysiological results in patients with VM and MD and patients who fulfilled the diagnostic criteria for both diseases (VM-MD). EH was quantified visually following the classification of Nakashima et al. (21) and using volumetric local thresholding (VOLT) assessment implemented for HYDROPS-Mi2 images. As a result, EH was only present in a small proportion of VM patients (both with auditory symptoms) but frequently found in MD patients (**Tables 1**, **2**). Location and laterality of EH and neurophysiological testing classifications were positively associated (**Table 3**). In MD, visual semi-quantitative grading and volumetric quantification correlated highly to each other, as well as side differences in VOG during caloric irrigation and low tone hearing loss patterns in PTA. In VM, correlations were less pronounced and were also found between cochlear volumetric quantification parameters and PTA. VM-MD assumed an intermediate position between VM and MD.

To begin, the findings support some overlap of MD and VM (1, 31) based on the current diagnostic criteria. Hence, EH could be considered as inner ear damage due to different etiologies. The current diagnostic criteria recommend that whenever patients fulfill the criteria for both VM and MD – especially hearing loss documented by audiometry – MD should be diagnosed, even if migraine symptoms occur during the vestibular and auditory attacks (1). In contrast, the data show that EH's morphological evidence was present in patients with auditory symptoms regardless of whether they meet MD or VM criteria. VM patients who were mostly free from auditory symptoms did not show any morphological evidence of EH. Thus, a future revision of the official classification might consider patients with overlapping audio-vestibular dysfunction as a VM-MD overlap syndrome. EH's current anatomical evidence suggests a joint dysfunction of the inner ear rather than differential physiological mechanisms between the two disorders (3, 32). Unlike previous studies (33–37), no significant o/cVEMP differences were found between VM, MD, and VM-MD.

Evidence continues to emerge, suggesting common contributing factors in both diseases, VM and MD, such as inner ear vasospasm or vasculopathy, neuropeptide derangements, hormonal interactions, calcium channelopathies, or disturbance of salt metabolism (38–40). During a VM episode, a subpopulation of serotonergic and non-serotonergic dorsal raphe nucleus cells may comodulate the processing in the vestibular nuclei and the central amygdaloid nucleus, which also activates the central vestibular processing pathway and contributes to VM (41). It was shown that the trigeminal nerve could play an essential role in the development of VM attacks because it provides a dense sensory innervation of cerebral, basilar and meningeal blood vessels and thus of the inner ear arteries via the anterior inferior cerebellar artery (AICA). Indeed, it has been shown that the cochlea and the vestibular labyrinth receive trigeminal innervation via the ophthalmic branch that provides parasympathetic innervation to the basilar artery and the AICA (42). Activation of perivascular trigeminal nerve endings causes the release of substance P and calcitonin gene-related peptide (CGRP), leading to local neuroinflammation, permeability changes, vasodilatation, and edema (43, 44). Thus, the trigeminal nerve directly affects neuroinflammation and blood flow of the inner ear, supporting the notion that neurovascular effects of migraine can affect inner ear structures (42, 45–47) and explain symptoms and EH.

Moreover, chronically fluctuating hydropic inner ears are less able to auto-regulate their vasculature against the changes induced by acute migraine attacks and may ultimately manifest as persisting EH (47–50). Accordingly, cases have been reported with migraine-associated vascular changes that caused inner ear ischemia and EH, resulting in sensorineural hearing loss and MD-like symptoms (51) or migraine-associated hearing loss with a severe bilateral EH without vertigo (52). Spreading cortical depression or spreading brainstem depression (53) are theorized to cause migraine aura (in this case, vertigo, dizziness, and auditory dysfunction) and symptoms that ultimately result also in substance P release from the trigeminal ganglion, leading to vasodilation, increased vascular permeability, and extravasation of plasma and neurogenic inflammation (54–56).

Although MD and VM's pathophysiological relationship is so far unclear (22), some researchers believe that the two disorders may represent a continuum syndrome rather than existing as separate conditions. VM could be caused primarily by an abnormality of the central and peripheral

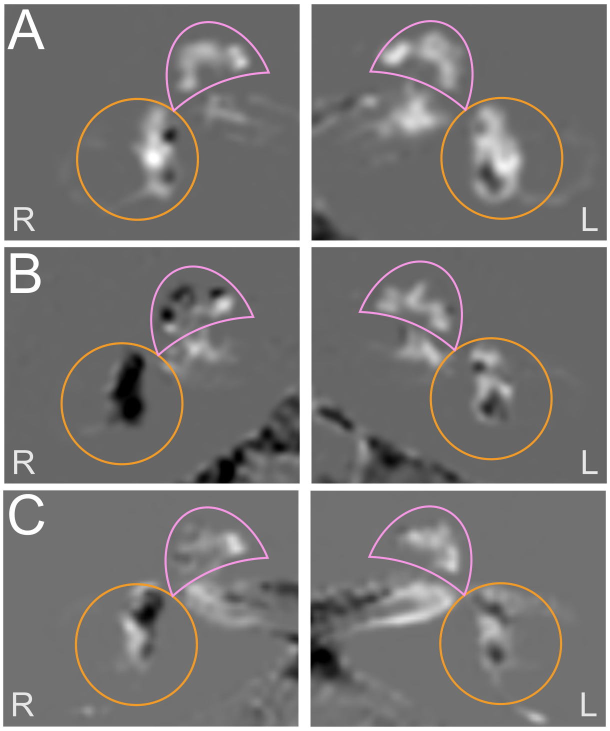

FIGURE 3 | Exemplary cases studies in each a VM, MD, and VM-MD patient. Each row depicts the left (L) and right I side of an exemplary HYDROPS-Mi2 single case image of each a VM **(A)**, MD **(B)**, and VM-MD **(C)** patient. In these images, the endolymphatic space (ELS) presents dark and the Gadolinium-enhanced perilymphatic space (PLS) as well as the bony labyrinth bright white. The cochlea is highlighted with a pink semicircle and the vestibulum with an orange circle. The neurophysiological results (PTA, vHIT waveforms, cVOG data, o/cVEMP waveforms) of all three cases are shown in the **Supplementary Figures 1**–**3**. The upper row depicts an exemplary VM single case **(A)**. The 53-year-old female was diagnosed with definite VM and reported migrainous headache with phono- and photophobia, nausea, vomiting, no ear symptoms, and no deficits in the neurotological testing results (PTA, bithermal caloric test, vHIT) (**Supplementary Figure 1**). The HYDROPS-Mi2 images of the left (L) and right side (R) show no endolymphatic hydrops (EH) on both sides following the classification of Nakashima et al. (21). The middle row shows an exemplary MD single case **(B)**. The 69-year-old male patient with definite MD exhibited profound hearing loss and aural fullness on the right ear during an attack and significant ipsilateral auditory (right-sided initial PTA of 36 dB with low tone hearing loss pattern) and ipsilateral vestibular dysfunction (>30% side difference in the caloric test; normal vHIT gain; oVEMP not reproducible on the right, cVEMP asymmetry ratio of 10% disadvantage of the right) immediately after an attack (**Supplementary Figure 2**). The HYDROPS-Mi2 images of the right inner ear show severe EH (grade 2) in both the cochlea and the vestibulum. There is no EH (grade 0) in the left inner ear. The lower row shows an exemplary VM-MD single case I. The 72-year old female patient with a constellation of clinical symptoms and diagnostic findings fit both definite VM and MD (VM-MD). During an attack, she described migrainous headache with phono- and photophobia, nausea, as well as bilateral ear symptoms (aural fullness, tinnitus). Neurophysiological testing revealed a right-sided auditory (PTA of 90 dB with low tone hearing loss pattern) and no pathological side difference in the caloric test, vHIT, or o/cVEMPs (**Supplementary Figure 3**). The HYDROPS-Mi2 images of the right inner ear show a mild EH (grade 1) in the cochlea and the vestibulum and no EH (grade 0) in the left inner ear.

vestibular pathways, whereas MD could mainly be associated with peripheral membranous labyrinthine dysfunction. The auditory symptoms in VM patients may be related to vasospasm- and hypoperfusion-induced ischemia of labyrinthine structures or serotonergic-induced extravasation (57). Histopathology has provided evidence that not every individual with EH presents with MD symptoms (58, 59), and not every individual with the clinical diagnosis of MD has EH (60), which is also the case in the current data. Earlier studies found EH in 60–90% of MD patients and EH's presence in asymptomatic contralateral sides in 65% of MD patients (61). Thus, there seems to be no match between the occurrence of EH and normal neurophysiological values. This could point to MD being a systemic disease, which has been argued before and should be further elucidated. The development of inner ear imaging allows EH to be demonstrated in a human *in vivo* and provides the basis for quantifying the endolymphatic space and its dilatation within a single imaging sequence (21, 61). Since it has been shown that EH can differently affect cochlear and vestibular compartments of the inner ear in patients with VM (62, 63), EH imaging has been used in the differential diagnosis of patients with suspected MD or VM (64). The finding that VM patients are only associated with EH when showing auditory symptoms suggests an MD-like pathology.

As a consequence, EH seems to point toward an inner ear pathology due to different etiologies. Fittingly, EH extent correlated with auditory and vestibular testing. However, EH was also observed in asymptomatic individuals (61) and post-mortem in individuals' temporal bone without ear diseases (65). Besides, the complaints reported by patients with VM and MD overlapped frequently. Therefore, some authors suggest that future diagnostic criteria should be based on pathophysiology and not only on symptoms (66).

Methodical Limitations

There are methodical limitations in the current study that need to be considered in the interpretation of the data. Although this study has a relatively high number of subjects per pathology, a significantly higher number of participants would likely show more robust results, especially given the division into definite and probable patient groups or the small group of diagnostic overlaps (VM-MD). Second, the persistence of EH is yet under discussion. There is evidence that it may fluctuate depending on the attack (VM) or become more likely depending on the disease's duration (MD). Accordingly, the present results should be treated with caution. Third, the statistical analysis suffers from a parallel evaluation of the categorical and scalar values. It would be desirable to develop a statistical model for both types of information. Fourth, the lack of selectivity of the classifications criticized in the study could also affect the statements made here. A study to examine the discriminatory power of symptoms and diagnostic results between VM and MD diagnoses would be crucial for future claims.

CONCLUSION

The current study on MRI imaging of EH has shown that (1) a cochlear and vestibular hydrops can occur in MD and VM patients with auditory symptoms; this suggests inner ear damage irrespective of MD diagnosis or VM. (2) The EH grades often correlated with auditory symptoms such as hearing impairment and tinnitus. (3) Further research is required to uncover whether migraine is one causative factor of inner ear pathology that leads to a common final pathway of EH or whether EH in VM patients with auditory symptoms suggests an additional pathology due to MD.

DATA AVAILABILITY STATEMENT

The original contributions presented in the study are included in the article/**Supplementary Material**, further inquiries can be directed to the corresponding author/s.

ETHICS STATEMENT

The studies involving human participants were reviewed and approved by Institutional Review Board at Jeonbuk National University Hospital. The patients/participants provided their written informed consent to participate in this study.

AUTHOR CONTRIBUTIONS

S-YO, VK, and MD designed and directed the project. BL and J-JK collected the data and wrote the manuscript with support from S-YO and N-RL. S-BH, RB, and JG verified the analytical methods and analyzed the image data. All authors contributed to the article and approved the submitted version.

FUNDING

This work was supported by the National Research Foundation of Korea (NRF) grant funded by the Korean government (Ministry of Science and ICT) (No. 2019R1A2C1004796) and the Fund of Biomedical Research Institute, Jeonbuk National University Hospital.

SUPPLEMENTARY MATERIAL

The Supplementary Material for this article can be found online at: https://www.frontiersin.org/articles/10.3389/fneur.2021.594481/full#supplementary-material

The following figures show the neurophysiological results of the exemplary case studies in each patient with vestibular migraine (VM, **Supplementary Figure 1**), Meniére's disease (MD, **Supplementary Figure 2**), or with both disease characteristics (VM-MD, **Supplementary Figure 3**). The results consist of pure tone audiograms (PTA, **A**), video-oculography with response waveforms after caloric irrigation. **(B)** Head impulse test waveforms **(C)**, cervical and ocular vestibular evoked myogenic potentials (c/oVEMP, **D**, **E**) for the left (L) and right (R) side, respectively. "L/R" in **(D)** (cVEMP) means the response of the left/right sternocleidomastoid muscle (SCM) during the stimulation on the ipsilateral left/right ear. "L/R" in **(E)** (oVEMP) means the left/right stimulating ear with recordings on the contralateral extraocular muscles.

Supplementary Figure 1 | Neurophysiological results for the exemplary VM case. The 53-year-old female was diagnosed with definite VM and reported migrainous headache with phono- and photophobia, nausea, vomiting, no ear symptoms. Fittingly the neurotological testing results show no deficits (PTA, bithermal caloric response, vHIT, c/oVEMPs).

Supplementary Figure 2 | Neurophysiological results for the exemplary MD case. The 69-year-old male patient with definite MD exhibited profound hearing loss and aural fullness on the right ear during an attack and significant ipsilateral auditory (right-sided initial PTA of 36 dB with low tone hearing loss pattern) and ipsilateral vestibular dysfunction with >30% side difference in the caloric test. He showed normal vHIT gain and normal cVEMP but increased oVEMP asymmetry ratio of 57% due to increased ipsilateral oVEMP amplitude immediately after an attack.

Supplementary Figure 3 | Neurophysiological results for the exemplary VM-MD case. The 72-year old female patient with a constellation of clinical symptoms and diagnostic findings that fit both definite VM and MD (VM-MD). During an attack, she described migrainous headache with phono- and photophobia, nausea, as well as bilateral ear symptoms (aural fullness, tinnitus). Neurophysiological testing revealed a right-sided auditory (PTA of 90 dB with low tone hearing loss pattern) and no pathological side difference in the caloric test, vHIT, or o/cVEMPs.

REFERENCES

1. Lempert T, Olesen J, Furman J, Waterston J, Seemungal B, Carey J, et al. Vestibular migraine: diagnostic criteria. *J Vestib Res.* (2012) 22:167–72. doi: 10.3233/VES-2012-0453
2. Lopez-Escamez JA, Carey J, Chung W-H, Goebel JA, Magnusson M, Mandalà M, et al. Diagnostic criteria for Menière's disease. *J Vestib Res.* (2015) 25:1–7. doi: 10.3233/VES-150549
3. Neff BA, Staab JP, Eggers SD, Carlson ML, Schmitt WR, Abel KMV, et al. Auditory and vestibular symptoms and chronic subjective dizziness in patients with Ménière's disease, vestibular migraine, and Ménière's disease with concomitant vestibular migraine. *Otol Neurotol.* (2012) 33:1235–44. doi: 10.1097/MAO.0b013e31825d644a
4. Chu C-H, Liu C-J, Fuh J-L, Shiao A-S, Chen T-J, Wang S-J. Migraine is a risk factor for sudden sensorineural hearing loss: a nationwide population-based study. *Cephalalgia.* (2013) 33:80–6. doi: 10.1177/0333102412468671
5. Rassekh CH, Harker LA. The prevalence of migraine in Meniere's disease. *The Laryngoscope.* (1992) 102:135–8. doi: 10.1288/00005537-199202000-00006
6. Radtke A, Lempert T, Gresty MA, Brookes GB, Bronstein AM, Neuhauser H. Migraine and Ménière's disease: is there a link? *Neurology.* (2002) 59:1700–4. doi: 10.1212/01.wnl.0000036903.22461.39
7. Liu YF, Xu H. The intimate relationship between vestibular migraine and meniere disease: a review of pathogenesis and presentation. *Behav Neurol.* (2016) 2016:3182735. doi: 10.1155/2016/3182735
8. Hallpike CS, Cairns H. Observations on the pathology of Ménière's syndrome: (section of otology). *Proc R Soc Med.* (1938) 31:1317–36.
9. Lawrence M, Mccabe BF. Inner-ear mechanics and deafness. Special consideration of Meniere's syndrome. *J Am Med Assoc.* (1959) 171:1927–32. doi: 10.1001/jama.1959.03010320017005
10. Gates P. Hypothesis: could Meniere's disease be a channelopathy? *Internal Med J.* (2005) 35:488–9. doi: 10.1111/j.1445-5994.2005.00891.x
11. Greco A, Gallo A, Fusconi M, Marinelli C, Macri GF, de Vincentiis M. Meniere's disease might be an autoimmune condition? *Autoimmun Rev.* (2012) 11:731–8. doi: 10.1016/j.autrev.2012.01.004
12. Kirsch V, Becker-Bense S, Berman A, Kierig E, Ertl-Wagner B, Dieterich M. Transient endolymphatic hydrops after an attack of vestibular migraine: a longitudinal single case study. *J Neurol.* (2018) 265:51–3. doi: 10.1007/s00415-018-8870-3

13. Matsumoto M, Nishimura T. Mersenne twister: a 623-dimensionally equidistributed uniform pseudorandom number generator. *ACM Trans Model Comput Simul.* (1998) 8:3–30. doi: 10.1145/272991.272995
14. Oh S-Y, Kim D-H, Yang T-H, Shin B-S, Jeong S-K. Clinical classification and neuro-vestibular evaluation in chronic dizziness. *Clin Neurophysiol.* (2015) 126:180–6. doi: 10.1016/j.clinph.2014.03.030
15. Jongkees LB, Maas JP, Philipszoon AJ. Clinical nystagmography. A detailed study of electro-nystagmography in 341 patients with vertigo. *Pract Otorhinolaryngol.* (1962) 24:65–93.
16. Horubia V. Quantitative vestibular function tests and the clinical examination. In: Herdman SJ, editor. *Vestibular Rehabilitation.* Philadelphia, PA: Davis (2020). p. 113–64.
17. Oh S-Y, Kim J-S, Yang T-H, Shin B-S, Jeong S-K. Cervical and ocular vestibular-evoked myogenic potentials in vestibular neuritis: comparison between air- and bone-conducted stimulation. *J Neurol.* (2013) 260:2102–9. doi: 10.1007/s00415-013-6953-8
18. Shin B-S, Oh S-Y, Kim JS, Kim T-W, Seo M-W, Lee H, et al. Cervical and ocular vestibular-evoked myogenic potentials in acute vestibular neuritis. *Clin Neurophysiol.* (2012) 123:369–75. doi: 10.1016/j.clinph.2011.05.029
19. Todd NPM, Rosengren SM, Aw ST, Colebatch JG. Ocular vestibular evoked myogenic potentials (OVEMPs) produced by air- and bone-conducted sound. *Clin Neurophysiol.* (2007) 118:381–90. doi: 10.1016/j.clinph.2006.09.025
20. Naganawa S, Kawai H, Taoka T, Sone M. Improved HYDROPS: imaging of endolymphatic hydrops after intravenous administration of gadolinium. *Magn Reson Med Sci.* (2017) 16:357–61. doi: 10.2463/mrms.tn.2016-0126
21. Nakashima T, Naganawa S, Pyykko I, Gibson WPR, Sone M, Nakata S, et al. Grading of endolymphatic hydrops using magnetic resonance imaging. *Acta Otolaryngol Suppl.* (2009) 560:5–8. doi: 10.1080/00016480902729827
22. Kirsch V, Nejatbakhshesfahani F, Ahmadi S-A, Dieterich M, Ertl-Wagner B. A probabilistic atlas of the human inner ear's bony labyrinth enables reliable atlas-based segmentation of the total fluid space. *J Neurol.* (2019) 266:52–61. doi: 10.1007/s00415-019-09488-6
23. Gerb J, Ahmadi SA, Kierig E, Ertl-Wagner B, Dieterich M, Kirsch V. VOLT: a novel open-source pipeline for automatic segmentation of endolymphatic space in inner ear MRI. *J Neurol.* (2020) 267:185–96. doi: 10.1007/s00415-020-10062-8
24. Fedorov A, Beichel R, Kalpathy-Cramer J, Finet J, Fillion-Robin JC, Pujol S, et al. 3D Slicer as an image computing platform for the quantitative imaging network. *Magn Reson Imag.* (2012) 30:1323–41. doi: 10.1016/j.mri.2012.05.001
25. Schindelin J, Arganda-Carreras I, Frise E, Kaynig V, Longair M, Pietzsch T, et al. Fiji: an open-source platform for biological-image analysis. *Nat Methods.* (2012) 9:676–82. doi: 10.1038/nmeth.2019
26. Legland D, Arganda-Carreras I, Andrey P. MorphoLibJ: integrated library and plugins for mathematical morphology with ImageJ. *Bioinformatics.* (2016) 32:3532–4. doi: 10.1093/bioinformatics/btw413
27. Schneider CA, Rasband WS, Eliceiri KW. NIH Image to ImageJ: 25 years of image analysis. *Nat Methods.* (2012) 9:671–5. doi: 10.1038/nmeth.2089
28. Meijering EH, Niessen WJ, Viergever MA. Quantitative evaluation of convolution-based methods for medical image interpolation. *Med Image Anal.* (2001) 5:111–26. doi: 10.1016/s1361-8415(00)00040-2
29. Johnson HJ, Harris G, Williams K. BRAINSFit: mutual information registrations of whole-brain 3D images, using the insight toolkit. *Insight J.* (2007) 1:1–10. Available online at:https://www.researchgate.net/publication/222899257_BRAINSFIT_Mutual_information_registrations_of_whole-brain_3D_Images_using_the_insight_toolkit
30. Niblack W. *An Introduction to Digital Image Processing*. First *English Edition*. Englewood Cliffs, NJ: Prentice Hall (1986).
31. Lopez-Escamez JA, Carey J, Chung W-H, Goebel JA, Magnusson M, Mandalà M, et al. [Diagnostic criteria for Menière's disease according to the classification committee of the Bárány Society]. *HNO.* (2017) 65:887–93. doi: 10.1007/s00106-017-0387-z
32. Murofushi T, Tsubota M, Kitao K, Yoshimura E. Simultaneous presentation of definite vestibular migraine and definite Ménière's disease: overlapping syndrome of two diseases. *Front Neurol.* (2018) 9:749. doi: 10.3389/fneur.2018.00749
33. Dlugaiczyk J, Habs M, Dieterich M. Vestibular evoked myogenic potentials in vestibular migraine and Menière's disease: cVEMPs make the difference. *J Neurol.* (2020) 267:169–80. doi: 10.1007/s00415-020-09902-4
34. Baier B, Dieterich M. Vestibular-evoked myogenic potentials in "vestibular migraine" and Menière's disease: a sign of an electrophysiological link? *Ann N Y Acad Sci.* (2009) 1164:324–7. doi: 10.1111/j.1749-6632.2009.03868.x
35. Rizk HG, Liu YF, Strange CC, Van Ausdal CH, English RC, McRackan TR, et al. Predictive value of vestibular evoked myogenic potentials in the diagnosis of Menière's disease and vestibular migraine. *Otol Neurotol.* (2020) 41:828–35. doi: 10.1097/MAO.0000000000002636
36. Salviz M, Yuce T, Acar H, Taylan I, Yuceant GA, Karatas A. Diagnostic value of vestibular-evoked myogenic potentials in Ménière's disease and vestibular migraine. *J Vestib Res.* (2016) 25:261–6. doi: 10.3233/VES-160567
37. Zuniga MG, Janky KL, Schubert MC, Carey JP. Can vestibular-evoked myogenic potentials help differentiate Ménière disease from vestibular migraine? *Otolaryngol Head Neck Surg.* (2012) 146:788–96. doi: 10.1177/0194599811434073
38. Charles A. The pathophysiology of migraine: implications for clinical management. *Lancet Neurol.* (2018) 17:174–82. doi: 10.1016/S1474-4422(17)30435-0
39. Baloh RW. Neurotology of migraine. *Headache.* (1997) 37:615–21. doi: 10.1046/j.1526-4610.1997.3710615.x
40. Campbell DA, Hay KM, Tonks EM. An investigation of the salt and water balance in migraine. *Br Med J.* (1951) 2:1424–9. doi: 10.1136/bmj.2.4745.1424
41. Halberstadt AL, Balaban CD. Serotonergic and nonserotonergic neurons in the dorsal raphe nucleus send collateralized projections to both the vestibular nuclei and the central amygdaloid nucleus. *Neuroscience.* (2006) 140:1067–77. doi: 10.1016/j.neuroscience.2006.02.053
42. Vass Z, Shore SE, Nuttall AL, Miller JM. Direct evidence of trigeminal innervation of the cochlear blood vessels. *Neuroscience.* (1998) 84:559–67. doi: 10.1016/s0306-4522(97)00503-4
43. Moskowitz MA. Neurogenic inflammation in the pathophysiology and treatment of migraine. *Neurology.* (1993) 43:S16–20.
44. Prins M, van der Werf F, Baljet B, Otto JA. Calcitonin gene-related peptide and substance P immunoreactivity in the monkey trigeminal ganglion, an electron microscopic study. *Brain Res.* (1993) 629:315–8. doi: 10.1016/0006-8993(93)91337-r
45. Vass Z, Shore SE, Nuttall AL, Jancsó G, Brechtelsbauer PB, Miller JM. Trigeminal ganglion innervation of the cochlea–a retrograde transport study. *Neuroscience.* (1997) 79:605–15. doi: 10.1016/s0306-4522(96)00641-0
46. Vass Z, Steyger PS, Hordichok AJ, Trune DR, Jancsó G, Nuttall AL. Capsaicin stimulation of the cochlea and electric stimulation of the trigeminal ganglion mediate vascular permeability in cochlear and vertebro-basilar arteries: a potential cause of inner ear dysfunction in headache. *Neuroscience.* (2001) 103:189–201. doi: 10.1016/s0306-4522(00)00521-2
47. Vass Z, Dai CF, Steyger PS, Jancsó G, Trune DR, Nuttall AL. Co-localization of the vanilloid capsaicin receptor and substance P in sensory nerve fibers innervating cochlear and vertebro-basilar arteries. *Neuroscience.* (2004) 124:919–27. doi: 10.1016/j.neuroscience.2003.12.030
48. Sarna B, Abouzari M, Lin HW, Djalilian HR. A hypothetical proposal for association between migraine and Meniere's disease. *Med Hypotheses.* (2020) 134:109430. doi: 10.1016/j.mehy.2019.109430
49. Brechtelsbauer PB, Ren TY, Miller JM, Nuttall AL. Autoregulation of cochlear blood flow in the hydropic guinea pig. *Hear Res.* (1995) 89:130–6. doi: 10.1016/0378-5955(95)00130-4
50. Miller JM, Ren TY, Nuttall AL. Studies of inner ear blood flow in animals and human beings. *Otolaryngol Head Neck Surg.* (1995) 112:101–13. doi: 10.1016/S0194-59989570308-X
51. Lee H, Lopez I, Ishiyama A, Baloh RW. Can migraine damage the inner ear? *Arch Neurol.* (2000) 57:1631–4. doi: 10.1001/archneur.57.11.1631
52. Liu IY, Ishiyama A, Sepahdari AR, Johnson K, Ishiyama G. Bilateral endolymphatic hydrops in a patient with migraine variant without vertigo: a case report. *Headache.* (2017) 57:455–9. doi: 10.1111/head.12976
53. Richter F, Bauer R, Lehmenkühler A, Schaible H-G. Spreading depression in the brainstem of the adult rat: electrophysiological parameters and influences on regional brainstem blood flow. *J Cereb Blood Flow Metab.* (2008) 28:984–94. doi: 10.1038/sj.jcbfm.9600594

54. Malhotra R. Understanding migraine: potential role of neurogenic inflammation. *Ann Indian Acad Neurol.* (2016) 19:175–82. doi: 10.4103/0972-2327.182302
55. Harriott AM, Takizawa T, Chung DY, Chen S-P. Spreading depression as a preclinical model of migraine. *J Headache Pain.* (2019) 20:45. doi: 10.1186/s10194-019-1001-4
56. Brain SD, Grant AD. Vascular actions of calcitonin gene-related peptide and adrenomedullin. *Physiol Rev.* (2004) 84:903–934. doi: 10.1152/physrev.00037.2003
57. Espinosa-Sanchez JM, Lopez-Escamez JA. New insights into pathophysiology of vestibular migraine. *Front Neurol.* (2015) 6:12. doi: 10.3389/fneur.2015.00012
58. Rauch SD, Merchant SN, Thedinger BA. Meniere's syndrome and endolymphatic hydrops. Double-blind temporal bone study. *Ann Otol Rhinol Laryngol.* (1989) 98:873–83. doi: 10.1177/000348948909801108
59. Belal A, Antunez JC. Pathology of endolymphatic hydrops. *J Laryngol Otol.* (1980) 94:1231–40. doi: 10.1017/s0022215100090058
60. Belal A, Ylikoski J. Pathologic significance of Meniere's symptom complex. A histopathologic and electron microscopic study. *Am J Otolaryngol.* (1980) 1:275–84. doi: 10.1016/s0196-0709(80)80030-5
61. Pyykkö I, Nakashima T, Yoshida T, Zou J, Naganawa S. Meniere's disease: a reappraisal supported by a variable latency of symptoms and the MRI visualisation of endolymphatic hydrops. *BMJ Open.* (2013) 3:e001555. doi: 10.1136/bmjopen-2012-001555
62. Gürkov R, Kantner C, Strupp M, Flatz W, Krause E, Ertl-Wagner B. Endolymphatic hydrops in patients with vestibular migraine and auditory symptoms. *Eur Arch Otorhinolaryngol.* (2014) 271:2661–7. doi: 10.1007/s00405-013-2751-2
63. Viirre ES, Baloh RW. Migraine as a cause of sudden hearing loss. *Headache.* (1996) 36:24–8. doi: 10.1046/j.1526-4610.1996.3601024.x
64. Gürkov R. Menière and friends: imaging and classification of hydropic ear disease. *Otol Neurotol.* (2017) 38:e539–44. doi: 10.1097/MAO.0000000000001479
65. Foster CA, Breeze RE. Endolymphatic hydrops in Ménière's disease: cause, consequence, or epiphenomenon? *Otol Neurotol.* (2013) 34:1210–4. doi: 10.1097/MAO.0b013e31829e83df
66. Brantberg K, Trees N, Baloh RW. Migraine-associated vertigo. *Acta Otolaryngol.* (2005) 125:276–9. doi: 10.1080/00016480510003165

Conflict of Interest: The authors declare that the research was conducted in the absence of any commercial or financial relationships that could be construed as a potential conflict of interest.

frontiers in Neurology

ORIGINAL RESEARCH
published: 22 April 2021
doi: 10.3389/fneur.2021.647296

Intravenous Delayed Gadolinium-Enhanced MR Imaging of the Endolymphatic Space: A Methodological Comparative Study

Rainer Boegle [1,2,3], Johannes Gerb [1,2], Emilie Kierig [1,2], Sandra Becker-Bense [1,2], Birgit Ertl-Wagner [4,5], Marianne Dieterich [1,2,3,6] and Valerie Kirsch [1,2,3]*

[1] Department of Neurology, University Hospital, Ludwig-Maximilians-Universität, Munich, Germany, [2] German Center for Vertigo and Balance Disorders-IFB (Integriertes Forschungs- und Behandlungszentrum), University Hospital, Ludwig-Maximilians-Universität, Munich, Germany, [3] Graduate School of Systemic Neuroscience (GSN), Ludwig-Maximilians-Universität, Munich, Germany, [4] Department of Radiology, The Hospital for Sick Children, University of Toronto, Toronto, ON, Canada, [5] Department of Radiology, University Hospital, Ludwig-Maximilians-Universität, Munich, Germany, [6] Munich Cluster for Systems Neurology (SyNergy), Munich, Germany

Edited by:
*Stefan K. Plontke,
Martin Luther University of
Halle-Wittenberg, Germany*

Reviewed by:
*Alexander Gussew,
Universitätsklinikum Halle, Germany
Arne Ernst,
Unfallkrankenhaus Berlin, Germany*

***Correspondence:**
*Valerie Kirsch
valerie.kirsch@med.lmu.de*

Specialty section:
*This article was submitted to
Neuro-Otology,
a section of the journal
Frontiers in Neurology*

Received: *29 December 2020*
Accepted: *24 February 2021*
Published: *22 April 2021*

Citation:
*Boegle R, Gerb J, Kierig E,
Becker-Bense S, Ertl-Wagner B,
Dieterich M and Kirsch V (2021)
Intravenous Delayed
Gadolinium-Enhanced MR Imaging of
the Endolymphatic Space: A
Methodological Comparative Study.
Front. Neurol. 12:647296.
doi: 10.3389/fneur.2021.647296*

In-vivo non-invasive verification of endolymphatic hydrops (ELH) by means of intravenous delayed gadolinium (Gd) enhanced magnetic resonance imaging of the inner ear (iMRI) is rapidly developing into a standard clinical tool to investigate peripheral vestibulo-cochlear syndromes. In this context, methodological comparative studies providing standardization and comparability between labs seem even more important, but so far very few are available. One hundred eight participants [75 patients with Meniere's disease (MD; 55.2 ± 14.9 years) and 33 vestibular healthy controls (HC; 46.4 ± 15.6 years)] were examined. The aim was to understand (i) how variations in acquisition protocols influence endolymphatic space (ELS) MR-signals; (ii) how ELS quantification methods correlate to each other or clinical data; and finally, (iii) how ELS extent influences MR-signals. Diagnostics included neuro-otological assessment, video-oculography during caloric stimulation, head-impulse test, audiometry, and iMRI. Data analysis provided semi-quantitative (SQ) visual grading and automatic algorithmic quantitative segmentation of ELS area [2D, mm^2] and volume [3D, mm^3] using deep learning-based segmentation and volumetric local thresholding. Within the range of 0.1–0.2 mmol/kg Gd dosage and a 4 h ± 30 min time delay, SQ grading and 2D- or 3D-quantifications were independent of signal intensity (SI) and signal-to-noise ratio (SNR; FWE corrected, $p < 0.05$). The ELS quantification methods used were highly reproducible across raters or thresholds and correlated strongly (0.3–0.8). However, 3D-quantifications showed the least variability. Asymmetry indices and normalized ELH proved the most useful for predicting quantitative clinical data. ELH size influenced SI (cochlear basal turn $p < 0.001$), but not SNR. SI could not predict the presence of ELH. In conclusion, (1) Gd dosage of 0.1–0.2 mmol/kg after 4 h ± 30 min time delay suffices for ELS quantification. (2) A consensus is needed on a clinical SQ grading classification including a standardized level of evaluation reconstructed to anatomical fixpoints. (3) 3D-quantification methods of the ELS are best suited for correlations with clinical variables and should include both ears and ELS values reported relative or normalized to size. (4) The presence of ELH increases signal intensity in the basal cochlear turn weakly, but cannot predict the presence of ELH.

Keywords: endolymphatic hydrops, endolymphatic space, inner ear imaging, gadolinium based contrast agent, intravenous, convolutional neural network, deep learning, volumetric local thresholding

INTRODUCTION

In-vivo non-invasive verification of endolymphatic hydrops (ELH) by means of delayed gadolinium (Gd) enhanced magnetic resonance imaging of the inner ear (iMRI) is rapidly developing into a standard clinical tool to investigate episodic vertigo (1–3). This is due to iMRI allowing pre-mortem detection of ELH for the first time (4, 5), demonstrating that ELH is not pathognomonic to Menière's disease (MD) (6–8), but rather a concomitant that can be found in various etiologies of episodic vertigo (9–13). Consequently, the clinical prevalence and pathophysiological significance of ELH has yet to be conclusively clarified. Understanding the underpinnings of the ELH syndrome requires a systematic investigation of pathologies involving endolymphatic space (ELS) changes as well as its base physiological condition.

Data acquisition protocols have undergone a continuous optimization of MR sequences (14, 15), as well as a steady minimization of procedural invasiveness (via a shift from intratympanic to intravenous application), duration and Gd dosage (16–18). A variety of cochlear and vestibular ELH quantification conventions have been suggested, including ELS semi-quantitative visual grading (19–25), manual measurement (26–28), semi-automatic (29, 30), and automatic algorithmic area ratio (AR), and volumetric segmentation (31, 32).

Given the plurality of approaches (some manual, some algorithmic), not all published results are inherently comparable. ELH features may vary greatly depending on ELS classification (for an overview, see **Table 1**) and data analysis choices. In this context, methodological comparative studies providing normalization and standard values between the methods and classifications used seem all the more important but still remain rare. On this note, this study aims to investigate the following questions:

(i) How variations in data acquisition protocols, such as Gd dosage or time delay, influence signal intensity (SI) and signal-to-noise ratio (SNR) within the ELS.

(ii) How ELH measures correlate with each other, as well as with clinical symptoms or neurophysiological testing.

(iii) How ELH influences SNR and SI within the ELS.

MATERIALS AND METHODS

Setting and Institutional Review Board Approval

All data was acquired at the Interdisciplinary German Center for Vertigo and Balance Disorders (DSGZ) and the Department of Neurology of Munich University Hospital (LMU) between 2016 and 2019. Institutional Review Board approval was obtained before the initiation of the study (no. 641-15). All participants provided informed oral and written consent in accordance with the Declaration of Helsinki before inclusion in the study.

Study Population

One hundred eight consecutive participants [75 patients with Meniere's disease (MD) and 33 vestibular healthy controls (HC)] underwent delayed intravenous gadolinium-enhanced magnetic resonance imaging (iMRI) for exclusion or verification of ELH. The diagnosis of Meniere's disease (MD) was based on the Classification Committee of the Bárány Society 2015 (33). HC were inpatients of the Department of Neurology without symptoms or underlying pathologies of the peripheral and central vestibular and auditory system that underwent MRI with a contrast agent as part of their diagnostic workup and agreed to undergo iMRI sequences after 4 h. HC underwent audio-vestibular testing to confirm the soundness of their peripheral end organs. The reasons for their admission to the clinic included movement disorders ($n = 6$), epilepsy ($n = 5$), optic neuritis ($n = 4$), trigeminal neuralgia ($n = 4$), headache ($n = 4$), idiopathic facial nerve palsy ($n = 3$), viral meningitis ($n = 3$), subdural hematoma ($n = 2$), spinal inflammatory lesion ($n = 1$), and decompensated esophoria ($n = 1$). The laterality quotient for right-handedness was assessed with the 10-item inventory of the Edinburgh test (34, 35). The inclusion criterion was age between 18 and 85 years. The exclusion criteria were other neurological or psychiatric disorders, as well as any MR-related contraindications (36), poor image quality, or missing MR sequences.

Abbreviations: ±, standard deviation; 2D, two-dimensional; 3D, three-dimensional; AR, area ratio; AI, asymmetry index; B, bilateral; c, cochlea; contra, contralateral; CEMD, central eye movement disorder; CISS, constructive interference in steady-state; d, definite; Diff-ER, ELS ratio of the side difference; DL, deep learning; ELH, endolymphatic hydrops; ELS, endolymphatic space; ER, ELS ratio; FLAIR, fluid-attenuated inversion recovery; Gd, gadolinium; GBCA, Gd-based contrast agents; Gd-DOTA, gadoteric acid (trade name: Dotarem®); Gd-Do3A, gadobutrol (trade name: Gadovist®); Gd-DTPA-BM, gadodiamide (trade name: Omniscan®); Gd-DTPA, gadopentetic acid (trade name: Magnevist®); Gd-HP-DO3A, gadoteridol (trade name: ProHance®); GLM, general linear model; GRAPPA, generalized auto-calibrating partially parallel acquisition; HC, healthy controls; HIT, head-impulse test; iMRI, delayed intravenous gadolinium-enhanced MRI of the inner ear; ipsi, ipsilateral; iv, intravenous; L, left; R, right; MD, Meniere's disease; minEn, minimum energy statistic; MMD, maximum mean discrepancy; MRI, magnetic resonance imaging; n, number; p, possible; ROI, region-of-interest; std, standard deviation; SNR, signal-to-noise ratio; SVV, subjective visual vertical; TFS, total fluid space; v, vestibulum; vHIT, video-oculography during head-impulse test; VM, vestibular migraine; VOG, video-oculography.

TABLE 1 | Semi-quantitative (SQ) grading conventions at a glance.

	Nakashima et al. (19)	**Gürkov et al. (24)** **Yang et al. (25)**	**Baráth et al. (20)**	**Attyé et al. (81)**	**Kirsch et al. (22)** **Boegle et al. (present data)**	**Bernaerts et al. (21)** **Bernaerts and de Foer (23)**
COCHLEA						
Slice of evaluation	*Midmodiolar level*	*Not specified*	*Midmodiolar level*	*Same as Nakashima et al. (19)*	*Midmodiolar level*	*Midmodiolar level*
Grade 0	No displacement of RM, interscalar septum, scala tympani, cochlear duct, scala vestibuli visible	No enlargement of ELS, PLS is clearly visible	No displacement of RM, interscalar septum, scala tympani, cochlear duct, scala vestibuli visible		**"X-mas tree"** made of circles with **"very thin, clear, hypointense line"** (cp. **Figure 1A**).	**"Very thin, clear, hypointense line"** (=non-enhancing scala media or ELS) between clearly enhancing scala vestibuli and scala tympani (=PLS)
Grade 1	Displacement of RM, cochlear duct < scala vestibuli	ELS is enlarged and bulging into PLS	Irregular dilation and partial obstruction of the scala vestibuli, cochlear duct indirectly visible as nocular black cut-out of the scala vestibuli		**"X-mas tree"** with **"X-mas lights"**, where ELS is slightly enlarged and indirectly visible as a nodular black cut out (cp. **Figure 1B**).	**"X-mas tree"** (=enhancing scala vestibuli and scala tympani) with **"X-mas balls"** (=nodular enlargement non-enhancing scala media)
Grade 2	Displacement of RM, cochlear duct > scala vestibuli	Scala media is scalloping into the scala tympani, PLS has a semicircular appearance			**"X-mas tree"** with **"X-mas balls"**, where ELS is bulding into scala tympani whilst giving the PLS a semicircular appearance (cp. **Figure 1C**).	
Grade 3		A severely distended scala media causes a flattened appearance of the perilymph space	No scala vestibuli visible		**"X-mas tree"** with **"X-mas garlands"**, where ELS is distended and causes a flattened appearance of the PLS (cp. **Figure 1D**).	**"X-mas tree"** (=enhancing scala vestibuli and scala tympani) with **"X-mas garlands"** (=linear enlarged non-enhancing scala media)
VESTIBULUM						
Slice of evaluation	*Lowest slice of vestibulum L-SCC still visible*	*Same as Nakashima et al. (19)*	*Midmodiolar level*	*Axial slice through inferior part of vestibulum*	*Vestibulum inferior part; L-SCC still visible*	*Vestibulum inferior part*
Grade 0	AR <33.3%		AR <50%, sacculus and utriculus are distinguishable	SURI <1, no saccular abnormality	Sacculus < utriculus, otoliths still distinguishable (cp. **Figure 1A**).	AR <50%,sacculus < utriculus, otoliths are distinguishable
Grade 1	33.3%< AR <50%			SURI ≥1	Sacculus (sign should remain as is) utriculus, otoliths are still distinguishable (cp. **Figure 1B**).	Sacculus ≥ utriculus, otoliths are distinguishable
Grade 2	AR >50%		AR >50%, PLS remains visible with circular rim enhancement	No sacculus visible	Sacculus & utriculus are confluent, PLS rim visible (cp. **Figure 1C**).	Sacculus and utriculus are confluent, PLS remains visible with circular rim enhancement
Grade 3			No PLS visible		No otolith organs distinguishable, no PLS visible (cp. **Figure 1D**).	No PLS visible

AR, area ratio; ELS, endolymphatic space; L-SCC, lateral semicircular canal; PLS, perilymphatic space; SURI, ratio ≥ 1 between the area of the sacculus and the area of the utriculus, RM, Reissner's membrane. The bold text highlights the main or most important characteristics.

Nomenclature

In the following, "ipsilateral" refers to the clinically leading side (or affected side) and "contralateral" to the opposite side (or non-affected side). In the case of patients presenting without a leading clinical side, a pseudorandom number generator ["Mersenne Twister" algorithm (37), uniform distribution] was used to generate a random number between 1 (=minimum value) and 9 (=maximum value). Even numbers meant "left side = ipsilateral side" and uneven numbers indicated "right = ipsilateral side." "Vegetative symptoms" refers to nausea and/or vomiting due to the episodic vertigo attack. "Ear symptoms" includes attack-associated tinnitus, hearing loss, ear pressure, and/or ear pain both uni- and bilaterally that fit the criteria for MD. "Other ear symptoms" refers to non-MD ear symptoms.

Measurement of the Auditory, Semicircular Canal, and Otolith Functions

Diagnostic workup included a thorough neurological workup (e.g., history-taking, clinical examination), neuro-orthoptic assessment [e.g., Frenzel glasses, fundus photography, and adjustments of the subjective visual vertical (SVV)], video-oculography (VOG) during caloric stimulation and head impulse test (HIT), as well as ocular (o) and cervical (c) vestibular evoked myogenic potentials (VEMPs) and pure tone audiometry (PTA).

A tilt of the SVV is a sensitive sign of a graviceptive vestibular tone imbalance. SVV was assessed with the subject sitting in an upright position in front of a half-spherical dome with the head fixed on a chin rest (38). A mean deviation of >2.5° from the true vertical was considered a pathological tilt of SVV.

The impairment of the vestibulo-ocular reflex (VOR) in higher frequencies was measured by HIT (39) using high-frame-rate VOG with EyeSeeCam [(40), EyeSeeTech, Munich, Germany]. A median gain during head impulses <0.6 (eye velocity in °/s divided by head velocity in °/s) was considered a pathological VOR (41). Furthermore, canal responsiveness in lower frequencies was assessed by caloric testing with VOG, which was performed for both ears with 30°C cold and 44°C warm water. Vestibular paresis was defined as >25% asymmetry between the right- and left-sided responses (42). The caloric asymmetry index ($\mathrm{AI_C}$) was calculated based on the slow-phase velocity of the caloric nystagmus: $AI_C\,[\%] = \frac{(R_{33^\circ C}+R_{44^\circ C})-(L_{33^\circ C}+L_{44^\circ C})}{(R_{33^\circ C}+R_{44^\circ C})+(L_{33^\circ C}+L_{44^\circ C})} \times 100$.

Vestibular evoked myogenic potentials (VEMPs) are short-latency, mainly otolith-driven vestibular reflexes elicited by air-conducted sound (ACS), or bone-conducted vibration (BCV) and recorded from the inferior oblique eye muscle (ocular or oVEMPs) or the sternocleidomastoid muscle (cervical or cVEMPs). VEMPs were recorded with the Eclipse platform (Interacoustics, Middelfart, Denmark), as described previously (43, 44). Only those VEMP responses that were clearly discernible from background noise were included in the analysis. To avoid bias due to examiners, only the asymmetry index ($\mathrm{AI_{o/cV}}$) of VEMP amplitudes and latencies was analyzed in detail (45).

Delayed Intravenous Gadolinium-Enhanced MRI of the Inner Ear

Data Acquisition

Four hours after intravenous injection of a standard dose (0.1–0.2 mmol/kg body weight, i.e., 0.1 −0.1 mmol/kg body weight) of Gadobutrol (Gadovist®, Bayer, Leverkusen, Germany), MR imaging (MRI) data were acquired in a whole-body 3 Tesla MRI scanner (Magnetom Skyra, Siemens Healthcare, Erlangen, Germany) with a 20-channel head coil. We used a 3D-FLAIR sequence to differentiate endolymph from perilymph and bone, and a CISS sequence to delineate the total inner ear fluid space from the surrounding bone. The T2-weighted, three-dimensional, fluid-attenuated inversion recovery sequence (3D-FLAIR) had the following parameters: TR 6,000 ms, TE 134 ms, TI 2,240 ms, FA 180°, FOV 160 × 160 mm^2, 36 slices, base resolution 320, averages 1, acceleration factor of 2 using a parallel imaging technique with a generalized auto-calibrating partially parallel acquisition (GRAPPA) algorithm, slice thickness 0.5 mm, acquisition time 15:08 min. The high-resolution, strongly T2-weighted, 3D constructive interference steady state (CISS) sequence of the temporal bones was performed to evaluate the anatomy of the whole-fluid-filled labyrinthine spaces and had the following parameters: TR 1,000 ms, TE 133 ms, FA 100°, FOV 192 × 192 mm^2, 56 slices, base resolution 384, averages 4, acceleration factor of 2 using GRAPPA algorithm, slice thickness of 0.5 mm and acquisition time 8:36 min. The presence of ELH was observed on the 3D-FLAIR images as enlarged negative-signal spaces inside the labyrinth, according to a previously reported method (18, 46).

Signal Quality Assessment

Signal quality was validated using signal-to-noise ratio (SNR) and signal-homogeneity (SH) in different regions of interest (ROIs). ROIs were labeled in the left and right inner ear within the "endolymph" and "perilymph" fluid, "cochlear basal turn," as well as in the surrounding tissue or subject matter, such as the "petrous bone," "cerebellum," "medulla," and "air."

In detail, the endolymph ROI consisted of 0.6 mm^2 circular 2D-selections of the left/right utricle. The perilymph ROIs consisted of multiple 0.6 mm^2 circular 2-D selections in the perilymphatic space (PLS) on both sides and were spread within the inner ear to obtain a signal intensity map. Said selections were placed in the vestibulum, twice inside the basal cochlea turn, the apex cochleae, the horizontal semicircular canal (hSCC) as well as the posterior SCC (pSCC). ROIs in the surrounding tissue or subject matter ("petrous bone," "cerebellum," "medulla oblongata," and "air") consisted of 60.8 mm^2 circular selections. Signal intensity extraction (mean, minimum, and maximum) was performed on axial slices of the FLAIR raw images via the "Analyze Regions" plugin of the "MorphoLibJ toolbox" (47) within ImageJ (48).

SNR was calculated in each ROI as $SNR\,(ROI) = \frac{S(ROI)}{std(air)}$, i.e., the fraction of mean signal intensity in an ROI S(ROI), and the standard deviation (STD) of the region labeled "air," std(air). The label "air" was defined as "MRI signal measure of background variations in the signal devoid of fluid." In other words, a region's SNR was calculated as a mean signal relative to the extent of the background variation.

The signal's statistical homogeneity was examined between ROIs for each group, and between groups for each ROI. SH was defined as the identical distribution of two samples except for shifts and scaling of the overall distribution. The median of each sample was removed and the interquartile range was scaled to the value of one. The two samples were then compared using *the minimum statistical energy* [*minEn*; (49)] and *the maximum mean discrepancy* [*MMD*; (50)], whilst adding 10,000 permutations with a threshold of maximally one failed test to reach statistical significance. Consequently, two samples were deemed to have different distributions if they diverged in shape, either due to kurtosis, skewness or the extent, and number of outliers. Note that no correction for multiple testing was applied in these tests in order to be more sensitive toward violations of SH, i.e., significant differences.

Semi-quantitative Grading of the Endolymphatic Space

Semi-quantitative (SQ) grading of the endolymphatic space (ELS) was performed independently by three experienced head and neck radiologists or neurologists (BE-W, VK, and JG) who were blinded to the clinical patient data. Rater statistical homogeneity was calculated just as the signal's statistical homogeneity. The ELS's characterization in the vestibulum and cochlea was based on criteria previously described (22) and can be viewed in **Table 1** and is described in further detail in **Figures 1A,B**, grade 0–3.

The characterization describes a 4-point grading for the cochlear and vestibular ELH. The cochlear grading is done on the midmodiolar level (19) and the vestibular grading on the inferior

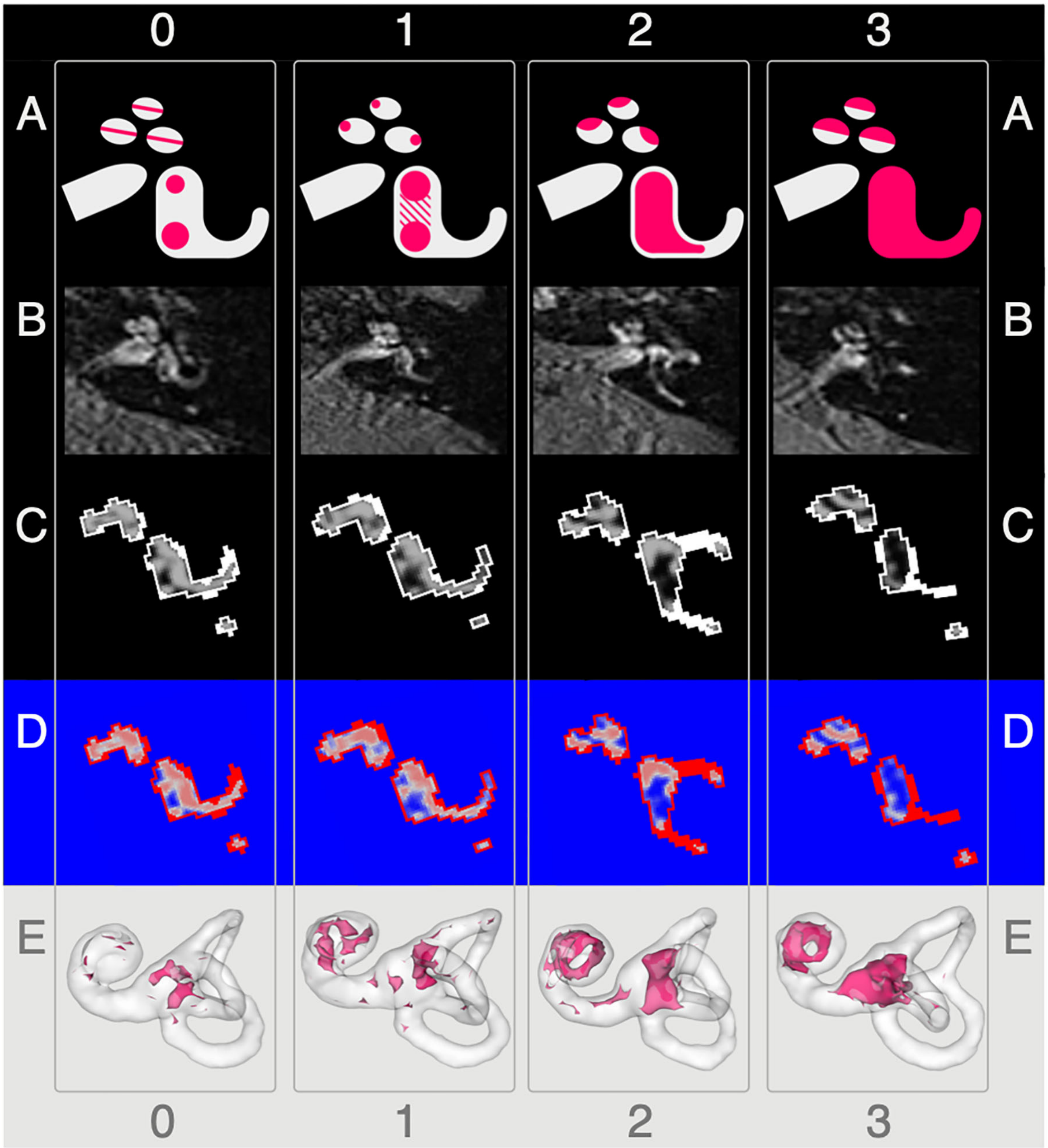

FIGURE 1 | Semi-quantitative (SQ) grading used for the endolymphatic hydrops. The vertical columns show the different semi-quantitative (SQ) grades from 0 to 3 used [cf. **Table 1**; according to a classification first described in Kirsch et al. (9)]. The horizontal rows each give an overview of how each grade looks **(A)**, in FLAIR raw data **(B)**, after VOLT processing **(C)**, as used for 2D quantification **(D)**, and as used for 3D quantification **(E)**. A detailed description of each grade is given in the second paragraph of subsection 'Semi-quantitative Grading of the Endolymphatic Space'.

part of the vestibulum, where the left semicircular canal (L-SCC) is still visible (19). The cochlear grading can be thought of as a fusion of previously described grading suggestions (21–24). Grade 0 (*no vestibular ELH*) can be reduced to "X-mas tree built from circles that are divided by "very thin, clear, hypointense lines" [cp. also Figure 1 of (23), Figure 1A in (21)] that represent the non-enhanced ELS (scala media) between the enhanced PLS (scala vestibuli and tympani). Grade 1 *(mild cochlear ELH)* can be reduced to "X-mas tree with lights," where the ELS is slightly enlarged and indirectly visible as a nodular black cut out of the scala vestibuli [cp. further Figure 2 in (24), Figure 1B in (21)]. Grade 2 (*marked cochlear ELH*) can be reduced to "X-mas tree with X-mas balls," where the ELS is bulging into the scala tympani whilst giving the PLS a semicircular appearance [cp. Figure 3 in (24)]. Grade 3 (*severe cochlear ELH*) can be reduced to "X-mas tree with garlands," where the severely distended ELS is causes a flattened appearance of the PLS [cp. also Figure 4 in (24), Figure 5A in (21), Figure 1C in (20)]. The vestibular grading is a fusion of previously described grading suggestions (21–23). Grade 0 (*no vestibular ELH*) can be reduced to "sacculus<utriculus," where the otolith organs are distinguishable and the sacculus is smaller than the utriculus [cp. also Figure 2A in (21), Figure 6 in (23)]. Grade 1 (*mild vestibular ELH*) can be reduced to "sacculus≥utriculus," where the sacculus is as large or larger than the utriculus [cp. also Figure 2B in (21), Figure 9 in (23)]. Grade 2 (*marked vestibular ELH*) can be reduced to "sacculus and utriculus are confluent," where the otoliths organs are no longer distinguishable with a surrounding PLS rim [cp. also Figure 2C in (21), Figure 7 in (23)]. Grade 3 (*severe vestibular ELH*) can be reduced to "otolith organs not distinguishable" with no PLS visible [cp. also Figure 2D in (21), Figure 8 in (23)].

2D- and 3D-Quantification of the Endolymphatic Space

Segmentation of the total fluid space (TFS) was based on a recently proposed (Ahmadi et al., under review) and pre-trained volumetric deep convolutional neural network (CNN) with V-net architecture (51) that was deployed via the TOMAAT module (52) in 3D–Slicer toolbox [version 4.11 (53)]. ELS and PLS were differentiated within the TFS using Volumetric Local Thresholding [VOLT; (31)] using ImageJ Fiji (48) with the "Fuzzy and artificial neural networks image processing toolbox" (54) and the "MorphoLibJ Toolbox" (47).

The resulting 3D volume can be regarded as a probabilistic map of the inner ear, which includes the classification into its two different compartments (ELS and PLS). The final classification strongly depends on the chosen cutoff. Based on empirical observations (31), 2D- and 3D-quantifications were examined at three cutoff variations (c6, c8, and c10). Each cutoff matches a percentage of positive classifications. For example, cutoff 6 (c6) corresponds to 79.2%, cutoff 8 (c8) to 70.8%, and cutoff 10 (c10) to 62.5% classifications into endolymphatic space. Examples of the pipeline outputs can be viewed in **Figure 1C**.

2D-quantification was done on axial slices of the VOLT volume. The mid-modiolar level was chosen for the cochlea and the inferior part of the vestibulum where the lateral semicircular canal (L-SCC) is still visible was selected for the vestibulum. However, the majority of volumes allowed for both a cochlear and vestibular measurement on the same slice. Easier visual selection was enabled by a look-up-table (LUT, "phase") included in ImageJ that was applied to the VOLT volumes. An example can be seen in **Figure 1D**. Areas were then measured using the "Analyze Regions" plugin which is part of the "MorpholibJ Toolbox" (47).

3D-quantification was done on the VOLT volume that included the entire inner ear. The cochlear volume was cropped using a cylindrical volumetric selection and applied to the VOLT volumes. The volume of the vestibulum including otolith organs and semicircular canals arose from subtracting the cochlear volume from the inner ear VOLT volume. Measurements were performed using the "Analyze Regions (3D)" plugin of the "MorpholibJ Toolbox" (47). A visualization can be seen in **Figure 1E**.

Parameters Derived From Endolymphatic Space Measures

The ELS ratio, $ER\ [\%] = \frac{ELS}{TFS} \times 100$, was calculated for 2D- and 3D-quantification of the ELS analogous to the area ratio (AR) in previous classification conventions (19–21). ER indicates the relative size of the ELH to the TFS and as such is independent of the absolute size which might differ between subjects (for example due to body size).

ELS symmetry between both inner ears was assessed via the ratio of ELS side differences $Diff - ER\ [\%] = ERi - ERc$, where ERi and $ERc$are the respective ipsilateral and contralateral ELS ratios in percent relative to the TFS. Another parameter was the asymmetry index, $AI\ [\%] = \frac{(ELSi\ ELSc)}{(ELSi\ +ELSc)} \times 100$, where ELS_i is the semi-, 2D- or 3D-quantification of the ipsilateral ELS and ELS_c of the contralateral ELS. The asymmetry index can be interpreted as a normalized difference and as such is also independent of the individual TFS.

Areas and volumes were normalized according to their TFS, if ${}_{c/v/a}TFS^{c8}_{e2D/3D} > {}_{c/v/a}TFS^{c8}_{mean\ 2D/3D} + 2.5 \times std\ (TFS)$, where "*e*" is the individual value and "*mean*" is the mean of the respective group (HC or MD). For an overview of TFS, see **Figure 6**.

Statistics and Validation Parameters

All statistics were implemented with self-written scripts in MATLAB version 7.19.0 (R2019b) using the "Statistics and Machine Learning" toolbox provided with MATLAB (Natick, Massachusetts: the MathWorks Inc.). ELS quantification measures were validated and compared using parameters describing different characteristics on different levels (i.e., between groups, ELS analysis methods, and diagnostic methods) and between different entities (i.e., inter-rater, inter-threshold, and inter-ROI). Parameters considered the ordering of subjects between samples (concordance), Spearman correlations between samples (rank-correlation), the form of the distribution of samples via "*minimum statistical energy*" and "*maximum mean discrepancy*" (statistical homogeneity), and covariance between samples via ANCOVA (analysis of covariance). All statistical tests used multiple comparison correction, if multiple tests (e.g., more than two regions or two thresholds) were compared independently with each other. The FWE level was set at $p = 0.05/N$ with N being the number of tests (e.g., regions, thresholds), i.e., Bonferroni correction.

Influence of Gd Dosage, Gd Time Delay on SNR and via SNR on SQ Grading, 2D- or 3D-Quantitatification

The influence of Gd dosage and time delay (from Gd injection to MR measurement) on the SNR and signal intensity (SI), as well as SNR, Gd dosage and time delay on SQ grading, 2D- or 3D- quantification measures was evaluated using ANCOVA modeling. The model included interaction of the group with each individual variable as well as the interaction of group, dosage and time delay variables. Additionally, covariates of no interest, such as age and BMI, were included. In other words, we checked whether SNR, Gd dosage, and Gd time delay each had an influence on the ELH measure in question, as well as the interaction of Gd dosage and Gd time delay, allowing for the possibility that the relationship might be different for each group.

Interrelations Between SQ Gradings and 2D- or 3D Quantification

Statistical Homogeneity

Statistical homogeneity between SQ grading, and 2D- or 3D- quantification methods between groups was, in principle, calculated in the same way as the signal statistical homogeneity (cf. signal quality validation). First, the median of each group was removed and the interquartile range was scaled to the value of one. The two groups were then compared using *minEn* and *MMD test statistics* whilst using 10,000 permutations between groups. Any instance of a random permutation with a higher test-statistic than the unpermuted groups was considered a failure. The groups were deemed statistically homogeneous if at most one test failed, otherwise the groups were deemed inhomogeneous, as they could be distinguished based solely on their distribution shape (kurtosis and skewness or the extent and number of outliers). Note that no correction for multiple comparisons was performed here in order to be more sensitive to violations of SH, i.e., significant differences.

Rater Repeatability and Reliability

Repeatability and reliability of the three different raters for SQ grading, as well as of the three different thresholds (c6, c8, and c10) for 2D- or 3D-quantification were measured using rank-based correlations and Kendall's W measure for concordance (55). This assessment shows whether the ordering of subjects between raters is similar and therefore can be assumed to be repeatable over the raters. Furthermore, we compared ratings by subtracting the SQ grading scores between raters to see if the extent of differences in rating values differed. Correction for multiple comparisons, i.e., multiple tests was done over data types (SQ, 2D and 3D), therefore $p_{(\mathrm{FWE})} = 0.05$ was set to $p = 0.05/\mathrm{N}$ with $N = 3$ for the three data types.

Interrelations Between SQ Grading, 2D- and 3D-Quantification

Interrelations between SQ grading, 2D- and 3D-quantification were examined via Spearman, i.e., rank-based correlations. Significant rank correlations indicated that the ordering of subjects was very similar or concordant across these measures. Rank-correlation was used so that linear as well as non-linear relationships could be examined and the gradings (ordinal measures) could be related to the quantitative measures. Correction for multiple comparisons $p_{(\mathrm{FWE})} = 0.05/\mathrm{N}$, i.e., Bonferroni correction, was done over all pairs of correlations in each correlation matrix, i.e., for SQ-×-2D quantification and SQ-×-3D quantification $N = 12\text{-}\times 12 = 144$ and for the correlation of asymmetry indices $N = 6\text{-}\times 6 = 36$.

Influence of Thresholds on Quantitative Measures

The influence of VOLT thresholds (c6, c8, and c10) on group differences was assessed using general linear model (GLM) based two-sample *t*-tests (including age as a covariate of no interest). The resulting slopes for the effects of thresholds and their standard errors were used to calculate *t*-statistic values for each group comparison at each threshold. Furthermore, a slope difference test (56) was used to check if group differences depended on the VOLT thresholds. A slope difference test compares differences in slopes with standard errors for the group differences across thresholds to determine if group differences depended on the cutoff-threshold. Correction for multiple comparisons $p_{(\mathrm{FWE})} = 0.05/\mathrm{N}$, i.e., Bonferroni correction, was done for three tests of between threshold comparisons resulting from three thresholds (c6,c8,c10), i.e., c6-vs-c8, c6-vs-c10, and c8-vs-c10, and therefore $N = 3$.

Covariance of Clinical Measures and iMRI

Clinical (e.g., disease duration, number of attacks) and diagnostic measures (e.g., HIT, calorics, and VEMPs), as well as parameters derived from ELS measures in SQ gradings and 2D- and 3-D quantifications (*ER*, *Diff-ER*, and *AI*) were included in an analysis of covariance (ANCOVA). An overview of clinical symptoms and diagnostic measures can be viewed in **Table 2**. Furthermore, the analysis accounted for categorical variables, such as symptoms like headache, and continuous covariates, such as body mass index (BMI) and the age of the patients. For detection of diverging trends between MD or HC, parameters derived from ELS measures were allowed interactions with the group. That means each group was allowed to have a different trend in the model. We used Bonferroni-correction for the *post-hoc* assessment of the individual factors in the ANCOVA.

Influence of ELH Presence on SNR and SI

The influence of the presence and extent of ELH on SNR and SI was examined with two approaches. First, SNR and SI data were investigated using classifications derived from SQ grades and 3D-quantification measures. The SQ grades were used to distinguish between "no ELH" and "ELH present," while the 3D-quantification was used to distinguish between "low/small ELH" and "high/large ELH." For the classification using SQ grades, all grades equal to zero (SQ grade == 0) were allocated to "no ELH" and the rest to "definite ELH present." For the classification using 3D-quantification, data values below the median were in the "low ELH" class and data values above the

TABLE 2 | Clinical syndrome and diagnostic characteristics.

		MD		HC
	All	**Definite**	**Probable**	**All**
	***n* = 75**	***n* = 35**	***n* = 40**	***n* = 33**
Age [in years]	55.2 ± 14.9	54.8 ± 14.1	55.6 ± 15.8	42.1 ± 18.9
Age range	22–81	27–77	22–81	20–84
Gender	36 females	14 females	22 females	19 females
Handedness	97% RH, 3% LH	100% RH	93% RH, 7% LH	97% RH, 3% LH
(A) Clinical syndrome				
Type of vertigo	73% Ro, 25% Sw, 2% Lh	83% Ro, 14% Sw, 3% Lh	64% Ro, 33% Sw, 3% Lh	–
Duration of illness [in months]	56.8 ± 88.7	49.0 ± 84.9	63.5 ± 92.4	–
Number of attacks altogether	48.7 ± 56.6	47.2 ± 49.1	49.8 ± 62.7	–
Number of attacks in the last 3 months	15.0 ± 37.8	18.5 ± 52.4	12.4 ± 21.2	–
Duration of attacks [in hours]	5.0 ± 6.9 (0.5–24)	3.2 ± 3.0 (0.5–12)	6.7 ± 8.7 (0.5–24)	–
Time since last attack [in days]	35.1 ± 44.7 (1–180)	36.1 ± 43.4 (1–180)	33.9 ± 47.0 (1–180)	–
Nausea, Vomiting	86.7%	97.1%	77.5%	–
VM-Headache	1.3%	0%	2.5%	–
Sensitivity to light or noise	9.7%	8.6%	10.0%	–
Focal neurological deficits	8.0%	0%	15%	–
History of migraine	1.7%	3.1%	0%	–
Family history of migraine	5.1%	0%	11.5%	–
Other-Headache	22.7%	28.6%	17.5%	–
MD-Ear-symptoms	84.0%	94.3%	75.0%	–
MD-bilateral	25.3%	31.4%	20.0%	–
MD-ipsilateral	81.3%	94.3%	70.0%	–
MD-contralateral	8.0%	11.4%	5.0%	–
Other-Ear-symptoms	8.0%	2.9%	12.5%	–
Other-bilateral	8.0%	2.9%	12.5%	–
Other-ipsilateral	9.3%	0%	15%	–
Other-contralateral	0%	0%	0%	–
(B) Diagnostic characteristics				
CEMD	9.3%	2.9%	15%	0%
PEMD ipsilateral	53.3%	60.0%	47.5%	0%
SVV ipsilateral, pathologic	28%	34.3%	22.5%	0%
Caloric ipsilateral, pathologic	83.6%	94.3%	73.7%	0%
Caloric contralateral, pathologic	0%	0%	0%	0%
Caloric bilateral, pathologic	1.4%	0%	2.6%	0%
Caloric ipsilateral [°/s]	7.6 ± 6.9 (0.8–40.6)	7.8 ± 7.8 (0.9–40.3)	7.5 ± 6.1 (0.8–34.4)	13.8 ± 4.5 (3.8–24.2)
Caloric contralateral [°/s]	12.8 ± 8.4 (1.6–55.0)	13.8 ± 9.7 (1.6–55.0)	11.9 ± 7.0 (2.7–32.5)	19 ± 11 (4.8–50.1)
Caloric Asymmetry-Index [%]	34.8 ± 22.7 (0.7–90.6)	36.4 ± 23.3 (0.9–40.6)	33.3 ± 22.2 (0.8–90.6)	0.2 ± 19.8 (0.8–48.3)
HIT ipsilateral, pathologic	48.4%	51.6%	45.5%	0%
HIT bilateral, pathologic	6.3%	6.5%	6.1%	0%
HIT ipsilateral [gain at 60ms]	0.8 ± 0.2 (0.2–1.1)	0.7 ± 0.2 (0.2–1.02)	0.8 ± 0.2 (0.4–1.1)	1 ± 0.1 (0.8–1.1)
HIT contralateral [gain at 60 ms]	0.8 ± 0.2 (0.4–1.1)	0.8 ± 0.2 (0.4–1.01)	0.9 ± 0.1 (0.6–1.09)	0.9 ± 0.1 (0.8–1.0)
Audio MD-typical ipsilateral	76.2%	93.3%	60.6%	0%
Audio MD-atypical ipsilateral	3.2%	0%	6.1%	0%
Audio Presbyacusis-typical	0%	0%	0%	0%
Audio low-frequency ipsilateral [dB]	41.3 ± 23.1 (8.0–110.0)	49.9 ± 20.3 (10.0–110.0)	33.7 ± 22.9 (8.0–92.0)	20.0 ± 3 (8.0–35.0)
Audio low-frequency contralateral [dB]	21.1 ± 14.4 (7.0–77.0)	20.3 ± 11.6 (7.0–63.0)	20.3 ± 11.6 (7.0–63.0)	18 ± 6 (15–33.0)

CEMD, central eye movement disorder; Lh, light-headedness; PEMD, peripheral eye movement disorder; Ro, rotational vertigo; Sw, swaying vertigo.

median in the "high ELH" class. The SNR and SI data were analyzed using two-sample t-tests and Wilcoxon rank-sum tests for differences from these classifications. The two tests (i.e., a parametric and non-parametric test), were used to ensure that any of the significant differences found were not purely dependent on the assumed distribution. Correction for multiple comparisons $p_{(\mathrm{FWE})} = 0.05/\mathrm{N}$, i.e., Bonferroni correction, was done for five tests between regions (split by ELH) comparisons, i.e., $N = 5$ (see **Figures 5A,B**).

Then, the inverse question was asked. This time SQ and 3D-quantification values were compared following SI or SNR value classification and then analyzed accordingly for differences with two-sample t-tests and Wilcoxon rank-sum tests. For both SI and SNR classification, "*low SI or SNR class*" was defined by their values below the respective median, and "*high SI or SNR class*" by their values above the respective median. Correction for multiple comparisons $p_{(\mathrm{FWE})} = 0.05/\mathrm{N}$, i.e., Bonferroni correction, was done separately for the test between SNR (split by ELH 3D-quantification) and 3D-quantification (split by SI). The number of tests for the SNR comparison was $N = 2$, and the number of tests for ELH 3D-quantification was $N = 4$ (see **Figures 5C,D**).

RESULTS

Descriptive Statistics

Seventy-five MD patients (35 females; aged 22–81 years, mean age 56.6 ± 14.9 years; 97% RH) and 33 HC participants (20 females; aged 20–84 years, mean age 42.1 ± 18.9 years; 94% RH) were included in the study. An overview of the most important clinical features in MD compared to HC can be seen in **Table 2**. An overview of the ELS grading for HC and MD can be viewed in **Table 3**.

Influences of Signal Quality on ELS Quantification Methods (i)

- The signal intensity (SI) of each region of interest significantly (FWE-corrected, $p < 0.05$) depended on Gd dosage (range: 0.08–0.28 ml/kg; mean ± std: 0.17 ± 0.05 ml/kg; 48% of subjects got 1 dose, 12% 1.5 doses; 40% got 2 doses of 0.1 ml/kg) and Gd time delay (range: 2 h and 51 min to 5 h and 20 min; mean ± std: 4 h and 24 ± 25 min; 25% are between 3 and 4 h, 50% are between 4 and 4 h and 31 min and the remaining 25% were longer). However, the effect sizes (eta-squared) were small (5–12%).
- The mean SNR (range: 24.8–130.49; mean ± std: 64.82 ± 20.64) was significantly related to Gd dosage and time delay (FWE-corrected, $p = 0.006$), but only 6.8% of the total variance (r-squared) could be explained. If looked at separately, Gd dosage (4.2%, FWE-corrected, $p = 0.03$) and Gd time delay (5.3%, FWE-corrected, $p = 0.02$) explained even less of the variance. See **Figure 2** for an overview of the minor influence of the iMRI acquisition parameters on SNR.
- The mean SNR was significantly different between the MD and HC group ($p < 0.05$). SNR asymmetry between left and right ear was not significantly related to Gd dosage, Gd time delay, or Gd dosage × Gd time delay.
- SQ gradings and 2D- or 3D- quantifications were not significantly related to Gd dosage, Gd time delay, Gd dosage × Gd time delay interaction, SI or SNR (FWE corrected, $p \leq 0.05$). There were some simple significant relationships ($p < 0.05$ uncorrected) for the iMRI variables with Gd dosage and SNR, but all these relationships were small in effect size (around 0.5–5% omega squared).

Interrelations Between ELS Quantification Methods (ii)

- Inter-rater SQ gradings (R1-3) were statistically homogeneous, as were 2D- and 3D- quantification values including ipsi- and contralateral or cochlea and vestibulum.
- Inter-rater SQ gradings (R1-3) were highly matched in the vestibular (v) and cochlear (c) part of the inner ear for all subjects (HC, MD) and slightly less for MD only. The results can be viewed in **Table 4** (column SQ) and suggest a high but imperfect reproducibility due to remaining variability.
- Inter-threshold (c6, c8, and c10) 2D- and 3D-quantification was highly concordant. These results can be viewed in **Table 4** (column 2D and 3D) and indicate an almost perfect agreement over VOLT thresholds with a basically perfect reproducibility.
- SQ grades correlated strongly with 2D-quantification values (range of correlation from 0.3 to 0.7) and 3D-quantification values (range of correlation from 0.3 to 0.7). The correlations of 2D- and 3D-quantification values with SQ grades was mainly driven by the MD group, due to the higher variability within the group, compared to HC group which did not vary much in grades or 2D- and 3D-quantification values (cp. **Figure 3**, plots on the left and in the middle).
- 2D- and 3D-quantification correlated substantially (range of correlation from 0.3 to 0.8) for the total inner ear, cochlea, and vestibulum on both the ipsilateral and contralateral side. However, there were no significant correlations of the ipsilateral with the contralateral sides (cp. **Figure 3**, plots on the right). AI_{SQ} (asymmetry-index of SQ quantification) correlated significantly (range of correlation from 0.3 to 0.7) with AI_{2D} and AI_{3D} (asymmetry-indices of 2D- and 3D-quantification) except for the cochlear AI in the 2D- and 3D-quantifications in the c6-cutoff (cAI_{2D}^{c6} and cAI_{3D}^{c6}, cp. **Figure 3**).
- Inter-rater SQ grading differences did not differ strongly between R1-3. **Figure 4** shows the results in more detail. For the vestibular part, the percentage of ratings that agreed, i.e., showed zero differences, was 54.6% (R2-R1), 50% (R3-R1), and 67.6% (R3-R2), while the percentage of differences of maximally one grade apart was 85.2% (R2-R1), 90.7% (R3-R1), and 98.2% (R3-R2). For the cochlear part, the percentage of ratings that agreed was 53.7% (R2-R1), 53.7% (R3-R1), and 71.3% (R3-R2), while the percentage of differences of maximally one grade apart was 88.9% (R2-R1), 90.7% (R3-R1), and 97.2% (R3-R2).
- Inter-threshold 2D- and 3D-quantification measures were statistically homogenous and showed group differences for each threshold.
- Clinical variables correlated with symmetry parameters derived from SQ grading and 2D- or 3D-quantification values such as the asymmetry index (AI) or the plain ELH

TABLE 3 | Semi-quantitative (SQ) grading, 2D- and 3D-quantification of the ELS.

								MD										**HC**				
					All					**Definite**					**Probable**					**All**		
					(*n* = 75)					**(*n* = 35)**					**(*n* = 40)**					**(*n* = 33)**		
(A) EH presence [%]																						
			R1	**R2**	**R3**	**R1-3**		**R1**	**R2**	**R3**	**R1-3**		**R1**	**R2**	**R3**	**R1-3**		**R1**	**R2**	**R3**	**R1-3**	
Ipsilateral	ELS		80%	69%	85%	78%		86%	83%	91%	87%		75%	57%	80%	71%		9%	39%	27%	25%	
	cELS		65%	60%	67%	64%		74%	74%	74%	74%		57%	48%	60%	55%		6%	21%	9%	12%	
	vELS		72%	61%	69%	68%		74%	74%	80%	76%		70%	50%	60%	60%		9%	33%	27%	23%	
Contralateral	ELS		73%	44%	72%	63%		77%	37%	77%	64%		70%	50%	68%	63%		21%	27%	27%	25%	
	cELS		59%	32%	40%	44%		57%	23%	37%	39%		60%	40%	43%	48%		15%	21%	9%	15%	
	vELS		61%	36%	56%	51%		63%	34%	71%	56%		60%	38%	43%	47%		21%	24%	24%	23%	
(B) SQ grading																						
Grades			**0**	**1**	**2**	**3**		**0**	**1**	**2**	**3**		**0**	**1**	**2**	**3**		**0**	**1**	**2**	**3**	
Ipsilateral	ELS	R1-3	15%	15%	13%	5%		9%	14%	17%	3%		20%	15%	10%	8%		73%	9%	0%	0%	
	cELS	R1-3	33%	35%	27%	5%		26%	34%	37%	3%		40%	35%	18%	8%		91%	9%	0%	0%	
	vELS	R1-3	31%	31%	24%	15%		20%	26%	40%	14%		40%	35%	10%	15%		73%	27%	0%	0%	
Contralateral	ELS	R1-3	28%	20%	8%	1%		23%	23%	9%	3%		33%	18%	8%	0%		73%	6%	0%	0%	
	cELS	R1-3	60%	28%	11%	1%		63%	23%	11%	3%		57%	33%	10%	0%		91%	9%	0%	0%	
	vELS	R1-3	44%	39%	15%	3%		29%	51%	17%	3%		57%	28%	13%	3%		76%	24%	0%	0%	
Percentage		R1-3	**Min**	**25%**	**50%**	**75%**	**Max**	**Min**	**25%**	**50%**	**75%**	**Max**	**Min**	**25%**	**50%**	**75%**	**Max**	**Min**	**25%**	**50%**	**75%**	**Max**
AI [%]	ELS	R1-3	0	0	33	100	100	0	20	33	92	100	0	0	43	100	100	0	0	0	0	100
	cELS	R1-3	0	0	50	100	100	0	0	100	100	100	0	0	33	100	100	0	0	0	0	100
	vELS	R1-3	0	0	33	100	100	0	0	33	88	100	0	0	27	100	100	0	0	0	0	100
(C) 2D-quantification																						
			Mean	**Std**	**25%**	**50%**	**75%**	**Mean**	**Std**	**25%**	**50%**	**75%**	**Mean**	**Std**	**25%**	**50%**	**75%**	**Mean**	**Std**	**25%**	**50%**	**75%**
Ipsilateral	ELS	c8	5.5	2.7	3.4	5.2	7.4	6.3	2.8	4.5	6.2	8.5	4.7	2.4	3.1	4.4	6.5	3.4	1.3	2.5	3.3	4
[mm^2]	cELS	c8	1.4	0.9	0.8	1.2	1.9	1.6	0.9	0.9	1.4	2.3	1.2	0.9	0.5	1.2	1.5	1	0.5	0.7	1.1	1.3
	vELS	c8	4.1	2.2	2.6	3.6	5.8	4.7	2.4	3.3	4.9	6.2	3.5	1.9	2.3	3.2	4.8	2.4	1.1	1.7	2.3	2.9
Contralateral	ELS	c8	3.7	1.8	2.6	3.3	4.5	3.9	1.9	2.7	3.5	4.8	3.5	1.7	2.6	3.3	4	3.6	1.2	2.7	3.8	4.5
[mm^2]	cELS	c8	1	0.6	0.6	0.8	1.3	1.1	0.7	0.4	1	1.8	0.9	0.5	0.6	0.8	1.2	1.1	0.7	0.7	1	1.4
	vELS	c8	2.6	1.5	1.8	2.2	3.3	2.8	1.5	2	2.4	3.6	2.5	1.6	1.7	2.1	2.7	2.5	0.9	1.8	2.4	3.1
AI [%]	ELS	c8	16.1	28.2	0.2	14.8	34.6	20.7	27.2	5.1	22.7	45.8	12.1	28.7	0.7	14.7	31.1	4.0	20.4	17.3	7.02	12.7
	cELS	c8	13.2	40.4	5.6	17.9	34.2	17.3	41.4	5	14.3	46.1	9.6	39.8	6.6	18.8	33.3	2.5	32.5	27.0	0	22.9
	vELS	c8	17.9	33.8	0.9	21.4	38.6	20.5	34.8	0.9	28.6	45.7	15.7	33.2	0.6	21.4	30.0	3.2	24.6	16.5	1.5	9.5
ER [%]	ELS	c8	14.71	6.97	10.09	13.7	20.44	16.61	6.85	11.14	16.67	21.52	13.05	6.73	7.24	11.99	17.54	9.33	3.22	7.18	8.66	11.04
Ipsilateral	cELS	c8	8.4	5.1	4.8	7.9	11.6	9.4	5.1	5.5	8.6	13.2	7.6	5	3.3	7.3	9.7	6.3	2.8	4.5	6.3	7.9
	vELS	c8	19.7	10.3	11.9	19.2	27.7	22.3	10.7	13.8	23.1	30.3	17.4	9.5	11.1	16.1	23.8	11.7	4.8	8.8	10.7	15.1
ER [%]	ELS	c8	9.7	4.1	7.3	8.9	11.6	10.4	4.5	7.3	9.6	13	9.1	3.7	7.3	8.8	9.9	9.9	2.7	7.6	10.3	12.4

(Continued)

TABLE 3 | Continued

			MD															**HC**				
			All					**Definite**					**Probable**					**All**				
			(*n* = 75)					**(*n* = 35)**					**(*n* = 40)**					**(*n* = 33)**				
Contralateral	cELS	c8	6.2	3.7	3.4	5.3	8.3	6.8	4.2	2.7	6.3	10.8	5.7	3.1	3.8	5.1	7.4	7	4.1	4.6	6.3	8.2
	vELS	c8	12.3	6.4	9.1	10.5	14.2	13.4	6.7	9.2	12	17.4	11.4	6.1	8.2	9.9	13	12.1	3.9	9.3	11.7	14.9
ER [%]-	ELS	c8	5	7.4	0.3	3.2	9.9	6.2	8	−0.5	6.3	12.3	3.9	6.6	0.3	3.2	6.5	−0.6	3.7	−3	−0.7	2.3
Difference	cELS	c8	2.3	6.2	−0.4	2.1	6.5	2.7	6.8	−0.4	2.5	6.7	1.9	5.8	−0.7	2.1	5.1	−0.7	4.6	−2.6	0	1.9
	vELS	c8	7.3	10.8	0.2	6.2	12	8.9	12.5	1.1	9.9	18	6	9.1	0	6.2	9.8	−0.5	5.4	−4	−0.4	2.4
TFS	ELS	c8	36.9	3.8	34.5	36.6	39.3	37.2	3.6	35.3	37.1	39.6	36.6	3.9	34	36.5	38.5	36.2	3.7	34.1	37.1	39
Ipsilateral	cELS	c8	16.3	1.7	15.5	16.4	17.4	16.5	1.6	15.3	16.6	17.6	16.3	1.8	15.6	16.4	17.3	15.8	1.8	14.9	15.9	16.8
[mm^2]	vELS	c8	20.5	2.6	18.8	20.1	22.4	20.8	2.6	19.3	21.1	22.4	20.3	2.6	18.4	19.8	22.5	20.5	2.5	18.8	20.9	21.9
TFS	ELS	c8	37.3	3.9	35.3	37.1	39.4	37.1	3.5	35	36.6	39.4	37.5	4.2	35.3	37.1	39.4	36.6	3.3	34.2	37.1	37.9
Contralateral	cELS	c8	16.2	1.8	15.2	16.1	17.3	16.3	1.4	15.3	16.2	17.1	16.2	2.1	15.1	15.9	17.8	16.1	1.6	14.9	15.8	17.2
[mm^2]	vELS	c8	21.1	2.7	19.5	20.8	22.7	20.8	2.5	18.5	20.7	22.3	21.3	2.8	19.6	20.8	22.8	20.4	2.2	18.7	20.4	22.3
(D) 3D-quantification																						
			Mean	**Std**	**25%**	**50%**	**75%**	**Mean**	**Std**	**25%**	**50%**	**75%**	**Mean**	**Std**	**25%**	**50%**	**75%**	**Mean**	**Std**	**25%**	**50%**	**75%**
Ipsilateral	ELS	c8	23.5	8.4	17.7	20.9	30.1	26	9	17.8	26.9	32.1	21.2	7.2	16.9	19.8	23.4	16.1	5.6	12.1	15.4	18.5
[mm^3]	cELS	c8	6.8	3.5	4.4	5.4	9	7.8	3.6	4.8	7.2	10.7	5.9	3.1	4.4	4.9	6.9	5	2.4	3.5	4.6	6
	vELS	c8	16.6	6.1	12.4	15.3	20.5	18.2	7	13	19.3	22.2	15.3	4.9	12.2	14.8	17.2	11.1	3.6	9	11.6	12.9
Contralateral	ELS	c8	17.2	4.6	14.4	16.3	20	17.4	4.5	14.9	17.4	20	17.1	4.7	14.4	16.2	19.9	16.2	3.9	13.2	16.5	19.2
[mm^3]	cELS	c8	5	2	3.7	4.6	6.4	5.3	2.3	3.7	4.8	6.5	4.8	1.8	3.6	4.6	6	5	2	3.2	4.7	6.1
	vELS	c8	12.2	3.8	9.8	11.4	14.3	12.2	3.2	10	12.8	14.2	12.3	4.4	9.6	11.4	14.4	11.2	3	8.8	11.7	13.1
AI [%]	ELS	c8	13.4	16.1	1.1	10	22.8	17.5	17.0	2.9	17.5	32.0	9.7	14.5	0.3	10	18.8	1.9	15.9	12.3	0.6	5.9
	cELS	c8	11.9	25.8	5.4	7.94	29.4	17.6	27.1	3.1	20.8	31.7	6.9	23.9	10.6	2.5	26.6	0.8	23.9	15.1	6.8	13.1
	vELS	c8	13.5	16.9	1.1	12.7	25.9	16.4	18.3	0.52	18.4	32.9	10.7	15.3	1.5	9.1	14.7	1.6	17.12	12.0	3.8	7.4
ER [%]	ELS	c8	8.5	2.8	6.4	7.5	10.8	9.3	2.9	7	9.6	11.9	7.7	2.5	6	7.3	8.9	5.9	1.6	4.8	5.9	6.5
Ipsilateral	cELS	c8	7	3.3	4.7	6	9.8	8	3.3	5.2	7.4	11	6.2	3	4.6	5.2	6.5	5.5	2.2	4	5.1	6.6
	vELS	c8	9.2	3.1	7	8.8	11.3	10	3.4	8.4	10.6	12.7	8.5	2.7	6.2	8.1	10.2	6.2	1.7	5.4	6.2	7
ER [%]	ELS	c8	6.2	1.3	5.4	6.1	6.9	6.2	1.3	5.6	6.4	7.2	6.1	1.3	5.3	6	6.7	6	1.2	4.8	6	6.8
Contralateral	cELS	c8	5.3	1.9	4	5.1	6.2	5.4	2	4	5	6.7	5.2	1.9	4	5.1	5.7	5.4	2.1	3.9	5	7
	vELS	c8	6.7	1.8	5.4	6.3	7.8	6.7	1.7	5.3	7.2	7.9	6.6	1.9	5.6	6.2	7.2	6.2	1.4	5.4	6.5	7
ER [%]-	ELS	c8	2.3	2.8	0.2	1.3	4	3.1	2.9	0.7	2.5	6.1	1.6	2.4	−0.1	1.3	2.7	0	1.7	−1	0	0.8
Difference	cELS	c8	1.8	3.5	−0.6	1	3.8	2.6	3.6	−0.5	2.4	5	1	3.3	−0.6	0.1	2.1	0.1	2.4	−1.4	0	1.6
	vELS	c8	2.5	3	0	1.9	4.7	3.3	3.3	0.3	3.2	6.3	1.9	2.6	−0.1	1.6	2.9	−0.1	1.9	−1.3	−0.5	0.9
TFS	ELS	c8	275.7	29.2	258	271.4	295	276.9	26.8	259.2	275	296.4	274.8	31.5	252.8	271.4	295	267.4	37.2	251	271.1	291
Ipsilateral	cELS	c8	95.2	12.2	86.7	93.4	103	96.7	12.3	87.5	96.7	105.4	93.9	12.2	85.8	93.4	102	88.6	14.4	80.5	88.2	98.4
[mm^3]	vELS	c8	179.9	20.1	166	182	192	178.6	17.6	166.5	176.3	192.7	181	22.2	165.7	182	192	178.7	27.1	166	178.6	195
TFS	ELS	c8	276.5	31.2	257	269.1	298	277.3	30	256.8	275.1	300.9	275.8	32.5	258.6	269.1	298	269.9	25.7	248	270.6	290
Contralateral	cELS	c8	94.8	13.3	86.2	93	103	95.9	13.1	86.7	95	104.2	93.8	13.6	83	90.6	102	91.3	12.5	80.3	89.8	96.3
[mm^3]	vELS	c8	182.4	20.6	171	183.3	193	181.3	19.5	171.5	178.2	192.7	183.4	21.7	171.4	183.4	193	178.6	17.8	168	180.7	190

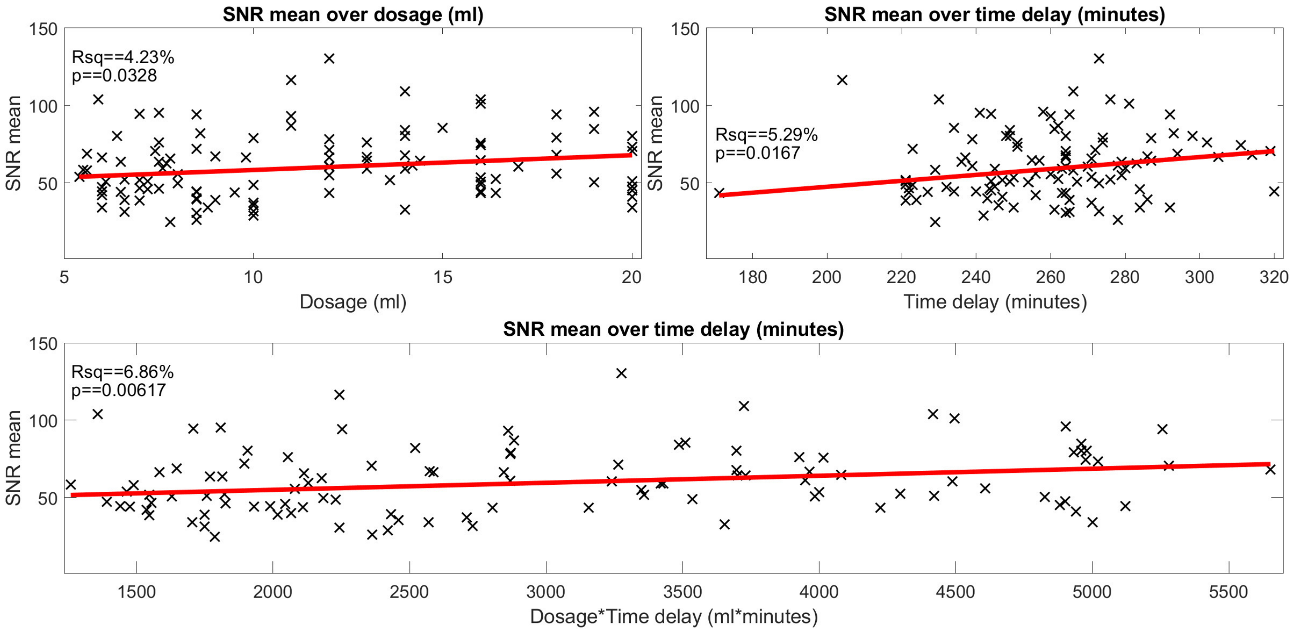

FIGURE 2 | Influence of gadolinium (Gd) dosage and Gd time delay on the signal-to-noise ratio (SNR) (belonging to question i). The scatter plot of the signal-to-noise ratio (SNR) over the gadolinium (Gd) dosage (in ml, plot in the top left), of the SNR over the time delay (in minutes, plot in the top right) and of the SNR over the interaction of Gd dosage×time delay (ml × minutes, plot in the bottom). SNR data points are plotted as black crosses and the trend lines of the fitted model are plotted as red lines. The SNR depended significantly on dosage, time delay as well as the interaction of dosage × time delay. However, the effect size was very small (4.2, 5.3, and 6.8% of explained variance, respectively). The SNR displayed here "SNR mean" is the mean of the SNRs calculated for each region of interest, i.e., the two inside the basal cochlear turn (CBT), the apex cochleae (AC), the horizontal semicircular canal (hSCC) as well as the posterior SCC (pSCC). For each region, the SNR is the mean signal divided by the standard deviation of the region labeled "air." The left and the right ear are averaged for each region, before regions are averaged to form "SNR mean".

TABLE 4 | Interrelations between ELS quantification methods.

	Vestibulum			Cochlea		
	3D	**2D**	**SQ**	**3D**	**2D**	**SQ**
(A) MD + HC						
W	0.99	0.99	0.74	0.99	0.97	0.70
p-Value	6e-180	7e-175	5e-26	1e-180	3e-124	1e-20
F-Value	238.1	213.3	5.7	242.2	69.9	4.7
(B) MD						
W	0.99	0.99	0.71	0.99	0.98	0.62
p-Value	4e-125	7e-129	2e-15	2e-128	2e-103	8e-09
F-Value	238.5	268.5	4.9	264.5	120.3	3.2

W = Kendall's coefficient of concordance between multiple rankings. Its value ranges from 0 to 1, unity being attained for perfect agreement between rankings.

difference between ipsilateral and contralateral side for the inner ear, vestibulum, and cochlea. The *AI* worked for un-normalized data and its results were comparable to the normalized data, while the pure differences between ipsilateral and contralateral sides were only useful when the data was first normalized to the fraction ER [%] of the total fluid space (TFS, cf. legend on standard values). This indicates that relative proportions of both ears, and the relative size of ELH are most useful for predicting quantitative clinical data from iMRI measures. Fittingly, vestibular AI for the 3D-quantification data explained 35% of the variance of the number of attacks in the 3 months prior to the examination and another 16% of variance could be explained by the AI for the 3D-quantification data of the whole of the inner ear (vestibular and cochlear parts combined). A more detailed clinical study and discussion can be found in another work (57).

Influences on Signal Quality (iii)

- There were significant differences in SI due to the presence of ELH in the following ROIs: cochlear basal turn [$p_{(t-\text{test})}$

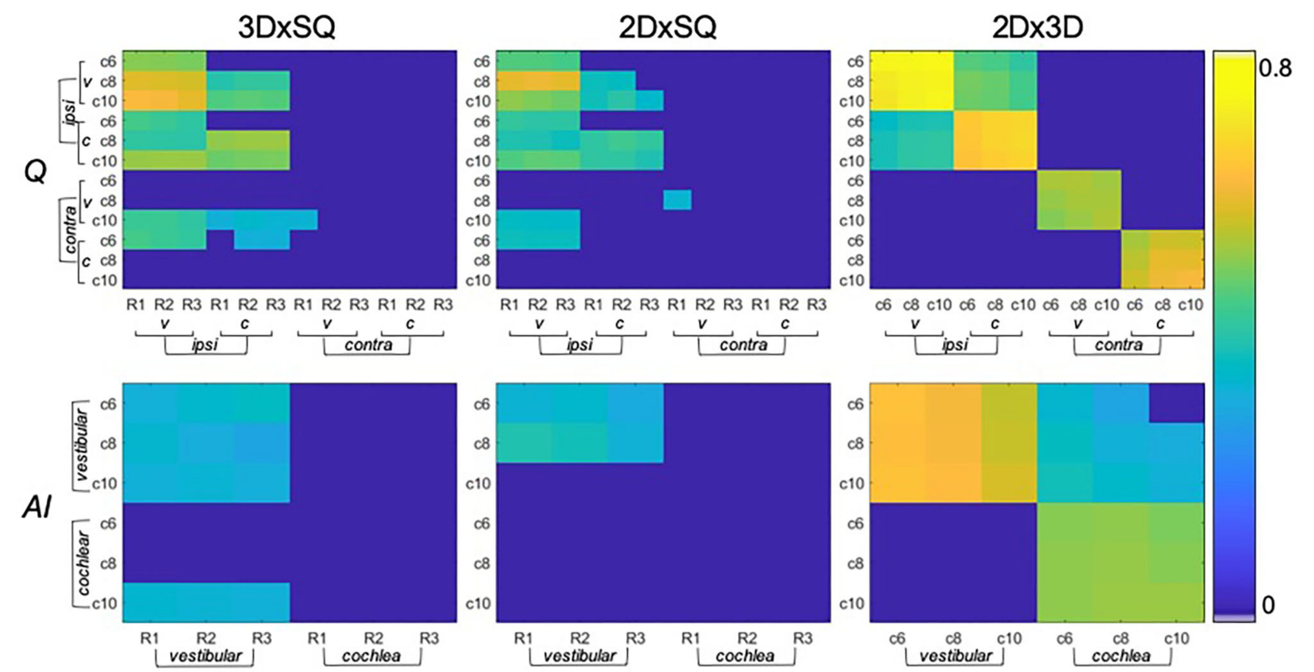

FIGURE 3 | Significant correlations between endolymphatic hydrops (ELH) quantification methods (belonging to question ii). The top row shows the correlations between semi-quantitative (SQ) gradings (x-axis) and 2D- or 3D- quantification values (y-axis) for vestibulum (v) or cochlea (c), and for the ipsilateral (ipsi) or contralateral side (contra). In addition, SQ gradings are rater-specific (R1-R3), and 2D- or 3D- quantification values are cutoff-specific (c6, c8, and c10). The higher the significant results ($p < 0.05$ FWE-corrected) correlated, the more they are colored in yellow (thresholded to 0–0.8). Overall, SQ gradings and 2D- or 3D-quantification values correlated with the respective other method, although to a higher extent on the ipsilateral side (on the contralateral side in c10) and vestibular part of the inner ear. The bottom row shows the corresponding correlations between methods (SQ gradings and 2D- or 3D- quantification values) for the respective asymmetry-index (*AI*).

$= 0.0009$ and $p_{(\text{rank-sum})} = 0.0003$], apex cochleae [$p_{(t\text{-test})} = 0.002$ and $p_{(\text{rank-sum})} = 0.001$], hSCC [$p_{(t\text{-test})} = 0.038$ and $p_{(\text{rank-sum})} = 0.022$], and pSCC [$p_{(\text{t-test})} = 0.046$ and $p_{(\text{rank-sum})} = 0.018$]. Generally, higher ELH 3D-quantification values had higher SI values. However, due to a significant spread, SI could not distinguish the presence of ELH from the absence of ELH (tested by means of the split of SI values based on defining "absence of ELH" as an SQ grading equal to zero and "presence of ELH" as all grades higher than zero). Fittingly, the opposite approach (splitting ELH values by SI brightness) did not show significant differences. For an overview, please see **Figure 5**. The signal intensity SI was significantly different between the MD and HC group for both ROIs in the cochlear basal turn, but not for the cochlear apex, hSCC, or pSCC ($p < 0.05$ FWE). The group differences in iMRI variables between the MD and HC groups persisted after removing effects of Gd dosage, time delay, and SNR, indicating that iMRI assessment was not significantly affected by the differences in Gd dosage, time delay, and SNR in the present dataset.

- SNR was not influenced significantly by the presence or absence of an ELH. Selecting SNR values for all SQ grades $= 0$ ("absence of ELH") and comparing them with the remaining SNR values (where SQ grades >0, "presence of ELH") led to two-sample t-test $p = 0.99$ and two-sample rank-sum test $p = 0.94$. Furthermore, comparing the SNR values for low ELH values (3D-quantification values below the median) with SNR values for high ELH values (3D-quantification values above the median) did not show any significant differences in SNR (two-sample t-test $p = 0.31$ and two-sample rank-sum test $p = 0.45$). Analog to this, splitting ELH values due to low SNR values vs. high SNR values did not result in significant differences [$p_{(t\text{-test})} = 0.66$ and $p_{(\text{rank-sum})} = 0.47$ on the ipsilateral side and $p_{(\text{t-testtest})} = 0.2$ and $p_{(\text{rank-sum})} = 0.16$ for the contralateral side]. For an overview, see **Figure 5**.

Standard Values

- Areas and volumes were normalized according to their TFS (total fluid space/surface) and can be viewed in **Figure 6**.
- Our calculations showed that the chosen threshold did not change the group differences between MD and HC. The grading-specific 2D- and 3D-quantification values, the TFS values and resulting ratios can be seen in **Figures 6**, **7**. Furthermore, we show the relationship of 2D- and 3D-quantification for the vestibular and cochlear part broken down by SQ grades in **Figure 8** and **Table 5**. While grades increase, one can observe that 2D- as well as 3D-quantification increased.
- ELH 3D-quantification values (see also **Figure 6**): The medians (ipsilateral, contralateral) of the vestibular data were (15 mm^3, 11 mm^3) for the MD group and (12 mm^3, 12 mm^3)

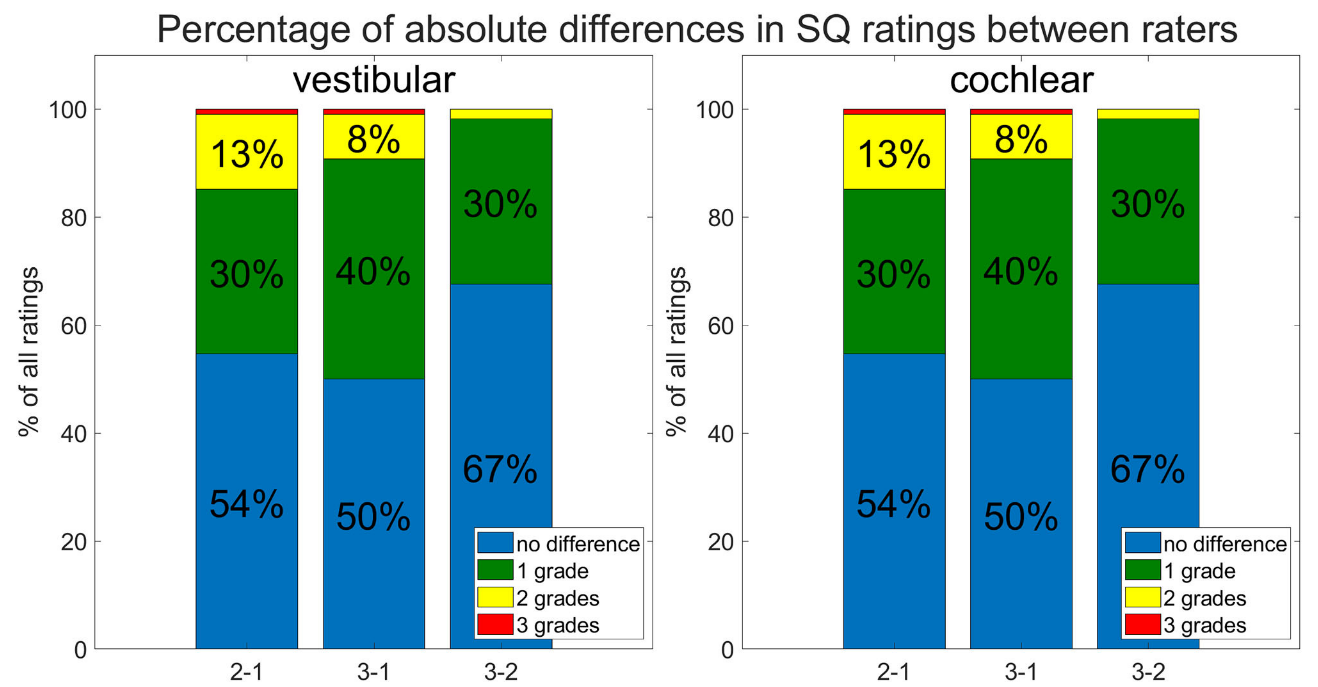

FIGURE 4 | Inter-rater and -threshold between ELH quantification methods (belonging to question ii). Shown are differences between the three raters. The differences between raters are shown as percentages of the total number of subjects rated. Most grades between raters agree (no difference; in blue), and the next largest difference was by 1 grade (in green), the remaining differences between raters were mostly 2 grades (in yellow) and rarely 3 grades (in red) apart.

for the vestibular healthy control (HC) group. The medians of the cochlear data were (5.4 mm^3, 4.6 mm^3) for the MD group and (4.6 mm^3, 4.7 mm^3) for the HC group.

- Total fluid space (TFS) 3D-quantification values of the vestibular and cochlear part of the inner ear [in mm^3] that were used for normalizing the data of each individual to generate ELS ratio (ER) [%], the percentage of the TFS occupied by the ELH. The medians (ipsilateral, contralateral) of the vestibular TFS data were (182 mm^3, 183 mm^3) for the MD group and (179 mm^3, 181 mm^3) for the HC group. The medians of the cochlear TFS data were (93 mm^3, 93 mm^3) for the MD group and (88 mm^3, 90 mm^3) for the HC group.
- Therefore, the medians (ipsilateral, contralateral) of the vestibular ER [%] data were (8.8%, 6.3%) for the MD group and (6.3%, 6.5%) for the HC group. The medians of the cochlear ER [%] data were (6.0%, 5.1%) for the MD group and (5.1%, 5.0%) for the HC group.
- ELH 2D-quantification values (see also **Figure 7**): The medians (ipsilateral, contralateral) of the vestibular data were (3.6 mm^2, 2.2 mm^2) for the MD group and (2.3 mm^2, 2.4 mm^2) for the vestibular healthy control (HC) group. The medians of the cochlear data were (1.2 mm^2, 0.8 mm^2) for the MD group and (1.1 mm^2, 1.0 mm^2) for the HC group.
- Total fluid surface (TFS) 2D-quantification values of the vestibular and cochlear part of the inner ear, in [mm^2] that were used for normalizing the data of each individual to generate ELS ratio (ER) [%], the percentage of the TFS occupied by the ELH. The medians (ipsilateral, contralateral) of the vestibular TFS data were (20.1 mm^2, 20.8 mm^2) for the MD group and (20.9 mm^2, 20.4 mm^2) for the HC group. The medians of the cochlear TFS data were (16.4 mm^2, 16.1 mm^2) for the MD group and (15.9 mm^2, 15.8 mm^2) for the HC group.
- Therefore, the medians (ipsilateral, contralateral) of the vestibular ER [%] data were (19.2%, 10.5%) for the MD group and (10.7%, 11.7%) for the HC group. The medians of the cochlear ER [%] data were (7.9%, 5.3%) for the MD group and (6.3%, 6.3%) for the HC group.

DISCUSSION

This methodological study with 108 participants (75 MD, 33 HC) focused on comparability and parametrization of different ELS quantification methods (SQ grading of three raters, 2D- or 3D-quantification of three cutoffs) used in iMRI and their (i) interrelations with subtle variations in data acquisition protocols (that influence SNR or SI); (ii) correlations to each other, clinical symptoms, or neurophysiological testing; and (iii) the influence of ELH on signal quality. The results were as follows: (i) Within the range of 0.1–0.2 mmol/kg (mean ± std: 0.16 ± 0.05 mmol/kg) Gd dosage and a 3 h 41 min to 5 h 19 min (mean ± std: 4 h 39 min ± 25 min) time delay, SQ gradings, and 2D- or 3D-quantifications were independent of signal intensity (SI) and signal-to-noise ratio (SNR), but they were found to be significantly related to Gd dosage and time delay themselves. (ii) The ELS quantification methods used were highly

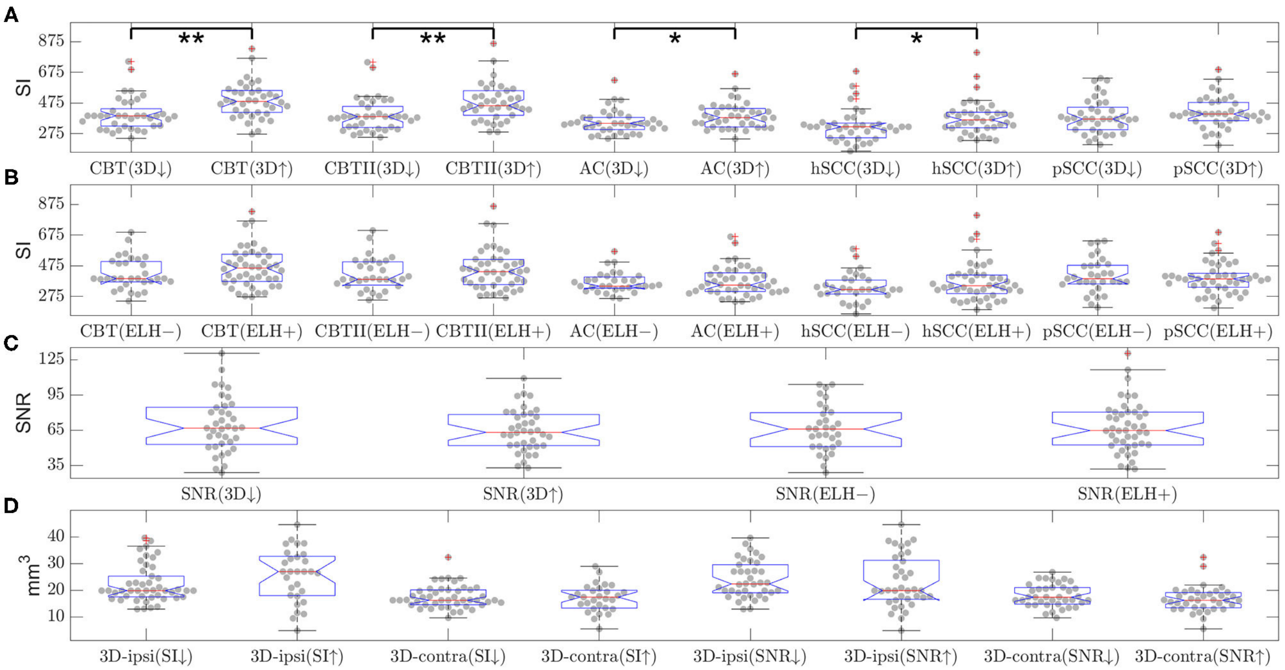

FIGURE 5 | Influence of endolymphatic hydrops (ELH) on signal intensity (SI) or signal-to-noise ratio (SNR) and vice versa (belonging to question iii). The top two rows **(A,B)** show the signal intensity (SI) in various areas of the inner ear. The SI values are split by either **(A)** 3D-quantification values (below or above median, indicated by a downward-arrow or an upward-arrow) or **(B)** endolymphatic hydrops (ELH) being absent ["−"] or present ["+"]. Here, "ELH absence" is defined as the average semi-quantitative (SQ) rating being zero and "ELH presence" is defined as the average rating being non-zero. Significant differences are indicated by black lines and p-values for the group differences evaluated with two-sample *t*-test or rank-sum test ($^{**}p < 0.001$ and $^{*}p < 0.05$). The third row **(C)** shows the mean SNR split by 3D-quantification values (below or above median; indicated by a downward-arrow or an upward-arrow), as well as the mean SNR split by ELH being absent ["−"] or present ["+"], where presence is defined as ELH being non-zero and absence as ELH rating being zero. The group differences were evaluated with the two-sample *t*-test and the rank-sum test; neither of these was significant. The fourth row **(D)** shows the 3D-quantification values split by mean SI values (below or above median; indicated by a downward-arrow or an upward-arrow), as well as the 3D-quantification values split by SNR values (below or above median; indicated by a downward-arrow or an upward-arrow). The group differences were evaluated with the two-sample *t*-test and the rank-sum test; neither of these was significant.

reproducible across raters (SQ gradings) or thresholds (2D- and 3D-quantification), although 3D-quantifications showed least variability in comparison to 2D-quantifications and SQ gradings. The relative proportions of both ears, and the relative size of ELH proved to be most useful for predicting quantitative clinical data from iMRI measures. (iii) ELH size significantly influenced SI but not SNR. In contrast, SI could not predict ELH size. In the following, results (i–iii) will be discussed.

Within a Specific Dosage and Time Delay Range ELS Quantification Methods Remain Independent of Signal Intensity (i)

The 3D fluid-attenuated inversion recovery (3D- FLAIR) imaging used has high sensitivity to low concentrations of Gd-based contrast agents (GBCA) in fluid compared with conventional T_1-weighted imaging (58). In particular, the heavily T_2-weighted 3D-FLAIR imaging with a long effective echo time is very sensitive to subtle T1 shortening and can detect low concentrations of GBCAs in the perilymphatic space after intravenous administration of a single dose of GBCA (18, 59, 60). In the tested Gd dosage and Gd time delay range (see above), at most weak influences on SNR and no influence on ELS quantification methods were found. It can therefore be assumed that, although Gd dosage and Gd time delay certainly have an influence on iMRI quality parameters, the sweet spot for ELH quantification by iMRI is within the range of the tested parameters. These results tie in well with earlier studies that showed strongest enhancement in 3D FLAIR sequences between 3 and 6 h (61), and optimally 4 h (62) after intravenous administration of 0.1 mmol/kg gadolinium diethylenetriaminepentaacetic acid (standard dose Gd-DTPA, Magnevist®), or 4.5 h (63) after intravenous administration of a standard dose gadoteridol (0.1 mmol/kg Gd-HP-DO3A, ProHance®), double dose (0.2 mmol/kg) Gd-HP-DO3A (64) or triple dose (0.3 mmol/kg) of Gd-DTPA-BMA, Omniscan® (65).

Another feature of the good performance within the chosen ranges may be the homogeneous distribution of the contrast agent in the entire volume of the inner ear (66, 67).

Further improvement of SNR and visualization in terms of rapid, morphological enhancement for analysis of the temporal and spatial distribution in the PLS of the inner ear can be achieved through careful selection of MR sequences (59, 68),

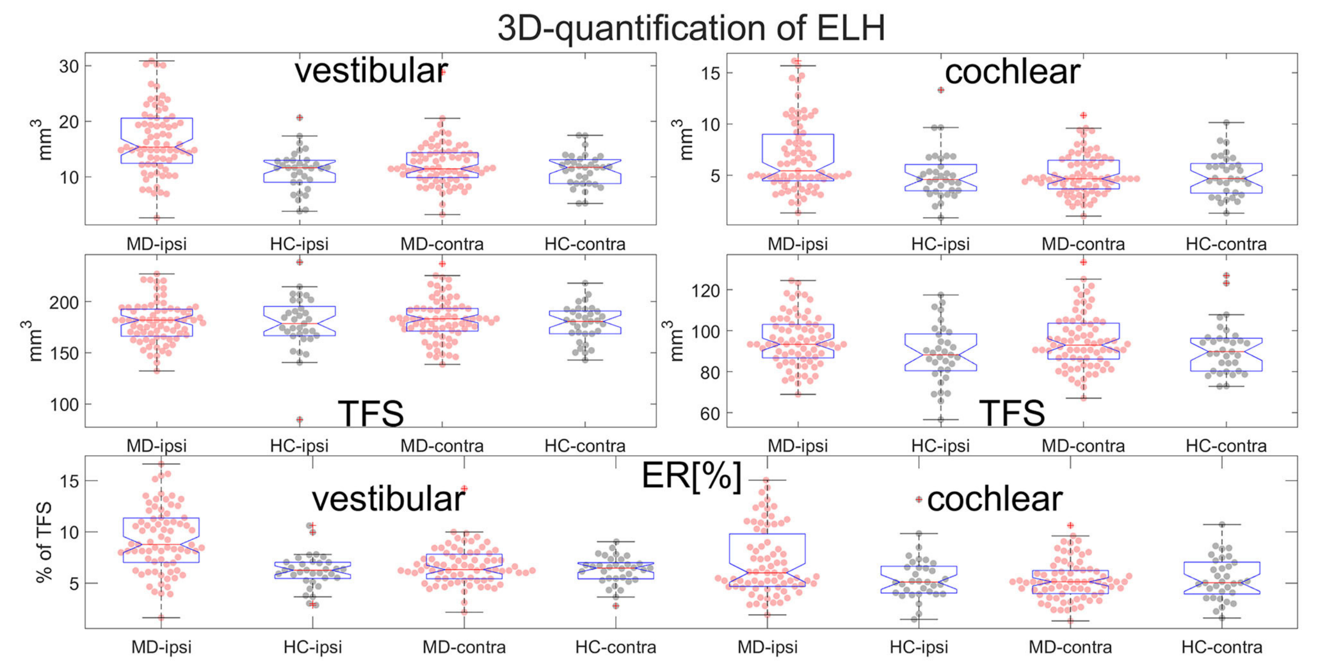

FIGURE 6 | Normalization and group differences for 3D-quantification of endolymphatic hydrops (ELH). 3D-quantification values of endolymphatic hydrops (ELH) in the vestibular and cochlear part of the inner ear [in mm^3] (top). 3D-quantification values of the total fluid space (TFS) of the vestibular and cochlear part of the inner ear [in mm^3] (middle row) that were used for normalizing the data of each individual to ELS ratio (ER) [%], the percentage of the TFS occupied by the ELH (bottom row).

combination (69, 70), and post-processing (14) of MR sequences, MR Gd complex (71), MR coil, and MR field strength (72).

Is There a Hierarchy Within ELS Quantification Methods? (ii)

In line with the only comparative methodological study of ELS quantification methods published to date in 11 participants (9 patients and 2 healthy controls) (26), SQ grading and 2D- or 3D- quantification methods were found to be reliable and useful for the diagnosis of endolymphatic hydrops. However, the degree of reliability based on comparisons between raters or thresholds increased from SQ grading to 2D- and again to 3D-quantification methods. The increase in repeatability corresponds to the decrease in dependency of human decision (visually > specific slice in 2D > whole volume in 3D) and increase of automatization and data points (semi-quantitative < area < volume).

Another aspect that makes relying solely on SQ grading tricky is the comparability of methods between different research groups, besides inter-rater disparities. SQ grading conventions (cf. **Table 1**) vary in grading resolution from three [in cochlea (19–21, 23) and vestibulum (19, 24, 25)] to four steps [in cochlea (22, 24, 25) and vestibulum (21–23)]. Accordingly, not all ELH grade results in cochlea or vestibulum correspond to each other due to the usage of different conventions [as an example grade 1 in (19, 20, 24)], or not at all [as an example (73)]. Based on either manually drawn (28, 74) regions of interest (ROIs) or a convolutional neural network (CNN) segmentation (32), 2D quantification methods already offer an increased comparability and variability of information. However, the comparability of the results remains limited by the slice selection for the calculation of the ratio and the differing slices emerging from slice planning or MRI setup (sequence type, slice thickness, slice resolution). Concerning these issues, 3D-quantification can be a solution (no slice selection, independent of slice planning) or at least an improvement (sequence type, slice thickness, slice resolution). In addition, more information (data points) enables better fitting of diagnostic and clinical parameters (75). Yet here, too, methodological variations affect reproducibility and availability of results. The critical points are the segmentation of the inner ear from the background [manually (29), via atlas (76, 77), or CNN (31); (Ahmadi et al., under review)] and the ELS and PLS from the TFS [manually (26), semi-automatic (29), automatic (31)], as well as the availability of the software solutions [commercial (26, 28, 29, 78) vs. open source (31)]. The less human-dependent and the more automated, the more reproducible the method in most cases. Therefore, the usefulness of the available quantification methods depends on its intended application. While visual SQ grading is highly useful in a clinical setting, automated 3D-quantification seems most suitable for research.

ELS Patterns in MD, HC (ii)

Significant differences between groups could especially be found for the ipsilateral (or affected) side of the MD group vs. HC group, as was already shown for 4-point [cochlea: (24, 25)] and 3-point [cochlea: (79); vestibulum: (80); sacculum (81)] ELS SQ

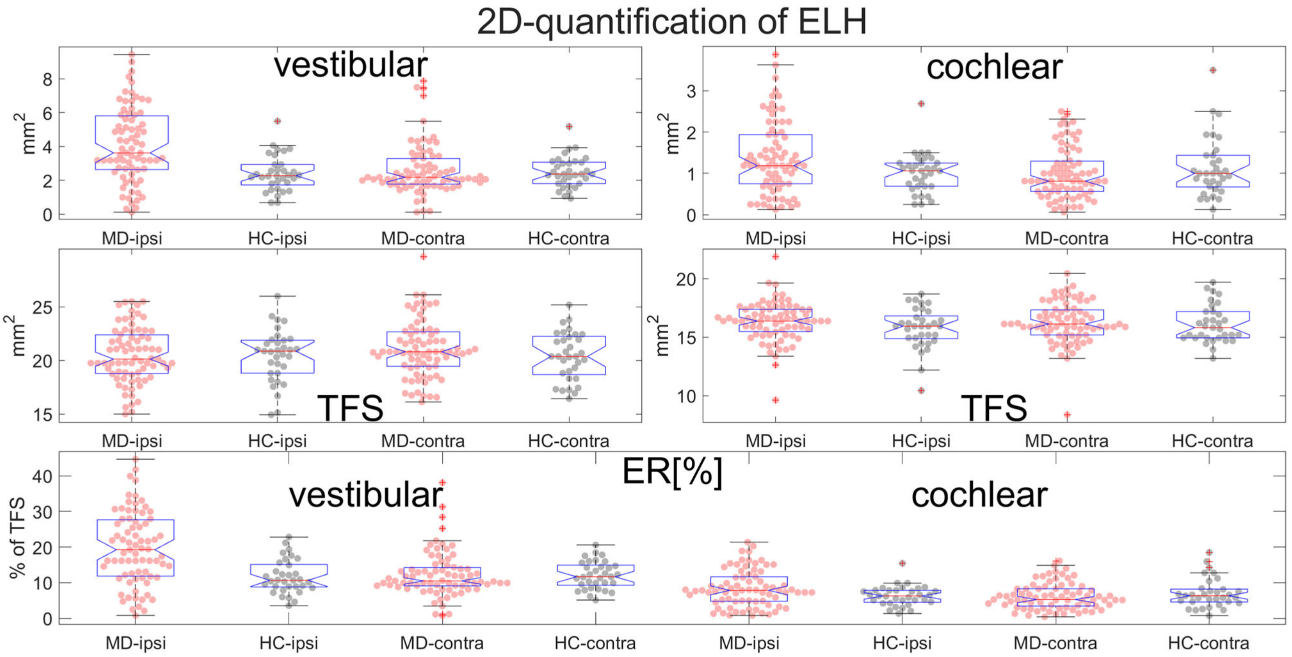

FIGURE 7 | Normalization and group differences for 2D-quantification of endolymphatic hydrops (ELH). 2D-quantification values of endolymphatic hydrops (ELH) in the vestibular and cochlear part of the inner ear, in [mm^2] (top row). 2D-quantification values of the total fluid surface (TFS) of the vestibular and cochlear part of the inner ear, in [mm^2] (middle row) that were used for normalizing the data of each individual to ELS ratio (ER) [%], the percentage of the TFS occupied by the ELH (bottom row).

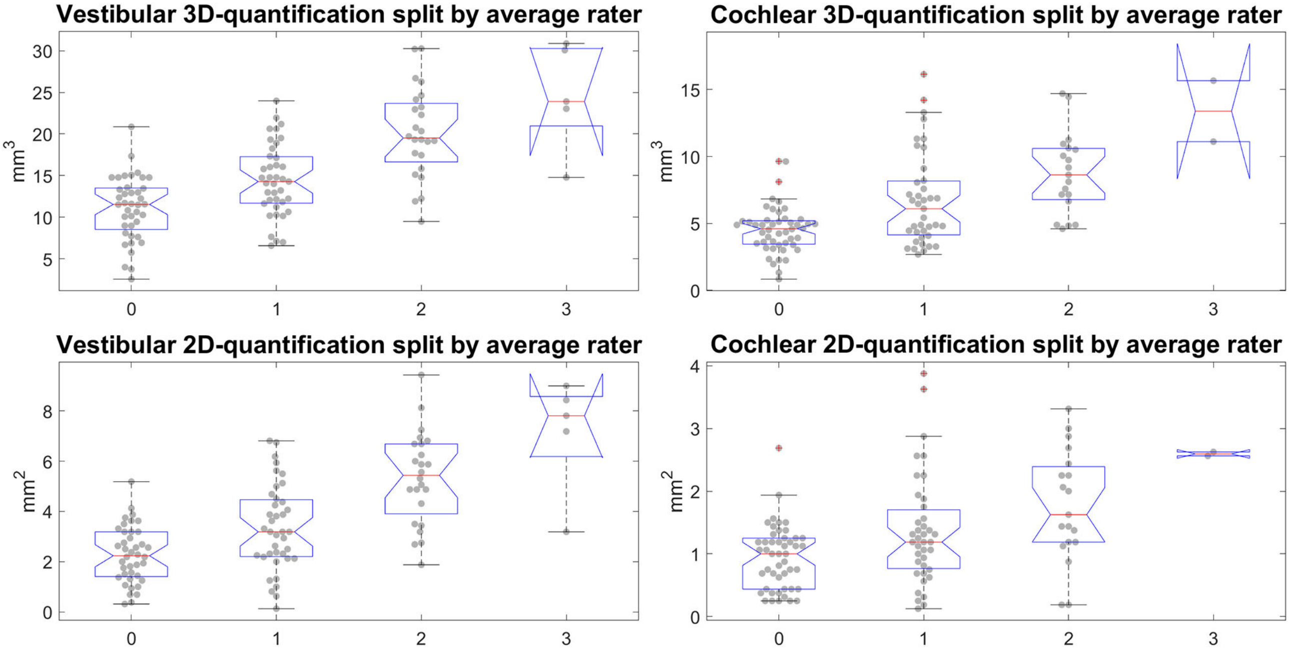

FIGURE 8 | Semi-quantitative (SQ) grade-specific 2D- and 3D-quantification values. These four plots show the quantitative endolymphatic hydrops (ELH) measures (3D-quantification in the top row and 2D-quantification in the bottom row) split up along the semi-quantitative visual grading steps (from grade 0 to grade 3 in steps of 1). This means each boxplot with data points overlaid shows the distribution of quantitative measures that correspond to the respective grading. The grading here is of the average over the three raters, rounded to the nearest integer to preserve gradings going from 0 to 3 in steps of 1. The top row shows the distributions for the 3D-quantification of ELH for vestibular and cochlear parts of the inner ear, left and right, respectively, while the bottom row shows the distributions for the 2D-quantification of ELH for vestibular and cochlear parts of the inner ear.

TABLE 5 | SQ-specific 2D- and 3D-quantification of the ELS.

			Grade 0 **No hydrops** **Mean ± std (min–max)**	**Grade 1** **Mild hydrops** **Mean ± std (min–max)**	**Grade 2** **Marked hydrops** **Mean ± std (min–max)**	**Grade 3** **Severe hydrops** **Mean ± std (min–max)**
(A) 2D-quantification						
c6	Inner ear [mm^2]	R1-3	2.15 ± 1.32 (0.25–4.81)	3.57 ± 1.81 (0.19–6.81)	5.91 ± 1.92 (2.44–9.75)	6.31 ± 2.75 (3.19–8.38)
	Cochlea [mm^2]	R1-3	0.56 ± 0.40 (0–1.31)	0.96 ± 0.77 (0–3)	1.29 ± 0.72 (0.06–2.56)	1.78 ± 0.13 (1.69–1.88)
	Vestibulum [mm^2]	R1-3	1.88 ± 1.24 (0.13–4.25)	2.67 ± 1.62 (0–5.63)	4.18 ± 1.68 (1.13–8.63)	5.89 ± 2.04 (2.56–8)
c8	Inner ear [mm^2]	R1-3	3.08 ± 1.54 (0.63–6.00)	4.77 ± 2.07 (0.5–8.5)	7.59 ± 2.20 (3.25–11.13)	8.19 ± 3.32 (4.38–10.44)
	Cochlea [mm^2]	R1-3	0.89 ± 0.51 (0.25–1.94)	1.38 ± 0.92 (0.13–3.88)	1.76 ± 0.89 (0.19–3.31)	2.59 ± 0.04 (2.56–2.63)
	Vestibulum [mm^2]	R1-3	2.45 ± 1.39 (0.31–5.19)	3.45 ± 1.84 (0.13–6.81)	5.34 ± 1.84 (1.88–9.44)	7.13 ± 2.30 (3.19–9)
c10	Inner ear [mm^2]	R1-3	4.46 ± 1.87 (1.44–7.63)	6.01 ± 2.27 (1.19–10.63)	9.07 ± 2.28 (4.38–12.75)	9.77 ± 3.26 (6.06–12.19)
	Cochlea [mm^2]	R1-3	1.31 ± 0.54 (0.56–2.13)	1.84 ± 1.00 (0.44–4.44)	2.25 ± 1.00 (0.44–3.88)	3.22 ± 0.04 (3.19–3.25)
	Vestibulum [mm^2]	R1-3	3.21 ± 1.64 (0.56–6.38)	4.24 ± 1.98 (0.56–8)	6.25 ± 1.98 (2.19–10.13)	8.10 ± 2.56 (3.81–10.31)
TFS	Cochlea [mm^2]	R1-3	15.54 ± 1.49 (12.63–18.63)	16.64 ± 1.20 (14.13–9.63)	16.59 ± 2.48 (9.63–21.88)	16.50 ± 1.24 (15.63–17.38)
	Vestibulum [mm^2]	R1-3	19.45 ± 2.92 (15.00–24.63)	20.63 ± 2.66 (15.63–25.5)	20.78 ± 2.13 (17.31–25.19)	21.74 ± 3.03 (18–25.5)
c6	Inner ear ER [%]	R1-3	6.10 ± 3.74 (0.85–13.68)	9.54 ± 4.72 (0.64–17.76)	15.71 ± 4.90 (5.58–25.12)	16.99 ± 7.20 (8.73–21.93)
	Cochlea ER [%]	R1-3	3.51 ± 2.43 (0.00–7.78)	5.67 ± 4.33 (0–16.78)	7.93 ± 4.35 (0.29–14.96)	10.80 ± 0.01 (10.79–10.8)
	Vestibulum ER [%]	R1-3	9.50 ± 6.43 (0.82–21.79)	12.78 ± 7.61 (0–25.07)	20.09 ± 7.76 (5.96–40.83)	27.02 ± 8.95 (12.97–37.10)
c8	Inner ear ER [%]	R1-3	8.78 ± 4.36 (2.12–17.05)	12.75 ± 5.29 (1.71–21.55)	20.20 ± 5.64 (6.91–28.50)	22.10 ± 8.95 (11.99–29.00)
	Cochlea ER [%]	R1-3	5.65 ± 3.09 (1.44–11.48)	8.22 ± 5.14 (0.78–21.38)	10.83 ± 5.34 (0.86–18.90)	15.75 ± 0.91 (15.11–16.4)
	Vestibulum ER [%]	R1-3	12.49 ± 7.18 (2.08–26.60)	16.46 ± 8.52 (0.79–30.36)	25.71 ± 8.55 (9.93–44.67)	32.72 ± 10.1 (16.14–41.74)
c10	Inner ear ER [%]	R1-3	12.70 ± 5.20 (4.88–21.67)	16.10 ± 5.75 (4.06–27.96)	24.16 ± 5.91 (9.30–31.88)	26.35 ± 8.60 (16.61–32.90)
	Cochlea ER [%]	R1-3	8.34 ± 3.33 (3.94–15.25)	10.95 ± 5.58 (2.23–24.49)	13.84 ± 6.11 (2.57–21.99)	19.57 ± 1.74 (18.35–20.80)
	Vestibulum ER [%]	R1-3	16.34 ± 8.41 (3.75–32.69)	20.31 ± 9.01 (3.54–37.85)	30.07 ± 9.20 (11.59–47.93)	37.15 ± 10.9 (19.30–47.83)
(B) 3D-quantification						
c6	Inner ear [mm^3]	R1-3	11.17 ± 3.85 (2.70–19.11)	14.52 ± 4.97 (7.48–27.97)	22.78 ± 5.54 (13.50–32.76)	23.13 ± 8.61 (13.50–30.10)
	Cochlea [mm^3]	R1-3	3.15 ± 1.23 (0.76–6.20)	4.65 ± 2.93 (1.5–12.91)	6.49 ± 2.51 (2.89–11.80)	10.62 ± 2.62 (8.77–12.46)
	Vestibulum [mm^3]	R1-3	8.27 ± 3.25 (1.38–14.53)	10.43 ± 3.63 (4.52–17.96)	14.81 ± 4.68 (5.56–25.53)	18.23 ± 5.43 (10.19–24.39)
c8	Inner ear [mm^3]	R1-3	16.59 ± 5.24 (4.81–26.95)	20.73 ± 6.03 (11.02–36.47)	30.61 ± 6.78 (19.10–44.54)	31.16 ± 10.2 (19.78–39.56)
	Cochlea [mm^3]	R1-3	4.58 ± 1.60 (1.31–8.11)	6.57 ± 3.51 (2.67–16.14)	8.73 ± 3.00 (4.59–14.70)	13.39 ± 3.22 (11.11–15.67)
	Vestibulum [mm^3]	R1-3	12.29 ± 4.39 (2.56–20.86)	14.78 ± 4.48 (7–23.98)	20.12 ± 5.42 (9.48–30.26)	24.53 ± 6.49 (14.78–30.87)
c10	Inner ear [mm^3]	R1-3	23.06 ± 6.63 (7.97–35.78)	27.87 ± 6.83 (15.34–44.95)	38.85 ± 8.05 (24.97–56.85)	39.68 ± 11.5 (27.13–49.73)
	Cochlea [mm^3]	R1-3	6.38 ± 2.03 (2.05–10.05)	8.74 ± 3.96 (4.02–18.84)	11.12 ± 3.38 (6.19–18.26)	16.15 ± 4.24 (13.16–19.15)
	Vestibulum [mm^3]	R1-3	17.10 ± 5.45 (4.64–27.53)	19.78 ± 5.19 (9.52–29.81)	25.78 ± 6.15 (14.06–36.55)	31.28 ± 7.41 (20.41–38.59)
TFS	Cochlea [mm^3]	R1-3	90.0 ± 10.6 (68.96–105.82)	95.4 ± 11.2 (74.25–117.52)	99.90 ± 14.1 (75.5–124.47)	97.1 ± 17.6 (84.63–109.56)
	Vestibulum [mm^3]	R1-3	178.6 ± 18.3 (149.7–219.7)	181.2 ± 23.3 (132.2.0.0.221.7)	176.8 ± 18.2 (140.3–227.3)	190.4 ± 11.2 (175.0–199.6)
c6	Inner ear ER [%]	R1-3	4.12 ± 1.23 (1.15–6.25)	5.32 ± 1.83 (2.90–9.82)	8.05 ± 1.68 (4.46–10.73)	8.25 ± 2.84 (4.98–9.94)
	Cochlea ER [%]	R1-3	3.49 ± 1.48 (1.10–8.19)	4.76 ± 2.67 (1.49–12.02)	6.55 ± 2.46 (2.59–11.11)	10.87 ± 0.72 (10.36–11.38)
	Vestibulum ER [%]	R1-3	4.57 ± 1.63 (0.87–7.07)	5.82 ± 2.04 (2.43–9.62)	8.30 ± 2.26 (3.57–13.20)	9.51 ± 2.51 (5.60–12.22)
c8	Inner ear ER [%]	R1-3	6.13 ± 1.66 (2.04–8.82)	7.60 ± 2.21 (4.44–12.81)	10.83 ± 2.04 (6.18–14.11)	11.12 ± 3.32 (7.29–13.15)
	Cochlea ER [%]	R1-3	5.07 ± 1.86 (1.90–10.71)	6.76 ± 3.17 (2.78–15.03)	8.81 ± 2.90 (3.88–13.85)	13.71 ± 0.83 (13.13–14.3)
	Vestibulum ER [%]	R1-3	6.79 ± 2.17 (1.62–10.14)	8.24 ± 2.54 (3.99–12.84)	11.30 ± 2.53 (6.09–16.61)	12.81 ± 2.96 (8.12–15.47)
c10	Inner ear ER [%]	R1-3	8.53 ± 2.07 (3.38–11.71)	10.20 ± 2.47 (6.19–15.79)	13.75 ± 2.42 (8.28–17.95)	14.16 ± 3.61 (10.0–16.25)
	Cochlea ER [%]	R1-3	7.04 ± 2.25 (2.98–13.26)	9.03 ± 3.52 (4.21–17.54)	11.24 ± 3.29 (5.36–16.24)	16.51 ± 1.37 (15.55–17.48)
	Vestibulum ER [%]	R1-3	9.48 ± 2.66 (2.94–13.39)	11.01 ± 2.95 (5.99–15.97)	14.50 ± 2.79 (9.03–20.09)	16.35 ± 3.29 (11.22–19.42)

grading, 2D-quantification [cochlea: (82); vestibulum: (82)] and 3D-quantification [cochlea: (30, 57); vestibulum: (30, 57)] results.

Clinical variables correlated highest with symmetry parameters derived from SQ grading and 2D- or 3D-quantification values such as the asymmetry index (*AI*) or the plain ELH difference between ipsilateral and contralateral side for the inner ear, vestibulum, and cochlea. Recent studies using ELS asymmetry indexes confirm this inclination (57). A more detailed clinical study and discussion can be found in another work (76). To date, correlations were found for

SQ grades 3-point [electrocochleography (EcochG) (83, 84)] and 4-point ordinal cochlear scale [PTA (24–26, 79); auditory symptoms (85, 86); disease duration (24, 79); but not for the glycerol test (25)]. Furthermore, correlations were found for 3-point ordinal vestibular scale [cVEMP-side difference (SD) (24); PTA (11, 25, 87); oVEMP-amplitudes (88), but not with VOG during caloric stimulation SD (24, 89) or the glycerol test (25)]. SQ correlations coincided with 2D-quantification [cochlea: PTA (82); vestibulum: SP/AP ratio of ECoG (82)] and 3D-quantification [cochlea: PTA (26); vestibulum: duration of illness >30 months (26), side difference in response to caloric irrigation (57)] correlation results.

ELH Extent Influences Signal Intensity in the Basal Cochlear Turn (iii)

Zhang et al. (90) investigated 19 MD patients following double-dose iMRI and found that the signal intensity ratio of the cochlear basal turns in the affected ear was significantly higher than in the unaffected ear and that there was a positive correlation between the signal intensity ratio of the cochlear basal turn and the grades of cochlear and vestibular hydrops in the affected ear. The SNR was assessed and calculated manually according to (91) using the signal in perilymph of both cochlear basal turns and noise in coplanar circular 50 mm^2 ROIs in the cerebellum. The interpretation of these findings was that increased permeability of the blood-labyrinth barrier (higher SNR) may play a role in the process of endolymphatic hydrops in MD.

The results of the current study suggest, however, a general pathophysiological effect tied to the extent of the ELH and not MD as a pathology, since higher ELH 3D-quantification values had higher signal intensity (SI) values in the cochlear basal turn, apex cochlea, and hSCC ROIs. Within MD, SI only in the cochlear basal turn was significantly higher on the ipsilateral side when compared to the contralateral side. The SI was generally different between the MD and HC groups, indicating an effect of ELH also on signal presentation. SNR differed between the MD and HC groups; however, the effect was small and the group differences in ELH were not significantly affected by SNR, indicating that the group differences are a persistent effect of the underlying condition and not related to the imaging settings that were used in the current study.

Normalization and Standardization of ELS Values

Clinical variables correlated better and more correctly with relative (AI) or normalized values [to the fraction ER [%] of the total fluid space]. This indicates that relative proportions of both ears, and the relative size of ELH are most useful for predicting quantitative clinical data from iMRI measures (57).

However, to date not many iMRI ELS values have been published in absolute (26, 30, 92) and relative sizes (26, 28, 85, 93–95); those that have been published were mostly group-specific but not grade-specific, and one grade-specific but relative (26). In **Table 5**, 2D- and 3D-quantifications, relative, and normalized to TFS are presented.

Recommendations for Future iMRI Studies

The following methodological recommendations for future studies can be derived from the present work and the current available literature:

- MR setup: Improved hybrid of reversed image of positive endolymph signal and native image of positive perilymph **s**ignal (iHYDROPS-Mi2) (15) or 3D-real inversion recovery (3D-real IR) (28, 96), highest possible MRI field strength (72), smallest possible isotropic voxel size, deep learning reconstruction denoising (14) if applicable.
- MR measurement: 4 h ±30 min after single-dose (0.1 mmol/kg) intravenous application (64) of Dotarem (Gd-DOTA, 100% morphological enhancement) or Gadovist (Gd-Do3A, 88% morphological enhancement) (71).
- SQ grading: 4-point ordinal scale (0: no hydrops, 1: mild hydrops, 2: marked hydrops, 3: severe hydrops) for cochlear and vestibular SQ grading (cp. **Table 1**), preferably with a level of evaluation reconstructed to distinctive anatomical fixpoints.
- Scalar ELS values: 3D-quantification, optimally using algorithm-based segmentation of both the TFS (Seyed-Ahmad et al., under review); (76, 77) and ELS (31, 32) should be included. 2D-quantification if 3D-quantification is not available. Reported values should be normalized for TFS size.
- Correlations with clinical variables should include both ears and are most promising in symmetry parameters, such as asymmetry-indices for un-normalized data and relative size ELS for normalized data.

Methodological Limitations and Outlook

There are methodological limitations in the current study that need to be considered in the interpretation of the data. First, despite the comparatively wide range of contrast agent dosage and delay time within this study, the results should be (to some degree) considered specific to the study's MR settings (MR sequence, MR contrast agent, intravenous application). Second, despite the extensive analyses within this study, it was not possible to try all, but only representations of the methods used in this study [SQ following **Figure 1** and (22), 2D- and 3D-quantification using VOLT (31)]. Third, the study lacks histological confirmation of endolymphatic hydrops. However, the *in-vivo* acquisition of histological specimens in Menière's disease is currently not possible. Fourth, the size of the control group ($n = 33$) was small in comparison to the MD group ($n = 105$). However, due to findings of signal intensity in the dendate nucleus and globus pallidus on unenhanced T1-weighted MR images (97–99) that are still under investigation, measurements were restricted to inpatients of the Department of Neurology that underwent MRI with a contrast agent as part of their diagnostic workup and agreed to undergo iMRI sequences after 4 h.

CONCLUSION

The current comparative methodological study has shown that: (1) A Gd dosage of 0.1–0.2 mmol/kg after 4 h ± 30 min Gd time delay will provide sufficient SNR when using recommended MR sequences and contrast agents. (2) An agreed upon clinical SQ grading classification including a standardized level of evaluation reconstructed to anatomical fixpoints is needed to provide unambiguous comparability between labs. (3) 3D-quantification methods of the ELS using algorithm-based segmentation of the TFS and ELS seem to be best suited for research purposes. Correlations with clinical variables should include both ears and ELS values reported relative or normalized to size. (4) The presence of ELH increases signal intensity in the basal cochlear turn weakly, but cannot predict the presence of ELH.

DATA AVAILABILITY STATEMENT

The original contributions presented in the study are included in the article/supplementary material, further inquiries can be directed to the corresponding author/s.

ETHICS STATEMENT

The studies involving human participants were reviewed and approved by Ethics Committee of the Medical Faculty of the Ludwig-Maximilians-Universität, Munich, Germany. The patients/participants provided their written informed consent to participate in this study.

AUTHOR CONTRIBUTIONS

RB: conception and design of the study, analysis of the data, and drafting the manuscript. JG, EK, SB-B, and BE-W: acquisition, analysis of the data, and drafting of the manuscript. MD: conception and design of the study, drafting the manuscript, and providing funding. VK: conception and design of the study, acquisition, analysis of the data, drafting the manuscript, and providing funding. All authors contributed to the article and approved the submitted version.

FUNDING

This work was partially funded by the Friedrich-Baur-Stiftung (FBS), the German Federal Ministry of Education and Research (BMBF) in connection with the foundation of the German Center for Vertigo and Balance Disorders (DSGZ; grant number 01 EO 0901) and the German Research Foundation (DFG) in connection with the Munich Cluster for Systems Neurology (SyNergy; grant number: EXC2145, project ID: 390857198), and the German Foundation for Neurology (DSN).

ACKNOWLEDGMENTS

This was part of the dissertation of JG. We thank K. Göttlinger for copyediting the manuscript.

REFERENCES

1. Strupp M, Brandt T, Dieterich M. *Vertigo - Leitsymptom Schwindel*. 3rd ed. Berlin Heidelberg: Springer-Verlag (2021). doi: 10.1007/978-3-662-61397-9
2. Pyykkö I, Zou J, Gürkov R, Naganawa S, Nakashima T. Imaging of temporal bone. *Adv Otorhinolaryngol*. (2019) 82:12–31. doi: 10.1159/000490268
3. van der Lubbe MFJA, Vaidyanathan A, Van Rompaey V, Postma AA, Bruintjes TD, Kimenai DM, et al. The "hype" of hydrops in classifying vestibular disorders: a narrative review. *J Neurol.* (2020) 267:197–211. doi: 10.1007/s00415-020-10278-8
4. Rauch SD, Merchant SN, Thedinger BA. Meniere's syndrome and endolymphatic hydrops. Double-blind temporal bone study. *Ann Otol Rhinol Laryngol.* (1989) 98:873–83. doi: 10.1177/000348948909801108
5. Nakashima T, Pyykkö I, Arroll MA, Casselbrant ML, Foster CA, Manzoor NF, et al. Meniere's disease. *Nat Rev Dis Prim.* (2016) 2:16028. doi: 10.1038/nrdp.2016.28
6. Nakada T, Yoshida T, Suga K, Kato M, Otake H, Kato K, et al. Endolymphatic space size in patients with vestibular migraine and Ménière's disease. *J Neurol.* (2014) 261:2079–84. doi: 10.1007/s00415-014-7458-9
7. Suga K, Kato M, Yoshida T, Nishio N, Nakada T, Sugiura S, et al. Changes in endolymphatic hydrops in patients with Ménière's disease treated conservatively for more than 1 year. *Acta Oto-Laryngologica.* (2015) 135:866–70. doi: 10.3109/00016489.2015.1015607
8. Attyé A, Eliezer M, Galloux A, Pietras J, Tropres I, Schmerber S, et al. Endolymphatic hydrops imaging: differential diagnosis in patients with Meniere disease symptoms. *Diagn Interv Imaging.* (2017) 98:699–706. doi: 10.1016/j.diii.2017.06.002
9. Kirsch V, Ertl-Wagner B, Berman A, Gerb J, Dieterich M, Becker-Bense S. High-resolution MRI of the inner ear enables syndrome differentiation and specific treatment of cerebellar downbeat nystagmus and secondary endolymphatic hydrops in a postoperative ELST patient. *J Neurol.* (2018) 265:48–50. doi: 10.1007/s00415-018-8858-z
10. Zwergal A, Kirsch V, Gerb J, Dlugaiczyk J, Becker-Bense S, Dieterich M. Neurootologie: Grenzfälle zwischen Ohr und Gehirn. *Nervenarzt.* (2018) 89:1106–14. doi: 10.1007/s00115-018-0598-x
11. Attyé A, Eliezer M, Medici M, Tropres I, Dumas G, Krainik A, et al. In vivo imaging of saccular hydrops in humans reflects sensorineural hearing loss rather than Meniere's disease symptoms. *Eur Radiol.* (2018) 28:2916–22. doi: 10.1007/s00330-017-5260-7
12. Eliezer M, Hautefort C, Van Nechel C, Duquesne U, Guichard J-P, Herman P, et al. Electrophysiological and inner ear MRI findings in patients with bilateral vestibulopathy. *Eur Arch Otorhinolaryngol.* (2020) 277:1305–14. doi: 10.1007/s00405-020-05829-8
13. Jerin C, Krause E, Ertl-Wagner B, Gürkov R. Clinical features of delayed endolymphatic hydrops and intralabyrinthine schwannoma : an imaging-confirmed comparative case series. English version. *HNO.* (2017) 65:41–5. doi: 10.1007/s00106-016-0199-6
14. Naganawa S, Nakamichi R, Ichikawa K, Kawamura M, Kawai H, Yoshida T, et al. MR imaging of endolymphatic hydrops: utility of iHYDROPS-Mi2 combined with deep learning reconstruction denoising. *Magn Reson Med Sci.* (2020) doi: 10.2463/mrms.mp.2020-0082. [Epub ahead of print].
15. Naganawa S, Kawai H, Taoka T, Sone M. Improved HYDROPS: Imaging of endolymphatic hydrops after intravenous administration of gadolinium. *Magn Reson Med Sci.* (2017) 16:357–61. doi: 10.2463/mrms.tn.2016-0126
16. Yamazaki M, Naganawa S, Tagaya M, Kawai H, Ikeda M, Sone M, et al. Comparison of contrast effect on the cochlear perilymph after intratympanic and intravenous gadolinium injection. *Am J Neuroradiol.* (2012) 33:773–8. doi: 10.3174/ajnr.A2821
17. Naganawa S, Satake H, Iwano S, Fukatsu H, Sone M, Nakashima T. Imaging endolymphatic hydrops at 3 tesla using 3D-FLAIR with intratympanic Gd-DTPA administration. *Magn Reson Med Sci.* (2008) 7:85–91. doi: 10.2463/mrms.7.85
18. Naganawa S, Yamazaki M, Kawai H, Bokura K, Sone M, Nakashima T. Visualization of endolymphatic hydrops in Ménière's disease with single-dose intravenous gadolinium-based contrast media using heavily T(2)-weighted 3D-FLAIR. *Magn Reson Med Sci.* (2010) 9:237–42. doi: 10.2463/mrms.9.237

19. Nakashima T, Naganawa S, Pyykko I, Gibson WPR, Sone M, Nakata S, et al. Grading of endolymphatic hydrops using magnetic resonance imaging. *Acta Otolaryngol Suppl.* (2009) 560:5–8. doi: 10.1080/00016480902729827
20. Baráth K, Schuknecht B, Naldi AM, Schrepfer T, Bockisch CJ, Hegemann SCA. Detection and grading of endolymphatic hydrops in Menière disease using MR imaging. *Am J Neuroradiol.* (2014) 35:1387–92. doi: 10.3174/ajnr.A3856
21. Bernaerts A, Vanspauwen R, Blaivie C, van Dinther J, Zarowski A, Wuyts FL, et al. The value of four stage vestibular hydrops grading and asymmetric perilymphatic enhancement in the diagnosis of Menière's disease on MRI. *Neuroradiology.* (2019) 61:421–9. doi: 10.1007/s00234-019-02155-7
22. Kirsch V, Becker-Bense S, Berman A, Kierig E, Ertl-Wagner B, Dieterich M. Transient endolymphatic hydrops after an attack of vestibular migraine: a longitudinal single case study. *J Neurol.* (2018) 265(Suppl. 1):51–3. doi: 10.1007/s00415-018-8870-3
23. Bernaerts A, De Foer B. Imaging of Ménière disease. *Neuroimaging Clin North Am.* (2019) 29:19–28. doi: 10.1016/j.nic.2018.09.002
24. Gürkov R, Flatz W, Louza J, Strupp M, Ertl-Wagner B, Krause E. *In vivo* visualized endolymphatic hydrops and inner ear functions in patients with electrocochleographically confirmed Ménière's disease. *Otol Neurotol.* (2012) 33:1040–5. doi: 10.1097/MAO.0b013e31825d9a95
25. Yang S, Zhu H, Zhu B, Wang H, Chen Z, Wu Y, et al. Correlations between the degree of endolymphatic hydrops and symptoms and audiological test results in patients with Menière's disease: a reevaluation. *Otol Neurotol.* (2018) 39:351–6. doi: 10.1097/MAO.0000000000001675
26. Homann G, Vieth V, Weiss D, Nikolaou K, Heindel W, Notohamiprodjo M, et al. Semi-quantitative vs. volumetric determination of endolymphatic space in Menière's disease using endolymphatic hydrops 3T-HR-MRI after intravenous gadolinium injection. *PLoS ONE.* (2015) 10:e0120357. doi: 10.1371/journal.pone.0120357
27. Naganawa S, Suzuki K, Nakamichi R, Bokura K, Yoshida T, Sone M, et al. Semi-quantification of endolymphatic size on MR imaging after intravenous injection of single-dose gadodiamide: comparison between two types of processing strategies. *Magn Reson Med Sci.* (2013) 12:261–9. doi: 10.2463/mrms.2013-0019
28. Ohashi T, Naganawa S, Takeuchi A, Katagiri T, Kuno K. Quantification of endolymphatic space volume after intravenous administration of a single dose of gadolinium-based contrast agent: 3D-real inversion recovery versus HYDROPS-Mi2. *Magn Reson Med Sci.* (2019) 19:119–24. doi: 10.2463/mrms.mp.2019-0013
29. Gürkov R, Berman A, Dietrich O, Flatz W, Jerin C, Krause E, et al. MR volumetric assessment of endolymphatic hydrops. *Eur Radiol.* (2015) 25:585–95. doi: 10.1007/s00330-014-3414-4
30. Inui H, Sakamoto T, Ito T, Kitahara T. Magnetic resonance-based volumetric measurement of the endolymphatic space in patients with Meniere's disease and other endolymphatic hydrops-related diseases. *Auris Nasus Larynx.* (2019) 46:493–7. doi: 10.1016/j.anl.2018.11.008
31. Gerb J, Ahmadi SA, Kierig E, Ertl-Wagner B, Dieterich M, Kirsch V. VOLT: a novel open-source pipeline for automatic segmentation of endolymphatic space in inner ear MRI. *J Neurol.* (2020) 267:185–96. doi: 10.1007/s00415-020-10062-8
32. Cho YS, Cho K, Park CJ, Chung MJ, Kim JH, Kim K, et al. Automated measurement of hydrops ratio from MRI in patients with Ménière's disease using CNN-based segmentation. *Sci Rep.* (2020) 10:7003. doi: 10.1038/s41598-020-63887-8
33. Lopez-Escamez JA, Carey J, Chung W-H, Goebel JA, Magnusson M, Mandalà M, et al. Diagnostic criteria for Menière's disease. *J Vestib Res.* (2015) 25:1–7. doi: 10.3233/VES-150549
34. Oldfield RC. The assessment and analysis of handedness: the Edinburgh inventory. *Neuropsychologia.* (1971) 9:97–113. doi: 10.1016/0028-3932(71)90067-4
35. Salmaso D, Longoni AM. Problems in the assessment of hand preference. *Cortex.* (1985) 21:533–49. doi: 10.1016/s0010-9452(58)80003-9
36. Dill T. Contraindications to magnetic resonance imaging. *Heart.* (2008) 94:943–8. doi: 10.1136/hrt.2007.125039
37. Matsumoto M, Nishimura T. Mersenne twister: a 623-dimensionally equidistributed uniform pseudo-random number generator. *ACM Trans Model Comput Simul.* (1998) 8:3–30. doi: 10.1145/272991.272995
38. Dieterich M, Brandt T. Ocular torsion and tilt of subjective visual vertical are sensitive brainstem signs. *Ann Neurol.* (1993) 33:292–9. doi: 10.1002/ana.410330311
39. Halmagyi GM, Curthoys IS. A clinical sign of canal paresis. *Arch Neurol.* (1988) 45:737–9. doi: 10.1001/archneur.1988.00520310043015
40. Schneider E, Villgrattner T, Vockeroth J, Bartl K, Kohlbecher S, Bardins S, et al. EyeSeeCam: an eye movement-driven head camera for the examination of natural visual exploration. *Ann N Y Acad Sci.* (2009) 1164:461–7. doi: 10.1111/j.1749-6632.2009.03858.x
41. Strupp M, Kim J-S, Murofushi T, Straumann D, Jen JC, Rosengren SM, et al. Bilateral vestibulopathy: diagnostic criteria consensus document of the classification committee of the Bárány society. *J Vestib Res.* (2017) 27:177–89. doi: 10.3233/VES-170619
42. Jongkees LB, Maas JP, Philipszoon AJ. Clinical nystagmography. A detailed study of electro-nystagmography in 341 patients with vertigo. *Pract Otorhinolaryngol.* (1962) 24:65–93.
43. Dlugaiczyk J, Habs M, Dieterich M. Vestibular evoked myogenic potentials in vestibular migraine and Menière's disease: cVEMPs make the difference. *J Neurol.* (2020) 267(Suppl. 1):169–80. doi: 10.1007/s00415-020-09902-4
44. Curthoys IS, Dlugaiczyk J. Physiology, clinical evidence and diagnostic relevance of sound-induced and vibration-induced vestibular stimulation. *Curr Opin Neurol.* (2020) 33:126–35. doi: 10.1097/WCO.0000000000000770
45. Ertl M, Boegle R, Kirsch V, Dieterich M. On the impact of examiners on latencies and amplitudes in cervical and ocular vestibular-evoked myogenic potentials evaluated over a large sample (N = 1,038). *Eur Arch Otorhinolaryngol.* (2016) 273:317–23. doi: 10.1007/s00405-015-3510-3
46. Nahmani S, Vaussy A, Hautefort C, Guichard J-P, Guillonet A, Houdart E, et al. Comparison of enhancement of the vestibular perilymph between variable and constant flip angle-delayed 3D-FLAIR sequences in Menière disease. *Am J Neuroradiol.* (2020) doi: 10.3174/ajnr.A6483
47. Legland D, Arganda-Carreras I, Andrey P. MorphoLibJ: integrated library and plugins for mathematical morphology with ImageJ. *Bioinformatics.* (2016) 32:3532–4. doi: 10.1093/bioinformatics/btw413
48. Schindelin J, Arganda-Carreras I, Frise E, Kaynig V, Longair M, Pietzsch T, et al. Fiji: an open-source platform for biological-image analysis. *Nat Methods.* (2012) 9:676–82. doi: 10.1038/nmeth.2019
49. Székely GJ, Rizzo ML. Energy statistics: a class of statistics based on distances. *J Statist Plan Inference.* (2013) 143:1249–72. doi: 10.1016/j.jspi.2013.03.018
50. Gretton A, Borgwardt K, Rasch M, Schölkopf B, Smola A. A kernel two-sample test. *J Mach Learn Res.* (2012) 13:723–73. doi: 10.5555/2503308.2188410
51. Milletari F, Navab N, Ahmadi S-A. V-Net: fully convolutional neural networks for volumetric medical image segmentation. *arXiv:160604797.* (2016). Available online at: http://arxiv.org/abs/1606.04797
52. Milletari F, Frei J, Aboulatta M, Vivar G, Ahmadi S-A. Cloud deployment of high-resolution medical image analysis with TOMAAT. *IEEE J Biomed Health Inform.* (2019) 23:969–77. doi: 10.1109/JBHI.2018.2885214
53. Fedorov A, Beichel R, Kalpathy-Cramer J, Finet J, Fillion-Robin J-C, Pujol S, et al. 3D slicer as an image computing platform for the quantitative imaging network. *Magn Reson Imaging.* (2012) 30:1323–41. doi: 10.1016/j.mri.2012.05.001
54. Nizamutdinov V. *Neural Network and Fuzzy Logic Based Plugins for ImageJ.* (2015). Available online at: https://github.com/astartes91/imagej-neural-fuzzy-plugins
55. Kendall MG, Smith BB. The problem of m rankings. *Ann Math Statist.* (1939) 10:275–87. doi: 10.1214/aoms/1177732186
56. Armitage P, Berry G, Matthews JNS. Modelling continuous data. In: *Statistical Methods in Medical Research.* 4th edn. Oxford: John Wiley & Sons, Ltd. (2002). p. 312–77. doi: 10.1002/9780470773666.ch11
57. Oh S-Y, Dieterich M, Lee BN, Boegle R, Kang J-J, Lee N-R, et al. Endolymphatic hydrops in patients with vestibular migraine and concurrent Meniere's disease. *Front. Neurol.* (2021) 12:594481. doi: 10.3389/fneur.2021.594481
58. Fukuoka H, Takumi Y, Tsukada K, Miyagawa M, Oguchi T, Ueda H, et al. Comparison of the diagnostic value of 3 T MRI after intratympanic injection of GBCA, electrocochleography, and the glycerol test in patients with Meniere's disease. *Acta Oto-Laryngol.* (2012) 132:141–5. doi: 10.3109/00016489.2011.635383

59. Naganawa S, Kawai H, Sone M, Nakashima T. Increased sensitivity to low concentration gadolinium contrast by optimized heavily T2-weighted 3D-FLAIR to visualize endolymphatic space. *Magn Reson Med Sci.* (2010) 9:73–80. doi: 10.2463/mrms.9.73
60. Naganawa S. The technical and clinical features of 3D-FLAIR in neuroimaging. *Magn Reson Med Sci.* (2015) 14:93–106. doi: 10.2463/mrms.2014-0132
61. Hirai T, Ando Y, Yamura M, Kitajima M, Hayashida Y, Korogi Y, et al. Transthyretin-related familial amyloid polyneuropathy: evaluation of CSF enhancement on serial T1-weighted and fluid- attenuated inversion recovery images following intravenous contrast administration. *Am J Neuroradiol.* (2005) 26:2043–8.
62. Naganawa S, Komada T, Fukatsu H, Ishigaki T, Takizawa O. Observation of contrast enhancement in the cochlear fluid space of healthy subjects using a 3D-FLAIR sequence at 3 Tesla. *Eur Radiol.* (2006) 16:733–7. doi: 10.1007/s00330-005-0046-8
63. Naganawa S, Suzuki K, Yamazaki M, Sakurai Y. Serial scans in healthy volunteers following intravenous administration of gadoteridol: time course of contrast enhancement in various cranial fluid spaces. *Magn Reson Med Sci.* (2014) 13:7–13. doi: 10.2463/mrms.2013-0056
64. Suzuki H, Teranishi M, Sone M, Yamazaki M, Naganawa S, Nakashima T. Contrast enhancement of the inner ear after intravenous administration of a standard or double dose of gadolinium contrast agents. *Acta Otolaryngol.* (2011) 131:1025–31. doi: 10.3109/00016489.2011.598552
65. Naganawa S, Koshikawa T, Nakamura T, Fukatsu H, Ishigaki T, Aoki I. High-resolution T1-weighted 3D real IR imaging of the temporal bone using triple-dose contrast material. *Eur Radiol.* (2003) 13:2650–8. doi: 10.1007/s00330-003-1922-8
66. Yamazaki M, Naganawa S, Kawai H, Sone M, Nakashima T. Gadolinium distribution in cochlear perilymph: differences between intratympanic and intravenous gadolinium injection. *Neuroradiology.* (2012) 54:1161–9. doi: 10.1007/s00234-012-1078-9
67. Iida T, Teranishi M, Yoshida T, Otake H, Sone M, Kato M, et al. Magnetic resonance imaging of the inner ear after both intratympanic and intravenous gadolinium injections. *Acta Oto-Laryngol.* (2013) 133:434–8. doi: 10.3109/00016489.2012.753640
68. Mamourian AC, Hoopes PJ, Lewis LD. Visualization of intravenously administered contrast material in the CSF on fluid-attenuated inversion-recovery MR images: an *in vitro* and animal-model investigation. *Am J Neuroradiol.* (2000) 21:105–111.
69. Naganawa S, Yamazaki M, Kawai H, Bokura K, Sone M, Nakashima T. Imaging of Ménière's disease by subtraction of MR cisternography from positive perilymph image. *Magn Reson Med Sci.* (2012) 11:303–9. doi: 10.2463/mrms.11.303
70. Naganawa S, Yamazaki M, Kawai H, Bokura K, Sone M, Nakashima T. Imaging of Ménière's disease after intravenous administration of single-dose gadodiamide: utility of multiplication of MR cisternography and HYDROPS image. *Magn Reson Med Sci.* (2013) 12:63–8. doi: 10.2463/mrms.2012-0027
71. Counter SA, Nikkhou-Aski S, Damberg P, Berglin CE, Laurell G. Ultra-high-field (9.4 T) MRI analysis of contrast agent transport across the blood-perilymph barrier and intrastrial fluid-blood barrier in the mouse inner ear. *Otol Neurotol.* (2017) 38:1052–9. doi: 10.1097/MAO.0000000000001458
72. Counter SA. MRI evidence of endolymphatic impermeability to the gadolinium molecule in the in vivo mouse inner ear at 9.4 Tesla. *Open Neuroimag J.* (2013) 7:27–31. doi: 10.2174/1874440001307010027
73. Naganawa S, Yamazaki M, Kawai H, Bokura K, Sone M, Nakashima T. Imaging of Ménière's disease after intravenous administration of single-dose gadodiamide: utility of subtraction images with different inversion time. *Magn Reson Med Sci.* (2012) 11:213–9. doi: 10.2463/mrms.11.213
74. Naganawa S, Kanou M, Ohashi T, Kuno K, Sone M. Simple estimation of the endolymphatic volume ratio after intravenous administration of a single-dose of gadolinium contrast. *Magn Reson Med Sci.* (2016) 15:379–85. doi: 10.2463/mrms.mp.2015-0175
75. Sepahdari AR, Ishiyama G, Vorasubin N, Peng KA, Linetsky M, Ishiyama A. Delayed intravenous contrast-enhanced 3D FLAIR MRI in Meniere's disease: correlation of quantitative measures of endolymphatic hydrops with hearing. *Clinical Imaging.* (2015) 39:26–31. doi: 10.1016/j.clinimag.2014.09.014
76. Kirsch V, Nejatbakhshesfahani F, Ahmadi S-A, Dieterich M, Ertl-Wagner B. A probabilistic atlas of the human inner ear's bony labyrinth enables reliable atlas-based segmentation of the total fluid space. *J Neurol.* (2019) 266(Suppl. 1):52–61. doi: 10.1007/s00415-019-09488-6
77. Ahmadi S-A, Raiser T, Ruehl RM, Flanagin VL, zu Eulenburg P. IE-map: a novel *in-vivo* atlas template of the human inner ear. *Sci Rep.* (2021) 11:3293. doi: 10.1038/s41598-021-82716-0
78. Ito T, Inui H, Miyasaka T, Shiozaki T, Matsuyama S, Yamanaka T, et al. Three-Dimensional magnetic resonance imaging reveals the relationship between the control of vertigo and decreases in endolymphatic hydrops after endolymphatic sac drainage with steroids for Meniere's disease. *Front Neurol.* (2019) 10:46. doi: 10.3389/fneur.2019.00046
79. Shi S, Guo P, Li W, Wang W. Clinical features and endolymphatic hydrops in patients with MRI evidence of hydrops. *Ann Otol Rhinol Laryngol.* (2019) 128:286–92. doi: 10.1177/0003489418819551
80. Shimono M, Teranishi M, Yoshida T, Kato M, Sano R, Otake H, et al. Endolymphatic hydrops revealed by magnetic resonance imaging in patients with acute low-tone sensorineural hearing loss. *Otol Neurotol.* (2013) 34:1241–6. doi: 10.1097/MAO.0b013e3182990e81
81. Attyé A, Eliezer M, Boudiaf N, Tropres I, Chechin D, Schmerber S, et al. MRI of endolymphatic hydrops in patients with Meniere's disease: a case-controlled study with a simplified classification based on saccular morphology. *Eur Radiol.* (2017) 27:3138–46. doi: 10.1007/s00330-016-4701-z
82. Cho YS, Ahn JM, Choi JE, Park HW, Kim Y-K, Kim H-J, et al. Usefulness of intravenous gadolinium inner ear MR imaging in diagnosis of Ménière's disease. *Sci Rep.* (2018) 8:17562. doi: 10.1038/s41598-018-35709-5
83. Hornibrook J, Flook E, Greig S, Babbage M, Goh T, Coates M, et al. MRI inner ear imaging and tone burst electrocochleography in the diagnosis of Ménière's disease. *Otol Neurotol.* (2015) 36:1109–14. doi: 10.1097/MAO.0000000000000782
84. He B, Zhang F, Zheng H, Sun X, Chen J, Chen J, et al. The correlation of a 2D volume-referencing endolymphatic-hydrops grading system with extra-tympanic electrocochleography in patients with definite Ménière's disease. *Front Neurol.* (2021) 11:595038. doi: 10.3389/fneur.2020.595038
85. Gürkov R, Kantner C, Strupp M, Flatz W, Krause E, Ertl-Wagner B. Endolymphatic hydrops in patients with vestibular migraine and auditory symptoms. *Eur Arch Otorhinolaryngol.* (2014) 271:2661–7. doi: 10.1007/s00405-013-2751-2
86. Jerin C, Floerke S, Maxwell R, Gürkov R. Relationship between the extent of endolymphatic hydrops and the severity and fluctuation of audiovestibular symptoms in patients with Menière's disease and MRI evidence of hydrops. *Otol Neurotol.* (2018) 39:e123–30. doi: 10.1097/MAO.0000000000001681
87. Eliezer M, Poillon G, Maquet C, Gillibert A, Horion J, Marie J-P, et al. Sensorineural hearing loss in patients with vestibular schwannoma correlates with the presence of utricular hydrops as diagnosed on heavily T2-weighted MRI. *Diagn Interv Imaging.* (2019) 100:259–68. doi: 10.1016/j.diii.2019.01.006
88. Katayama N, Yamamoto M, Teranishi M, Naganawa S, Nakata S, Sone M, et al. Relationship between endolymphatic hydrops and vestibular-evoked myogenic potential. *Acta Oto-Laryngol.* (2010) 130:917–23. doi: 10.3109/00016480903573187
89. Kato M, Teranishi M, Katayama N, Sone M, Naganawa S, Nakashima T. Association between endolymphatic hydrops as revealed by magnetic resonance imaging and caloric response. *Otol Neurotol.* (2011) 32:1480–5. doi: 10.1097/MAO.0b013e318235568d
90. Zhang W, Hui L, Zhang B, Ren L, Zhu J, Wang F, et al. The correlation between endolymphatic hydrops and clinical features of Meniere disease. *Laryngoscope.* (2020) 131:E144–50. doi: 10.1002/lary.28576
91. Shi S, Guo P, Wang W. Magnetic resonance imaging of Ménière's disease after intravenous administration of gadolinium. *Ann Otol Rhinol Laryngol.* (2018) 127:777–82. doi: 10.1177/0003489418794699
92. Inui H, Sakamoto T, Ito T, Kitahara T. Volumetric measurements of the inner ear in patients with Meniere's disease using three-dimensional magnetic resonance imaging. *Acta Oto-Laryngol.* (2016) 136:888–93. doi: 10.3109/00016489.2016.1168940
93. Naganawa S, Ohashi T, Kanou M, Kuno K, Sone M, Ikeda M. Volume quantification of endolymph after intravenous administration of a single dose of gadolinium contrast agent: comparison of 18- versus

8-minute imaging protocols. *Magn Reson Med Sci.* (2015) 14:257–62. doi: 10.2463/mrms.2014-0118

94. Ito T, Inui H, Miyasaka T, Shiozaki T, Hasukawa A, Yamanaka T, et al. Endolymphatic volume in patients with Meniere's disease and healthy controls: three-dimensional analysis with magnetic resonance imaging. *Laryngoscope Investig Otolaryngol.* (2019) 4:653–8. doi: 10.1002/lio2.313
95. Ito T, Kitahara T, Inui H, Miyasaka T, Kichikawa K, Ota I, et al. Endolymphatic space size in patients with Meniere's disease and healthy controls. *Acta Oto-Laryngol.* (2016) 136:879–82. doi: 10.3109/00016489.2016.1169556
96. Naganawa S, Satake H, Kawamura M, Fukatsu H, Sone M, Nakashima T. Separate visualization of endolymphatic space, perilymphatic space and bone by a single pulse sequence; 3D-inversion recovery imaging utilizing real reconstruction after intratympanic Gd-DTPA administration at 3 Tesla. *Eur Radiol.* (2008) 18:920–4. doi: 10.1007/s00330-008-0854-8
97. Adin ME, Kleinberg L, Vaidya D, Zan E, Mirbagheri S, Yousem DM. Hyperintense dentate nuclei on T1-weighted MRI: relation to repeat gadolinium administration. *Am J Neuroradiol.* (2015) 36:1859–65. doi: 10.3174/ajnr.A4378
98. Barbieri S, Schroeder C, Froehlich JM, Pasch A, Thoeny HC. High signal intensity in dentate nucleus and globus pallidus on unenhanced T1-weighted MR images in three patients with impaired renal function and vascular calcification. *Contrast Media Mol Imaging.* (2016) 11:245–50. doi: 10.1002/cmmi.1683
99. Errante Y, Cirimele V, Mallio CA, Di Lazzaro V, Zobel BB, Quattrocchi CC. Progressive increase of T1 signal intensity of the dentate nucleus on unenhanced magnetic resonance images is associated with cumulative doses of intravenously administered gadodiamide in patients with normal renal function, suggesting dechelation. *Investigat Radiol.* (2014) 49:685–90. doi: 10.1097/RLI.0000000000000072

Conflict of Interest: The authors declare that the research was conducted in the absence of any commercial or financial relationships that could be construed as a potential conflict of interest.

frontiers
in Neurology

SYSTEMATIC REVIEW
published: 20 May 2021
doi: 10.3389/fneur.2021.662264

MRI With Gadolinium as a Measure of Blood-Labyrinth Barrier Integrity in Patients With Inner Ear Symptoms: A Scoping Review

Christopher I. Song[1], *Jacob M. Pogson*[1,2,3], *Nicholas S. Andresen*[1] *and Bryan K. Ward*[1*]

[1] *Department of Otolaryngology-Head and Neck Surgery, Johns Hopkins University School of Medicine, Baltimore, MD, United States,* [2] *Department of Neurology, Johns Hopkins University School of Medicine, Baltimore, MD, United States,* [3] *Department of Neurology, Royal Prince Alfred Hospital, Camperdown, NSW, Australia*

Objective: Capillaries within the inner ear form a semi-permeable barrier called the blood-labyrinth barrier that is less permeable than capillary barriers elsewhere within the human body. Dysfunction of the blood-labyrinth barrier has been proposed as a mechanism for several audio-vestibular disorders. There has been interest in using magnetic resonance imaging (MRI) with intravenous gadolinium-based contrast agents (GBCA) as a marker for the integrity of the blood labyrinth barrier in research and clinical settings. This scoping review evaluates the evidence for using intravenous gadolinium-enhanced MRI to assess the permeability of the blood-labyrinth barrier in healthy and diseased ears.

Methods: A systematic search was conducted of three databases: PubMed, EMBASE, CINAHL PLUS. Studies were included that used GBCA to study the inner ear and permeability of the blood-labyrinth barrier. Data was collected on MRI protocols used and inner ear enhancement patterns of healthy and diseased ears in both human and animal studies.

Results: The search yielded 14 studies in animals and 53 studies in humans. In healthy animal and human inner ears, contrast-enhanced MRI demonstrated gradual increase in inner ear signal intensity over time that was limited to the perilymph. Signal intensity peaked at 100 min in rodents and 4 h in humans. Compared to controls, patients with idiopathic sudden sensorineural hearing loss and otosclerosis had increased signal intensity both before and shortly after GBCA injection. In patients with Ménière's disease and vestibular schwannoma, studies reported increased signal at 4 h, compared to controls. Quality assessment of included studies determined that all the studies lacked sample size justification and many lacked adequate control groups or blinded assessors of MRI.

Conclusions: The included studies provided convincing evidence that gadolinium crosses the blood-labyrinth barrier in healthy ears and more rapidly in some diseased ears. The timing of increased signal differs by disease. There was a lack of evidence that these findings indicate general permeability of the blood-labyrinth barrier. Future studies with consistent and rigorous methods are needed to investigate the relationship between

Edited by:
Stefan K. Plontke,
Martin Luther University of
Halle-Wittenberg, Germany

Reviewed by:
Jeremy Hornibrook,
University of Canterbury, New Zealand
Andreas Deistung,
Universitätsklinikum Halle, Germany

****Correspondence:***
Bryan K. Ward
bward15@jh.edu

Specialty section:
This article was submitted to
Neuro-Otology,
a section of the journal
Frontiers in Neurology

Received: *31 January 2021*
Accepted: *16 April 2021*
Published: *20 May 2021*

Citation:
Song CI, Pogson JM, Andresen NS and Ward BK (2021) MRI With Gadolinium as a Measure of Blood-Labyrinth Barrier Integrity in Patients With Inner Ear Symptoms: A Scoping Review.
Front. Neurol. 12:662264.
doi: 10.3389/fneur.2021.662264

gadolinium uptake and assessments of inner ear function and to better determine whether signal enhancement indicates permeability for molecules other than gadolinium.

Keywords: otosclerosis, Ménière's disease, inner ear, blood-labyrinth barrier, gadolinium, MRI

INTRODUCTION

Living tissues need a steady supply of nutrients to support metabolism and clear waste. Blood vessels lined by endothelial cells transport these metabolic resources, and capillaries are the site at which nutrients and waste are exchanged. Capillaries have different features depending on the needs of nearby tissues, being more porous, for example in the liver, or more restrictive in the retina (1). In some locations, such as the brain, capillaries form junctions that are so impermeable they create a continuous

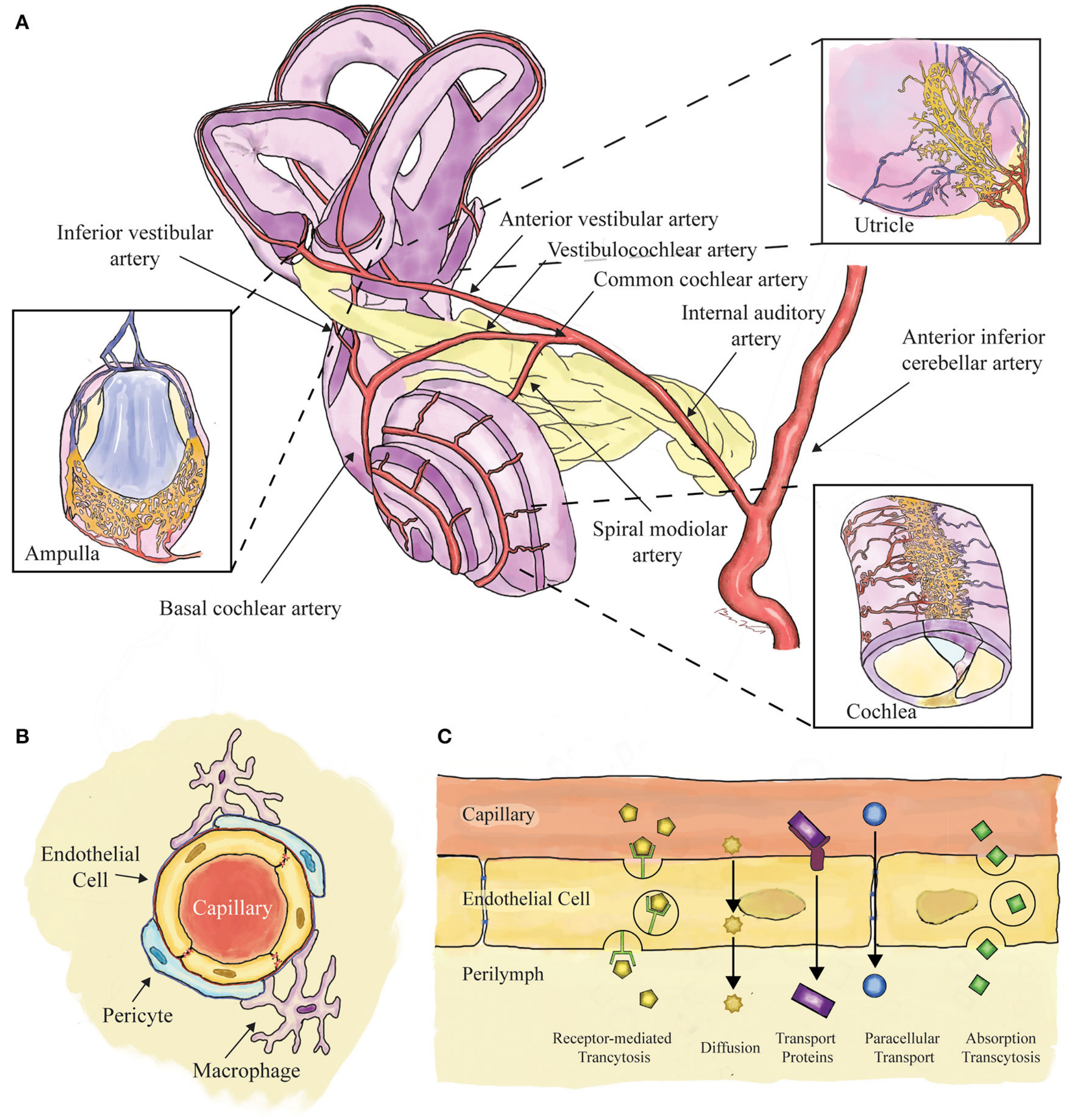

FIGURE 1 | Schematic showing the components of the blood-labyrinth barrier. **(A)** Blood supply to the labyrinth is shown, with insets showing capillary beds near the sensory epithelia of the ampullae, otoconial organs, and cochlea. **(B)** Capillaries of the blood-labyrinth barrier include endothelial cells with tight junctions, surrounded by pericytes and resident macrophages that regulate permeability. **(C)** Examples of hypothetical mechanisms by which molecules can transit across the barrier are shown.

TABLE 1 | Modifications made to the NIH quality assessment checklist.

Modified NIH quality assessment checklist

Original question	**Specific interpretation used**
Was the research question or objective in this paper clearly stated?	Was the assessment of abnormal inner ear enhancement or blood-labyrinth barrier breakdown a specified goal of the research?
Was the study population clearly specified and defined?	Was the study population specified as a single or multi-center sample? Was the sampling method described?
Was the participation rate of eligible persons at least 50%? Were all the subjects selected or recruited from the same or similar populations (including the same time period)? Were inclusion and exclusion criteria for being in the study pre-specified and applied uniformly to all participants?	Were the inclusion criteria specific and applied uniformly?
Was a sample size justification, power description, or variance and effect estimates provided?	Was a power analysis included to justify sample sizes?
For the analyses in this paper, were the exposure(s) of interest measured prior to the outcome(s) being measured?	Were patients included in the study prior to MRI assessment?
Was the timeframe sufficient so that one could reasonably expect to see an association between exposure and outcome if it existed?	Did patients undergo MRI within a reasonable time frame from symptom onset in studies of disease states? (i.e., within 30 days for ISSHL)
For exposures that can vary in amount or level, did the study examine different levels of the exposure as related to the outcome (e.g., categories of exposure, or exposure measured as continuous variable)?	Were both pre-contrast and post-contrast MRI evaluated?
Were the exposure measures (independent variables) clearly defined, valid, reliable, and implemented consistently across all study participants?	Were the MRI protocol and contrast dose and agent clearly described?
Was the exposure(s) assessed more than once over time?	Was MRI performed and assessed at varying time points following contrast administration?
Were the outcome measures (dependent variables) clearly defined, valid, reliable, and implemented consistently across all study participants?	Was the measurement of contrast enhancement done with clearly specified and reliable methods?
Were the outcome assessors blinded to the exposure status of participants?	Was it clearly specified that MRI findings were evaluated by individuals blinded to the clinical status of patients?
Was loss to follow-up after baseline 20% or less? Were key potential confounding variables measured and adjusted statistically for their impact on the relationship between exposure(s) and outcome(s)?	Were reasonable controls used as comparisons to diseased ears?

If no interpretations are specified, the original question was sufficient for our purposes. MRI, magnetic resonance imaging, ISSHL, idiopathic sudden sensorineural hearing loss.

barrier. In the inner ear, a blood-labyrinth barrier was first proposed to explain differential uptake of intravenously injected compounds between the endolymph and perilymph spaces (2).

Intravenously injected compounds reach the inner ear via the labyrinthine artery, a branch of the anterior inferior cerebellar artery, that subsequently branches into smaller vessels to supply the labyrinth and cochlea (**Figure 1A**). Capillary networks in the inner ear are clustered around the stria vascularis and spiral ligament in the cochlea, and the sensory epithelia of the vestibular system (3). These capillary networks are—like in the eye and brain—the presumed location of the blood-labyrinth barrier, composed of endothelial cells with tight-junctions surrounded by pericytes and resident macrophages (4) (**Figure 1B**). These barriers tightly regulate ion composition within the endolymph and perilymph, and are permeable to water, glucose, and small molecules (5, 6). Molecules transit across the barrier *via* a variety of mechanisms including diffusion, endocytosis, and transcellular protein transport (7) (**Figure 1C**).

The role of the blood-labyrinth barrier in clinical medicine is receiving increased attention. Studies have shown that several hours following intravenous administration of gadolinium-based contrast agents (GBCA), the perilymphatic space of the inner ear enhances on magnetic resonance imaging (MRI) studies (8). MRI using stronger static magnetic fields and new pulse sequences has improved spatial resolution and takes advantage of this contrast between the endolymph-filled membranous labyrinth and the surrounding perilymphatic space. These MRI techniques have emerged as a useful research tool in the study of Ménière's disease, a disorder in which patients commonly have a swelling of the membranous labyrinth (9). It is presumed that the increased signal intensity reflects GBCA crossing the blood-labyrinth barrier.

More recently, studies have begun exploring the use of GBCA to determine the integrity of the blood-labyrinth barrier in disease. In addition to transmitting small molecules, capillaries also allow the transit of white blood cells into tissues (10). During inflammation, released cytokines can activate capillary endothelial cells, increasing capillary permeability (11). Increased permeability may have deleterious effects on the inner ear (4). An imaging marker of the permeability of the blood-labyrinth barrier could provide diagnostic and prognostic information and aid the development of new therapies for inner ear diseases. The aim of this scoping review was to assess the evidence for the use of GBCA as a marker of permeability of the blood-labyrinth barrier in animals and humans with inner ear disease.

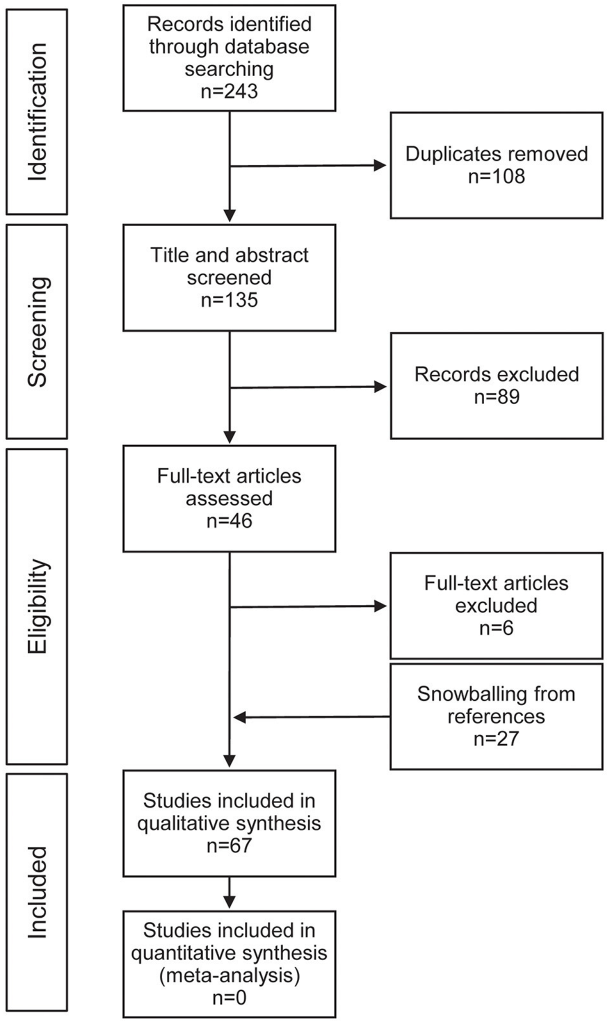

FIGURE 2 | Preferred reporting items for systematic reviews and meta-analyses (PRISMA) flow diagram for study selection.

METHODS

A scoping review was performed with the aim of synthesizing knowledge regarding the use of MRI to assess the integrity of the blood-labyrinth barrier. A broad search was performed using three databases: PubMed, EMBASE, and CINAHL Plus. This search was performed on 10/5/2020 using controlled vocabulary (e.g., MeSH terms in PubMed) and keywords related to the concepts of the "inner ear," "contrast-enhanced MRI," and the "blood-labyrinth barrier" (see **Supplementary Material**). The search strategy was created with assistance from staff at the Welch Medical Library at Johns Hopkins Medicine.

Two study members (CS and BW) independently evaluated articles and included those that met the following inclusion criteria: aims to assess the blood-labyrinth barrier with MRI, uses a GBCA administered via intravenous injection, includes original data, is not a case report (i.e., must include data from more than one individual), and is written in English language. Additional articles were included *via* a snowballing approach, where the references in each included article were assessed using the same inclusion criteria.

For both clinical and animal studies we recorded data on enhancement of inner ear structures in diseased and healthy ears, the imaging protocol, MRI static magnetic field strength, the GBCA and dose, and the time from contrast injection to image acquisition.

All co-authors reviewed the included studies and two study members (CS and BW) also evaluated the quality and risk of bias of each clinical research article using a modified version of the National Institutes of Health (NIH) Quality Assessment Tool for Cross-Sectional Studies (12) (**Table 1**).

Since the goal of this scoping review was to qualitatively describe the current literature and map key concepts in this field, test statistics were not performed.

RESULTS

Literature Search

Our database search yielded 243 citations, 88 from PubMed, 109 from EMBASE, and 46 from CINAHL Plus. After duplicate articles were removed, there were 135 unique search results. After full text review with the application of selection criteria we had 40 included publications. Additional review of the references from the initial included publications yielded an additional 27 citations that met the selection criteria and were included in the final analysis (**Figure 2**).

Animal Studies

There were 14 animal studies in this review that evaluated MRI of healthy and diseased inner ears of guinea pigs and/or mice. Eleven of these studies administered contrast agent in doses of 1.5 mmol/kg and used MRI scanners of magnetic field strengths 4.7 Tesla (T) or greater. Studies in healthy ears of guinea pigs and mice reported increased signal intensity within the perilymph, consistent with GBCA uptake, that increased over time and peaked at 100 min, whereas no enhancement was seen in the endolymph (13–18). Enhancement was first seen in the cochlea with relative greater signal in the scala tympani than the scala vestibuli, followed by the utricle and saccule, and the ampullated ends of the semicircular canals (19, 20). The areas correspond to capillary networks in the inner ear, suggesting entry of GBCA at the blood-labyrinth barrier. Comparison of different GBCA found some variation in signal intensity and uptake kinetics, but intravenous administration of both macrocyclic and linear agents reliably led to enhancement of perilymph (20, 21). In mice, all GBCAs led to enhancement of perilymph with increasing intensity over time from 15–105 min (20). Gadobutrol (Gadovist) was shown to have the most rapid uptake and greatest signal enhancement while gadopentetate dimeglumine (Magnevist) had the slowest and lowest intensity of enhancement (20). In three studies, mechanical trauma to and inflammation of the inner ear were found to increase the rate of signal intensity rise in the inner ear following intravenous GBCA over 15–80 min above the rate in control animals (14, 19, 22).

TABLE 2 | Quality assessment of included human studies with the NIH quality assessment tool.

Author	Clear Research Question	Clearly Specified Pop.	Participation >50%	Uniform Inclusion Criteria	Sample Size Justification	Exposure measured before outcome	Sufficient Timeframe	Varied Exposure Levels Measured	Clearly Defined Exposure	Exposure Assessed Over time	Clearly Defined Outcome	Assessors Blinded	<20% Loss to Follow-up	Confounders Addressed
Sartoretti-Schefer (34)	N	N	NA	N	N	Y	Y	Y	N	N	N	N	NA	Y
Sartoretti-Schefer (35)	N	Y	NA	Y	N	Y	N	Y	N	N	N	N	NA	N
Fitzgerald and Mark (36)	N	N	NA	Y	N	Y	N	N	N	N	N	N	NA	N
Stokroos et al. (37)	Y	N	NA	Y	N	Y	N	N	N	N	N	N	NA	N
Strupp et al. (38)	Y	N	NA	Y	N	Y	Y	N	Y	N	N	N	NA	N
Schick et al. (39)	N	N	NA	N	N	Y	N	N	N	N	N	Y	NA	N
Naganawa et al. (40)	Y	Y	NA	Y	N	NA	NA	Y	Y	Y	N	N	NA	NA
Naganawa et al. (33)	Y	Y	NA	Y	N	NA	NA	Y	Y	Y	Y	N	NA	NA
Cadoni et al. (41)	N	Y	NA	Y	N	Y	Y	Y	N	N	N	N	NA	N
Sugiura et al. (42)	Y	Y	NA	Y	N	Y	Y	Y	Y	N	N	N	NA	Y
Sone et al. (43)	Y	Y	NA	N	N	Y	Y	Y	Y	N	N	N	NA	N
Carfrae et al. (8)	Y	N	NA	Y	N	Y	Y	N	Y	N	N	Y	NA	Y
Yoshida et al. (44)	Y	Y	NA	Y	N	Y	Y	Y	Y	Y	Y	N	NA	N
Yamazaki et al. (45)	Y	Y	NA	Y	N	Y	Y	Y	Y	N	Y	N	NA	Y
Lee et al. (46)	Y	Y	NA	N	N	Y	N	Y	Y	N	Y	N	NA	Y
Nakata et al. (47)	N	N	NA	Y	N	Y	Y	Y	Y	N	Y	Y	NA	Y
Tagaya et al. (48)	Y	N	NA	N	N	Y	Y	N	Y	N	Y	Y	NA	Y
Tanigawa et al. (49)	Y	Y	NA	Y	N	Y	N	Y	Y	N	Y	Y	NA	N
Suzuki et al. (50)	Y	Y	NA	N	N	Y	Y	N	Y	N	Y	N	NA	N
Tagaya et al. (51)	Y	N	NA	N	N	Y	Y	N	Y	N	Y	Y	NA	Y
Naganawa et al. (52)	Y	Y	NA	N	N	Y	Y	Y	Y	Y	Y	Y	NA	N
Sano et al. (53)	Y	N	NA	N	N	Y	N	Y	Y	Y	Y	Y	NA	Y
Berrettini et al. (54)	Y	Y	NA	Y	N	Y	Y	Y	Y	N	Y	N	NA	Y
Ishikawa et al. (55)	Y	Y	NA	Y	N	Y	Y	Y	Y	N	Y	N	NA	Y

(Continued)

TABLE 2 | Continued

Author	Clear Research Question	Clearly Specified Pop.	Participation >50%	Uniform Inclusion Criteria	Sample Size Justification	Exposure measured before outcome	Sufficient Timeframe	Varied Exposure Levels Measured	Clearly Defined Exposure	Exposure Assessed Over time	Clearly Defined Outcome	Assessors Blinded	<20% Loss to Follow-up	Confounders Addressed
Kim et al. (56)	Y	N	Y	Y	N	Y	N	Y	Y	Y	Y	Y	NA	Y
Tanigawa et al. (57)	Y	N	NA	Y	N	Y	N	Y	Y	N	Y	Y	NA	N
Liao et al. (58)	N	N	Y	Y	N	Y	Y	Y	Y	N	Y	Y	NA	Y
Lombardo et al. (59)	Y	Y	Y	Y	N	Y	Y	N	Y	N	Y	Y	NA	Y
Naganawa et al. (60)	Y	Y	Y	Y	N	Y	Y	N	Y	N	Y	N	NA	Y
Pakdaman et al. (61)	Y	Y	Y	Y	N	Y	N	N	Y	N	Y	N	NA	Y
Attye et al. (62)	N	Y	NA	Y	N	Y	Y	N	Y	N	N	Y	NA	Y
Berrettini et al. (63)	Y	N	NA	Y	N	Y	Y	N	Y	N	Y	Y	NA	Y
Byun et al. (64)	Y	Y	Y	Y	N	Y	Y	Y	N	Y	N	Y	NA	Y
Eliezer et al. (65)	Y	Y	NA	Y	N	Y	Y	Y	Y	N	Y	Y	NA	Y
Bernaerts et al. (66)	Y	Y	NA	Y	N	Y	Y	N	Y	N	N	Y	NA	N
Conte et al. (67)	Y	Y	Y	Y	N	Y	Y	N	Y	N	Y	N	NA	Y
Eliezer et al. (68)	Y	Y	NA	Y	N	Y	N	N	Y	N	N	Y	NA	Y
Wang et al. (69)	Y	Y	NA	Y	N	Y	N	N	N	N	Y	Y	NA	Y
Bowen et al. (70)	Y	N	NA	Y	N	Y	Y	Y	Y	Y	Y	N	NA	Y
Eliezer et al. (71)	Y	N	NA	Y	N	Y	Y	N	Y	N	N	Y	NA	N
Eliezer et al. (72)	N	N	NA	N	N	N	N	N	Y	N	N	Y	NA	N
Kahn et al. (73)	N	Y	NA	Y	N	Y	Y	N	Y	N	N	Y	NA	N
Laine et al. (74)	Y	Y	NA	Y	N	Y	Y	N	Y	N	Y	Y	NA	Y

Details of each quality assessment category is explained in ***Table 1****. Studies that did not describe participation and follow-up details were described as "not available" (NA) for ">50% patient participation" and "<20% loss to follow up." For studies of healthy human ears, "not available" (NA) was used to describe "Exposure measured before outcome" and "Sufficient Timeframe".*

TABLE 3 | Summary of findings in studies of idiopathic sudden sensorineural hearing loss and vestibular neuritis.

Author	*n*	Controls (*n*)	MRI Timing (time after contrast)	MRI protocol	Gd agent (dose in mmol/kg)	Signal assessment	Findings regarding enhancement	Correlation with symptoms and prognosis
Idiopathic sudden sensorineural hearing loss and vestibular neuritis								
Stokroos et al. (37)	27	ND	Pre, Post (ND)	>1T MRI, T1W	ND	Qualitative	1 (3.7%) had high signal intensity pre- and post-contrast enhancement.	ND
Strupp et al. *(38)	60	ND	Post (ND)	1.5T, T1W and T2W	Gd-DTPA (0.2)	Qualitative	No enhancement in any patient (0%).	ND
Cadoni et al. (41)	54	ND	Pre, Post (ND)	1.5T, T1W and 3D-FLAIR	Gd-DTPA (ND)	Qualitative	2 (3.7%) had pre-contrast high signal intensity, 1 (1.9%) had post-contrast enhancement.	ND
Sugiura et al. (42)	8	Contralateral ear (8)	Pre, Post (10 min)	3T, 3D-FLAIR	Gadodiamide (0.1)	Qualitative	4 (50%) had pre-contrast high signal intensity, 1(12.5%) had enhancement at 10 min.	2 (100%) patients with vertigo had pre-contrast high signal intensity. Patient with post-contrast enhancement had poor outcome.
Yoshida et al. (44)	48**	Contralateral ear (48)	Pre, Post (10 min)	3T, 3D-FLAIR	Gadodiamide (0.1)	Qualitative	31 (65%) had pre-contrast high signal intensity, 16 (33%) had enhancement at 10 min.	8 (80%) with high signal intensity in labyrinth had vertigo. High signal intensity pre-contrast, not post-contrast, correlated with worse prognosis.
Tagaya et al. (48)	10	Contralateral ear (9)	Pre, Post (4 h)	3T, 3D-FLAIR	Gadoteridol (0.1,0.2)	Quantitative	5/10 (50%) of patients had signal enhancement over controls after 4 h.	ND
Berrettini et al. (54)	23	Healthy controls and contralateral ear (20)	Pre, Post (ND)	3T, 3D-FLAIR	Gadobutrol (0.1)	Qualitative	13 (57%) had pre-contrast high signal intensity, 8 (35%) had post-contrast enhancement.	Patients with pre-contrast high signal intensity had lower initial hearing levels. Enhancement pattern not correlated with prognosis.
Kim et al. (56)	30	Contralateral ear (30)	Post (10 min, 4 hr)	3T, 3D-FLAIR	Gd-DTPA (0.2)	Quantitative	Enhancement in affected ears was only greater than unaffected at 10 min.	ND

(Continued)

TABLE 3 | Continued

Idiopathic sudden sensorineural hearing loss and vestibular neuritis

Author	*n*	Controls (*n*)	MRI Timing (time after contrast)	MRI protocol	Gd agent (dose in mmol/kg)	Signal assessment	Findings regarding enhancement	Correlation with symptoms and prognosis
Tanigawa et al. (57)	11 pre, 18 post	ND	Pre, Post (ND)	3T, 3D-FLAIR	Gadodiamide (0.1)	Qualitative	2 (11%) had pre-contrast high signal intensity, 1 (9%) had post-contrast enhancement.	High signal intensity only seen in patients with more severe impairment. Patient with post-contrast enhancement had significant improvement
Liao et al. (58)	54	Contralateral ear (54)	Pre, Post (10 min)	1.5T, 3D-FLAIR, 3D-FIESTA-C, FSPGR	Gadobutrol (0.1)	Quantitative, Qualitative	Visual: 32 (59%) had pre- and post-contrast high signal intensity. Quantitative: 43 (80%) had pre-contrast high signal intensity, 37 (69%) had post-contrast enhancement.	Degree of enhancement asymmetry correlated to final hearing loss.
Pakdaman et al. (61)	11	Contralateral ear (32)	Post (4 h)	3T, hT2W-3D-FLAIR	Gadopentetate dimeglumine (0.2)	Quantitative	No significant signal difference between affected and contralateral ears.	ND
Byun et al. *(64)	29	Contralateral ear (29)	Pre, Post (10 min, 4 h)	3T, 3D-FLAIR	Gd-DTPA (0.2)	Qualitative	3 (10%) had enhancement at 10 min, 20 (69%) had enhancement at 4 h.	Duration of spontaneous nystagmus was correlated to enhancement at 4 h.
Eliezer et al. *(68)	30	Healthy controls (26)	Post (4 h)	3T, 3D-FLAIR	Gadobutrol (0.1)	Qualitative	26 (87%) had post-contrast enhancement.	ND
Wang et al. (69)	100	Contralateral ear (100)	Post (4 h)	3T, 3D-FLAIR	Meglumine gadopentetate (0.2)	Quantitative, Qualitative	65 (65%) had post-contrast enhancement.	Enhancement correlated to more severe hearing loss. Degree of enhancement asymmetry correlated to final hearing loss.

*Studies designated with (*) indicate studies of patients with vestibular neuritis. All other studies included in the table involved patients with idiopathic sudden sensorineural hearing loss (ISSHL). Data not included by authors in each study is depicted as "not described" (ND). Under the column MRI delay, "ND" is used to describe studies that did not report a specific delay time and is assumed to have performed MRI immediately after contrast injection. "Pre" indicates a scan was performed prior to the administration of contrast. Quantitative signal assessment methods involve the use of signal intensity measurements with regions of interest within the inner ear as compared to other imaged regions such as the cerebellum. **eight patients from Suguira 2006. T, tesla; Gd, gadolinium; FLAIR, fluid-attenuated inversion recovery; FIESTA, fast imaging employing steady-state acquisition; hT2W, heavily T2-weighted; FSPGR, fast spoiled gradient-echo; Gd-DTPA, gadolinium with diethylenetriaminepentacetate; T1W, T1-weighted; T2W, T2-weighted.*

TABLE 4 | Summary of findings in studies of Ménière's disease.

				Ménière's disease				
Author	***n***	**Controls (*n*)**	**MRI delay**	**MRI protocol**	**Gd agent (dose)**	**Signal assessment**	**Findings regarding enhancement**	**Correlation with symptoms**
Fitzgerald et al. (36)	13	ND	Pre, Post (ND)	1.5T, T2W	ND	Qualitative	1 (8%) had abnormal MRI findings.	ND
Carfrae et al. (8)	7	Healthy controls (4)	Post (4 h)	3T, T1W	Gadodiamide (0.3)	Qualitative	All (100%) patients and controls had enhancement by 4 h.	ND
Suzuki et al. (50)	32	ND	Post (4 h)	hT2W-3D- FLAIR and 3D- FLAIR, 3T	Gadoteridol (0.1) and Gadodiamide (0.2)	Quantitative	Signal intensity was higher in patients who received a double dose vs. single dose of contrast.	No correlation between hearing level and signal intensity.
Tagaya et al. (48)	12	Contralateral ear (10)	Post (4 h)	3D FLAIR and 3D rIR, 3T	Gadoteridol (0.2)	Quantitative	Signal intensity of diseased ears was higher than contralateral ears.	ND
Sano et al. (53)	6	Contralateral ear (7)	Post (10 min, 4 h)	hT2W-3D- FLAIR	Gadodiamide (0.1)	Quantitative	Signal intensity of diseased ears greater than contralateral at 4 h but not 10 min in definite and possible Ménière's.	ND
Naganawa et al. (52)	10	ND	Pre, Post (10 min, 3.5–4.5 h)	3T, hT2W-3D-FLAIR	Gadodiamide (0.1)	Quantitative	No pre-contrast increased signal intensity or 10 m enhancement. Increased signal intensity seen at 3.5–4 h.	ND
Naganawa et al. (60)	9	Healthy controls (8)	Post (4 h)	hT2W-3D-FLAIR, 3T	Gadodiamide (0.1)	Quantitative	Signal intensity of disease ears not higher than controls.	ND
Pakdaman et al. (61)	32	Contralateral ear (43)	Post (4 h)	hT2W-3D-FLAIR, 3T	Gadopentetate dimeglumine (0.2)	Quantitative	Symptomatic ears had higher signal intensity than contralateral ears.	All ears with symptomatic hydrops had enhancement
Attye et al. (62)	200	Healthy controls (30)	Post (4.5–5.5 h)	3T, 3D-FLAIR	Gadoterate meglumine (0.1)	Qualitative	15 (7.5%) had enhancement of the semicircular canals.	ND
Eliezer et al. (65)	20	Contralateral ear (20)	Post (4 h)	3T, 3D-FLAIR	Gd-DOTA and Gadobutrol (0.1,0.2)	Quantitative, Qualitative	No difference in signal intensity between symptomatic and asymptomatic for either Gd agent ($p = 0.14$).	ND

(Continued)

TABLE 4 | Continued

Author	*n*	Controls (*n*)	MRI delay	MRI protocol	Gd agent (dose)	Signal assessment	Findings regarding enhancement	Correlation with symptoms
Ménière's disease								
Bernaerts et al. (66)	78	Contralateral ear (78)	Post (4 h)	3T, 3D-FLAIR	Gadobutrol (0.2)	Qualitative	51 (65%) symptomatic ears had enhancement, 2 (2.6%) contralateral ears had enhancement.	ND
Kahn et al. (73)	31	Healthy controls*** (23)	Post (4 h)	3T, 3D-FLAIR	Gadobutrol (0.1)	Qualitative	26/35 (74%) symptomatic ears had enhancement, 2/27 (7.4%) asymptomatic ears of Meniere's patients had enhancement. No (0%) enhancement in control ears.	Enhancement correlated to hearing level but not duration of disease

*Data not included by authors in each study is depicted as "not described" (ND). Under the column MRI delay, "ND" is used to describe studies that did not report a specific delay time and is assumed to have performed MRI immediately after contrast injection. "Pre" indicates a scan was performed prior to the administration of contrast. Quantitative signal assessment methods involve the use of signal intensity measurements with regions of interest within the inner ear as compared to other imaged regions such as the cerebellum. ***Control ears were asymptomatic ears of patients with unilateral disease (hearing loss, vestibular neuritis), T, tesla; Gd, gadolinium; FLAIR, fluid-attenuated inversion recovery; FIESTA, fast imaging employing steady-state acquisition; hT2W, heavily T2-weighted; FSPGR, fast spoiled gradient-echo; Gd-DTPA, gadolinium with diethylenetriaminepentacetate; DOTA, dodecane tetraacetic acid; rIR, real inversion recovery; T1W, T1-weighted; T2W, T2-weighted.*

Human Studies

Our search yielded 53 studies in humans. Of these, 43 were cross-sectional studies and 10 were descriptive case series. Case series were defined as studies that provided only descriptive characteristics of included patients. The case series provided a useful historical framework for subsequent studies but were not included in our analysis (23–32). In healthy human ears, described in two included studies, enhancement of the inner ear peaked at 4 h following intravenous injection of 0.1 and 0.3 mmol/kg GBCA using 3T MRI and 3D fluid-attenuated inversion recovery (FLAIR) pulse sequences (8, 33).

Our quality assessment found flaws in methodological rigor across the included studies (**Table 2**). Assessment of the included cross-sectional studies with the NIH quality assessment tool found that none (0%) of the studies provided sample size justification, 20 (47%) either did not specify whether the MRI assessment was blinded or had used assessors that were not blinded, and 18 (42%) lacked a control population for comparing abnormal enhancement. Additionally, 35 (81%) did not assess enhancement at multiple time points, and 21 (49%) did not provide data on signal intensity with different levels of contrast exposure (e.g., signal intensity before and after contrast administration).

Contrast-enhanced MRI in patients with idiopathic sudden sensorineural hearing loss (ISSHL) was described in 14 included studies (**Table 3**). These studies reported increased signal intensity within the affected inner ear on 3D-FLAIR imaging taken before and after contrast administration. However, not all patients demonstrated increased signal intensity at either time point. Two studies noted that hyperintensity of the diseased ears was more prevalent in MRI acquired before contrast was administered, as opposed to images taken shortly after or at 4 h after GBCA injection (44, 54). Others reported an increased prevalence of abnormal enhancement of diseased ears when MRI was performed 4 h after GBCA administration as compared to MRI performed shortly after GBCA administration (58, 64). One study reported a correlation between increased signal in the diseased ear and poorer prognosis, but the association was only observed for pre-contrast imaging (44). Another study described a poorer prognosis when increased signal was observed on MRI performed 4 h after contrast administration (69). A third study reported a correlation between enhancement seen on MRI taken shortly after contrast injection and poorer initial hearing level but did not find a correlation with prognosis for hearing recovery (54).

MRI findings in patients with Ménière's disease were described in 12 studies (**Table 4**). These studies reported increased enhancement of the affected ear in MRI acquired 4 h after contrast but no abnormal hyperintensity in imaging before contrast or at imaging 10 min after contrast. One study compared imaging taken 10 min and 4 h after contrast injection and reported an increase in signal intensity over controls only at 4 h (52). This observation was supported by one other study; however, this study only included one patient with unilateral definite Ménière's disease, and three with possible Ménière's disease (53). One study reported a correlation between

TABLE 5 | Summary of findings in studies of vestibular schwannoma.

Vestibular schwannoma								
Author	***n***	**Controls (n)**	**MRI delay**	**MRI protocol**	**Gd agent (dose)**	**Signal assessment**	**Findings regarding enhancement**	**Correlation with symptoms**
Yamazaki et al. (45)	28 pre, 18 post	Contralateral ear (28)	Pre, Post (10 min)	3D-FLAIR, 3D-T2W, 3 T/1.5 T	Gd-DTPA or Gadodiamide (0.1)	Quantitative	Pre- and post-contrast signal intensity of affected ears was higher than controls.	Pre- and post-contrast signal intensity not correlated to hearing level
Lee et al. (46)	34	Contralateral ear (34)	Post (7 min)	3T, 3D-FLAIR	Gadopentetate dimeglumine (0.1)	Quantitative, Qualitative	Visual: 33 (97%) had cochlear enhancement, 31 (94%) had vestibular enhancement. Quantitative: Signal intensity was higher in affected ears.	No correlation between signal intensity and degree of hearing loss
Ishikawa et al. (55)	21	Normal controls (27)	Post (ND)	3D-FIESTA	Gd-DTPA or Gadodiamide (0.1)	Quantitative, Qualitative	Visual: 20 (95%) had decreased signal compared to controls. Quantitative: Affected ears had decreased signal intensity.	ND
Bowen et al. (70)	8	ND	Pre, Post (10 min, 5–8 h)	3T, 3D-FLAIR	ND	Quantitative	2 (25%) had enhancement at 10 min, 6 (75%) at 5–8 h. Signal intensity at 5–8 h was higher than at 10 min.	Signal intensity at 5–8 h correlated to word recognition scores but not initial symptoms, tumor size, or tumor growth.

Data not included by authors in each study is depicted as "not described" (ND). Contrast delay described as "ND" is used to describe studies that did not report a specific delay time and is assumed to have performed MRI immediately after contrast injection. Quantitative signal assessment methods involve the use of signal intensity measurements with regions of interest within the inner ear as compared to other imaged regions such as the cerebellum. T, tesla; Gd, gadolinium; FLAIR, fluid-attenuated inversion recovery; FIESTA, fast imaging employing steady-state acquisition; hT2W, heavily T2-weighted; FSPGR, fast spoiled gradient-echo; Gd-DTPA, gadolinium with diethylenetriaminepentacetate; T2W, T2-weighted.

enhancement on imaging 4 h after contrast and both the degree of hearing loss and severity of endolymphatic hydrops (73), while another study found no association between enhancement and hearing loss (50).

Five included studies examined MRI findings in patients with vestibular schwannoma (**Table 5**). Two studies reported enhancement of inner ear structures 7–10 min after contrast administration (45, 46). This was supported by another study which found decreased signal on 3D-FIESTA shortly after contrast injection which, similar to hyperintensity on 3D-FLAIR, suggests increased protein content in the inner ear (55). Another study reported a greater enhancement 5–8 h after contrast injection as compared to imaging immediately after contrast injection (70). Signal intensity at 5–8 h was correlated with poorer hearing as measured by pure tone thresholds and word recognition scores (70). The other studies with imaging performed shortly after GBCA administration reported no correlation between signal intensity and hearing level or tumor size (45, 46).

Four studies reported on MRI findings in patients with otosclerosis (**Table 6**). Two described increased signal intensity on MRI before and shortly after contrast administration (59, 63). Two studies reported a correlation between enhancement and disease stage (60, 63), while another study reported no correlation between enhancement and degree of hearing loss (74).

Our review also included 10 studies reporting abnormal inner ear enhancement in patients with sudden facial nerve paralysis (34, 35, 47), DFNA9 (mutation in the COCH gene) (67), Cogan syndrome (25), viral and bacterial labyrinthitis (23, 24, 30), and other inner ear abnormalities (39, 43, 49, 72).

DISCUSSION

Damage to the blood-labyrinth barrier has been implicated in the pathophysiology of inner ear disorders such as Ménière's disease and ISSHL (54, 75). Recently, investigators have begun using intravenous contrast-enhanced MRI to assess the permeability of this barrier as a potential tool in research and for diagnosis. The goal of this review was to evaluate current evidence for the role of gadolinium-based contrast in understanding blood-labyrinth barrier function and its utility in evaluating the integrity of this barrier in disease states of the inner ear.

Studies of both healthy and diseased ears of animals and humans demonstrated enhancement of inner ear structures following the administration of IV-gadolinium. In healthy ears of mice and guinea pigs, enhancement peaked and plateaued at

TABLE 6 | Summary of findings in studies of otosclerosis.

Otosclerosis								
Author	***n***	**Controls (*n*)**	**MRI delay**	**MRI protocol**	**Gd agent (dose)**	**Signal assessment**	**Findings regarding enhancement**	**Correlation with symptoms**
Lombardo et al. (59)	11	Matched controls (11)	Pre, post (ND)	3D-FLAIR, 3T	Gadoterate meglumine (0.1)	Quantitative, Qualitative	9 (82%) had pre-contrast enhancement, 8 (73%) had post-contrast enhancement.	ND
Berrettini et al. (63)	38	Healthy controls (11)	Pre, Post (ND)	3T, 3D-FLAIR	Gadoterate meglumine (0.1)	Quantitative, Qualitative	26 (68%) had pre-contrast enhancement, 14 (37%) had post-contrast enhancement.	Post-contrast enhancement correlated to more advanced disease.
Naganawa et al. (60)	12	Healthy controls (8)	Post (4 h)	hT2W-3D-FLAIR, 3T	Gadodiamide (0.1)	Quantitative	Signal intensity of diseased ears was higher than controls.	Signal intensity correlated to more advanced disease.
Laine et al. (74)	29	Healthy controls***	Post (4 h)	3T, 3D-FLAIR	Gadobutrol (0.1)	Quantitative, Qualitative	8 (21%) of affected ears had visual enhancement. Signal intensity of affected ears was higher than contralateral ears.	No correlation between signal intensity and level of hearing loss or vertigo.

*Data not included by authors in each study is depicted as "not described" (ND). Contrast delay described as "ND" is used to describe studies that did not report a specific delay time and is assumed to have performed MRI immediately after contrast injection. Quantitative signal assessment methods involve the use of signal intensity measurements with regions of interest within the inner ear as compared to other imaged regions such as the cerebellum. ***Control ears were asymptomatic ears of patients with unilateral disease (acute vestibular syndrome). T, tesla; Gd, gadolinium; FLAIR, fluid-attenuated inversion recovery; hT2W, heavily T2-weighted.*

100 min after contrast administration. Further studies in animal ears affected by mechanical trauma (14) and inflammation (22) demonstrated increased enhancement, suggesting that disease states may increase the inner ear's permeability to gadolinium-based agents, potentially through alterations in the blood-labyrinth barrier. Studies have not sought to identify the mechanism(s) by which gadolinium crosses the blood-labyrinth barrier. Notably, these animal studies used an MRI magnetic field strength of at least 4.7 T, which exceeds the standard used in most human studies (1.5 and 3.0 T). Animals were also administered gadolinium at doses that were up to 15 times greater than the clinical standard of 0.1 mmol/kg for humans. Studies in healthy humans reported reliable gadolinium uptake within the inner ear 4 h after injection with either 0.1 (33) or 0.3 (8) mmol/kg gadolinium using a 3 T MRI scanner.

Pathologies such as ISSHL, Ménière's disease, otosclerosis, and vestibular schwannoma have been shown to alter this baseline GBCA enhancement by increasing the intensity of signal on MRI within inner ear structures. Although abnormal enhancement was well-described by most studies, there were conflicting reports of correlations between this enhancement and clinical characteristics such as prognosis and disease severity.

Although increased enhancement was common in these diseases, there were distinct differences by disease in the time of the observed increased signal. In both ISSHL and otosclerosis, hyperintense inner ear signal was present even before contrast was administered and just minutes after GBCA injection. Meanwhile, enhancement in patients with Ménière's disease or vestibular schwannoma was reported after a delay of four or more hours from contrast administration. Hyperintensity prior to contrast injection in cerebrospinal fluid has been hypothesized to result from increased protein content and could be a hypothesis for the increased pre-contrast signal seen in some patients with ISSHL and otosclerosis (76). Quicker uptake of contrast, or increased baseline signal, could indicate more severe blood-labyrinth barrier damage resulting in greater passage of GBCA and possibly protein into the perilymph. Alternatively, GBCA could have different routes of entry into perilymph, depending on the pathophysiology of the disease. The kinetics of enhancement with gadolinium could be important for evaluating the blood-labyrinth barrier in different disease states. However, due to the current paucity of studies on the time course of enhancement in disease, it is impossible to make a reliable comparison of blood-labyrinth barrier permeability in different disease states. Only two studies with few patients reported on enhancement findings at two time points in patients with Ménière's disease (52). While this early data is promising, studies with images taken at multiple time points are needed to better describe differences in the pattern of enhancement among different inner ear diseases compared to control ears.

Our analysis of the evidence was hampered by study design. Most notably there was a lack of adequate control groups, sample size justifications, and clear patient recruitment details. Compounding these quality issues was the substantial degree of variability in study protocols—particularly regarding the contrast agents used and the methods for determining enhancement. Counter et al. demonstrated that although linear and macrocyclic GBCA agents were useful in enhancing the inner ear structures, there was a distinct heterogenicity in kinetics (20). This makes it difficult to compare studies using different GBCA agents, given the importance of consistent enhancement kinetics when comparing uptake patterns in different disease states.

Additionally, there was no consensus on how to distinguish between normal and abnormal enhancement patterns. In studies that used controls, either from contralateral ears or healthy volunteers, some studies used subjective, visual assessment. Others used more objective measures of signal intensity normalized to signal from regions of the scan that were presumably unaffected by the disease. The consistency of control groups used in studies on systemic diseases or disease that can affect both ears such as Ménière's disease is particularly important. One included study found that asymptomatic ears of patients with Ménière's disease had increased signal intensity on contrast-enhanced MRI compared to controls (61), while another study described contrast enhancement of the asymptomatic ear in two patients with clinically unilateral Ménière's disease (66).

The goal of this scoping review was to evaluate the usefulness of IV-gadolinium MRI in assessing blood-labyrinth barrier permeability in healthy and diseased ears. Following intravenous administration of GBCA, GBCA enters the inner ear in healthy ears after a delay, presumably through the blood-labyrinth barrier. Despite these observations in healthy animals and humans, we found no conclusive evidence to support the assumption that gadolinium can be used to directly measure the health of the blood-labyrinth barrier. Our review also found a lack of studies that could correlate abnormal enhancement of the inner ear with a more general breakdown of the blood labyrinth barrier. While there is compelling evidence demonstrating increased GBCA uptake in diseased ears, future work must be done to clarify if any connection exists between abnormal enhancement and breakdown of the blood-labyrinth barrier. Furthermore, different disease states may affect the blood-labyrinth barrier by different mechanisms. There is a gap in the current literature regarding the mechanisms of GBCA uptake into the perilymph, the time course of uptake in diseased human ears, and the natural course of GBCA efflux from the perilymph. Rigorous future studies with adequate controls, clear patient recruitment methods, and objective measures of enhancement patterns are needed to determine the utility of contrast-enhanced MRI in assessing the integrity of the blood-labyrinth barrier.

DATA AVAILABILITY STATEMENT

The original contributions presented in the study are included in the article/**Supplementary Material**, further inquiries can be directed to the corresponding author.

AUTHOR CONTRIBUTIONS

BW and CS conceived of the concept of the article and the study design, applied the article quality assessment, and performed the initial draft of the manuscript. BW designed **Figure 1**. CS performed the initial search, designed **Figure 2**, and constructed the tables. All authors reviewed the included articles. All authors reviewed and approved the final submitted version of the manuscript.

FUNDING

BW is supported by clinician-scientist awards from the American Otological Society and Johns Hopkins University School of Medicine, as well as K23DC018302. NA is supported by T32DC000027. JP is supported by a Junior Fellowship from the Garnett Passe and Rodney Williams Memorial Foundation and by philanthropy received from the Cinquegrana, Lott, and Schwerin families through Prof. David Zee at Johns Hopkins University.

ACKNOWLEDGMENTS

The authors would like to acknowledge the help of Rachael Lebo at the Welch Medical Library who assisted CS with the development of the initial search.

SUPPLEMENTARY MATERIAL

The Supplementary Material for this article can be found online at: https://www.frontiersin.org/articles/10.3389/fneur.2021.662264/full#supplementary-material

REFERENCES

1. Pournaras CJ, Rungger-Brändle E, Riva CE, Hardarson SH, Stefansson E. Regulation of retinal blood flow in health and disease. *Prog Retin Eye Res.* (2008) 27:284–330. doi: 10.1016/j.preteyeres.2008.02.002
2. Misrahy GA, Spradley JF, Beran AV, Garwood VP. Permeability of cochlear partitions: comparison with blood-brain barrier. *Acta Otolaryngol.* (1960) 52:525–34. doi: 10.3109/00016486009123183
3. Mazzoni A. The vascular anatomy of the vestibular labyrinth in man. *Acta Oto-Laryngol Suppl.* (1990) 472:1–83. doi: 10.3109/00016489009121137
4. Zhang W, Dai M, Fridberger A, Hassan A, Degagne J, Neng L, et al. Perivascular-resident macrophage-like melanocytes in the inner ear are essential for the integrity of the intrastrial fluid-blood barrier. *Proc Natl Acad Sci USA.* (2012) 109:10388–93. doi: 10.1073/pnas.1205210109
5. Juhn SK, Rybak LP, Prado S. Nature of blood-labyrinth barrier in experimental conditions. *Ann Otol Rhinol Laryngol.* (1981) 90(2 Pt 1):135–41. doi: 10.1177/000348948109000208
6. Juhn SK, Rybak LP, Fowlks WL. Transport characteristics of the blood–perilymph barrier. *Am J Otolaryngol.* (1982) 3:392–6. doi: 10.1016/S0196-0709(82)80016-1
7. Nyberg S, Abbott NJ, Shi X, Steyger PS, Dabdoub A. Delivery of therapeutics to the inner ear: the challenge of the blood-labyrinth barrier. *Sci Transl Med.* (2019) 11:eaao0935. doi: 10.1126/scitranslmed.aao0935
8. Carfrae MJ, Holtzman A, Eames F, Parnes SM, Lupinetti A. 3 Tesla delayed contrast magnetic resonance imaging evaluation of Meniere's

disease. *Laryngoscope.* (2008) 118:501–5. doi: 10.1097/MLG.0b013e31815c1a61

9. Rauch SD, Merchant SN, Thedinger BA. Meniere's syndrome and endolymphatic hydrops. Double-blind temporal bone study. *Ann Otol Rhinol Laryngol.* (1989) 98:873–83. doi: 10.1177/000348948909801108
10. Hirose K, Discolo CM, Keasler JR, Ransohoff R. Mononuclear phagocytes migrate into the murine cochlea after acoustic trauma. *J Comp Neurol.* (2005) 489:180–94. doi: 10.1002/cne.20619
11. Ichimiya I, Yoshida K, Hirano T, Suzuki M, Mogi G. Significance of spiral ligament fibrocytes with cochlear inflammation. *Int J Pediatr Otorhinolaryngol.* (2000) 56:45–51. doi: 10.1016/S0165-5876(00)00408-0
12. Study Quality Assessment Tools | NHLBI, NIH. Available online at: http://www.nhlbi.nih.gov/health-topics/study-quality-assessment-tools (accessed January 19, 2021).
13. Counter SA, Bjelke B, Klason T, Chen Z, Borg E. Magnetic resonance imaging of the cochlea, spiral ganglia and eighth nerve of the guinea pig. *Neuroreport.* (1999) 10:473–9. doi: 10.1097/00001756-199902250-00006
14. Counter SA, Bjelke B, Borg E, Klason T, Chen Z, Duan ML. Magnetic resonance imaging of the membranous labyrinth during in vivo gadolinium (Gd-DTPA-BMA) uptake in the normal and lesioned cochlea. *Neuroreport.* (2000) 11:3979–83. doi: 10.1097/00001756-200012180-00015
15. Zou J, Pyykko I, Bretlau P, Klason T, Bjelke B. In vivo visualization of endolymphatic hydrops in guinea pigs: magnetic resonance imaging evaluation at 4.7 tesla. *Ann Otol Rhinol Laryngol.* (2003) 112:1059–65. doi: 10.1177/000348940311201212
16. Zou J, Pyykkö I, Counter SA, Klason T, Bretlau P, Bjelke B. In vivo observation of dynamic perilymph formation using 4.7 t MRI with gadolinium as a tracer. *Acta Otolaryngol (Stockh).* (2003) 123:910. doi: 10.1080/00016480310000548
17. Zou J, Zhang W, Poe D, Zhang Y, Ramadan UA, Pyykko I. Differential passage of gadolinium through the mouse inner ear barriers evaluated with 4.7T MRI. *Hear Res.* (2010) 259:36–43. doi: 10.1016/j.heares.2009.09.015
18. Counter SA, Nikkhou S, Brene S, Damberg P, Sierakowiak A, Klason T, et al. MRI evidence of endolymphatic impermeability to the gadolinium molecule in the in vivo mouse inner ear at 9.4 tesla. *Open Neuroimaging J.* (2013) 7:27–31. doi: 10.2174/1874440001307010027
19. Counter SA, Zou J, Bjelke B, Klason T. 3D MRI of the in vivo vestibulo-cochlea labyrinth during Gd-DTPA-BMA uptake. *Neuroreport.* (2003) 14:1707–12. doi: 10.1097/00001756-200309150-00010
20. Counter SA, Nikkhou-Aski S, Damberg P, Berglin CE, Laurell G. Ultra-high-field (9.4 T) MRI analysis of contrast agent transport across the blood-perilymph barrier and intrastrial fluid-blood barrier in the mouse inner ear. *Otol Neurotol.* (2017) 38:1052–9. doi: 10.1097/MAO.0000000000001458
21. Videhult Pierre P, Rasmussen JE, Nikkhou Aski S, Damberg P, Laurell G. High-dose furosemide enhances the magnetic resonance signal of systemic gadolinium in the mammalian cochlea. *Otol Neurotol.* (2020) 41:545–53. doi: 10.1097/MAO.0000000000002571
22. Floc'h JL, Tan W, Telang RS, Vlajkovic SM, Nuttall A, Rooney WD, et al. Markers of cochlear inflammation using MRI. *J Magn Reson Imaging JMRI.* (2014) 39:150–61. doi: 10.1002/jmri.24144
23. Seltzer S, Mark AS. Contrast enhancement of the labyrinth on MR scans in patients with sudden hearing loss and vertigo: evidence of labyrinthine disease. *AJNR Am J Neuroradiol.* (1991) 12:13–6.
24. Mark AS, Seltzer S, Nelson-Drake J, Chapman JC, Fitzgerald DC, Gulya AJ. Labyrinthine enhancement on gadolinium-enhanced magnetic resonance imaging in sudden deafness and vertigo: correlation with audiologic and electronystagmographic studies. *Ann Otol Rhinol Laryngol.* (1992) 101:459–64. doi: 10.1177/000348949210100601
25. Majoor M.H.J.M., Albers F.W.J., Casselman J.W. Clinical relevance of magnetic resonance imaging and computed tomography in Cogan's syndrome. *Acta Otolaryngol (Stockh).* (1993) 113:625–31. doi: 10.3109/00016489309135875
26. Albers FW, Demuynck KM, Casselman JW. Three-dimensional magnetic resonance imaging of the inner ear in idiopathic sudden sensorineural hearing loss. *ORL J Oto-Rhino-Laryngol Its Relat Spec.* (1994) 56:1–4. doi: 10.1159/000276599
27. Sone M, Mizuno T, Naganawa S, Nakashima T. Imaging analysis in cases with inflammation-induced sensorineural hearing loss. *Acta Otolaryngol.* (2009) 129:239–43. doi: 10.1080/00016480802226163
28. Peng R, Chow D, De Seta D, Lalwani AK. Intensity of gadolinium enhancement on MRI is useful in differentiation of intracochlear inflammation from tumor. *Otol Neurotol.* (2014) 35:905–10. doi: 10.1097/MAO.0000000000000300
29. Mark AS, Fitzgerald D. Segmental enhancement of the cochlea on contrast-enhanced MR: correlation with the frequency of hearing loss and possible sign of perilymphatic fistula and autoimmune labyrinthitis. *AJNR Am J Neuroradiol.* (1993) 14:991–6.
30. Fitzgerald DC, Mark AS. Viral cochleitis with gadolinium enhancement of the cochlea on magnetic resonance imaging scan. *Otolaryngol–Head Neck Surg.* (1999) 121:130–2. doi: 10.1016/S0194-5998(99)70141-5
31. Wilson DF, Talbot JM, Hodgson RS. Magnetic resonance imaging-enhancing lesions of the labyrinth and facial nerve. Clinical correlation. *Arch Otolaryngol Head Neck Surg.* (1994) 120:560–4. doi: 10.1001/archotol.1994.01880290070012
32. Hegarty JL, Patel S, Fischbein N, Jackler RK, Lalwani AK. The value of enhanced magnetic resonance imaging in the evaluation of endocochlear disease. *Laryngoscope.* (2002) 112:8–17. doi: 10.1097/00005537-200201000-00002
33. Naganawa S, Komada T, Fukatsu H, Ishigaki T, Takizawa O. Observation of contrast enhancement in the cochlear fluid space of healthy subjects using a 3D-FLAIR sequence at 3 Tesla. *Eur Radiol.* (2006) 16:733–7. doi: 10.1007/s00330-005-0046-8
34. Sartoretti-Schefer S, Wichmann W, Valavanis A. Idiopathic, herpetic, and HIV-associated facial nerve palsies: abnormal MR enhancement patterns. *AJNR Am J Neuroradiol.* (1994) 15:479–85.
35. Sartoretti-Schefer S, Scherler M, Wichmann W, Valavanis A. Contrast-enhanced MR of the facial nerve in patients with posttraumatic peripheral facial nerve palsy. *AJNR Am J Neuroradiol.* (1997) 18:1115–25.
36. Fitzgerald DC, Mark AS. Sudden hearing loss: frequency of abnormal findings on contrast-enhanced MR studies. *AJNR Am J Neuroradiol.* (1998) 19:1433–6.
37. Stokroos RJ, Albers FW, Krikke AP, Casselman JW. Magnetic resonance imaging of the inner ear in patients with idiopathic sudden sensorineural hearing loss. *Eur Arch Oto-Rhino-Laryngol.* (1998) 255:433–6. doi: 10.1007/s004050050093
38. Strupp M, Jager L, Muller-Lisse U, Arbusow V, Reiser M, Brandt T. High resolution Gd-DTPA MR imaging of the inner ear in 60 patients with idiopathic vestibular neuritis: no evidence for contrast enhancement of the labyrinth or vestibular nerve. *J Vestib Res Equilib Orientat.* (1998) 8:427–33. doi: 10.3233/VES-1998-8603
39. Schick B, Brors D, Koch O, Schafers M, Kahle G. Magnetic resonance imaging in patients with sudden hearing loss, tinnitus and vertigo. *Otol Neurotol.* (2001) 22:808–12. doi: 10.1097/00129492-200111000-00016
40. Naganawa S, Koshikawa T, Nakamura T, Fukatsu H, Ishigaki T, Aoki I. High-resolution T1-weighted 3D real IR imaging of the temporal bone using triple-dose contrast material. *Eur Radiol.* (2003) 13:2650–8. doi: 10.1007/s00330-003-1922-8
41. Cadoni G, Cianfoni A, Agostino S, Scipione S, Tartaglione T, Galli J, et al. Magnetic resonance imaging findings in sudden sensorineural hearing loss. *J Otolaryngol.* (2006) 35:310–6. doi: 10.2310/7070.2006.0066
42. Sugiura M, Naganawa S, Teranishi M, Nakashima T. Three-dimensional fluid-attenuated inversion recovery magnetic resonance imaging findings in patients with sudden sensorineural hearing loss. *Laryngoscope.* (2006) 116:1451–4. doi: 10.1097/01.mlg.0000228005.78187.23
43. Sone M, Mizuno T, Sugiura M, Naganawa S, Nakashima T. Three-dimensional fluid-attenuated inversion recovery magnetic resonance imaging investigation of inner ear disturbances in cases of middle ear cholesteatoma with labyrinthine fistula. *Otol Neurotol.* (2007) 28:1029–33. doi: 10.1097/MAO.0b013e3181587d95
44. Yoshida T, Sugiura M, Naganawa S, Teranishi M, Nakata S, Nakashima T. Three-dimensional fluid-attenuated inversion recovery magnetic resonance imaging findings and prognosis in sudden sensorineural hearing

loss. *Laryngoscope.* (2008) 118:1433–7. doi: 10.1097/MLG.0b013e318172ef85

45. Yamazaki M, Naganawa S, Kawai H, Nihashi T, Fukatsu H, Nakashima T. Increased signal intensity of the cochlea on pre- and post-contrast enhanced 3D-FLAIR in patients with vestibular schwannoma. *Neuroradiology.* (2009) 51:855–63. doi: 10.1007/s00234-009-0588-6
46. Lee IH, Kim H-J, Chung WH, Kim E, Moon JW, Kim ST, et al. Signal intensity change of the labyrinth in patients with surgically confirmed or radiologically diagnosed vestibular schwannoma on isotropic 3D fluid-attenuated inversion recovery MR imaging at 3 T. *Eur Radiol.* (2010) 20:949–57. doi: 10.1007/s00330-009-1626-9
47. Nakata S, Mizuno T, Naganawa S, Sugiura M, Yoshida T, Teranishi M, et al. 3D-FLAIR MRI in facial nerve paralysis with and without audio-vestibular disorder. *Acta Otolaryngol (Stockh).* (2010) 130:632–6. doi: 10.3109/00016480903338123
48. Tagaya M, Teranishi M, Naganawa S, Iwata T, Yoshida T, Otake H, et al. 3 Tesla magnetic resonance imaging obtained 4 hours after intravenous gadolinium injection in patients with sudden deafness. *Acta Otolaryngol (Stockh).* (2010) 130:665–9. doi: 10.3109/00016480903384176
49. Tanigawa T, Tanaka H, Sato T, Nakao Y, Katahira N, Tsuchiya Y, et al. 3D-FLAIR MRI findings in patients with low-tone sudden deafness. *Acta Otolaryngol (Stockh).* (2010) 130:1324–8. doi: 10.3109/00016489.2010.496461
50. Suzuki H, Teranishi M, Sone M, Yamazaki M, Naganawa S, Nakashima T. Contrast enhancement of the inner ear after intravenous administration of a standard or double dose of gadolinium contrast agents. *Acta Otolaryngol (Stockh).* (2011) 131:1025–31. doi: 10.3109/00016489.2011.598552
51. Tagaya M, Yamazaki M, Teranishi M, Naganawa S, Yoshida T, Otake H, et al. Endolymphatic hydrops and blood-labyrinth barrier in Meniere's disease. *Acta Otolaryngol (Stockh).* (2011) 131:474–9. doi: 10.3109/00016489.2010.534114
52. Naganawa S, Yamazaki M, Kawai H, Bokura K, Sone M, Nakashima T. Visualization of endolymphatic hydrops in Meniere's disease after single- dose intravenous gadolinium-based contrast medium: timing of optimal enhancement. *Magn Reson Med Sci.* (2012) 11:43–51. doi: 10.2463/mrms.11.43
53. Sano R, Teranishi M, Yamazaki M, Isoda H, Naganawa S, Sone M, et al. Contrast enhancement of the inner ear in magnetic resonance images taken at 10 minutes or 4 hours after intravenous gadolinium injection. *Acta Otolaryngol (Stockh).* (2012) 132:241–6. doi: 10.3109/00016489.2011.639085
54. Berrettini S, Seccia V, Fortunato S, Forli F, Bruschini L, Piaggi P, et al. Analysis of the 3-dimensional fluid-attenuated inversion-recovery (3D-FLAIR) sequence in idiopathic sudden sensorineural hearing loss. *JAMA Otolaryngol– Head Neck Surg.* (2013) 139:456–64. doi: 10.1001/jamaoto.2013.2659
55. Ishikawa K, Haneda J, Okamoto K. Decreased vestibular signal intensity on 3D-FIESTA in vestibular schwannomas differentiating from meningiomas. *Neuroradiology.* (2013) 55:261–70. doi: 10.1007/s00234-012-1100-2
56. Kim TY, Park DW, Lee YJ, Lee JY, Lee SH, Chung JH, et al. Comparison of inner ear contrast enhancement among patients with unilateral inner ear symptoms in mr images obtained 10 minutes and 4 hours after gadolinium injection. *AJNR Am J Neuroradiol.* (2015) 36:2367–72. doi: 10.3174/ajnr.A4439
57. Tanigawa T, Shibata R, Tanaka H, Gosho M, Katahira N, Horibe Y, et al. Usefulness of three-dimensional fluid-attenuated inversion recovery magnetic resonance imaging to detect inner-ear abnormalities in patients with sudden sensorineural hearing loss. *J Laryngol Otol.* (2015) 129:11–5. doi: 10.1017/S0022215114003028
58. Liao W-H, Wu H-M, Wu H-Y, Tu T-Y, Shiao A-S, Castillo M, et al. Revisiting the relationship of three-dimensional fluid attenuation inversion recovery imaging and hearing outcomes in adults with idiopathic unilateral sudden sensorineural hearing loss. *Eur J Radiol.* (2016) 85:2188–94. doi: 10.1016/j.ejrad.2016.10.005
59. Lombardo F, Cori S, Aghakhanyan G, Montanaro D, Marchi D, Frijia F, et al. 3D-Flair sequence at 3T in cochlear otosclerosis. *Eur Radiol.* (2016) 26:3744–51. doi: 10.1007/s00330-015-4170-9
60. Naganawa S, Kawai H, Taoka T, Suzuki K, Iwano S, Satake H, et al. Cochlear lymph fluid signal increase in patients with otosclerosis after intravenous administration of gadodiamide. *Magn Reson Med Sci.* (2016) 15:308–15. doi: 10.2463/mrms.mp.2015-0121
61. Pakdaman MN, Ishiyama G, Ishiyama A, Peng KA, Kim HJ, Pope WB, et al. Blood-labyrinth barrier permeability in meniere disease and idiopathic sudden sensorineural hearing loss: findings on delayed postcontrast 3D-FLAIR MRI. *AJNR Am J Neuroradiol.* (2016) 37:1903–8. doi: 10.3174/ajnr.A4822
62. Attye A, Eliezer M, Galloux A, Pietras J, Tropres I, Schmerber S, et al. Endolymphatic hydrops imaging: differential diagnosis in patients with Meniere disease symptoms. *Diagn Interv Imaging.* (2017) 98:699–706. doi: 10.1016/j.diii.2017.06.002
63. Berrettini S, Lombardo F, Bruschini L, Ciabotti A, Raffaello C, Sara DC, et al. 3D fluid attenuated inversion recovery (FLAIR) magnetic resonance imaging at different stages of otosclerosis. *Eur Arch Oto-Rhino-Laryngol.* (2018) 275:2643–52. doi: 10.1007/s00405-018-5093-2
64. Byun H, Chung JH, Lee SH, Park CW, Park DW, Kim TY. Clinical value of 4-hour delayed gadolinium-Enhanced 3D FLAIR MR Images in Acute Vestibular Neuritis. *Laryngoscope.* (2018) 128:1946–51. doi: 10.1002/lary.27084
65. Eliezer M, Poillon G, Gillibert A, Horion J, Cruypeninck Y, Gerardin E, et al. Comparison of enhancement of the vestibular perilymph between gadoterate meglumine and gadobutrol at 3-Tesla in Meniere's disease. *Diagn Interv Imaging.* (2018) 99:271–7. doi: 10.1016/j.diii.2018.01.002
66. Bernaerts A, Vanspauwen R, Blaivie C, van Dinther J, Zarowski A, Wuyts FL, et al. The value of four stage vestibular hydrops grading and asymmetric perilymphatic enhancement in the diagnosis of Menière's disease on MRI. *Neuroradiology.* (2019) 61:421–9. doi: 10.1007/s00234-019-02155-7
67. Conte G, Lo Russo F, Caschera L, Zanetti D, Castorina P, Sina C, et al. Audiovestibular Phenotypes and Advanced Magnetic Resonance Imaging Features of Cochlin Gene Mutation Carriers. *Audiol Neurootol.* (2019) 24:166–73. doi: 10.1159/000501292
68. Eliezer M, Maquet C, Horion J, Gillibert A, Toupet M, Bolognini B, et al. Detection of intralabyrinthine abnormalities using post-contrast delayed 3D-FLAIR MRI sequences in patients with acute vestibular syndrome. *Eur Radiol.* (2019) 29:2760–9. doi: 10.1007/s00330-018-5825-0
69. Wang J, Ren T, Sun W, Liang Q, Wang W. Post-contrast 3D-FLAIR in idiopathic sudden sensorineural hearing loss. *Eur Arch Oto-Rhino-Laryngol.* (2019) 276:1291–9. doi: 10.1007/s00405-019-05285-z
70. Bowen AJ, Carlson ML, Lane JI. Inner Ear Enhancement With Delayed 3D-FLAIR MRI Imaging in Vestibular Schwannoma. *Otol Neurotol.* (2020) 41:1274–9. doi: 10.1097/MAO.0000000000002768
71. Eliezer M, Hautefort C, Van Nechel C, Duquesne U, Guichard J-P, Herman P, et al. Electrophysiological and inner ear MRI findings in patients with bilateral vestibulopathy. *Eur Arch Oto-Rhino-Laryngol.* (2020) 277:1305–14. doi: 10.1007/s00405-020-05829-8
72. Eliezer M, Poillon G, Levy D, Guichard J-P, Toupet M, Houdart E, et al. Clinical and radiological characteristics of patients with collapse or fistula of the saccule as evaluated by inner ear MRI. *Acta Otolaryngol (Stockh).* (2020) 140:1–8. doi: 10.1080/00016489.2020.1713396
73. Kahn L, Hautefort C, Guichard J-P, Toupet M, Jourdaine C, Vitaux H, et al. Relationship between video head impulse test, ocular and cervical vestibular evoked myogenic potentials, and compartmental magnetic resonance imaging classification in meniere's disease. *Laryngoscope.* (2020) 130:E444–52. doi: 10.1002/lary.28362
74. Laine J, Hautefort C, Attye A, Guichard J-P, Herman P, Houdart E, et al. MRI evaluation of the endolymphatic space in otosclerosis and correlation with clinical findings. *Diagn Interv Imaging.* (2020) 101:537–45. doi: 10.1016/j.diii.2020.03.009
75. Ishiyama G, Lopez IA, Ishiyama P, Vinters HV, Ishiyama A. The blood labyrinthine barrier in the human normal and Meniere's disease macula utricle. *Sci Rep.* (2017) 7:253. doi: 10.1038/s41598-017-00330-5
76. Melhem ER, Jara H, Eustace S. Fluid-attenuated inversion recovery MR imaging: identification of protein concentration thresholds

for CSF hyperintensity. *AJR Am J Roentgenol.* (1997) 169:859–62. doi: 10.2214/ajr.169.3.9275912

Conflict of Interest: The authors declare that the research was conducted in the absence of any commercial or financial relationships that could be construed as a potential conflict of interest.

frontiers in Neurology

REVIEW
published: 21 September 2021
doi: 10.3389/fneur.2021.674100

Vestibular-Evoked Cerebral Potentials

Estelle Nakul[1], *Fabrice Bartolomei*[2,3] *and Christophe Lopez*[1]*

[1] *Centre National de la Recherche Scientifique (CNRS), Laboratoire de Neurosciences Cognitives (LNC), FR3C, Aix Marseille Univ, Marseille, France,* [2] *Institut de Neurosciences des Systèmes, Inserm, Aix Marseille Univ, Marseille, France,* [3] *Service de Neurophysiologie Clinique, Hôpital Timone, Aix Marseille Univ, Marseille, France*

The human vestibular cortex has mostly been approached using functional magnetic resonance imaging and positron emission tomography combined with artificial stimulation of the vestibular receptors or nerve. Few studies have used electroencephalography and benefited from its high temporal resolution to describe the spatiotemporal dynamics of vestibular information processing from the first milliseconds following vestibular stimulation. Evoked potentials (EPs) are largely used to describe neural processing of other sensory signals, but they remain poorly developed and standardized in vestibular neuroscience and neuro-otology. Yet, vestibular EPs of brainstem, cerebellar, and cortical origin have been reported as early as the 1960s. This review article summarizes and compares results from studies that have used a large range of vestibular stimulation, including natural vestibular stimulation on rotating chairs and motion platforms, as well as artificial vestibular stimulation (e.g., sounds, impulsive acceleration stimulation, galvanic stimulation). These studies identified vestibular EPs with short latency (<20 ms), middle latency (from 20 to 50 ms), and late latency (>50 ms). Analysis of the generators (source analysis) of these responses offers new insights into the neuroimaging of the vestibular system. Generators were consistently found in the parieto-insular and temporo-parietal junction—the core of the vestibular cortex—as well as in the prefrontal and frontal areas, superior parietal, and temporal areas. We discuss the relevance of vestibular EPs for basic research and clinical neuroscience and highlight their limitations.

Keywords: vestibular-evoked potentials, EEG, vestibular cortex, neuro-otology, vestibular system

Edited by:
Marianne Dieterich,
LMU Munich University
Hospital, Germany

Reviewed by:
Maurizio Versino,
ASST Settelaghi, Italy
Giuseppe Magliulo,
Sapienza University of Rome, Italy

***Correspondence:**
Christophe Lopez
christophe.lopez@univ-amu.fr

Specialty section:
This article was submitted to
Neuro-Otology,
a section of the journal
Frontiers in Neurology

Received: *28 February 2021*
Accepted: *20 August 2021*
Published: *21 September 2021*

Citation:
Nakul E, Bartolomei F and Lopez C
(2021) Vestibular-Evoked Cerebral
Potentials. Front. Neurol. 12:674100.
doi: 10.3389/fneur.2021.674100

INTRODUCTION

The vestibular system has long been associated with postural, oculomotor, and autonomic reflexes. Recent studies from neuroscience and neurology have provided a large corpus of data showing that vestibular functions reach far beyond oculomotor and postural reflex control (1, 2). For example, vestibular signals have been involved in several aspects of spatial cognition and memory (3, 4), affective processing (5), personality (6), awareness (7), body representations (8), and self-consciousness (9).

The vestibular contributions to sensorimotor control, awareness, and cognition rely on neural pathways from the inner ear to the vestibular nuclei, thalamus, and cerebral cortex (10, 11), as well as on vestibular pathways to the cerebellum and basal ganglia (12). Functional magnetic resonance imaging (fMRI) or positron emission tomography (PET) studies combined with caloric and galvanic vestibular stimulation identified a large thalamo-cortical vestibular network in the human brain (11, 13–16). The vestibular cortex encompasses the parieto-insular and operculo-insular cortex, the MT/MST complex, inferior parietal lobe (angular and supramarginal gyri), somatosensory cortex, precuneus, frontal cortex (premotor cortex and frontal eye fields), cingulate gyrus, and the hippocampus. Although there seems to be no primary vestibular cortex, functional and anatomical data suggest that the parietal operculum (area OP2), the posterior insula, and/or the retroinsular cortex are the core area underpinning vestibular information processing (11, 15–18). The operculo-insular and retroinsular cortex is considered the human homologue of the parieto-insular vestibular cortex (PIVC) described in several non-human primate species (19, 20). Anatomical studies and direct electrophysiological recordings in non-human primates corroborate results from fMRI and PET studies regarding the localization of the vestibular cortex [reviewed in (10)].

Understanding vestibular projections to the central nervous system is crucial to foster the diagnosis of central vestibular disorders, which concern 25% of patients referred to otoneurology units specialized in dizziness and vertigo (21). We note that despite the progress made over the last 20 years to localize the human vestibular cortex, the spatiotemporal dynamics of vestibular information processing is still poorly described when compared to the wealth of data accumulated in non-human primates using single cell recordings [e.g., (22–24)]. This is mainly due to the limitations of the imaging techniques that were mostly used to identify the vestibular cortex (fMRI, PET). The long latency of hemodynamic response and poor sampling frequency of fMRI and PET did not allow to precisely describe the time course of vestibular responses in the human brain. Another limitation of fMRI and PET studies is that most of them did not use *natural vestibular stimulation*—with physiologically relevant patterns of angular and linear accelerations—as head movements are precluded in scanners [for exceptions, see (25), and more recently (26, 27)]. Instead, fMRI and PET studies have used *artificial vestibular stimulation*, including caloric, galvanic, acoustic, and magnetic stimulation of the vestibular receptors or nerve. Artificial vestibular stimulation do not allow to explore brain responses to the range of head translations and rotations involved in everyday activities (28), which may hamper a full understanding of the vestibulo-thalamo-cortical functions. Moreover, the use of artificial vestibular stimulation [such as caloric vestibular stimulation] in an MRI scanner may create conflict between vestibular signals—indicating self-motion—and visual, somatosensory, and interoceptive signals—indicating that the participant is motionless in the scanner. Thus, some of the brain areas shown to respond to vestibular stimulation in neuroimaging studies, such as the temporo-parietal cortex (29), may also be involved in monitoring, processing, or solving multisensory conflicts (30).

In contrast with fMRI and PET, electroencephalography (EEG) and evoked potentials (EPs) allow to study vestibular information processing with a resolution below the millisecond rather than seconds. Electroencephalography allows to detect, quantify, and analyze brain electrical activity, including responses to sensory stimuli (31). Importantly, EEG is compatible with natural vestibular stimulation (i.e., whole-body rotations and translations) that limits the induction of multisensory conflicts inherent to artificial vestibular stimulation. Rotatory chairs and whole-body motion platforms allow to explore a large range of vestibular stimuli with highly precise and reproducible motion parameters (32, 33). As EEG allows to measure brain responses within the first milliseconds after a sensory stimulation is applied, neurologists and neurophysiologists commonly use sensory EPs to assess the integrity and functioning of sensory systems. Both latency and source localization of somatosensory EPs (34), visual EPs (35) and auditory EPs (36, 37) are well-described and EP approaches are used worldwide in clinical routine. Regarding the vestibular system, the EP approach is well-developed to assess vestibulo-ocular and vestibulocollic reflex pathways (38) through electromyographic recordings above the oculomotor and neck muscles, respectively (**Figure 1**). Vestibular stimulation by air-conducted sounds and bone-conducted vibrations (43) are now commonly used to assess the latency and amplitude of *cervical* vestibular-evoked myogenic potentials (cVEMPs, recorded above neck muscles) and *ocular* vestibular-evoked myogenic potentials (oVEMPs, recorded above oculomotor muscles). However, we note that *cerebral* vestibular-EPs [referred to as Vestibular-Evoked Potentials (VestEPs) in line with (44) and (33)] recorded over the scalp using EEG or magnetoencephalography (MEG) have been explored since decades but are not yet part of the clinical vestibular assessment.

This article reviews findings from electrophysiological investigations of VestEPs in humans. We outline the advantages and limitations of different vestibular stimulation methods for EPs approaches. We then describe the spatiotemporal characteristics of VestEPs, distinguishing between those of probable brainstem, cerebellar, and cortical origins. Finally, we present potential applications of the VestEPs to otoneurology and to cognitive neuroscience.

VESTIBULAR STIMULATION FOR NEUROIMAGING STUDIES AND THEIR APPLICATION TO VESTIBULAR-EVOKED POTENTIALS

The scarcity in VestEPs studies is largely due to technical challenges to stimulate the vestibular system in a well-controlled and reproducible way. A variety of techniques has been used to activate the vestibular receptors or vestibular nerve in humans. These techniques fall into two main groups. One group involves *natural* vestibular stimulation using whole-body rotations or translations on motorized devices. These techniques are compatible with EEG recordings and EPs approaches, but they are to date not compatible with "online" fMRI and PET recordings. The other group of techniques involves *artificial* stimulation of the vestibular end organs in participants keeping their head fixed in space. Cold and warm CVS with air or water, binaural or monaural GVS and sound-induced vestibular stimulation (SVS) are the most common techniques. These stimulation techniques are fully compatible with neuroimaging and electrophysiological recordings. However, although they have been largely used in fMRI and PET studies, they have not often been used in EEG studies. This section briefly presents the

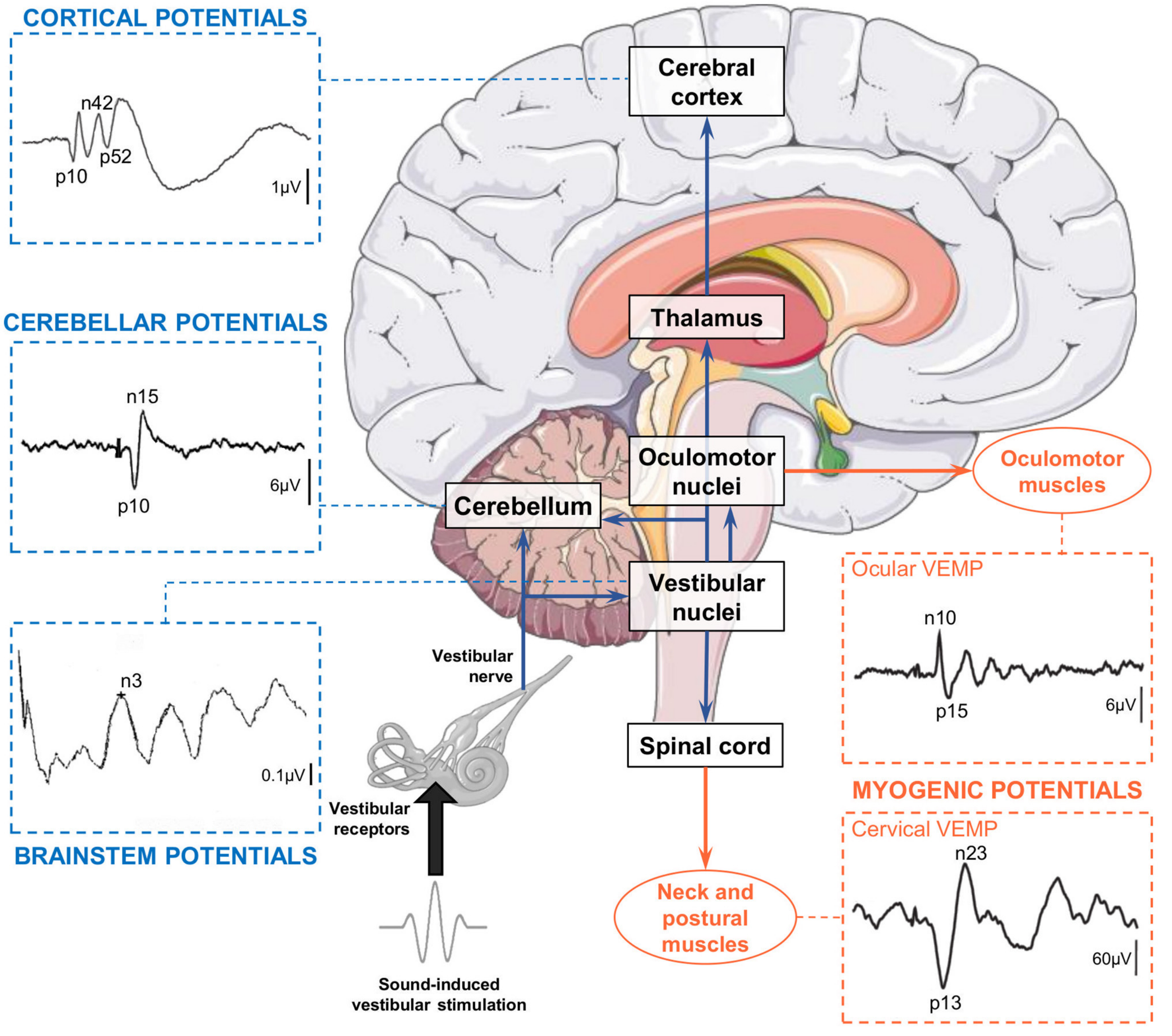

FIGURE 1 | Electrical potentials evoked by sound-induced vestibular stimulation can be recorded along the pathways from the otolithic receptors to the central nervous system and muscles. Vestibular-evoked myogenic potentials (VEMPs) are recorded over extraocular, neck, and postural muscles. Cervical VEMPs reflect an inhibitory reflex and are recorded with electrodes over the sternocleidomastoid muscle ipsilateral to the stimulation. Ocular VEMPs reflect an excitatory reflex and are recorded with electrodes placed over the inferior oblique muscle contralateral to the stimulation. Both traces are adapted from (39). Vestibular-evoked cerebral potentials (VestEPs) are recorded from electrodes placed on the scalp or neck. Brainstem potentials are characterized by an n3 component observed under electrode P3 [this example recorded in a healthy participant is adapted from (40)]. Cerebellar potentials: Grand mean evoked potentials showing probable cerebellar components p10 and n15 observed under electrode P08 [illustration adapted from cf. Govender et al. (41) with permissions from Springer Nature]. Cortical potentials: Grand mean evoked potentials showing components p10, n42 and p52 observed under electrode FCz [illustration adapted from (42)]. Brain illustration from Servier Medical Art (smart.servier.com).

main techniques for vestibular stimulation [for detailed reviews see (15, 45, 46)] with their advantages and limitations to measure VestEPs using EEG.

Rotatory Chairs and Whole-Body Motion Platforms

Passive whole-body motion has been used to investigate VestEPs, mostly using rotatory chairs combined with EEG recordings (44, 47–54). To our knowledge, the first study presenting results from EEG recordings in participants sitting on a rotating chair was conducted by Greiner et al. (47). Chairs rotating around an earth-vertical axis stimulate the horizontal semicircular canals in participants sitting upright, and stimulate the vertical canals in participants lying supine or lying on their side (55). Rotations can also be applied only to the head, for example in lying participants with their head inserted and firmly held in a rotating drum (56). As summarized in a literature review by Ertl and Boegle (46), "most studies used smooth motion profiles like raised-cosine velocity profiles with peak velocities above 100°/s" or "used transient stimuli with duration shorter than 100 ms and peak accelerations up to 12,500°/s^2" (32, 51, 57). Such controlled stimuli allow to study vestibular-evoked responses time-locked to different motion parameters (i.e., onset, offset, peak velocity). Voluntary, active head rotations with accelerations up to 12,000°/s^2 have also been used (58, 59).

Linear motion platforms and tilting devices deliver natural stimulation to the otolithic receptors (the utricule and the saccule) (60). When compared to the processing of semicircular canal signals, there is only scarce description of how the vestibulo-thalamo-cortical system processes otolithic signals (61). Devices allowing whole-body translations are less common than rotating chairs in basic science laboratories and hospitals, which may have hampered the description of otolithic responses.

New motion platforms with precise control of the amplitude, acceleration, and velocity of passively applied movements now allow to study responses to complex natural vestibular stimulation. Six-degree-of-freedom motion platforms, such as the Moog® 6DOF2000E (**Figure 2A**), provide comparisons with studies in macaques that have used the same platform to record single cell responses to whole-body rotations and translations (24, 64).

Rotatory chairs and whole-body motion platforms are incompatible with fMRI and PET, because head movements are precluded in scanners. To circumvent this issue, *passive* whole-body rotations and translations followed by offline PET recordings have been used in a recent study (65). Although this study is original in that it reports predominant bilateral activation in the deep part of the Heschl's gyrus, overlapping with the posterior insula, in response to natural whole-body motion, the response was recorded offline, and does not reflect the spatiotemporal pattern of vestibular information processing. Few studies have used blood-oxygen-level-dependent (BOLD) recordings after voluntary *active* head rotations to investigate vestibular responses (25–27). A main limitation of this approach is that vestibular responses are reduced in the brainstem and cerebellum during active compared to passive movements, as shown in animal studies (66–68). In addition, intraparietal neurons respond to different directions of movement depending on whether the movement is active or passive (69, 70). These differences in vestibular processing limit a direct comparison of neuroimaging data using active head motion with studies using passive body motion.

Application to VestEPs

Electroencephalography remains the best and most direct method to analyze the spatiotemporal dynamics of brain responses to natural vestibular stimuli, given its high temporal resolution below the milliseconds and its compatibility with recordings during natural, passive whole-body motion. One must, however, consider that rotatory chairs and motion platforms for body translations can induce mechanical and electromagnetic artifacts in the EEG signal, besides artifacts due to reflexive eye movements (i.e., vestibulo-ocular reflex) and muscles contractions (i.e., vestibulocollic and vestibulospinal reflexes). Rotatory chairs and motion platforms also generate auditory noise that needs to be controlled for. Finally, it should be noted that body rotations and translations activate the somatosensory and interoceptive systems, respectively, due to the pressure of the body against the chair or to the movement of bodily fluids, which can hardly be diminished.

Caloric Vestibular Stimulation

Caloric vestibular stimulation (CVS) is the most common technique to evaluate the semicircular canals functions (see **Figure 2B**). It consists in applying warm (≥44°C) or cold (≤30°C) water (or gas) in the auditory canal of participants lying supine, with their head tilted 30° forward. The fluid creates a temperature gradient in the semicircular canals, which induces an endolymphatic flow activating the hair cells in the crista ampullaris. The firing rate in the vestibular afferents increases or decreases accordingly to the increase or decrease in temperature in the inner ear. Caloric vestibular stimulation mostly activates the horizontal semicircular canal, with a weaker contribution of the anterior and posterior canals (71). This stimulation induces a nystagmus toward the stimulated ear with hot water or gas and induces a nystagmus toward the opposite ear with cold water or gas. These oculomotor responses are accompanied by complex sensations of rotation, floating, and tilting. These manifestations occur only after several seconds of stimulation and a clear onset is often difficult to determine. They can also last several minutes after the end of the stimulation. Caloric vestibular stimulation is fully compatible with fMRI, PET, EEG, and MEG and has been used in the pioneer vestibular neuroimaging studies about 40 years ago (72, 73). Recent neuroimaging studies showed that CVS activates several cortical areas, such as the inferior parietal lobule, superior temporal gyrus, insula, frontal cortex, and frontal eye fields as well as hippocampal, parahippocampal, and thalamic regions [(74–80); for a detailed review see (15)].

Application to VestEPs

Caloric vestibular stimulation has been used in early studies of VestEPs, especially in epileptic patients (81–85). These studies showed that CVS modulates brain rhythms (e.g., alpha rhythm desynchronization) and can trigger seizures in predisposed patients. However, CVS does not seem appropriate for EPs approaches for several reasons. First, the nystagmus evoked by CVS can create important artifacts to the EEG recordings. Second, as the exact onset of the effects of caloric stimulation on vestibular receptors is difficult to determine, this precludes EP approaches. Third, CVS cannot be repeated many times in a short period of time, which is required to calculate EPs. Finally, CVS activates the somatosensory, thermoceptive and nociceptive sensory systems, leading to unspecific activations of extravestibular pathways.

Galvanic Vestibular Stimulation

In contrast to CVS, galvanic vestibular stimulation (GVS) activates the vestibular end organs with a temporal precision under the microsecond. Galvanic vestibular stimulation consists in the application of a small transcutaneous electrical current (in

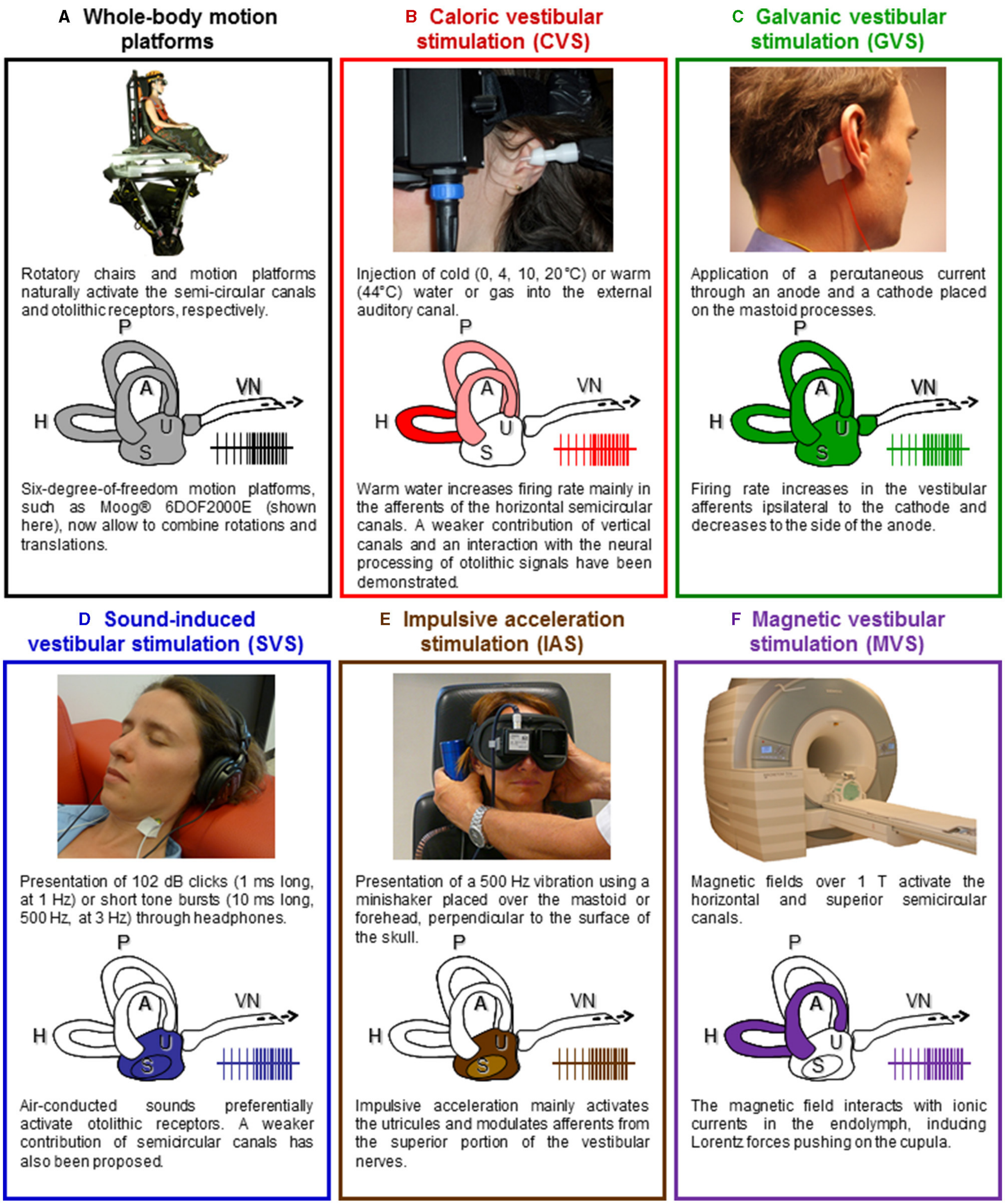

A Whole-body motion platforms

Rotatory chairs and motion platforms naturally activate the semi-circular canals and otolithic receptors, respectively.

Six-degree-of-freedom motion platforms, such as Moog® 6DOF2000E (shown here), now allow to combine rotations and translations.

B Caloric vestibular stimulation (CVS)

Injection of cold (0, 4, 10, 20 °C) or warm (44°C) water or gas into the external auditory canal.

Warm water increases firing rate mainly in the afferents of the horizontal semicircular canals. A weaker contribution of vertical canals and an interaction with the neural processing of otolithic signals have been demonstrated.

C Galvanic vestibular stimulation (GVS)

Application of a percutaneous current through an anode and a cathode placed on the mastoid processes.

Firing rate increases in the vestibular afferents ipsilateral to the cathode and decreases to the side of the anode.

D Sound-induced vestibular stimulation (SVS)

Presentation of 102 dB clicks (1 ms long, at 1 Hz) or short tone bursts (10 ms long, 500 Hz, at 3 Hz) through headphones.

Air-conducted sounds preferentially activate otolithic receptors. A weaker contribution of semicircular canals has also been proposed.

E Impulsive acceleration stimulation (IAS)

Presentation of a 500 Hz vibration using a minishaker placed over the mastoid or forehead, perpendicular to the surface of the skull.

Impulsive acceleration mainly activates the utricules and modulates afferents from the superior portion of the vestibular nerves.

F Magnetic vestibular stimulation (MVS)

Magnetic fields over 1 T activate the horizontal and superior semicircular canals.

The magnetic field interacts with ionic currents in the endolymph, inducing Lorentz forces pushing on the cupula.

FIGURE 2 | Vestibular stimulation techniques. **(A)** Rotating chairs stimulate the semicircular canals and linear motion platforms and tilting devices deliver natural stimulation to the otolithic receptors (the utricule and the saccule). New motion platforms with precise control of the amplitude, acceleration, and velocity of passively applied movements now allow to study responses to complex natural vestibular stimulation. Illustration adapted with permissions from (62). **(B)** Caloric vestibular stimulation (CVS) consists of irrigating the external auditory canal with warm or cold water or airflow. Caloric vestibular stimulation evokes a nystagmus and self-motion perception, often leading to vertigo and a sensation of dizziness. Illustration adapted from (15) with permissions from Elsevier. **(C)** Galvanic vestibular stimulation (GVS)

(Continued)

FIGURE 2 | consists of applying a weak transcutaneous current through an anode and a cathode placed over the mastoid processes. The cathode increases the firing rate in the ipsilateral vestibular afferents, while the anode decreases it. GVS stimulates simultaneously all otoliths and semicircular canals afferents. Illustration adapted from (15) with permissions from Elsevier. **(D)** Auditory stimuli such as clicks and short-tone bursts can stimulate the otolithic receptors. Illustration adapted from (15) with permissions from Elsevier. **(E)** 500 Hz vibrations applied on the mastoids or the forehead using a minishaker stimulate the otolithic receptors and induce ocular and cervical VEMPs. Illustration adapted from (63). **(F)** Based on the analysis of the nystagmus it evokes, magnetic vestibular stimulation (MVS) is thought to activate the horizontal and superior semicircular canals. It offers a way to produce long-duration vestibular stimulation, equivalent to a constant angular acceleration on a motion platform. A, H, P, anterior, horizontal, and posterior semicircular canals; S, saccule; U, utricule; VN, vestibular nerve.

general up to 5 mA) through a cathode and an anode placed on the skin over the mastoid processes (see **Figure 2C**). Galvanic vestibular stimulation can be applied monaurally (electrodes are on the same ear) or binaurally (electrodes are placed on the opposite ears), with continuous electrical stimulation, single square-wave pulse, or trains of pulses. Galvanic vestibular stimulation is thought to directly modulate the firing rate of the vestibular afferents (86), although a GVS may also stimulate the vestibular hair cells (87). The cathode increases the firing rate in the vestibular afferents, while the anode decreases it [reviewed in (88)]. Galvanic vestibular stimulation is an artificial vestibular stimulation in that it bypasses the mechanoelectrical transduction in the hair cells and activates afferent fibers from receptors that would never be activated together during naturalistic head movements. Continuous GVS induces, almost instantaneously, complex sensations of combined translation and rotation, which orientation and intensity can be modulated by the direction and intensity of the applied current. As early as the 1990s, neuroimaging studies have used GVS to localize the vestibular cortex. They identified areas such as the supramarginal gyrus, precuneus, posterior cingulum, superior and middle temporal gyrus, insula, frontal areas and frontal eye fields, inferior and superior occipital gyrus as well as hippocampal, parahippocampal, and thalamic areas [(89–93); for a detailed review see (15)].

Application to VestEPs

Trains of short electrical pulses, such as those used to evoke cVEMPs [e.g., 2-ms pulses at 5 Hz; (94)], generally do not evoke self-motion perception and are theoretically ideal to measure VestEPs. However, GVS can evoke muscular responses such as cVEMPs (94) also time-locked to the stimulation, which can contaminate VestEPs recordings using EEG. Galvanic vestibular stimulation is a transcutaneous stimulation that activates the somatosensory—and sometimes the nociceptive—system. More importantly, GVS generates electromagnetic artifacts that affect EEG recordings and may not be suppressed, preventing the observation of short latency VestEPs. One early study combined continuous GVS with EEG to investigate long latency VestEPs and described a series of positive and negative components with an onset latency around 60–80 ms which could last up to 500 ms after the stimulation (95). To our knowledge, only one EEG study has recently identified VestEPs of middle and long latency evoked by 3 ms square-wave pulses (96).

Sound-Induced Vestibular Stimulation

Sound-induced vestibular stimulation (SVS) offers the precise timing of GVS without electromagnetic artifacts and seems therefore particularly appropriate for event-related EEG studies (see **Figure 2D**). Short sounds are highly reproducible and repeatable stimuli whose onset and offset can be controlled with a millisecond precision. Short high sound pressure clicks at intensities around 100 dB-SPL and short tone-bursts at 500 Hz pressurize and activate otolithic receptors (43, 97, 98). Sound-induced vestibular stimulation is widely used in otoneurology to compare the latency and amplitude of cVEMPs and oVEMPs after stimulation of the right and left ear separately (38, 99, 100). Sound-induced vestibular stimulation does not seem to induce any vestibular perception although this has never been thoroughly investigated. Sound-induced vestibular stimulation has been used in neuroimaging studies of the vestibular system and revealed otolithic projections to frontal, parietal, and cingulate regions, similar to areas revealed using semicircular canal stimulation (101–103).

Application to VestEPs

Sound-induced vestibular stimulation allowed to identify VestEPs and to describe components of short (40, 104–109), middle (42, 108, 110, 111), and late latency (42, 110, 112). As described below, short, middle, and late VestEPs evoked by SVS have been associated to different generators along the vestibulo-thalamo-cortical pathways, so that SVS likely allows to study the spatiotemporal processing of vestibular information from the periphery to the cortex.

Vestibular-evoked potentials and auditory EPs show similar latencies and some responses to SVS appear to contain both auditory and vestibular contributions. Different techniques can then be used to disentangle them. As SVS de facto activates the auditory system, studies have used control auditory stimuli, modulating either the intensity or the frequency of sounds to separate vestibular and auditory responses (108, 111, 113). Most studies of VestEPs using SVS have used sounds below and above the vestibular threshold, determined as the intensity above which sounds evoke VEMPs for a given ear in a given individual (42, 107, 108, 110, 113–115). This allows to identify VestEPs, which only appear for SVS above the vestibular threshold, from auditory components appearing for SVS below and above the vestibular threshold. The validity of this approach has been confirmed in recent fMRI studies. An independent component analysis revealed a specific increase in BOLD response for SVS above the vestibular threshold in areas such as the insula, precuneus, inferior parietal lobule, middle cingulate cortex, and cerebellar uvula (116). Subsequent parametric analyses revealed vestibular-auditory integration in the caudal part of the superior temporal gyrus and posterior insula (117). However, some authors argued that in EEG studies it might be difficult to disambiguate between auditory and vestibular components because the time course of VestEPs during whole-body translation and the time course of auditory EPs overlap (33). In conclusion, SVS seems to be a useful and convenient technique to evoke VestEPs and study their cerebral origin using source analysis, provided that relevant controls and analyses are used to disentangle them from auditory components.

Impulsive Acceleration Stimulation

Impulsive acceleration stimulation [IAS; (46)] also referred to as “bone-conducted” stimulation (41), can be applied using a minishaker placed over one of the mastoids or on the forehead, at the hairline (Fz), perpendicular to the skull surface (see **Figure 2E**). Five hundred Hz vibrations stimulate the otolithic receptors and induce ocular and cervical VEMPs (43, 118, 119). These can be used to investigate unilateral vestibular loss, for example by comparing responses below both eyes (63).

Application to VestEPs

Impulsive acceleration stimulation has been used in a few studies to evoke VestEPs, as it creates rapid and highly reproducible translational accelerations up to 0.2 g (108, 120). However, IAS activates the somatosensory and auditory systems and can cause small head movements creating artifacts in fMRI and EEG studies. For these reasons, IAS remains rarely used for the study of central vestibular projections.

Magnetic Vestibular Stimulation

Magnetic vestibular stimulation (MVS) recently emerged as a new method to stimulate vestibular receptors (see **Figure 2F**). Magnetic fields over 1 T can induce a nystagmus in healthy participants that is absent in patients with a bilateral vestibular failure (121–123). Based on the analysis of the nystagmus it evokes, MVS is thought to activate the horizontal and superior semicircular canals (124). Magnetic vestibular stimulation interacts with ionic currents in the endolymph, inducing Lorentz forces pushing on the cupula. It offers a way to produce long-duration vestibular stimulation, equivalent to a constant angular acceleration on a rotatory chair. Accordingly, MVS over 3 T can induce sensations of rotation. Magnetic vestibular stimulation has been shown to modulate the BOLD response in vestibular and oculomotor areas, including the anterior cingulum, cerebellar vermis, and calcarine sulcus (125). Magnetic vestibular stimulation can be used as vestibular stimulation in conjunction with resting-state fMRI or fMRI studies of cognitive processes.

Application to VestEPs

Electrophysiological recordings can now be arranged in an MRI bore and several studies showed that EEG, with event-related potential approaches, can be recorded simultaneously as fMRI (126–128). However, MVS has several major caveats for EP approaches, which have been reviewed in Ertl and Boegle (46). Mostly, MVS precludes the application of repeated stimuli with a clear onset: as the magnetic field of the scanner is constant, MVS does not allow to compare changes in brain activity due to MVS with respect to a baseline (without MVS) with an event-related potential approach. Magnetic vestibular stimulation also induces a nystagmus, that needs to be controlled for or inhibited to avoid muscular artifacts in the EEG signals. Of note, the magnetic field interferes with electrophysiological recordings and careful artifact removal is required [e.g., (129, 130)].

Intraoperative Vestibular Nerve Stimulation

Direct electrical stimulation of the vestibular nerve can be combined with EEG recordings in patients undergoing vestibulocochlear nerve surgery. This was performed in rare studies during unilateral vestibular neurectomy for intractable Menière’s disease and during neuroma resection (131–133).

Application to VestEPs

Intraoperative vestibular nerve stimulation is close to early electrophysiological investigations of the vestibular cortex in cats and monkeys (134, 135) or to recent studies in rodents (136), which applied electrical stimulation to the vestibular nerve. Early human studies, using montages with only few electrodes, did not provide information regarding the generators of the VestEPs (131, 132). Electrical stimulation may spread to the facial nerve or the acoustic nerve and general anesthesia may alter vestibular information processing.

Conclusion

Major shortcomings have been emphasized for natural and artificial vestibular stimulations when neuroimaging the vestibular system is concerned (15, 46). To date, natural vestibular stimulation is not compatible with neuroimaging techniques with high spatial resolution such as fMRI. Most neuroimaging studies so far have used artificial stimulation to study the vestibular system with a high spatial resolution but a poor temporal resolution. By contrast, EEG has a high temporal resolution and is compatible with both natural and some artificial vestibular stimulations. However, EEG is known for its relatively low spatial resolution and the difficulty to accurately identify subcortical generators of signals recorded on the scalp. In addition to these issues of compatibility between stimulation and recording techniques, most artificial vestibular stimulation (and natural vestibular stimulation to a lesser extent) co-activate other sensory receptors. This includes mostly activation of auditory, somatosensory, interoceptive, as well as sometimes nociceptive systems, which are difficult to control for in neuroimaging studies. Moreover, artificial vestibular stimulation can induce sensory conflicts between vestibular information and other senses, contrary to natural vestibular stimulation.

With these limitations in mind, it seems feasible to investigate the spatiotemporal dynamics of vestibular information processing in the human central nervous system by carefully adapting the vestibular stimulation to each recording technique and using the necessary control conditions. The next section focuses on how VestEPs help understand the spatiotemporal dynamics of vestibular information processing.

VESTIBULAR-EVOKED POTENTIALS

Pioneering work described VestEPs in humans as early as the 1960s (47, 137, 138). Interestingly, VestEPs were also described in several animal species during the 1960s or the following decade using similar approaches [see for example studies in guinea pigs: (139); cats: (48, 140); non-human primates: (141)]. Early research focused on the influence of rotatory vestibular stimulation on EEG signals in epileptic patients. These studies showed that vestibular stimulation could activate temporal epileptic foci and sometimes trigger seizures (47, 85, 142–144). Another line of studies compared scalp responses between healthy participants and patients with a bilateral vestibulopathy or between the two sides in patients with a unilateral vestibular loss. They confirmed the existence of a vestibular response under scalp electrodes. The most consistent finding was a suppression of alpha rhythm over the temporo-parietal junction (47, 82, 143). Finally, early studies using CVS reported similar effects on EEG signals, showing that cerebral responses could also be evoked by artificial vestibular stimulation (82–85).

On the grounds of these pioneering studies and after improvement in recording techniques, VestEPs were described more precisely. **Supplementary Table 1** summarizes the studies considered in this review, together with the latencies and scalp location of the main VestEPs, as well as the electrode montages used to record them. To facilitate the literature review, we have classified VestEPs as short (<20 ms), middle (20–50 ms), and late (> 50 ms) depending on their peak latencies and their most probable generators, similarly to the classification of auditory EPs (145). In the text and in the figures, we chose to homogenize the report of the VestEPs components by indicating their positive (p) or negative (n) polarity followed by their reported peak latency (or average latency) expressed in ms post-stimulation onset. We therefore avoid the use of general labels relative to the order of appearance of the components, such as P1, N1, P2, and N2, which refer to very different latencies in different studies using different paradigms and stimulation parameters. The purpose of this is not to redefine common component names but to help the reader compare components latency and polarity in a simple way and avoid confusion.

SHORT LATENCY VESTIBULAR-EVOKED POTENTIALS

Vestibular-evoked potentials with a latency below 10 ms have been related to signal conduction in the vestibular nerve and vestibular information processing in the vestibular nuclei (40, 56, 57, 104–106, 109, 132, 133, 146, 147). Vestibular-evoked potentials with a peak latency between 10 and 20 ms have been attributed to myogenic, cerebellar or cortical sources (41, 42, 56, 57, 107, 108, 110, 113–115, 120, 133, 148–150). In this section, we describe the short latency components that emerge across the studies and briefly discuss their origin.

Short Latency Responses Under 10 ms

Responses with the shortest latency have been observed during perioperative stimulation of the vestibular nerve. An early study using direct electrical vestibular nerve stimulation in nine patients operated on for intractable Menière's disease revealed a negative potential with a latency of 2 ms and an amplitude of 0.5 μV (132). This response was suppressed after vestibular neurectomy, indicating its vestibular origin. In a later study, a similar stimulation elicited VestEPs with an onset of 3.5–5 ms and peak latency of 9.5 ms in 11 patients with 30 electrodes on the scalp (133). These responses were recorded bilaterally, but the larger responses were observed under ipsilateral electrodes at the lower part of the temporal scalp region.

A series of studies using rapid and passive head rotations in the yaw plane, consisting of impulses at 10,000°/s², report similar responses. Some studies identified a forehead positive peak at 3.5 ms, a negative peak at 6 ms, and a positive peak at 8.4 ms (56, 57). Another study recorded a response onset around 2.2 ms, followed by a positive peak at 2.9 ms, and other components with peak latencies at 5.1, 7.0, and 8.6 ms (147). The responses amplitude ranged from 0.3 to 0.6 μV. Horizontal lateral translations also triggered responses with 3 and 6 ms peak latencies (146). Impulsive acceleration stimulation also evoked components with latencies of 1.9, 2.4, and 4.5 ms (151). Of note, skin surface recordings and intracranial recordings in the cat vestibular nuclei with the same acceleration impulses revealed that irregular neurons responded with a 3.5 ms latency to the onset of the head acceleration (152, 153). The authors proposed that the component with an onset around 2 ms reflects vestibular nerve activity, whereas the following components are of vestibular nuclei origin (152, 153).

More recent studies looking for vestibular components in the brainstem auditory-evoked potentials (BAEPs) have confirmed and extended such results. Brainstem auditory-evoked potentials are a standard for the clinical evaluation of hearing and brainstem auditory pathways (37). They consist of five to six vertex positive waves and likely present vestibular components of saccular origin. This was first suggested by studies in guinea pigs showing preserved short latency far field components after cochlear hair cells destruction (154, 155). In humans, a similar 3 ms latency negative peak, referred to as the n3, was identified using a classical BAEPs montage with loud clicks (40, 104, 109). Air-conducted tones pips, which delay BAEPs, induced a response similar to the n3, but with a 5 ms latency, referred to as the n5 (105, 106). The n3 and n5 are likely of vestibular origin, as they are found in deaf patients (104), but are absent in vestibular-defective patients, even when they show preserved hearing and a residual caloric nystagmus (109).

The n3 can be recorded at the vertex and the n5 is best observed ipsilaterally to the acoustic stimulation, over parietal areas. The short latency of the n3 and n5 components suggest that they are far-field potentials originating from the vestibular nuclei (104). Their absence in multiple sclerosis patients with demyelination in the lower pons confirms this origin (40, 105). In addition, an n6 component, also evoked by SVS but independent of the n5, was maximally recorded over the parieto-occipital area (106). Because it appears approximately 1 ms after the n5, this component has been proposed to originate in the rostral pons or the midbrain (106).

Short Latency Responses Above 10 ms

Vestibular-evoked potentials between 10 and 20 ms are the most investigated, and several components have been identified. These components are often considered as part of a biphasic wave (such as the p10–n15 and n15–p21 waves) or have been described as individual components with a given peak latency (such as the p10 and p21). We summarize below the main individual components reported in the literature (**Supplementary Table 1**).

Component p10

Several studies have described a positive component with an onset latency of 6–7 ms and a peak latency around 10 ms after whole-body rotations (56, 57), SVS (42, 107, 108, 110, 114, 115, 149), and direct electrical nerve stimulation (133). Several VestEPs seem to appear at this latency because they are recorded under different electrode locations. Using SVS, it was possible to show that the p10 (as well as subsequent components: n15, n17, and p21; see below) was of vestibular origin. The p10 (as well as n15, n17, and p21) was present in a patient with hearing loss and preserved vestibular function, but was abolished in a patient with impaired vestibular function and preserved hearing (107). In addition, it was absent for SVS below the vestibular threshold (i.e., the intensity at which VEMPs appear) and was observed above this threshold (42, 107, 108, 110).

Vestibular-evoked potentials with a latency near 10 ms were first showed frontally (56, 57, 133) or maximal at central electrode Cz with a small ipsilateral lateralization (107). De Waele et al. (133) proposed that such VestEPs reflect activation of several cortical areas. A dipole source analysis showed, within 6 ms, parallel activation of the ipsilateral temporo-parietal cortex, prefrontal, and/or frontal lobe, supplementary motor area, and contralateral parietal cortex [(133); **Figure 3A**]. These findings are in line with the observation that the posterior part of the postcentral gyrus (area 2) is activated within 5–6 ms after electrical vestibular nerve stimulation in the rhesus monkey (135).

A p10 component, followed by an n17 component, has also been observed at parietal electrode Pz [(108); **Figure 3B**] or at the inion (115). Several generators have been proposed for the p10 and n17 components. As the p10/n17 is concomitant to the oVEMP biphasic wave n10/p17, a myogenic or cerebral generator has been proposed (108, 113). Subsequent studies found that the p10 mirrors a frontal or infra-ocular n10 response (110) and supported the idea that they are two distinct responses (115).

A line of research suggests that the p10 may originate from the cerebellum (108, 110, 115, 149). Sound-induced vestibular stimulation evoked a p10/n17 response at occipital electrodes (PO7 and PO8) contralateral to the stimulated ear and at the inion (Iz), together with a n10/p17 complex under electrodes placed over the splenius muscles to record cerebellar activity (115). A source analysis found the contralateral cerebellum as the most likely origin of these responses (115). The fact that, as for the oVEMP n10/p17, the p10/n17 depends on gaze direction (115) indicates either a myogenic origin or the recording of cerebellar or cerebral mechanisms to regulate ocular responses to vestibular stimulation. To further investigate the cerebellar origin of these VestEPs, recent studies used extended EEG montages to record the electrocerebellogram, with electrodes over, laterally to and below the posterior fossa, thus over the inferior cerebellum (41, 120, 150, 156). With such montages, IAS revealed a p12/n17 biphasic wave (41, 120, 150). A source analysis showed the cerebellar origin of the p12/n17 (150). It was argued that the response could not be myogenic because neck muscles were relaxed during recordings, the response was lateralized, and the waveforms differed from those of cVEMPs (41). Although these recent results are very promising, one cannot exclude that neck muscle relaxation does not fully abolish a potential muscular contribution to the observed responses.

The above-mentioned results are not only encouraging for the electrophysiological investigation of the spatiotemporal dynamics of vestibular information processing, but also for the non-invasive electrophysiological study of cerebellar functions in general. The study of the cerebellum using EEG is indeed controversial due to the structure of the cerebellum, traditionally low EEG spatial sampling over the cerebellum, and non-realistic spherical head models for source analyses [reviewed in (157)]. However, more and more evidence supports the feasibility of EEG and MEG studies of cerebellar activity, provided that improvements are made to the usual EEG and MEG techniques (157). Todd and colleagues in their series of EEG studies have taken a first step toward these improvements by placing EEG electrodes more posteriorly in order to improve the chances to record cerebellar activity. However, caution should still be taken regarding the results of source localization, as improvements are still needed to adapt the current models which consider the head as a sphere and poorly integrate the cerebellum.

Component n15

Several SVS studies report a negative component with an onset latency around 8 ms and a peak latency of 15 ms. The n15 was best recorded under frontal [(107, 113, 148), **Figure 3B**] or prefrontal electrodes (42, 110). The vestibular origin of the n15 was confirmed by its presence in a patient with profound hearing loss but preserved vestibular function, and its absence in a patient with hypovestibular function but preserved hearing (107). The n15 amplitude increased in the case of superior canal dehiscence, supporting its vestibular origin (148).

The n15 was first thought of pure myogenic origin (107, 148, 158). Indeed, the n15 recorded frontally was similar in size and morphology to responses recorded around the eyes, and it was modulated by changes in gaze direction. In addition, a patient with superior canal dehiscence showed a very large n15 amplitude (up to 11.8 μV) for SVS at 42 dB above vestibular threshold, which is unusual for neurogenic potentials (107). However, left SVS seemed to induce a more asymmetrical n15 with an earlier contralateral onset (107) or larger responses for left compared to right SVS (114), which suggests that there may be a central origin to this component. By contrast, source localization suggested that the frontal n15 may have a cerebellar and cortical origin (108, 113). In particular, a Brain Electrical Source Analysis (BESA) localized the generators in the contralateral cerebellum or the precentral sulcus (108). A Low Resolution Electromagnetic Tomography Analysis (LORETA) localized the n15 generators in the right precuneus and cuneus (113). Altogether, these results indicate that the n15 may represent concomitant vestibular-induced

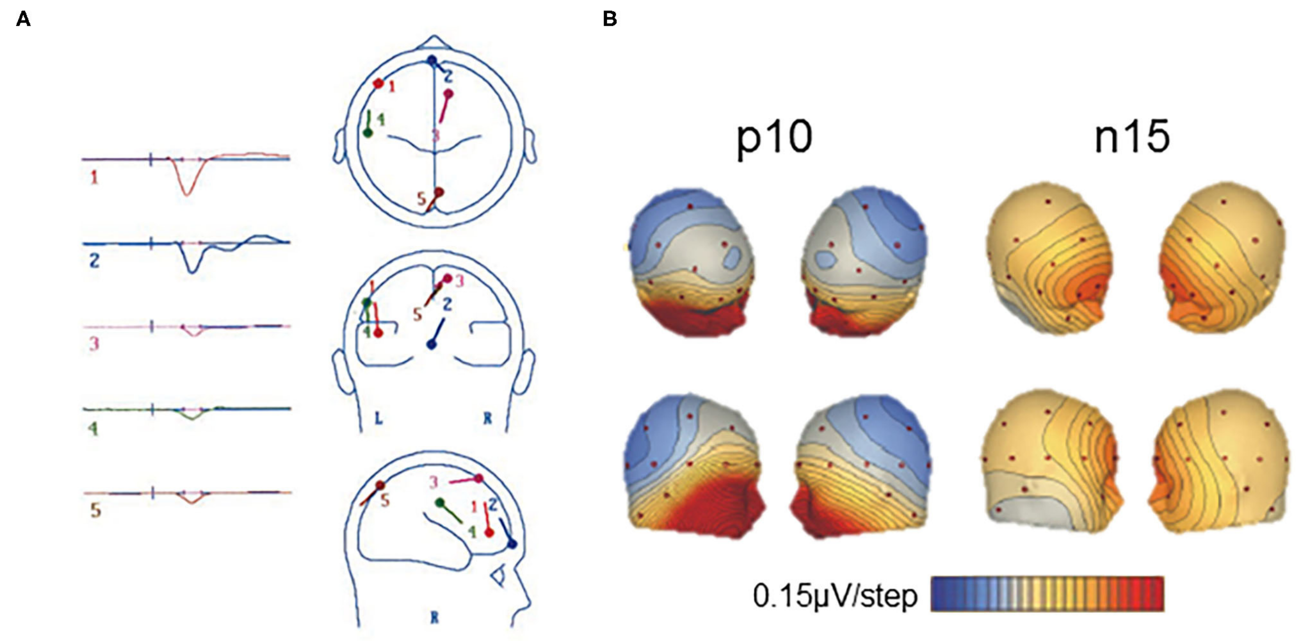

FIGURE 3 | Short latency vestibular-evoked cerebral potentials (VestEPs). **(A)** Source dipole analysis of grand average VestEPs with latencies under 10 ms. VestEPs were triggered by electrical stimulation of the vestibular nerve during surgery. Five dipoles were identified and localized: dipole 1 (red) is at the limit of the ipsilateral frontal and prefrontal lobes, dipole 2 (blue) is on the transverse frontopolar and/or frontomarginal gyrus of the prefrontal lobe, close to the midline, dipole 3 (pink) is on the contralateral anterior portion of the supplementary motor area (around the supplementary eye fields); dipole 4 (green) is on the ipsilateral temporoparietal area; dipole 5 (brown) is on the contralateral superior occipital gyrus, although close to the midline. Adapted from (133) with permissions from Springer Nature. **(B)** Voltage maps of the p10 and n15 evoked by left sound-induced vestibular stimulation. Positive potentials are indicated in blue and negative in red and contours are spaced at 0.15 μV. Adapted from (108) with permissions from Elsevier.

extraocular, cerebellar, and cortical activations around 15 ms. The cerebellar origin of a component better recorded at the frontal level remains however to be confirmed with the development of electrocerebellogram techniques.

Component p20

Components with a latency around 20 ms generally follow those detected near 10 or 15 ms with an inversed polarity under the same or closely located electrodes. An n20 component follows the p15 during whole-body rotations (56, 57, 147, 159) or SVS (137, 138). Likewise, in more recent studies, a positive component with a peak latency of 20–21 ms follows the n15 after SVS (107, 108, 113, 114). A p21 component has been reported under frontal electrodes (107, 108) or under posterior occipital electrodes and right temporal electrodes (113). Applying LORETA localized the p21 generators in the right precentral gyrus, with contributions of the right medial and superior temporal gyri (113).

Conclusion

Electroencephalography and averaging techniques have proven to be effective to study and assess the spatiotemporal dynamics of vestibular information processing within the first milliseconds after stimulation onset. Short-latency responses with a peak latency under 10 ms have been related to activity in the vestibular nerve or vestibular nuclei. This is in accordance with results from early studies in cats and monkeys where the vestibular nerve was directly stimulated and responses recorded in the animal brain (135, 160, 161). Potentials around 2 ms are likely to reflect vestibular nerve response while components with onsets near 2–3 ms and peak latencies observed within 10 ms after the stimulation are attributed to vestibular nuclei activity. Far-field components best recorded at the vertex, such as the n3 and n5, or recorded over parieto-occipital areas, such as the n6, may reflect vestibular information processing along the brainstem, from the lower pons to the rostral pons or midbrain, respectively.

Responses with a peak latency of 10–20 ms may be myogenic, but also reveal a rapid spreading of vestibular information to the cerebellum and cerebral cortex. To our knowledge, only one group documented cerebellar VestEPs in humans (41, 108, 110, 115, 120, 149, 150). Of note, short latency VestEPs were evoked by SVS or IAS at the mastoids, both techniques targeting the otolithic receptors, so that we lack information about the potential cerebellar evoked responses to semicircular canal stimulation. More systematic studies using stimulation techniques such as rotations are needed to better identify the origin of these responses in humans.

Several studies also suggest that vestibular information reaches the cerebral cortex within 6 to 15 ms after stimulation (107, 108, 113, 133). de Waele et al. (133) argued for simultaneous activation of several trisynaptic vestibulo-thalamo-cortical pathways, indicating that vestibular information rapidly spreads to different areas in the cortex. However, the hypothesis of a parallel processing in these areas is not consistent with recent electrophysiological studies in monkeys. Parieto-insular vestibular cortex responses to translations had shorter latency compared to responses in the ventral intraparietal (VIP) area and area MST, supporting the idea that the PIVC is "closer" to the periphery (23).

MIDDLE LATENCY VESTIBULAR-EVOKED POTENTIALS

Only few studies identified VestEPs with a latency between 20 and 50 ms. Here, we will focus on two biphasic VestEPs that seem to consistently emerge from EEG studies: a first VestEP with peak latencies around 20 and 30 ms and a second VestEP with peak latencies around 42 and 52 ms. Some studies also described individual peaks with similar latencies separately.

The "20–30 ms Complex"

A 20–30 ms complex was reported after SVS (111, 162), GVS (96), and skull vibration at the nasion (112). Sound-induced vestibular stimulation evoked a positive peak at 20 ms and a negative peak at 30 ms under fronto-central and centroparietal electrodes of a 32-channel EEG [(111); **Figure 4A**]. This 20–30 complex was also observed using a simplified Laplacian montage that could be used for clinical purposes (111). Another SVS study reported the p23, n24, and n32 components separately (108). Galvanic vestibular stimulation elicited a counterpart of the 20–30 ms complex with latencies of 25 and 35 ms (96). A BESA source analysis and results from an epileptic patient implanted with deep brain electrodes revealed that this complex originated from the bilateral anterior insula and posterior operculum (111). However, the comparison of source analyses revealed dipoles oriented differently in space in these regions for same latencies after SVS and GVS (96).

Skull vibration induced biphasic n26–p30 or p26–n35 responses for positive and negative stimulation polarity, respectively (112). Source localization revealed deep midline sources plausibly representing activity from the cingulate cortex, medial thalamus or basal ganglia, as well as bilateral frontal sources (112). Similar independent components were identified near 30 ms using whole-body rotations (147) and translations (163).

The "42–52 ms Complex"

Several recent studies identified a frontocentral n42–p52 complex using SVS (42, 108, 110) and IAS at the nasion (112). The n42–p52 complex was also referred to as the N*/P* response as it appears among auditory EPs. However, it was argued that the n42–p52 (N*/P*) complex represents a more specific vestibular response as its peak-to-peak slope increased linearly for SVS above the vestibular threshold, and it was not observed in a patient with an unilateral vestibular loss stimulated in the damaged ear [(42); **Figure 4B**]. Brain Electrical Source Analysis revealed that the n42/p52 was best explained by a mid-cingulate source, together with bilateral sources in the superior temporal cortex (42, 110). This is consistent with fMRI studies showing activity in the cingulate cortex following CVS (75, 164, 165) and GVS (89). Other studies reported positive individual components around 40 ms following whole-body rotations [(163); 38.9 ms] and translations [(33, 166, 167); p38.2 ms under parietal electrodes]. More recently, IAS on the left mastoid was also found to evoke n25, p40, and n53 components under Bz, an electrode placed over the cerebellum, two rows below Iz at the midline [(150); following a nomenclature proposed by Heine et al. (168)].

Conclusion

Four peaks are most consistently reported as VestEPs of middle latencies: they constitute the 20–30 complex and the 42–52 complex. These components presented little variability in their latencies and their amplitude increased with stimulation intensity, leading the authors to propose them as reliable markers of cortical vestibular information processing (112).

Studies of middle latency VestEPs localize generators in the operculo-insular complex and cingulate cortex, two key areas of the vestibular cortical network. The insular and cingulate contributions to vestibular processing is well-supported by anatomical evidence in non-human primates (20), meta-analyses of neuroimaging data (15, 16), and intracranial electrical stimulation in epileptic patients (169, 170).

LATE LATENCY VESTIBULAR-EVOKED POTENTIALS

Responses with a latency above 50 ms were already identified in VestEPs investigations from the 1960s (47, 49, 50, 95, 137, 138). However, these early studies did not report the latency of all observed components or mentioned series of components within a time range. Studies using whole-body rotations identified five to seven waves with latencies ranging from 70 to 850 ms (44, 171–176). Responses with latencies up to 3,000 ms have been reported (47). We summarize below some of the most consistently reported responses with latencies above 50 ms (see **Supplementary Table 1**).

Responses at 60–70 ms

Sound-induced vestibular stimulation has been shown to evoke a positive component with a peak latency of 60 ms under temporal electrodes, followed by a frontal component with a peak latency of 70 ms (111). The authors hypothesized that the 70 ms component may reflect crosstalk activity between vestibular areas 2v, 3nv, and the frontal eye fields (111). Galvanic vestibular stimulation also evoked responses at 50 and 80 ms under the same electrodes (96). Source analysis as well as data from an epileptic patient implanted with deep electrodes showed that the anterior insula and posterior opercular cortex responded to SVS [(111); **Figure 5A**]. Similar sources were observed for the response to GVS [(96); **Figure 5A**]. Impulsive acceleration stimulation evoked VestEPs with similar latencies under electrode FCz (112). These VestEPs consisted in a negative peak at 65 ms after positive polarity stimulation and a positive peak at 60 ms followed by a negative peak at 78 ms after negative polarity stimulation (112). Source analysis suggested a posterior cingulate contribution.

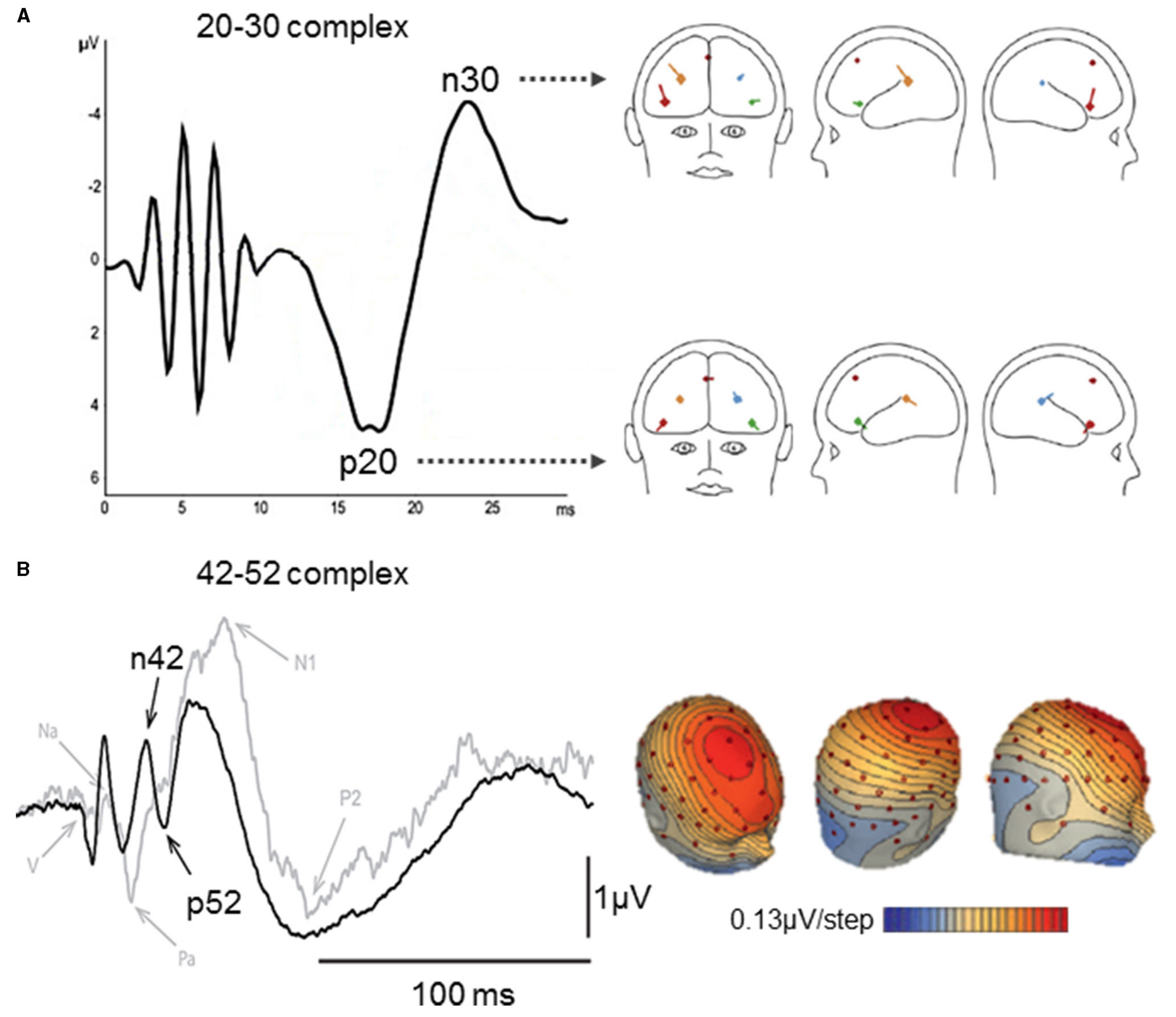

FIGURE 4 | Middle latency vestibular-evoked cerebral potentials (VestEPs). **(A)** The left part shows the 20–30 complex observed with a Laplacian montage (FC1 + FC2 + IO) – (TP9 + TP10), after short latency responses appearing within 10 ms. The right part shows BESA regional source activity for the p20 and n30 components, showing the junction of the anterior insula with the inferior frontal gyrus in the right hemisphere (bright red), the posterior parietal operculum (bright blue), a frontal source near areas 2v, 3aNV, and the frontal eye fields (dark red), the left inferior frontal gyrus (green), the left parietal operculum (brown). Adapted from (111) with permissions from Elsevier. **(B)** Left panel: Grand means of evoked potentials showing the n42–p52 response under electrode FCz after right acoustic stimulation in 10 healthy subjects (black curve) and a patient with a unilateral vestibular loss (gray curve). Right panel: Scalp voltage maps at 42 ms after acoustic stimulation (+18 dB above the vestibular threshold). Positive potentials are indicated in blue and negative in red and contours are spaced at 0.13 µV. Adapted from (42).

Responses at 80 ms

Whole-body translation evoked the n80, a negative component with a peak latency of 80 ms [(33, 166, 167); **Figure 5B**]. The n80 was most prominent under frontal electrodes, but a weaker occipital positivity was also observed with the same latency. The n80 amplitude increased with linear acceleration intensity (33, 166). This was explained by increased activity in the cingulate sulcus visual area, an area involved in self-motion processing (177).

Response at 110 ms

A positive component with a peak latency at 110 ms was reported after both SVS and acoustic control stimulation (111), as well as after GVS (96). This suggests a vestibular contribution to the late auditory EPs, around 100 ms.

Responses at 200 ms

An early study used a vertex referred to mastoid montage and showed a positive potential with a peak latency of 220 ms after

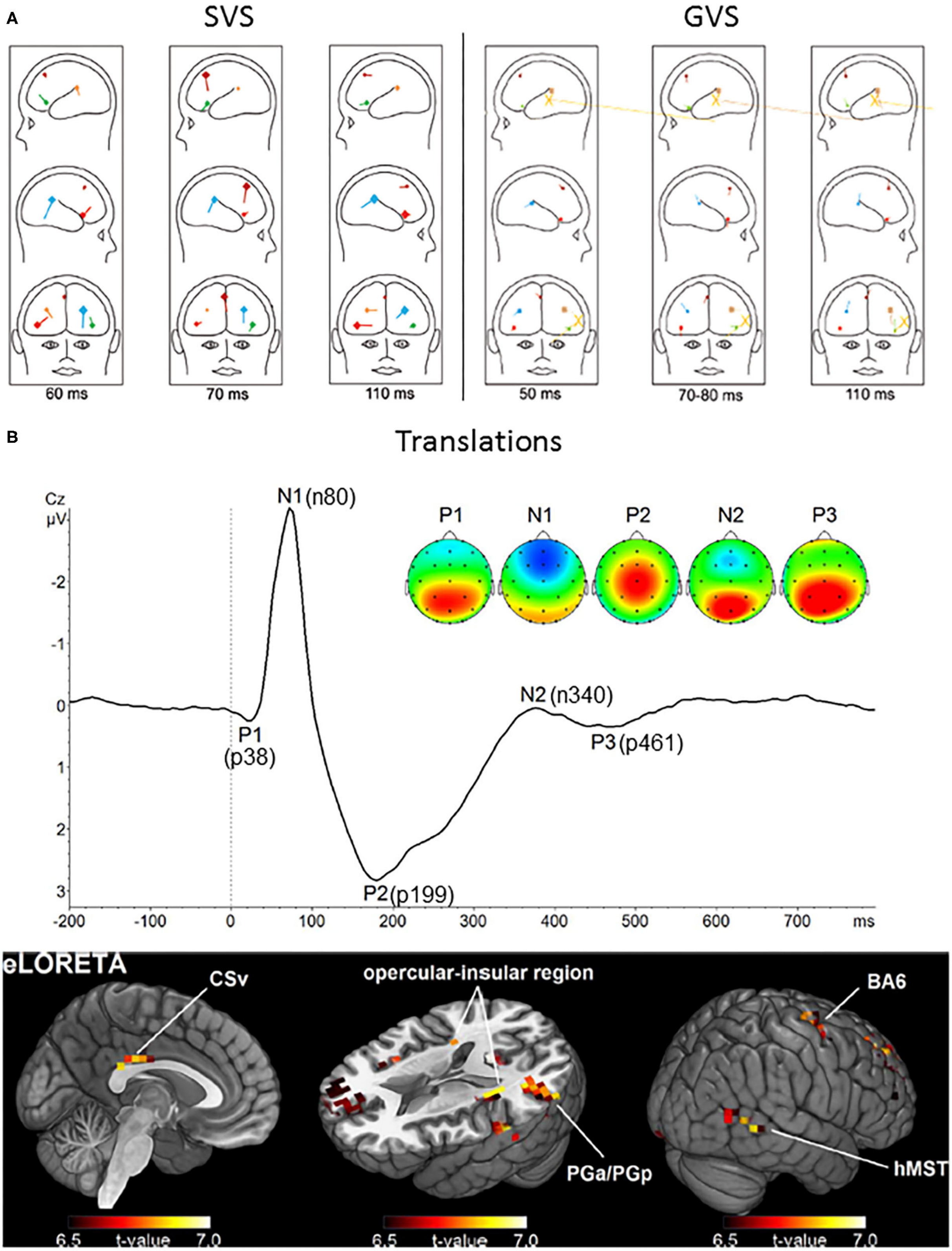

FIGURE 5 | Long latency vestibular-evoked cerebral potentials (VestEPs). **(A)** Sources of evoked potentials observed after SVS (left) and GVS (right). For SVS, BESA regional source activity projected to a head showing the junction of the anterior insula with the inferior frontal gyrus in the right hemisphere (bright red), the posterior parietal operculum (bright blue), a frontal source near areas 2v, 3aNV, and the frontal eye fields (dark red), the left inferior frontal gyrus (green), the left parietal

(Continued)

FIGURE 5 | operculum (brown). For GVS: frontal source (dark red), right anterior insula (light red), left anterior insula (light green); posterior operculum (light blue), left posterior operculum (brown). The yellow large dipoles marked with X represent the combined bilateral bipolar capacitive effects of the galvanic pulse removed with principal component analysis. Adapted from (96, 111). **(B)** Upper panel: Grand average response to translation recorded under electrode Cz. Four late latency VestEPs (n80, p199, n340, and p461, originally referred to as N1, P2, N2, and P3) appear after the middle latency component p38. Their characteristic topographies can be distinguished (positive in red, negative in blue). The p38, n340, and p461 components are dominated by strong bilateral activity (red) over parietal regions. The n80 component is best described by a negative potential (blue) detectable at frontal electrodes. The p199 component has a strong positive peak at electrode Cz. Lower panel: The mean activity of all five components suggests that the cingulate sulcus visual area (CSv), the opercular-insular region, Brodmann area (BA) 6, the inferior parietal lobule (PGa/PGp), and the human medial superior temporal area hMST are the main nodes in the processing of otolithic signals. Adapted from (33) with permissions from Academic Press.

the sudden stop of a rotation (178). This VestEPs was present in 30 healthy participants, but it was absent in two patients after labyrinthectomy. A subsequent study compared the p220 in 159 patients with infarct on the middle cerebral artery to those of 130 controls (179). Hundred and twelve patients showed delayed, decreased, or no evoked response at all, suggesting that vestibular evoked responses to rotations involved the temporo-parietal cortex. Hofferberth [(179), p. 125] concluded that there is a "*primary pathway of vestibular evoked potentials [...] from the vestibular nuclei via the midbrain to the thalamus and from the thalamus to the temporo-parietal cortex.*" This is very close to some descriptions of vestibular pathways, highlighting a main contribution of the temporo-parietal cortex (65, 89, 180, 181).

More recent studies using body translations revealed a positive component with a peak latency of 199 ms, best observed under electrode Cz [(33, 166, 167); **Figure 5B**]. As for the n80, the p199 amplitude increased with body acceleration and this increase was best explained by increased activity in the cingulate sulcus visual area.

Finally, we note that other EEG investigations using whole-body rotations have identified independent components with peak latencies at 200 ms (50, 182), or biphasic waves with peak latencies from 200 to 350 or 400 ms, maximally recorded at the vertex (49, 52, 178, 179, 183, 184).

Responses at 300–500 ms

Various responses have been described within the 300–500 ms time window after active (58, 59) and passive body rotations (32, 44, 47–49, 51, 52, 171, 174, 176, 185), as well as after body translation (33, 166, 167, 186). A seminal study compared human responses to animal responses that were already accepted as vestibular in origin (48). The authors used the sudden stop of yaw rotations as a stimulus both in cats with implanted electrodes and in humans who underwent scalp EEG recordings. They observed late diffuse responses with peak latencies of 300–600 ms in both species, which were prevalent in the preoccipital (area 19) and/or parastriate (area 18) regions in humans. Vestibular-evoked potentials with such late latencies likely reflect the processing of the acceleration profile, with peak amplitudes at peak accelerations (186) or movement inversion (32, 47).

Although their exact latency differ between studies, VestEPs around 300 ms have consistently been reported after passive whole-body rotations (32, 185) and translations (33). For example, whole-body rotations in the yaw plane evoked a vertex negative component with a peak latency near 300 ms (32, 185).

Similarly, whole-body translations evoked a negative component at 340 ms under parietal electrodes, accompanied by a weak negativity under electrode FCz, as well as a positive component at 461 ms which was best observed in centroparietal regions [(33); **Figure 5B**].

Conclusion

Late VestEPs are less well characterized than short and middle latency responses and they appear during a large time window after the stimulation onset. Based on two recent studies using body translations, Ertl et al. (166) proposed that responses with a latency under 220 ms may reflect physical properties of the stimulus, whereas later responses may reflect higher level perceptual and cognitive processes. Such transition from a sensory processing to a higher-level perceptual analysis has been proposed for the auditory system (187).

CONCLUSIONS AND PERSPECTIVES

We have reviewed results from pioneering electrophysiological studies and more recent studies using state-of-the-art EEG indicating that VestEPs can now be considered meaningful electrophysiological signatures of vestibular information processing from the vestibular nerve to the cerebral cortex, owing to the high temporal resolution of EEG. After summarizing the main findings regarding VestEPs with components of short (< 20 ms), middle (20–50 ms), and late (> 50 ms) latency, we discuss how VestEPs studies are informative regarding the parallel vs. hierarchical processing of vestibular signals in the cerebral cortex, and regarding hemispheric dominance of vestibular information processing. While underlining issues with replicability and variability of VestEPs across studies, we discuss the main limitations of VestEPs studies and highlight the difficulty to isolate components of vestibular origin while controlling for extravestibular sensory contributions. Finally, we open perspectives regarding the contributions of VestEPs studies to the fields of neurology, otoneurology, cognitive neuroscience, and systems neuroscience.

Main Findings and Their Link With Vestibular Processing Along Ascending Pathways

Vestibular-evoked potentials with short, middle and late latency mark the different steps and the spatiotemporal organization of vestibular information processing. Vestibular-evoked potentials with a short latency under 20 ms are the most investigated, but independent potentials or biphasic waves also emerge from the literature in the middle and late latency ranges.

Consistent with electrophysiological results from animal studies (152, 153), the first potentials around 2 ms likely reflect vestibular nerve activity, whereas following potentials around 3 ms indicate information processing in the vestibular nuclei (40, 56, 57, 104, 109, 132, 133, 146, 147). It has been proposed that components found at 5 and 6 ms may reflect the transmission of vestibular information along the brainstem (105, 106). Others proposed that vestibular signals reach the cortex as early as 6 ms after stimulation onset (133), that is with a latency equivalent to that necessary to trigger vestibulo-ocular and vestibulocollic reflexes. Reaching the cortex with such short latency may involve vestibular information in an alarm or preattentional system, in addition to top-down control of vestibulo-ocular and vestibulocollic reflexes.

Several components with peak latencies between 10 and 20 ms appear to reflect parallel spreading of vestibular information to the cerebellum (41, 108, 110, 115, 120, 149) and to several cortical regions, including the precentral sulcus, the precuneus, and cuneus, as well as several frontal areas (108, 113, 133). The exact origin and differentiation of these potentials remain to be clarified, and their cerebellar and cortical generators need to be disentangled from myogenic contributions (41, 108, 115). Alternatively, VestEPs with such latency could reflect the descending control of vestibular oculomotor reflexes.

Middle latency VestEPs (20–50 ms) have been associated to activity in the insular, posterior opercular and cingulate cortex in a series of recent EEG studies using SVS and GVS (42, 96, 111). These areas form the core region of the cortical vestibular network (11, 15, 16, 18, 188) and show strong functional connectivity with other cortical vestibular areas (189).

Results concerning VestEPs with late latencies (>50 ms) are more disparate. The heterogeneity of results from early studies may be due to differences in stimulation techniques, stimulation parameters for the same techniques, different levels of quality for control conditions and limitations of the recording systems/montages (placement and number of electrodes). Recent studies have identified more consistently several VestEPs components with late latency, which are informative about the later steps of vestibular information processing. A major finding about VestEPs with late latency is that components under 220 ms may reflect low-level sensory processing while components above 200 ms may reflect higher level perceptual and cognitive processes, and the conscious processing of vestibular information (166).

Parallel vs. Sequential Vestibular Information Processing in the Cerebral Cortex

One important question in vestibular neuroscience was to determine whether vestibular signals are transmitted to cortical areas through several parallel pathways with similar latencies, or whether vestibular signals reach a core vestibular area (activated earlier) before being distributed to secondary areas (activated later). The ability to answer this question depends on the temporal and spatial resolution of the recording technique.

Results from VestEPs studies reported above indicate that vestibular signals rapidly reach the cerebral cortex. The observation that several cortical areas may receive vestibular information in <10 ms after direct electrical stimulation of the vestibular nerve has been used to support the idea that there is no primary vestibular cortex, but rather parallel processing of vestibular signals in at least five cortical areas (133). This seems consistent with local field potentials recorded with overlapping latencies in several brain areas after electrical stimulation of the vestibular nerve in rats (136).

Our review of the literature shows that short, middle and late VestEPs have been found to originate from various cortical areas at similar or close latencies, such as both frontal and occipital activations at 10 ms, or later at 80 ms, for example. The studies available to date suggest that VestEPs with latencies between 10 and 20 ms may have a cerebellar origin (41, 108, 110, 115, 120, 149, 150), and/or a cerebral origin with several generators in the precentral sulcus (108) or the precuneus and cuneus (113) for the n15. Vestibular-evoked potentials with latencies from 20 to 30 ms have been associated to activity in the bilateral anterior insula and posterior operculum (111) while components with latencies from 40 to 50 ms have been associated with a mid-cingulate source with contributions of the bilateral superior temporal cortex (42, 110). Vestibular-evoked potentials with late latencies have been associated to various sources in all lobes. Altogether, these studies indicate a rapid diffusion of vestibular information in different areas of the cortex, distributed processing, and crosstalk mechanisms with recurrent processing lasting several hundreds of milliseconds after the stimulation.

The surface EEG and the event-related approach may lack the resolution to fully describe the spatiotemporal pattern of vestibular information processing as it reflect activity of too large assemblies of neurons. Local field potentials and single neurons recordings have a more appropriate spatiotemporal resolution. To our knowledge, local field potentials from intracranial electrodes were recorded in only one epileptic patient during SVS, providing similar findings as recordings from scalp electrodes in healthy participants (111). Interestingly, single neuron recordings in non-human primates have been compared in several cortical areas during natural whole-body displacements. A notable study in macaque by Chen et al. (23) compared the spatiotemporal tuning of neurons from the PIVC, area MSTd (dorsal part of area MST), and VIP during animal translations. On the basis of the response latency of the neurons, the authors propose that there is a "hierarchy in cortical vestibular processing, with PIVC being most proximal to the vestibular periphery and MSTd being most distal." Accordingly, vestibular signals would be first processed in the PIVC before being transmitted to area VIP and MSTd. Although this seems in contradiction with results from most VestEPs studies summarized here, it may just reflect the inability of EEG to grasp different patterns of responses of different cortical areas to acceleration, velocity, and position of whole-body motion as can do single neuron recordings (24).

Finally, we note it is difficult to compare the spatiotemporal dynamics of vestibular information processing as revealed by EEG analyses with data from fMRI and PET studies of the vestibular cortex. Given the low temporal resolution of these neuroimaging techniques, they have not been able to precisely describe the responses of vestibular cortical areas as a function of time, and never with the time resolution of the VestEPs summarized above. A study by Klingner et al. (190) analyzed the temporal pattern of several cortical responses measured with fMRI during 30 s of CVS using independent component analysis. The authors identified seven independent components representing cortical responses with different temporal profiles. Although the time course of these components differed significantly, with a trend for more lasting response for the component originating from the insula, retroinsular cortex, and superior temporal gyrus, there was no difference in the latency of the peak of the response for all components. Another study combining repeated short pulses of CVS and fMRI showed that during the 40 s following CVS there was a longer and stronger activation in the brainstem compared to activation in the cerebellum, thalamus, and right insula (78). The latency of the peak of the response and the response duration (>10 s) in these two studies can in no way be compared with the electrophysiological findings reported in our review of the literature. Altogether, this indicates the complementarity of EEG and fMRI approaches to better characterize the time course and location of vestibular information processing in the human brain.

Laterality of Vestibular Projections and Hemispheric Dominance in the Vestibulo-Thalamo-Cortical System

Another important question for vestibular neuroscience concerns the laterality of vestibular projections from one labyrinth to the cortex, and whether there is an overall hemispheric dominance for vestibular information processing, as shown by previous neuroimaging and anatomical studies (77, 102, 191).

Vestibular-evoked potentials with latencies under 10 ms can be recorded bilaterally, but larger amplitudes have been observed ipsilaterally to the perioperative stimulation of the vestibular nerve (133). This is in line with the projection of primary vestibular afferents to the ipsilateral vestibular nuclei, and the inhibition of contralateral vestibular nuclei through rich commissural pathways (192).

Studies of VestEPs with latencies between 10 and 20 ms have reported contradictory results as to the lateralization of the responses. Concerning the p10 evoked by SVS, some studies suggested larger ipsilateral responses with a right hemisphere dominance (107), in line with previous neuroimaging findings using the same type of SVS (102). Other studies found a contralateral dominance of a deep source, potentially cerebellar, for the same component (108, 110, 115). Using IAS, Todd et al. (120) reported an ipsilateral p12/n17 and a contralateral p19/n23, but only reported a contralateral p12/n17 in a subsequent study (150). They found that these EPs of potential cerebellar origin were larger on the right side for bone conducted sounds (108), an observation not confirmed with stronger vestibular stimulation (41). Secondary vestibular fibers project bilaterally to the cerebellum in both animals and humans (17, 192, 193). However, unlike in humans, animal studies converge on larger contralateral responses to vestibular stimulation in the vermis and flocculus (194). Neuroimaging studies have also suggested a contralateral activation of the cerebellum (78).

The few studies that have associated short latency VestEPs with cerebral sources seem to corroborate neuroimaging findings of bilateral responses, with larger responses in the ipsilateral and in the non-dominant hemisphere (77, 102). de Waele et al. (133) reported a larger p10 under ipsilateral compared to contralateral frontal electrodes. As expected, BESA revealed bilateral sources, with ipsilateral sources in the superior frontal gyrus and precentral gyrus, and contralateral sources in the anterior supplementary motor area near the frontal eye fields and in the superior occipital gyrus as well as a transverse prefrontal source (133). The n15 and p20 evoked by right ear SVS were found to originate from the right precuneus and cuneus and from the right precentral gyrus, medial and superior temporal gyri, respectively (113).

There are scarce data on the middle latency VestEPs. Regarding the 20–30 complex, larger amplitudes were observed in the anterior insula for left SVS compared to right SVS in right-handed participants (111). However, such lateralization effects were not reproduced with GVS (96) and IAS (112). Regarding the n42/p52 VestEPs, a weak right ear advantage has been reported for the peak-to-peak amplitude measured at electrode FCz, whereas a contralateral left ear advantage has been found for the n42 component when considered alone (110).

Recent studies on late VestEPs report no hemispheric dominance or contradictory results. Contralateral SVS evoked higher VestEPs amplitudes in the non-dominant hemisphere (111) but these results were not reproduced using GVS (96). Ertl et al. (166) found an effect of the direction of lateral passive translation on two components, the n80 and a positive component with a peak between 240 and 352 ms. Both VestEPs showed larger amplitudes under C3 (left to Cz) or C4 (right to Cz) depending on whether the participants were moved to the left or to the right, respectively. The effects were discussed in terms of lateralized somatosensory stimulation during body motion.

Altogether, results from the VestEPs studies indicate that components with different latencies have bilateral brain sources, thus information originating from one ear is processed in both cerebral hemispheres. The analysis of VestEPs amplitudes and their generators, however, is less conclusive regarding the determinants of hemispheric dominance in the vestibulo-thalamo-cortical system, when compared to the clear pattern that arises from PET and fMRI studies: (1) bilateral but larger activations in the hemisphere ipsilateral to the activated ear and (2) larger response in the non-dominant hemisphere, that is in the right cerebral hemisphere for the right-handed participants (77, 195, 196). We agree with Kammermeier et al. (111) in that this difference may in part be due to the "modalities of short-termed electric activity [for EEG studies] vs. long-term vascular or metabolic changes [for fMRI and PET studies]." More work is needed to investigate how VestEPs are influenced by the side of stimulation and the participants' handedness.

Replicability and Variability of Findings in VestEPs Studies

It may seem that a lack of replicability and large variability of VestEPs emerges from the collection of studies on the topic so far. First, we note that there are few available studies on VestEPs compared to the wealth of studies existing for well-defined visual, somatosensory, and auditory EPs (31). Second, a major obstacle to replicating results from one study to another is the enormous variability in the stimulation and recording procedures. Among the many sources of variability in the recorded vestibular responses, two categories seem particularly important.

Method of Vestibular Stimulation

The method of vestibular stimulation (see **Figure 1**) provides a major source of variation in the observed responses. As noted earlier, artificial stimulation of the vestibular system (GVS, CVS, SVS, IAS, MVS) differ from natural vestibular stimulation (rotatory chair, motion platform) in many aspects, including the type of vestibular receptor (otolithic, canalar) stimulated, the physical nature of the stimulation leading to activation of hair cells or the vestibular nerve, the co-activation of other sensory systems (such as hearing for SVS and interoception for body rotations), the duration of the stimulation, etc. The most commonly used artificial vestibular stimulation for VestEPs studies (SVS and IAS) are transient stimuli lasting in general a couple of milliseconds, whereas passive whole-body translations and rotations have a totally different temporal pattern, lasting in general more than 1 s [e.g., (32, 60)]. It is therefore difficult to directly compare the spatiotemporal dynamics of vestibular information processing for transient artificial vestibular stimulation and natural body motions (see below).

The Spatial Density of Recording Electrodes and the Montage

Very diverse electrode montages have been used to record VestEPs with a large variability in the spatial density of electrodes, as shown in **Supplementary Table 1**. Early studies have used montages close to those used for BAEP recordings, with a spatial density of electrodes insufficient to describe the spatiotemporal dynamics of vestibular information processing. As studies have used different references for the analysis of VestEPs (ear lobes, mastoid, average reference…), it is difficult to directly compare the shape and polarity of VestEPs components across studies. A consensus about standard electrode montage and reference should therefore be established in order to increase replicability of the results in future EEG studies of the vestibular system, as done for cVEMPs and oVEMPs recordings (43, 100), or for somatosensory (34), visual (35), and auditory (36, 37) EPs recordings.

The largest variability in the VestEPs waveforms arises from studies that investigated vestibular responses during natural whole-body translations and rotations. For example, studies of rotatory VestEPs identified only short or middle latency components (56, 57, 147), while others only identified late components (32, 44, 171, 173, 174, 176). This is very likely related to different stimulation parameters. In the case of short and middle VestEPs, the rotations applied to the head only were rapid horizontal (56, 57) or vertical (159) rotational acceleration impulses up to 12,000°/s² that could be applied at frequencies from 0.5 to 2 Hz. In the case of late VestEPs, whole-body rotations could consist in ramps with acceleration phases of 250 or 500 ms to reach an angular velocity of 60°/s maintained for 400 ms (171), step-wise accelerations of 53°/s² (173, 174) lasting 1 s, or accelerations of 15°/s² lasting 1 s (44) or 2 s (176), or transient "raised-cosine" rotations with a peak velocity of 110°/s for 1.3 s (32). Shorter and more intense rotations would therefore make it possible to observe short or middle latency VestEPs while longer rotations would allow to record later responses, possibly time-locked to changes in the acceleration profile.

More consistent results have been obtained with stimulation methods that use standardized stimuli such as short high sound pressure clicks at intensities around 100 dB-SPL. There is indeed a consensus about the parameters of the sounds (frequency, duration, intensity, number of stimulation) which are optimal to activate the otolithic receptors, and are commonly used for clinical investigations of cVEMPs and oVEMPs (38). Vestibular-evoked potentials have been consistently identified using very similar stimulation or recording techniques. For example, the same group has repeatedly reproduced the p10, n15, p21 components as well as the n42/p52 complex using bone conducted or air conducted tone bursts of 500 Hz lasting 6 ms (107, 114) or tone pips of 500 Hz lasting 2 ms (42, 108, 110). Different results were obtained using different parameters of SVS. They compared air-conducted and bone-conducted SVS, showing that they allow to record reproducible components such as the p10 and n15 while noting that bone conducted stimulation induces larger responses (108). They also compared left vs. right SVS (110), different references such as the linked earlobes or common average reference (42), and different inter-stimulus intervals (149). This shows how important the stimulation techniques and their parameters are to better characterize VestEPs.

Main Limits of VestEPs Studies

The study of the spatiotemporal dynamics of vestibular signal processing in the brain is limited by the fact that the vestibular system is multisensory in nature (197). Vestibular afferents project to the vestibular nuclei and cerebellum, where vestibular signals are processed and integrated with visual and somatosensory information (198). Vestibular signals are also integrated with visual and somatosensory signals in several thalamic nuclei and in several cortical areas, including the PIVC (199). This multisensory convergence can be evidenced by the modulation of the p12/n17 biphasic wave by optic flow (120).

As vestibular signals are mixed with other sensory information as early as the second synapse in the brainstem, most VestEPs recorded to date likely represent a multisensory response owing to the lack of specificity of the methods to stimulate the vestibular receptors (**Figure 2**). Natural and artificial vestibular stimulation often stimulates one or several extravestibular sensory systems, such as the auditory (for SVS, CVS, IAS, rotating chairs, and motion platforms), tactile (for GVS, CVS, IAS, rotating chairs, and motion platforms), nociceptive (for GVS and CVS), thermoceptive (for GVS and CVS), and interoceptive systems (for body rotations and translations). Thus, vestibular responses recorded over the scalp are mixed with time-locked responses from these sensory systems. During passive whole-body translations and rotations, a major sensory influence on VestEPs comes from the interoceptive system, as the body fluids move in a time-locked manner with the rotatory chair or motion platform. The interoceptive and vestibular systems are largely interconnected at both anatomical and functional levels. Interoceptive signals from visceral receptors can modulate vestibular signals as early as in the vestibular nuclei (200). Vestibular information is also integrated with interoceptive signals in the insula (80). Although visual, auditory, tactile, and nociceptive controls can be used, it is impossible to control for the interoceptive contributions to VestEPs, which cannot be switched off and are hardly manipulated. For example, late VestEPs responses are certainly not purely vestibular as they can also be observed in patients with a bilateral vestibular failure (32, 182).

Potential Applications of VestEPs in Neurology and Otoneurology

Despite these limitations, VestEPs represent a promising tool for the clinical investigation of the vestibular system. First, there seems to be little interindividual differences in VestEPs onset and peak latencies for electrical stimulations of the vestibular nerve (133) and for SVS (42, 110, 149). Second, VestEPs amplitude increases with the intensity of the electrical current applied to the vestibular nerve (131, 133), the intensity of SVS (42, 107), the impulsive acceleration in IAS (112) or the acceleration of the body rotation (44, 173, 184) or body translation (33, 60). The consistency of these characteristics makes VestEPs measurement appropriate for basic research and clinical investigations. Studies in large populations should first be conducted to establish normative values of latency and amplitude in healthy participants as a function of age, as done for VEMPs [i.e., tests of the otolithic function; (201, 202)] and for the video head impulse test [i.e., tests of the semicircular canals; (203)].

Sound-induced vestibular stimulation appears a convenient and reliable technique to standardize VestEPs as done for cVEMPs and oVEMPs, for which SVS is already routinely used in clinical testing. With many controlled repetitions possible in a relatively short period of time, SVS evokes short, middle, and long latency VestEPs which likely reflect the successive processing of vestibular information along the vestibulo-thalamo-cortical pathways (see **Figure 1**). Sound-induced vestibular stimulation allows to test each ear separately. Simplified montages could be used, such as Laplacian montages (111), or specific vertex-mastoid or parieto-frontal derivations for example (106). Interestingly, recordings with 32- and 64-channel EEG systems allowed to observe a reduction of the n42/p54 response in few patients with a bilateral (114) or unilateral (42) vestibular loss. A first step toward clinical applications of VestEPs would be to use SVS (and the appropriate auditory control conditions) to test larger samples of patients with various vestibular disorders and compare their responses to those from healthy participants.

Brainstem auditory evoked potentials have been proposed as a complement to cVEMPs to evaluate vestibular schwannoma (204), even though their cost-effectiveness may be lower than that of MRI (205). Compared to cVEMPs, far-field vestibular potentials have the advantage to be recorded even in patients who cannot properly contract their neck muscles, a condition for cVEMPs recording. It has been proposed that the n5 may be suitable to assess vestibular projections in clinical practice. First, the n3 component may only appear when BAEPs auditory components are drastically reduced. Second, the n5 can be observed with sounds of lower intensity, around 80 dB nHL, and allows for shorter testing times compared to the n3, which is best obtained using clicks over 100 dB nHL (105).

To record middle and late latency VestEPs in clinical practice, Kammermeier et al. (111) have proposed a simplified EEG setup with circular Laplacian montages around electrodes FC5/6 (over right and left anterior insula) and CP5/6 (right and left posterior opercula). They found reproducible n20, p30, and p60 responses, indicating that VestEPs of short, middle, and late latency can be recorded using simplified montages in clinical settings.

Vestibular-evoked potentials should be altered in patients with lesions in vestibular areas, providing a faster, simpler and less expensive equivalent to fMRI or PET for demonstrating reduced or altered activity in vestibular areas (206, 207). Vestibular-evoked potentials could help assess central vestibular processing in patients who report vestibular sensations but show no apparent vestibular end organs or nerve alterations and help identify the underlying pathology. Vestibular-evoked potentials could be an important diagnostic support in the investigation of central vestibular syndromes (21). Among these, the incidence of vestibular epilepsy is probably underestimated and pose important differential diagnostic problems with vestibular migraine and psychogenic forms of paroxysmal vertiginous manifestations (208, 209). It is possible that, as in other epilepsies, specific alterations of certain cerebral areas may be investigated by VestEPs in the future and that these alterations will be different in migraine and psychogenic disorders. One the one hand, there is evidence that patients with vestibular migraine have a different vestibular threshold and sensitivity to motion than healthy controls (210, 211). On the other hand, there is evidence that patients with persistent postural-perceptual dizziness (PPPD), a functional vestibular disorder (212) showed altered activity and connectivity in the vestibular cortical network, including areas processing visuo-vestibular integration and emotions (213–215). In an fMRI study, SVS evoked reduced activation and connectivity of key vestibular areas such as the posterior and anterior insula, hippocampus and anterior cingulate cortex in chronic subjective dizziness compared to healthy controls (213). We propose that VestEPs may provide more information on the temporal characteristics of vestibular processing linked with anxiety in this form of functional vestibular disorder.

Perspective of VestEPs for Cognitive and Systems Neuroscience

We propose that VestEPs analysis is a method to investigate the spatiotemporal characteristics of multisensory mechanisms underlying various pre-reflexive and cognitive functions. To meet such objectives, studies need to combine vestibular stimulation with cognitive tasks, as it has already been successfully done. A self-motion oddball detection task combined with VestEPs recording revealed a vestibular-evoked P3 component, a marker of infrequent change detection identified for other sensory modalities (216, 217). A perceptual decision making study (166) showed a positive component with latencies ranging from 240 to 352 ms, that may reflect expectation and decision-making processes involving self-motion signals (166), as it was not observed in previous recordings in participants not engaged in any task (33). Studies of the modulation of known EPs during vestibular stimulation, as well studies of the variations of VestEPs according to different multisensory stimuli or cognitive tasks are therefore feasible and could yield important insights into the vestibular contribution to perception and cognition.

Vestibular-evoked potentials may also offer the possibility to study more precisely the spatiotemporal dynamics of attentional and cognitive effects reported using other neuroimaging techniques. An fMRI study showed that attentional load in a visual tracking task decreased activity in the PIVC (218), possibly due to a downregulation of excitatory neurotransmitters and maintenance of inhibitory transmitters to reduce PIVC responses to thalamic inputs (219). Vestibular-evoked potentials may help to refine the timing of such phenomena as well as to study them in several areas simultaneously.

Although it is beyond the scope of the present review article to describe event-related synchronizations and desynchronizations during vestibular stimulation, response analysis in the time-frequency domain could also serve the same objectives as VestEPs analysis and provide additional information about the spatiotemporal dynamics of vestibular information processing in healthy participants and in patients. Indeed, EPs and event-related synchronizations/desynchronizations reflect different electrophysiological events. Evoked potentials are phase-locked events originating from post-synaptic responses of cortical neurons (220). By contrast, event-related synchronizations/desynchronizations are time-locked events, but not phase-locked events, reflecting more neuronal and synaptic characteristics, network connectivity, and modulation on more or less extended neuronal assemblies (220). A few studies investigated both VestEPs and responses in the time-frequency domain (32, 111, 166, 167, 171). Rotations were found to induce alpha rhythm desynchronization in central and parietal scalp regions (32, 171). This desynchronization was significantly reduced in patients with a bilateral vestibular failure when compared to healthy participants, indicating it is in part related to vestibular information processing (32). A more recent study found that body translations induced a delta and theta synchronization in the bilateral operculo-insular region, mid-orbital gyrus, and medial frontal gyrus, with additional contribution to the theta synchronization from cingulate sulcus visual area and anterior cingulate gyrus (167). Body translations and SVS were both associated with low beta synchronizations, observed at Cz 67.5 ms after maximum acceleration for translations (33), and localized in the right anterior insula and posterior operculum 20–80 ms after SVS (111). Delta, theta, mu, or gamma synchronizations and desynchronizations were also reported following passive body rotations (32, 171), translations (166, 167), and SVS (111). Here, again studies in larger populations, using standardized stimulation and recording techniques, or time-frequency or microstates (166) analyses would be needed to complement VestEPs findings.

Finally, MEG could also be used to study VestEPs and vestibular-related synchronizations and desynchronizations. Magnetoencephalography offers better source localization than EEG and would therefore be a good complement to the spatial localization of vestibular information processing, especially for investigations of deep sources such as the cerebellum (157). However, EEG remains the only recording technique fully compatible with more ecologically valid vestibular stimulation.

Conclusion

Vestibular-evoked potentials of short, middle, and late latency reveal the spatiotemporal properties of vestibular processing from the vestibular nerve to cortical areas. They represent promising tools for the clinical and experimental investigation of the vestibular system, its disorders and its relation to cognition.

AUTHOR CONTRIBUTIONS

EN and CL wrote the draft and revised the final manuscript. FB revised the final manuscript. All authors contributed to the article and approved the submitted version.

FUNDING

This work was supported by the ANR VESTISELF project, grant ANR-19-CE37-0027 of the French Agence Nationale de la Recherche to CL and FB.

SUPPLEMENTARY MATERIAL

The Supplementary Material for this article can be found online at: https://www.frontiersin.org/articles/10.3389/fneur.2021.674100/full#supplementary-material

REFERENCES

1. Brandt T, Strupp M, Dieterich M. Towards a concept of disorders of "higher vestibular function." *Front Integr Neurosci*. (2014) 8:47. doi: 10.3389/fnint.2014.00047
2. Lopez C. The vestibular system: balancing more than just the body. *Curr Opin Neurol.* (2016) 29:74–83. doi: 10.1097/WCO.0000000000000286
3. Smith PF. Vestibular-hippocampal interactions. *Hippocampus.* (1997) 7:465–71. doi: 10.1002/(SICI)1098-1063(1997)7:5<465::AID-HIPO3>3.0.CO;2-G
4. Brandt T, Schautzer F, Hamilton DA, Brüning R, Markowitsch HJ, Kalla R, et al. Vestibular loss causes hippocampal atrophy and impaired spatial memory in humans. *Brain J Neurol.* (2005) 128:2732–41. doi: 10.1093/brain/awh617
5. Mast FW, Preuss N, Hartmann M, Grabherr L. Spatial cognition, body representation and affective processes: the role of vestibular information beyond ocular reflexes and control of posture. *Front Integr Neurosci.* (2014) 8:44. doi: 10.3389/fnint.2014.00044

6. Smith P, Darlington C. Personality changes in patients with vestibular dysfunction. *Front Hum Neurosci.* (2013) 7:678. doi: 10.3389/fnhum.2013.00678
7. Vanzan S, Wilkinson D, Ferguson H, Pullicino P, Sakel M. Behavioural improvement in a minimally conscious state after caloric vestibular stimulation: evidence from two single case studies. *Clin Rehabil.* (2017) 31:500–7. doi: 10.1177/0269215516646167
8. Lopez C, Schreyer H-M, Preuss N, Mast FW. Vestibular stimulation modifies the body schema. *Neuropsychologia.* (2012) 50:1830–7. doi: 10.1016/j.neuropsychologia.2012.04.008
9. Blanke O. Multisensory brain mechanisms of bodily self-consciousness. *Nat Rev Neurosci.* (2012) 13:556–71. doi: 10.1038/nrn3292
10. Lopez C, Blanke O. The thalamocortical vestibular system in animals and humans. *Brain Res Rev.* (2011) 67:119–46. doi: 10.1016/j.brainresrev.2010.12.002
11. Dieterich M, Brandt T. The bilateral central vestibular system: its pathways, functions, and disorders. *Ann N Y Acad Sci.* (2015) 1343:10–26. doi: 10.1111/nyas.12585
12. Stiles L, Smith PF. The vestibular-basal ganglia connection: balancing motor control. *Brain Res.* (2015) 1597:180–8. doi: 10.1016/j.brainres.2014.11.063
13. Bottini G, Sterzi R, Paulesu E, Vallar G, Cappa SF, Erminio F, et al. Identification of the central vestibular projections in man: a positron emission tomography activation study. *Exp Brain Res.* (1994) 99:164–9.
14. Brandt T, Dieterich M. The vestibular cortex. Its locations, functions, and disorders. *Ann N Y Acad Sci.* (1999) 871:293–312. doi: 10.1111/j.1749-6632.1999.tb09193.x
15. Lopez C, Blanke O, Mast FW. The human vestibular cortex revealed by coordinate-based activation likelihood estimation meta-analysis. *Neuroscience.* (2012) 212:159–79. doi: 10.1016/j.neuroscience.2012.03.028
16. zu Eulenburg P, Caspers S, Roski C, Eickhoff SB. Meta-analytical definition and functional connectivity of the human vestibular cortex. *NeuroImage.* (2012) 60:162–9. doi: 10.1016/j.neuroimage.2011.12.032
17. Kirsch V, Keeser D, Hergenroeder T, Erat O, Ertl-Wagner B, Brandt T, et al. Structural and functional connectivity mapping of the vestibular circuitry from human brainstem to cortex. *Brain Struct Funct.* (2016) 221:1291–308. doi: 10.1007/s00429-014-0971-x
18. Frank SM, Greenlee MW. The parieto-insular vestibular cortex in humans: more than a single area? *J. Neurophysiol.* (2018) 120:1438–50. doi: 10.1152/jn.00907.2017
19. Grüsser OJ, Pause M, Schreiter U. Localization and responses of neurones in the parieto-insular vestibular cortex of awake monkeys (*Macaca fascicularis*). *J Physiol.* (1990) 430:537–57. doi: 10.1113/jphysiol.1990.sp018306
20. Guldin WO, Grüsser O-J. Is there a vestibular cortex? *Trends Neurosci.* (1998) 21:254–9. doi: 10.1016/S0166-2236(97)01211-3
21. Brandt T, Dieterich M. The dizzy patient: don't forget disorders of the central vestibular system. *Nat Rev Neurol.* (2017) 13:352–62. doi: 10.1038/nrneurol.2017.58
22. Angelaki DE, Dickman JD. Spatiotemporal processing of linear acceleration: primary afferent and central vestibular neuron responses. *J Neurophysiol.* (2000) 84:2113–32. doi: 10.1152/jn.2000.84.4.2113
23. Chen A, Deangelis GC, Angelaki DE. A comparison of vestibular spatiotemporal tuning in macaque cortical areas PIVC, VIP and MSTd. *J Neurosci Off J Soc Neurosci.* (2011) 31:3082–94. doi: 10.1523/JNEUROSCI.4476-10.2011
24. Laurens J, Liu S, Yu X-J, Chan R, Dickman D, DeAngelis GC, et al. Transformation of spatiotemporal dynamics in the macaque vestibular system from otolith afferents to cortex. *Elife.* (2017) 6:e20787. doi: 10.7554/eLife.20787
25. Petit L, Beauchamp MS. Neural basis of visually guided head movements studied with fMRI. *J Neurophysiol.* (2003) 89:2516–27. doi: 10.1152/jn.00988.2002
26. Schindler A, Bartels A. Human V6 integrates visual and extra-retinal cues during head-induced gaze shifts. *iScience.* (2018) 7:191–7. doi: 10.1016/j.isci.2018.09.004
27. Schindler A, Bartels A. Integration of visual and non-visual self-motion cues during voluntary head movements in the human brain. *Neuroimage.* (2018) 172:597–607. doi: 10.1016/j.neuroimage.2018.02.006
28. Carriot J, Jamali M, Cullen KE, Chacron MJ. Envelope statistics of self-motion signals experienced by human subjects during everyday activities: implications for vestibular processing. *PLoS ONE.* (2017) 12:e0178664. doi: 10.1371/journal.pone.0178664
29. Papeo L, Longo MR, Feurra M, Haggard P. The role of the right temporoparietal junction in intersensory conflict: detection or resolution? *Exp. Brain Res.* (2010) 206:129–39. doi: 10.1007/s00221-010-2198-2
30. Nguyen NT, Takakura H, Nishijo H, Ueda N, Ito S, Fujisaka M, et al. Cerebral hemodynamic responses to the sensory conflict between visual and rotary vestibular stimuli: an analysis with a multichannel near-infrared spectroscopy (NIRS) system. *Front Hum Neurosci.* (2020) 14:125. doi: 10.3389/fnhum.2020.00125
31. Schomer DL, Lopes da Silva FH (eds). *Niedermeyer's Electroencephalography: Basic Principles, Clinical Applications, and Related Fields*. Oxford, NY: Oxford University Press (2018).
32. Gale S, Prsa M, Schurger A, Gay A, Paillard A, Herbelin B, et al. Oscillatory neural responses evoked by natural vestibular stimuli in humans. *J Neurophysiol.* (2015) 115:1228–42. doi: 10.1152/jn.00153.2015
33. Ertl M, Moser M, Boegle R, Conrad J, Zu Eulenburg P, Dieterich M. The cortical spatiotemporal correlate of otolith stimulation: vestibular evoked potentials by body translations. *Neuroimage.* (2017) 155:50–9. doi: 10.1016/j.neuroimage.2017.02.044
34. Muzyka IM, Estephan B. Somatosensory evoked potentials. *Handb Clin Neurol.* (2019) 160:523–40. doi: 10.1016/B978-0-444-64032-1.00035-7
35. Odom JV, Bach M, Barber C, Brigell M, Marmor MF, Tormene AP, et al. Visual evoked potentials standard 2004. *Doc Ophthalmol Adv Ophthalmol.* (2004) 108:115–23. doi: 10.1023/b:doop.0000036790.67234.22
36. Plourde G. Auditory evoked potentials. *Best Pract Res Clin Anaesthesiol.* (2006) 20:129–39. doi: 10.1016/j.bpa.2005.07.012
37. Eggermont JJ. Auditory brainstem response. *Handb Clin Neurol.* (2019) 160:451–64. doi: 10.1016/B978-0-444-64032-1.00030-8
38. Welgampola MS, Colebatch JG. Characteristics and clinical applications of vestibular-evoked myogenic potentials. *Neurology.* (2005) 64:1682–8. doi: 10.1212/01.WNL.0000161876.20552.AA
39. Rosengren SM, Colebatch JG, Young AS, Govender S, Welgampola MS. Vestibular evoked myogenic potentials in practice: methods, pitfalls and clinical applications. *Clin Neurophysiol Pract.* (2019) 4:47–68. doi: 10.1016/j.cnp.2019.01.005
40. Papathanasiou E, Zamba-Papanicolaou E, Pantziaris M, Kyriakides T, Papacostas S, Myrianthopoulou P, et al. Click evoked neurogenic vestibular potentials (NVESTEPs): a method of assessing the function of the vestibular system. *Electromyogr Clin Neurophysiol.* (2003) 43:399–408.
41. Govender S, Todd NPM, Colebatch JG. Mapping the vestibular cerebellar evoked potential (VsCEP) following air- and bone-conducted vestibular stimulation. *Exp Brain Res.* (2020) 238:601–20. doi: 10.1007/s00221-020-05733-x
42. Todd NPM, Paillard AC, Kluk K, Whittle E, Colebatch JG. Vestibular receptors contribute to cortical auditory evoked potentials. *Hear Res.* (2014) 309:63–74. doi: 10.1016/j.heares.2013.11.008
43. Curthoys IS. The new vestibular stimuli: sound and vibration—anatomical, physiological and clinical evidence. *Exp Brain Res.* (2017) 1–16. doi: 10.1007/s00221-017-4874-y
44. Schneider D, Kolchev C, Constantinescu L, Claussen C. Vestibular Evoked Potentials (VestEP) and brain electrical activity mapping - a test of vestibular function - a review (1990–1996). *Int Tinnitus J.* (1996) 2:27–43.
45. Palla A, Lenggenhager B. Ways to investigate vestibular contributions to cognitive processes. *Front Integr Neurosci.* (2014) 8:40. doi: 10.3389/fnint.2014.00040
46. Ertl M, Boegle R. Investigating the vestibular system using modern imaging techniques—A review on the available stimulation and imaging methods. *J Neurosci Methods.* (2019) 326:108363. doi: 10.1016/j.jneumeth.2019.108363
47. Greiner GF, Collard M, Conraux C, Picart P, Rohmer F. Research on evoked potentials of vestibular origin in man. *Acta Otolaryngol. (Stockh).* (1967). 63:320–9.
48. Spiegel EA, Szekely EG, Moffet R. Cortical responses to rotation. I Responses recorded after cessation of rotation. *Acta Otolaryngol (Stockh).* (1968) 66:81–8. doi: 10.3109/00016486809126275

49. Salamy J, Potvin A, Jones K, Landreth J. Cortical evoked responses to labyrinthine stimulation in man. *Psychophysiology.* (1975) 12:55–61. doi: 10.1111/j.1469-8986.1975.tb03061.x
50. Gerull G, Giesen M, Keck W, Mrowinski D. Rotatory evoked cortical potentials in man. *Biomed Eng Biomed Tech.* (1981) 26:262–6. doi: 10.1515/bmte.1981.26.11.262
51. Hood JD. Vestibular and optokinetic evoked potentials. *Acta Otolaryngol (Stockh).* (1983) 95:589–93. doi: 10.3109/00016488309139448
52. Hood JD, Kayan A. Observations upon the evoked responses to natural vestibular stimulation. *Electroencephalogr Clin Neurophysiol.* (1985) 62:266–76. doi: 10.1016/0168-5597(85)90004-8
53. Hamid MA, Hughes GB. Vestibular evoked potentials in man: an overview. *Otolaryngol Head Neck Surg.* (1986) 95:347–8. doi: 10.1177/01945998860953P114
54. Probst T, Ayan T, Loose R, Skrandies W. Electrophysiological evidence for direction-specific rotary evoked potentials in human subjects–a topographical study. *Neurosci Lett.* (1997) 239:97–100. doi: 10.1016/s0304-3940(97)00899-9
55. Furman JM. Rotational testing. *Handb Clin Neurol.* (2016) 137:177–86. doi: 10.1016/B978-0-444-63437-5.00012-1
56. Elidan J, Sela M, Liebner E, Sohmer H. Short latency vestibular evoked response to angular acceleration impulse in human beings. *Otolaryngol Head Neck Surg.* (1991) 105:353–9. doi: 10.1177/019459989110500302
57. Elidan J, Leibner E, Freeman S, Sela M, Nitzan M, Sohmer H. Short and middle latency vestibular evoked responses to acceleration in man. *Electroencephalogr Clin Neurophysiol.* (1991) 80:140–5. doi: 10.1016/0168-5597(91)90151-m
58. Zangemeister WH, Phlebs U, Huefner G, Kunze K. Active head turning and correlated cerebral potentials. Experimental and clinical aspects. *Acta Otolaryngol (Stockh).* (1986) 101:403–15. doi: 10.3109/00016488609108625
59. Zangemeister WH, Hansen HC. Cerebral potentials evoked by fast head accelerations. *Neurol Res.* (1990) 12:137–46. doi: 10.1080/01616412.1990.11739933
60. Baudonnière PM, Belkhenchir S, Lepecq JC, Mertz S. Otolith-vestibular-evoked potentials in humans. Intensity, direction of acceleration (Z+, Z-), and BESA modeling of generators. *Ann N Y Acad Sci.* (1999) 871:384–6. doi: 10.1111/j.1749-6632.1999.tb09200.x
61. Cohen B, Hess BJM. Otolith function in spatial orientation and movement. *Ann N Acad Sci.* (1999) 871:xi–xiv, 1–464.
62. Lopez C, Falconer CJ, Mast FW. Being moved by the self and others: influence of empathy on self-motion perception. *PLoS ONE.* (2013) 8:e48293. doi: 10.1371/journal.pone.0048293
63. Dumas G, Curthoys IS, Lion A, Perrin P, Schmerber S. The skull vibration-induced nystagmus test of vestibular function-a review. *Front Neurol.* (2017) 8:41. doi: 10.3389/fneur.2017.00041
64. Chen A, DeAngelis GC, Angelaki DE. Macaque Parieto-insular vestibular cortex: responses to self-motion and optic flow. *J Neurosci Off J Soc Neurosci.* (2010) 30:3022–42. doi: 10.1523/JNEUROSCI.4029-09.2010
65. Devantier L, Hansen AK, Mølby-Henriksen J-J, Christensen CB, Pedersen M, Hansen KV, et al. Positron emission tomography visualized stimulation of the vestibular organ is localized in Heschl's gyrus. *Hum Brain Mapp.* (2020) 41:185–93. doi: 10.1002/hbm.24798
66. Roy JE, Cullen KE. Dissociating self-generated from passively applied head motion: neural mechanisms in the vestibular nuclei. *J Neurosci Off J Soc Neurosci.* (2004) 24:2102–11. doi: 10.1523/JNEUROSCI.3988-03.2004
67. Laurens J, Angelaki DE. A unified internal model theory to resolve the paradox of active versus passive self-motion sensation. *Elife.* (2017) 6:e28074. doi: 10.7554/eLife.28074
68. Cullen KE. Vestibular processing during natural self-motion: implications for perception and action. *Nat Rev Neurosci.* (2019) 20:346–63. doi: 10.1038/s41583-019-0153-1
69. Klam F, Graf W. Vestibular signals of posterior parietal cortex neurons during active and passive head movements in macaque monkeys. *Ann N Y Acad Sci.* (2003) 1004:271–82. doi: 10.1196/annals.1303.024
70. Klam F, Graf W. Discrimination between active and passive head movements by macaque ventral and medial intraparietal cortex neurons. *J Physiol.* (2006) 574:367–86. doi: 10.1113/jphysiol.2005.103697
71. Aw ST, Haslwanter T, Fetter M, Dichgans J. Three-dimensional spatial characteristics of caloric nystagmus. *Exp Brain Res.* (2000) 134:289–94. doi: 10.1007/s002210000460
72. Tuohimaa P, Aantaa E, Toukoniitty K, Makela P. Studies of vestibular cortical areas with short-living 15O2 isotopes. *ORL J Otorhinolaryngol Relat Spec.* (1983) 45:315–21. doi: 10.1159/000275661
73. Friberg L, Olsen TS, Roland PE, Paulson OB, Lassen NA. Focal increase of blood flow in the cerebral cortex of man during vestibular stimulation. *Brain.* (1985) 108:609–23. doi: 10.1093/brain/108.3.609
74. Bottini G, Karnath HO, Vallar G, Sterzi R, Frith CD, Frackowiak RS, et al. Cerebral representations for egocentric space: functional-anatomical evidence from caloric vestibular stimulation and neck vibration. *Brain J Neurol.* (2001) 124:1182–96. doi: 10.1093/brain/124.6.1182
75. Suzuki M, Kitano H, Ito R, Kitanishi T, Yazawa Y, Ogawa T, et al. Cortical and subcortical vestibular response to caloric stimulation detected by functional magnetic resonance imaging. *Brain Res Cogn Brain Res.* (2001) 12:441–9. doi: 10.1016/s0926-6410(01)00080-5
76. Deutschländer A, Bense S, Stephan T, Schwaiger M, Brandt T, Dieterich M. Sensory system interactions during simultaneous vestibular and visual stimulation in PET. *Hum Brain Mapp.* (2002) 16:92–103. doi: 10.1002/hbm.10030
77. Dieterich M, Bense S, Lutz S, Drzezga A, Stephan T, Bartenstein P, et al. Dominance for vestibular cortical function in the non-dominant hemisphere. *Cereb Cortex.* (2003) 13:994–1007. doi: 10.1093/cercor/13.9.994
78. Marcelli V, Esposito F, Aragri A, Furia T, Riccardi P, Tosetti M, et al. Spatio-temporal pattern of vestibular information processing after brief caloric stimulation. *Eur J Radiol.* (2009) 70:312–6. doi: 10.1016/j.ejrad.2008.01.042
79. Frank SM, Greenlee MW. An MRI-compatible caloric stimulation device for the investigation of human vestibular cortex. *J Neurosci Methods.* (2014) 235:208–18. doi: 10.1016/j.jneumeth.2014.07.008
80. zu Eulenburg P, Baumgärtner U, Treede RD, Dieterich M. Interoceptive and multimodal functions of the operculo-insular cortex: tactile, nociceptive and vestibular representations. *NeuroImage.* (2013) 83:75–86. doi: 10.1016/j.neuroimage.2013.06.057
81. Molnar L, Kekesi F, Gosztonyi G. The effect of labyrinthine stimulation on the normal and pathological electroencephalogram in man. Activation of latent epilepsy by caloric labyrinthine stimulation. *Arch Psychiatr Nervenkrankh Ver Mit Z Gesamte Neurol Psychiatr.* (1959) 199:152–71. doi: 10.1007/BF00352993
82. Karbowski K, Moret PR, Martin F. Etude de quelques effets de la stimulation labyrinthique sur la fonction cardio-pulmonaire et l'activité électrique cérébrale. *Stereotact Funct Neurosurg.* (1963) 23:227–44. doi: 10.1159/000104300
83. Karbowski K. Of the utility of caloric labyrinthine stimulation as an activation method in electroencephalography. *Confin Neurol.* (1965) 25:210–4.
84. Karbowski K. On the latency time in EEG disorders provoked by labyrinthine heat stimulation. *Confin Neurol.* (1966) 28:321–6.
85. Barac B. Vestibular influences upon the EEG of epileptics. *Electroencephalogr Clin Neurophysiol.* (1967) 22:245–52. doi: 10.1016/0013-4694(67)90227-1
86. Goldberg JM, Smith CE, Fernández C. Relation between discharge regularity and responses to externally applied galvanic currents in vestibular nerve afferents of the squirrel monkey. *J Neurophysiol.* (1984) 51:1236–56. doi: 10.1152/jn.1984.51.6.1236
87. Gensberger KD, Kaufmann A-K, Dietrich H, Branoner F, Banchi R, Chagnaud BP, et al. Galvanic vestibular stimulation: cellular substrates and response patterns of neurons in the vestibulo-ocular network. *J Neurosci Off J Soc Neurosci.* (2016) 36:9097–110. doi: 10.1523/JNEUROSCI.4239-15.2016
88. Fitzpatrick RC, Day BL. Probing the human vestibular system with galvanic stimulation. *J Appl Physiol Bethesda Md (1985).* (2004) 96:2301–16. doi: 10.1152/japplphysiol.00008.2004
89. Lobel E, Kleine JF, Bihan DL, Leroy-Willig A, Berthoz A. Functional MRI of galvanic vestibular stimulation. *J Neurophysiol.* (1998) 80:2699–709. doi: 10.1152/jn.1998.80.5.2699
90. Bense S, Stephan T, Yousry TA, Brandt T, Dieterich M. Multisensory cortical signal increases and decreases during vestibular galvanic stimulation (fMRI). *J Neurophysiol.* (2001) 85:886–99. doi: 10.1152/jn.2001.85.2.886

91. Stephan T, Deutschländer A, Nolte A, Schneider E, Wiesmann M, Brandt T, et al. Functional MRI of galvanic vestibular stimulation with alternating currents at different frequencies. *Neuroimage.* (2005) 26:721–32. doi: 10.1016/j.neuroimage.2005.02.049
92. Eickhoff SB, Weiss PH, Amunts K, Fink GR, Zilles K. Identifying human parieto-insular vestibular cortex using fMRI and cytoarchitectonic mapping. *Hum Brain Mapp.* (2006) 27:611–21. doi: 10.1002/hbm.20205
93. Eickhoff SB, Jbabdi S, Caspers S, Laird AR, Fox PT, Zilles K, et al. Anatomical and functional connectivity of cytoarchitectonic areas within the human parietal operculum. *J Neurosci.* (2010) 30:6409–21. doi: 10.1523/JNEUROSCI.5664-09.2010
94. Watson SR, Colebatch JG. Vestibulocollic reflexes evoked by short-duration galvanic stimulation in man. *J Physiol.* (1998) 513 (Pt 2):587–97. doi: 10.1111/j.1469-7793.1998.587bb.x
95. Molinari GA, Mingrino S. Cortical evoked responses to vestibular stimulation in man. *J Laryngol Otol.* (1974) 88:515–21. doi: 10.1017/s0022215100079019
96. Kammermeier S, Singh A, Bötzel K. Intermediate latency-evoked potentials of multimodal cortical vestibular areas: galvanic stimulation. *Front Neurol.* (2017) 8:587. doi: 10.3389/fneur.2017.00587
97. Colebatch JG, Halmagyi GM, Skuse NF. Myogenic potentials generated by a click-evoked vestibulocollic reflex. *J Neurol Neurosurg Psychiatry.* (1994) 57:190–7. doi: 10.1136/jnnp.57.2.190
98. Welgampola MS, Rosengren SM, Halmagyi GM, Colebatch JG. Vestibular activation by bone conducted sound. *J Neurol Neurosurg Psychiatry.* (2003) 74:771–8. doi: 10.1136/jnnp.74.6.771
99. Curthoys IS. A critical review of the neurophysiological evidence underlying clinical vestibular testing using sound, vibration and galvanic stimuli. *Clin Neurophysiol Off J Int Fed Clin Neurophysiol.* (2010) 121:132–44. doi: 10.1016/j.clinph.2009.09.027
100. Colebatch JG, Rosengren SM, Welgampola MS. Vestibular-evoked myogenic potentials. In: Furman JM, Lempert T, editors. Handbook of Clinical Neurology Neuro-Otology. Amsterdam: Elsevier (2016). p. 133–55. doi: 10.1016/B978-0-444-63437-5.00010-8
101. Miyamoto T, Fukushima K, Takada T, de Waele C, Vidal P-P. Saccular stimulation of the human cortex: a functional magnetic resonance imaging study. *Neurosci Lett.* (2007) 423:68–72. doi: 10.1016/j.neulet.2007.06.036
102. Janzen J, Schlindwein P, Bense S, Bauermann T, Vucurevic G, Stoeter P, et al. Neural correlates of hemispheric dominance and ipsilaterality within the vestibular system. *Neuroimage.* (2008) 42:1508–18. doi: 10.1016/j.neuroimage.2008.06.026
103. Schlindwein P, Mueller M, Bauermann T, Brandt T, Stoeter P, Dieterich M. Cortical representation of saccular vestibular stimulation: VEMPs in fMRI. *Neuroimage.* (2008) 39:19–31. doi: 10.1016/j.neuroimage.2007.08.016
104. Kato T, Shiraishi K, Eura Y, Shibata K, Sakata T, Morizono T, et al. A "neural" response with 3-ms latency evoked by loud sound in profoundly deaf patients. *Audiol Neurootol.* (1998) 3:253–64. doi: 10.1159/000013797
105. Papathanasiou ES, Zamba-Papanicolaou E, Pantziaris M, Kleopas K, Kyriakides T, Papacostas S, et al. Neurogenic vestibular evoked potentials using a tone pip auditory stimulus. *Electromyogr Clin Neurophysiol.* (2004) 44:167–73.
106. Papathanasiou ES, Lemesiou A, Hadjiloizou S, Myrianthopoulou P, Pantzaris M, Papacostas SS. A new neurogenic vestibular evoked potential (N6) recorded with the use of air-conducted sound. *Otol Neurotol Off Publ Am Otol Soc Am Neurotol Soc Eur Acad Otol Neurotol.* (2010) 31:528–35. doi: 10.1097/MAO.0b013e3181cdd6b7
107. Todd NPM, Rosengren SM, Colebatch JG. A short latency vestibular evoked potential (VsEP) produced by bone-conducted acoustic stimulation. *J Acoust Soc Am.* (2003) 114:3264–72. doi: 10.1121/1.1628249
108. Todd NPM, Rosengren SM, Colebatch JG. A source analysis of short-latency vestibular evoked potentials produced by air- and bone-conducted sound. *Clin Neurophysiol.* (2008) 119:1881–94. doi: 10.1016/j.clinph.2008.03.027
109. Murofushi T, Iwasaki S, Takai Y, Takegoshi H. Sound-evoked neurogenic responses with short latency of vestibular origin. *Clin Neurophysiol Off J Int Fed Clin Neurophysiol.* (2005) 116:401–5. doi: 10.1016/j.clinph.2004.09.005
110. Todd NPM, Paillard AC, Kluk K, Whittle E, Colebatch JG. Source analysis of short and long latency vestibular-evoked potentials (VsEPs) produced by left vs. right ear air-conducted 500 Hz tone pips. *Hear Res.* (2014) 312:91–102. doi: 10.1016/j.heares.2014.03.006
111. Kammermeier S, Singh A, Noachtar S, Krotofil I, Bötzel K. Intermediate latency evoked potentials of cortical multimodal vestibular areas: acoustic stimulation. *Clin Neurophysiol Off J Int Fed Clin Neurophysiol.* (2015) 126:614–25. doi: 10.1016/j.clinph.2014.06.036
112. Todd NPM, McLean A, Paillard A, Kluk K, Colebatch JG. Vestibular evoked potentials (VsEPs) of cortical origin produced by impulsive acceleration applied at the nasion. *Exp Brain Res.* (2014) 232:3771–84. doi: 10.1007/s00221-014-4067-x
113. McNerney KM, Lockwood AH, Coad ML, Wack DS, Burkard RF. Use of 64-channel electroencephalography to study neural otolith-evoked responses. *J Am Acad Audiol.* (2011) 22:143–55. doi: 10.3766/jaaa.22.3.3
114. Rosengren SM, Colebatch JG. Vestibular evoked potentials (VsEPs) in patients with severe to profound bilateral hearing loss. *Clin Neurophysiol Off J Int Fed Clin Neurophysiol.* (2006) 117:1145–53. doi: 10.1016/j.clinph.2005.12.026
115. Todd NP, Govender S, Colebatch JG. The inion response revisited: evidence for a possible cerebellar contribution to vestibular-evoked potentials produced by air-conducted sound stimulation. *J Neurophysiol.* (2017) 117:1000–13. doi: 10.1152/jn.00545.2016
116. Oh SY, Boegle R, Ertl M, Eulenburg PZ, Stephan T, Dieterich M. Auditory induced vestibular (otolithic) processing revealed by an independent component analysis: an fMRI parametric analysis. *J Neurol.* (2017) 264(Suppl 1):23–5. doi: 10.1007/s00415-017-8430-2
117. Oh S-Y, Boegle R, Ertl M, Stephan T, Dieterich M. Multisensory vestibular, vestibular-auditory, and auditory network effects revealed by parametric sound pressure stimulation. *Neuroimage.* (2018) 176:354–63. doi: 10.1016/j.neuroimage.2018.04.057
118. Halmagyi GM, Yavor RA, Colebatch JG. Tapping the head activates the vestibular system: a new use for the clinical reflex hammer. *Neurology.* (1995) 45:1927–9. doi: 10.1212/wnl.45.10.1927
119. Rosengren SM, Todd NPM, Colebatch JG. Vestibular evoked myogenic potentials evoked by brief interaural head acceleration: properties and possible origin. *J Appl Physiol Bethesda Md (1985).* (2009) 107:841–52. doi: 10.1152/japplphysiol.00296.2009
120. Todd NPM, Govender S, Colebatch JG. Vestibular cerebellar evoked potentials (VsCEPs) in humans and their modulation during optokinetic stimulation. *J Neurophysiol.* (2018) 120:3099–109 doi: 10.1152/jn.00502.2018
121. Roberts DC, Marcelli V, Gillen JS, Carey JP, Della Santina CC, Zee DS. MRI magnetic field stimulates rotational sensors of the brain. *Curr Biol.* (2011) 21:1635–40. doi: 10.1016/j.cub.2011.08.029
122. Ward BK, Otero-Millan J, Jareonsettasin P, Schubert MC, Roberts DC, Zee DS. Magnetic Vestibular Stimulation (MVS) as a technique for understanding the normal and diseased labyrinth. *Front Neurol.* (2017) 8:122. doi: 10.3389/fneur.2017.00122
123. Ward BK, Roberts DC, Otero-Millan J, Zee DS. A decade of magnetic vestibular stimulation: from serendipity to physics to the clinic. *J Neurophysiol.* (2019) 121:2013–9. doi: 10.1152/jn.00873.2018
124. Otero-Millan J, Zee DS, Schubert MC, Roberts DC, Ward BK. Three-dimensional eye movement recordings during magnetic vestibular stimulation. *J Neurol.* (2017) 264:7–12. doi: 10.1007/s00415-017-8420-4
125. Boegle R, Stephan T, Ertl M, Glasauer S, Dieterich M. Magnetic vestibular stimulation modulates default mode network fluctuations. *Neuroimage.* (2016) 127:409–21. doi: 10.1016/j.neuroimage.2015.11.065
126. Allen PJ, Polizzi G, Krakow K, Fish DR, Lemieux L. Identification of EEG events in the MR scanner: the problem of pulse artifact and a method for its subtraction. *Neuroimage.* (1998) 8:229–39. doi: 10.1006/nimg.1998.0361
127. Goldman RI, Stern JM, Engel J, Cohen MS. Acquiring simultaneous EEG and functional MRI. *Clin Neurophysiol.* (2000) 111:1974–80. doi: 10.1016/S1388-2457(00)00456-9
128. Mulert C, Jäger L, Pogarell O, Bussfeld P, Schmitt R, Juckel G, et al. Simultaneous ERP and event-related fMRI: focus on the time course of brain activity in target detection. *Methods Find Exp Clin Pharmacol.* (2002) 24(Suppl D):17–20.
129. Niazy RK, Beckmann CF, Iannetti GD, Brady JM, Smith SM. Removal of FMRI environment artifacts from EEG data using optimal basis

sets. *Neuroimage.* (2005) 28:720–37. doi: 10.1016/j.neuroimage.2005.06.067

130. Mantini D, Perrucci MG, Cugini S, Ferretti A, Romani GL, Del Gratta C. Complete artifact removal for EEG recorded during continuous fMRI using independent component analysis. *Neuroimage.* (2007) 34:598–607. doi: 10.1016/j.neuroimage.2006.09.037
131. Hausler R, Kasper A. [Threefold intraoperative electrophysiological monitoring of vestibular neurectomy]. *Ann Oto-Laryngol Chir Cervico Faciale Bull Soc Oto-Laryngol Hopitaux Paris.* (1991) 108:319–23.
132. Häusler R, Kasper A, Demierre B. Intraoperative electrically evoked vestibular potentials in humans. *Acta Otolaryngol (Stockh).* (1992) 112:180–5. doi: 10.1080/00016489.1992.11665400
133. de Waele C, Baudonnière PM, Lepecq JC, Tran Ba Huy P, Vidal PP. Vestibular projections in the human cortex. *Exp Brain Res.* (2001) 141:541–51. doi: 10.1007/s00221-001-0894-7
134. Mickle WA, Ades HW. Rostral projection pathway of the vestibular system. *Am J Physiol.* (1954) 176:243–6.
135. Fredrickson JM, Figge U, Scheid P, Kornhuber HH. Vestibular nerve projection to the cerebral cortex of the Rhesus monkey. *Exp Brain Res.* (1966) 2:318–27. doi: 10.1007/BF00234777
136. Rancz EA, Moya J, Drawitsch F, Brichta AM, Canals S, Margrie TW. Widespread vestibular activation of the rodent cortex. *J Neurosci.* (2015) 35:5926–34. doi: 10.1523/JNEUROSCI.1869-14.2015
137. Bickford RG, Jacobson JL, Cody DT. Nature of average evoked potentials to sound and other stimuli in man. *Ann N Y Acad Sci.* (1964) 112:204–23. doi: 10.1111/j.1749-6632.1964.tb26749.x
138. Cody DT, Jacobson JL, Walker JC, Bickford RG. Averaged evoked myogenic and cortical potentials to sound in man. *Ann Otol Rhinol Laryngol.* (1964) 73:763–77. doi: 10.1177/000348946407300315
139. Odkvist LM, Rubin AM, Schwarz DW, Fredrickson JM. Vestibular and auditory cortical projection in the guinea pig (Cavia porcellus). *Exp Brain Res.* (1973) 18:279–86. doi: 10.1007/BF00234598
140. Spiegel EA, Egyed J, Szekely EG. Cortical responses to rotation. II Responses recorded at the onset of rotation from the second somatic sensory and posterior areas. *Acta Otolaryngol (Stockh).* (1968) 66:261–72. doi: 10.3109/00016486809126293
141. Buettner UW, Büttner U, Henn V. Transfer characteristics of neurons in vestibular nuclei of the alert monkey. *J Neurophysiol.* (1978) 41:1614–28. doi: 10.1152/jn.1978.41.6.1614
142. Escalar G, Filippone A. [Induced vestibular stimulation and changes in the human electroencephalogram; three cases of psychomotor epilepsy with electro-clinical crisis activated by means of thermic vestibular stimulation]. *Sist Nerv.* (1955) 7:11–28.
143. Götze W, Knudsen U, Krokowski G, Münter M. Über den telemetrischen Nachweis des Einflusses von kreisförmigen positiven und negativen Beschleunigungen auf das EEG des Menschen. *Biomed Tech Eng.* (1964) 9:185–8. doi: 10.1515/bmte.1964.9.1-4.185
144. Karbowski K. Epileptic seizures induced by vestibular and auditory stimuli. In: Beaumanoir A, Gastaut H, Naquet R, editors. *Reflex Seizures and Reflex Epilepsies*. Genève: Médecine and Hygiène (1989) p. 255–63.
145. Celesia G. Brainstem auditory evoked potentials (BAEPs) and other auditory evoked potentials. In: Schomer DL, Lopes da Silva FH, editors. Niedermeyer's Electroencephalography: Basic Principles, Clinical Applications, and Related Fields. 6th ed. Oxford: Oxford University Press (2017). p. 976–1002.
146. Knox GW, Isaacs J, Woodard D, Johnson L, Jordan D. Short latency vestibular evoked potentials. *Otolaryngol–Head Neck Surg Off J Am Acad Otolaryngol-Head Neck Surg.* (1993) 108:265–9. doi: 10.1177/019459989310800310
147. Rodionov V, Elidan J, Sela M, Nitzan M, Sohmer H. Vertical plane short and middle latency vestibular evoked potentials in humans. *Ann Otol Rhinol Laryngol.* (1996) 105:43–8. doi: 10.1177/000348949610500107
148. Rosengren SM, McAngus Todd NP, Colebatch JG. Vestibular-evoked extraocular potentials produced by stimulation with bone-conducted sound. *Clin Neurophysiol Off J Int Fed Clin Neurophysiol.* (2005) 116:1938–48. doi: 10.1016/j.clinph.2005.03.019
149. Todd NPM, Govender S, Colebatch JG. Vestibular-dependent inter-stimulus interval effects on sound evoked potentials of central origin. *Hear Res.* (2016) 341:190–201. doi: 10.1016/j.heares.2016.07.017
150. Todd NPM, Govender S, Lemieux L, Colebatch JG. Source analyses of axial and vestibular evoked potentials associated with brainstem-spinal reflexes show cerebellar and cortical contributions. *Neurosci Lett.* (2021) 2021:135960. doi: 10.1016/j.neulet.2021.135960
151. Pyykkö I, Aalto H, Grönfors T, Starck J, Ishizaki H. Vestibular evoked responses in man: methodological aspects. *Acta Oto-Laryngol Suppl.* (1995) 520 (Pt 1):117–9. doi: 10.3109/00016489509125205
152. Elidan J, Langhofer L, Honrubia V. The neural generators of the vestibular evoked response. *Brain Res.* (1987) 423:385–90. doi: 10.1016/0006-8993(87)90868-7
153. Elidan J, Langhofer L, Honrubia V. The firing properties of second-order vestibular neurons in correlation with the far-field recorded vestibular-evoked response. *Laryngoscope.* (1989) 99:92–9. doi: 10.1288/00005537-198901000-00017
154. Cazals Y, Aran JM, Erre JP, Guilhaume A, Hawkins JE. "Neural" responses to acoustic stimulation after destruction of cochlear hair cells. *Arch Otorhinolaryngol.* (1979) 224:61–70. doi: 10.1007/BF00455225
155. Cazals Y, Aran JM, Erre JP, Guilhaume A. Acoustic responses after total destruction of the cochlear receptor: brainstem and auditory cortex. *Science.* (1980) 210:83–6. doi: 10.1126/science.6968092
156. Todd NPM, Govender S, Colebatch JG. The human electrocerebellogram (ECeG) recorded non-invasively using scalp electrodes. *Neurosci Lett.* (2018) 682:124–31. doi: 10.1016/j.neulet.2018.06.012
157. Andersen LM, Jerbi K, Dalal SS. Can EEG and MEG detect signals from the human cerebellum? *Neuroimage.* (2020) 215:116817. doi: 10.1016/j.neuroimage.2020.116817
158. Todd NPM, Rosengren SM, Aw ST, Colebatch JG. Ocular vestibular evoked myogenic potentials (OVEMPs) produced by air- and bone-conducted sound. *Clin Neurophysiol Off J Int Fed Clin Neurophysiol.* (2007) 118:381–90. doi: 10.1016/j.clinph.2006.09.025
159. Rodionov V, Elidan J, Sohmer H. Analysis of the middle latency evoked potentials to angular acceleration impulses in man. *Electroencephalogr Clin Neurophysiol.* (1996) 100:354–61. doi: 10.1016/0168-5597(96)95515-x
160. Walzl EM, Mountcastle VB. Projection of vestibular nerve to cerebral cortex of the cat. *Am J Physiol.* (1949) 159:595.
161. Sans A, Raymond J, Marty R. Thalamic and cortical responses to electric stimulation of the vestibular nerve in the cat. *Exp Brain Res.* (1970) 10:265–75. doi: 10.1007/BF00235050
162. Geisler CD, Frishkopf LS, Rosenblith WA. Extracranial responses to acoustic clicks in man. *Science.* (1958) 128:1210–1. doi: 10.1126/science.128.3333.1210
163. Trinus KF. Vestibular evoked potentials. *Adv Otorhinolaryngol.* (1997) 53:155–81. doi: 10.1159/000059043
164. Fasold O, von Brevern M, Kuhberg M, Ploner CJ, Villringer A, Lempert T, et al. Human vestibular cortex as identified with caloric stimulation in functional magnetic resonance imaging. *Neuroimage.* (2002) 17:1384–93. doi: 10.1006/nimg.2002.1241
165. Indovina I, Maffei V, Bosco G, Zago M, Macaluso E, Lacquaniti F. Representation of visual gravitational motion in the human vestibular cortex. *Science.* (2005) 308:416–9. doi: 10.1126/science.1107961
166. Ertl M, Klaus M, Mast FW, Brandt T, Dieterich M. Spectral fingerprints of correct vestibular discrimination of the intensity of body accelerations. *Neuroimage.* (2020) 219:117015. doi: 10.1016/j.neuroimage.2020.117015
167. Ertl M, Zu Eulenburg P, Woller M, Dieterich M. The role of delta and theta oscillations during ego-motion in healthy adult volunteers. *Exp. Brain Res.* (2021) 239:1073–83. doi: 10.1007/s00221-020-06030-3
168. Heine W, Dobrota M-A, Schomer D, Wigton R, Herman S. High-Density Adaptive ten ten: proposal for electrode nomenclature for high-density EEG. *J Clin Neurophysiol.* (2020) 37:263–70. doi: 10.1097/WNP.0000000000000632
169. Mazzola L, Lopez C, Faillenot I, Chouchou F, Mauguière F, Isnard J. Vestibular responses to direct stimulation of the human insular cortex. *Ann Neurol.* (2014) 76:609–19. doi: 10.1002/ana.24252
170. Caruana F, Gerbella M, Avanzini P, Gozzo F, Pelliccia V, Mai R, et al. Motor and emotional behaviours elicited by electrical stimulation of the human cingulate cortex. *Brain J Neurol.* (2018) 141:3035–51. doi: 10.1093/brain/awy219

171. Bertora GO, Bergmann JM. Cortical responses of vestibular reactions measured by topographic brain mapping and vestibular evoked potentials. *Acta Oto-Laryngol. Suppl.* (1995) 520(Pt 1):126–9.
172. Claussen C, Schneider D, Koltchev C. On the functional state of central vestibular structures in monoaural symptomatic tinnitus patients (BEAM-VbEP Study). *Int Tinnitus J.* (1995) 1:5–12.
173. Claussen C. Vestibular evoked responses: a new frontier in equilibriometry. *Acta Oto-Laryngol Suppl.* (1995) 520(Pt 1):113–6. doi: 10.3109/00016489509125204
174. Kolchev C. Vestibular late evoked potentials (VbEP) processed by means of brain electrical activity mapping (BEAM). *Acta Oto-Laryngol Suppl.* (1995) 520(Pt 1):130–3. doi: 10.3109/00016489509125209
175. Constantinescu L, Schneider D, Claussen C. Vestibular evoked potentials in two patients with bilateral vestibular loss. *Int Tinnitus J.* (1996) 2:45–57.
176. Schneider D, Schneider L, Claussen CF, Kolchev C. Cortical representation of the vestibular system as evidenced by brain electrical activity mapping of vestibular late evoked potentials. *Ear Nose Throat J.* (2001) 80:251–2, 255–8, 260 passim.
177. Smith AT, Wall MB, Thilo KV. Vestibular inputs to human motion-sensitive visual cortex. *Cereb Cortex.* (2012) 22:1068–77. doi: 10.1093/cercor/bhr179
178. Hofferberth B. Evoked potentials to rotatory stimulation. Preliminary results. *Acta Oto Laryngol Suppl.* (1984) 406:134–6. doi: 10.3109/00016488309123020
179. Hofferberth B. The clinical significance of vestibular evoked potentials (REP). *Acta Oto-Laryngol Suppl.* (1995) 520(Pt 1):124–5. doi: 10.3109/00016489509125207
180. Penfield W. Vestibular sensation and the cerebral cortex. *Ann Otol Rhinol Laryngol.* (1957) 66:691–8. doi: 10.1177/000348945706600307
181. Kahane P, Hoffmann D, Minotti L, Berthoz A. Reappraisal of the human vestibular cortex by cortical electrical stimulation study. *Ann Neurol.* (2003) 54:615–24. doi: 10.1002/ana.10726
182. Keck W. Rotatory evoked cortical potentials in normal subjects and patients with unilateral and bilateral vestibular loss. *Eur Arch Otorhinolaryngol.* (1990) 247:222–5.
183. Bumm P, Johannsen HS, Spreng M, Wiegand HP. [Slow evoked cortical potentials to rotary stimulation in man]. *Arztl Forsch.* (1970) 24:59–62.
184. Pirodda E, Ghedini S, Zanetti MA. Investigations into vestibular evoked responses. *Acta Otolaryngol.* (1987) 104:77–84. doi: 10.3109/00016488709109050
185. Kenmochi M, Ohashi T, Nishino H, Sato S. Cortical potentials evoked by horizontal rotatory stimulation: the effects of angular acceleration. *Acta Otolaryngol.* (2003) 123:923–7.
186. Nolan H, Butler JS, Whelan R, Foxe JJ, Bülthoff HH, Reilly RB. Electrophysiological source analysis of passive self-motion. *In: 2011 5th International IEEE/EMBS Conference on Neural Engineering (Cancun).* (2011) 53–6. doi: 10.1109/NER.2011.5910487
187. Joos K, Gilles A, Van de Heyning P, De Ridder D, Vanneste S. From sensation to percept: the neural signature of auditory event-related potentials. *Neurosci Biobehav Rev.* (2014) 42:148–56. doi: 10.1016/j.neubiorev.2014.02.009
188. Indovina I, Bosco G, Riccelli R, Maffei V, Lacquaniti F, Passamonti L, et al. Structural connectome and connectivity lateralization of the multimodal vestibular cortical network. *Neuroimage.* (2020) 222:117247. doi: 10.1016/j.neuroimage.2020.117247
189. Raiser TM, Flanagin VL, Duering M, van Ombergen A, Ruehl RM, Zu Eulenburg P. The human corticocortical vestibular network. *NeuroImage.* (2020) 223:117362. doi: 10.1016/j.neuroimage.2020.117362
190. Klingner CM, Volk GF, Flatz C, Brodoehl S, Dieterich M, Witte OW, et al. Components of vestibular cortical function. *Behav Brain Res.* (2013) 236:194–9. doi: 10.1016/j.bbr.2012.08.049
191. Dieterich M, Kirsch V, Brandt T. Right-sided dominance of the bilateral vestibular system in the upper brainstem and thalamus. *J Neurol.* (2017) 1–8. doi: 10.1007/s00415-017-8453-8
192. Barmack NH. Central vestibular system: vestibular nuclei and posterior cerebellum. *Brain Res Bull.* (2003) 60:511–41. doi: 10.1016/s0361-9230(03)00055-8
193. Park SY, Yeo SS, Jang SH, Cho IH. Anatomical location of the vestibulocerebellar tract in the healthy human brain: a diffusion tensor imaging study. *Brain Sci.* (2021) 1:199. doi: 10.3390/brainsci11020199
194. Precht W, Llinás R. Functional organization of the vestibular afferents to the cerebellar cortex of frog and cat. *Exp Brain Res.* (1969) 9:30–52. doi: 10.1007/BF00235450
195. Brandt T, Dieterich M. Does the vestibular system determine the lateralization of brain functions? *J Neurol.* (2015) 262:214–5. doi: 10.1007/s00415-014-7548-8
196. Dieterich M, Brandt T. Global orientation in space and the lateralization of brain functions. *Curr Opin Neurol.* (2018) 31:96–104. doi: 10.1097/WCO.0000000000000516
197. Angelaki DE, Cullen KE. Vestibular system: the many facets of a multimodal sense. *Annu Rev Neurosci.* (2008) 31:125–50. doi: 10.1146/annurev.neuro.31.060407.125555
198. Angelaki DE, Yakusheva TA. How vestibular neurons solve the tilt/translation ambiguity. Comparison of brainstem, cerebellum, and thalamus. *Ann N Y Acad Sci.* (2009) 1164:19–28. doi: 10.1111/j.1749-6632.2009.03939.x
199. Shinder ME, Newlands SD. Sensory convergence in the parieto-insular vestibular cortex. *J Neurophysiol.* (2014) 111:2445–64. doi: 10.1152/jn.00731.2013
200. Dutov AM. Responses of neurons of the vestibular nuclei to interoceptive stimulation. *Bull Exp Biol Med.* (1974) 78:849–51. doi: 10.1007/BF00803905
201. Ochi K, Ohashi T, Nishino H. Variance of vestibular-evoked myogenic potentials. *Laryngoscope.* (2001) 111:522–7. doi: 10.1097/00005537-200103000-00025
202. Lee SK, Cha CI, Jung TS, Park DC, Yeo SG. Age-related differences in parameters of vestibular evoked myogenic potentials. *Acta Otolaryngol (Stockh).* (2008) 128:66–72. doi: 10.1080/00016480701387108
203. McGarvie LA, MacDougall HG, Halmagyi GM, Burgess AM, Weber KP, Curthoys IS. The Video Head Impulse Test (vHIT) of semicircular canal function - age-dependent normative values of VOR gain in healthy subjects. *Front Neurol.* (2015) 6:154. doi: 10.3389/fneur.2015.00154
204. Valame DA, Gore GB. Role of cervical vestibular evoked myogenic potentials (cVEMP) and auditory brainstem response (ABR) in the evaluation of vestibular schwannoma. *Braz J Otorhinolaryngol.* (2017) 83:324–9. doi: 10.1016/j.bjorl.2016.04.003
205. Rafique I, Wennervaldt K, Melchiors J, Caye-Thomasen P. Auditory brainstem response - a valid and cost-effective screening tool for vestibular schwannoma? *Acta Otolaryngol. (Stockh).* (2016) 136:660–2. doi: 10.3109/00016489.2016.1157726
206. Dieterich M, Bartenstein P, Spiegel S, Bense S, Schwaiger M, Brandt T. Thalamic infarctions cause side-specific suppression of vestibular cortex activations. *Brain J Neurol.* (2005) 128:2052–67. doi: 10.1093/brain/awh551
207. Becker-Bense S, Dieterich M, Buchholz H-G, Bartenstein P, Schreckenberger M, Brandt T. The differential effects of acute right- vs. left-sided vestibular failure on brain metabolism. *Brain Struct Funct.* (2014) 219:1355–67. doi: 10.1007/s00429-013-0573-z
208. Hewett R, Guye M, Gavaret M, Bartolomei F. Benign temporo-parieto-occipital junction epilepsy with vestibular disturbance: an underrecognized form of epilepsy? *Epilepsy Behav.* (2011) 21:412–6. doi: 10.1016/j.yebeh.2011.05.017
209. Hewett R, Bartolomei F. Epilepsy and the cortical vestibular system: tales of dizziness and recent concepts. *Front Integr Neurosci.* (2013) 7:73. doi: 10.3389/fnint.2013.00073
210. Lewis RF, Priesol AJ, Nicoucar K, Lim K, Merfeld DM. Abnormal motion perception in vestibular migraine. *Laryngoscope.* (2011) 121:1124–5. doi: 10.1002/lary.21723
211. King S, Priesol AJ, Davidi SE, Merfeld DM, Ehtemam F, Lewis RF. Self-motion perception is sensitized in vestibular migraine: pathophysiologic and clinical implications. *Sci Rep.* (2019) 9:14323. doi: 10.1038/s41598-019-50803-y
212. Dieterich M, Staab JP. Functional dizziness: from phobic postural vertigo and chronic subjective dizziness to persistent postural-perceptual dizziness. *Curr Opin Neurol.* (2017) 30:107–13. doi: 10.1097/WCO.0000000000000417
213. Indovina I, Riccelli R, Chiarella G, Petrolo C, Augimeri A, Giofrè L, et al. Role of the Insula and vestibular system in patients with chronic subjective

dizziness: an fMRI study using sound-evoked vestibular stimulation. *Front Behav Neurosci.* (2015) 9:334. doi: 10.3389/fnbeh.2015.00334

214. Indovina I, Conti A, Lacquaniti F, Staab JP, Passamonti L, Toschi N. Lower functional connectivity in vestibular-limbic networks in individuals with subclinical agoraphobia. *Front Neurol.* (2019) 10:874. doi: 10.3389/fneur.2019.00874
215. Riccelli R, Passamonti L, Toschi N, Nigro S, Chiarella G, Petrolo C, et al. Altered insular and occipital responses to simulated vertical self-motion in patients with persistent postural-perceptual dizziness. *Front Neurol.* (2017) 8:529. doi: 10.3389/fneur.2017.00529
216. Nolan H, Whelan R, Reilly RB, Bulthoff HH, Butler JS. Acquisition of human EEG data during linear self-motion on a Stewart platform. In: *2009 4th International IEEE/EMBS Conference on Neural Engineering (Antalya)*. (2009) 585–8. doi: 10.1109/NER.2009.5109364
217. Nolan H, Butler JS, Whelan R, Foxe JJ, Bülthoff HH, Reilly RB. Neural correlates of oddball detection in self-motion heading: a high-density event-related potential study of vestibular integration. *Exp Brain Res.* (2012) 219:1–11. doi: 10.1007/s00221-012-3059-y
218. Frank SM, Sun L, Forster L, Tse PU, Greenlee MW. Cross-modal attention effects in the vestibular cortex during attentive tracking of moving objects. *J Neurosci.* (2016) 36:12720–8. doi: 10.1523/JNEUROSCI.2480-16.2016
219. Frank SM, Forster L, Pawellek M, Malloni WM, Ahn S, Tse PU, et al. Visual attention modulates glutamate-glutamine levels in vestibular cortex: evidence from magnetic resonance spectroscopy. *J Neurosci.* (2021) 41:1970–81. doi: 10.1523/JNEUROSCI.2018-20.2020
220. Pfurtscheller G, Lopes da Silva FH. Event-related EEG/MEG synchronization and desynchronization: basic principles. *Clin Neurophysiol.* (1999) 110:1842–57. doi: 10.1016/S1388-2457(99)00141-8

Conflict of Interest: The authors declare that the research was conducted in the absence of any commercial or financial relationships that could be construed as a potential conflict of interest.

frontiers | Frontiers in Neurology

ORIGINAL RESEARCH
published: 11 May 2022
doi: 10.3389/fneur.2022.663200

IE-Vnet: Deep Learning-Based Segmentation of the Inner Ear's Total Fluid Space

Seyed-Ahmad Ahmadi[1,2,3†], Johann Frei[4†], Gerome Vivar[1,5], Marianne Dieterich[1,2,6,7] and Valerie Kirsch[1,2,6*]*

[1] German Center for Vertigo and Balance Disorders, University Hospital, Ludwig-Maximilians-Universität, Munich, Germany, [2] Department of Neurology, University Hospital, Ludwig-Maximilians-Universität, Munich, Germany, [3] NVIDIA GmbH, Munich, Germany, [4] IT-Infrastructure for Translational Medical Research, University of Augsburg, Augsburg, Germany, [5] Computer Aided Medical Procedures (CAMP), Technical University of Munich (TUM), Munich, Germany, [6] Graduate School of Systemic Neuroscience (GSN), Ludwig-Maximilians-Universität, Munich, Germany, [7] Munich Cluster for Systems Neurology (SyNergy), Munich, Germany

Background: *In-vivo* MR-based high-resolution volumetric quantification methods of the endolymphatic hydrops (ELH) are highly dependent on a reliable segmentation of the inner ear's total fluid space (TFS). This study aimed to develop a novel open-source inner ear TFS segmentation approach using a dedicated deep learning (DL) model.

Methods: The model was based on a V-Net architecture (IE-Vnet) and a multivariate (MR scans: T1, T2, FLAIR, SPACE) training dataset (D1, 179 consecutive patients with peripheral vestibulocochlear syndromes). Ground-truth TFS masks were generated in a semi-manual, atlas-assisted approach. IE-Vnet model segmentation performance, generalizability, and robustness to domain shift were evaluated on four heterogenous test datasets (D2-D5, $n = 4 \times 20$ ears).

Results: The IE-Vnet model predicted TFS masks with consistently high congruence to the ground-truth in all test datasets (Dice overlap coefficient: 0.9 ± 0.02, Hausdorff maximum surface distance: 0.93 ± 0.71 mm, mean surface distance: 0.022 ± 0.005 mm) without significant difference concerning side (two-sided Wilcoxon signed-rank test, $p > 0.05$), or dataset (Kruskal-Wallis test, $p > 0.05$; *post-hoc* Mann-Whitney U, FDR-corrected, all $p > 0.2$). Prediction took 0.2 s, and was 2,000 times faster than a state-of-the-art atlas-based segmentation method.

Conclusion: IE-Vnet TFS segmentation demonstrated high accuracy, robustness toward domain shift, and rapid prediction times. Its output works seamlessly with a previously published open-source pipeline for automatic ELS segmentation. IE-Vnet could serve as a core tool for high-volume trans-institutional studies of the inner ear. Code and pre-trained models are available free and open-source under https://github.com/pydsgz/IEVNet.

Keywords: MRI, deep learning, endolymphatic hydros, endolymphatic and perilymphatic space, convolutional neural network CNN, VNet, segmentation (image processing), inner ear imaging

Edited by:
Joel Alan Goebel,
Washington University in St. Louis,
United States

Reviewed by:
Marc van Hoof,
Maastricht University Medical Centre,
Netherlands
Michael Eliezer,
Hôpital Lariboisière, France

****Correspondence:***
Seyed-Ahmad Ahmadi
ahmadi@cs.tum.edu
Valerie Kirsch
vkirsch@med.lmu.de

† These authors have contributed equally to this work

Specialty section:
This article was submitted to
Neuro-Otology,
a section of the journal
Frontiers in Neurology

Received: *02 February 2021*
Accepted: *04 April 2022*
Published: *11 May 2022*

Citation:
Ahmadi S-A, Frei J, Vivar G,
Dieterich M and Kirsch V (2022)
IE-Vnet: Deep Learning-Based
Segmentation of the Inner Ear's Total
Fluid Space.
Front. Neurol. 13:663200.
doi: 10.3389/fneur.2022.663200

1. INTRODUCTION

In-vivo non-invasive verification of endolymphatic hydrops (ELH) via intravenous delayed gadolinium (Gd) enhanced magnetic resonance imaging of the inner ear (iMRI) is increasingly becoming an essential standard clinical diagnostic tool to distinguish leading causes of peripheral vestibulocochlear syndromes (1, 2). In this context, a fast and easily reproducible, yet more importantly, comparable and standardized quantification method of the endolymphatic space (ELS) is a prerequisite in any setting, be it clinical or research (3). Unfortunately, such a quantification method is not entirely available yet despite many efforts.

At first glance, clinical radiology approaches offer fast and easily applicable visual semi-quantitative (SQ) ELH classifications (4–9). Nevertheless, given the plurality of visual SQ ELH classification approaches that may vary in wording, resolution (3- or 4-point ordinal scale), or evaluation level (anatomical fixpoint), and can be sensitive to human bias, published results cannot be considered inherently reproducible, comparable or standardized (10). Already an improvement in comparability, manual measurement of the ELS area in 2D within one MR-layer (11, 12), or better yet, the entire ELS volume 3D over multiple MR-layers (13, 14) remain dependent on human decisions.

Similar to optimizing entire iMR sequences in use to date (15–17), automatic ELS quantification is predetermined by two methodical sticking points (18): The first obstacle is to distinguish between total fluid space (TFS) within the entire inner ears bony labyrinth from the surrounding petrosal bone structures (19–21). The second difficulty is distinguishing the two different fluid spaces within the TFS (22, 23), namely ELS within the membranous labyrinth and the surrounding perilymphatic space (PLS) within the bony labyrinth. Current semi-automatic (24–26) or automatic (27, 28) 3D ELS quantification methods have mostly concentrated on ELS differentiation within TFS.

Most available 3D TFS segmentation approaches are either manual (24, 26), or atlas-based (29, 30). However, atlas-based segmentation uses deformable image registration that entails several challenges (31). On the one hand, careful parameterization and run-times between minutes to hours of computation to obtain accurate segmentation prohibit interactive analysis. Another challenge and important motivation for this study are that the thin structures of the TFS, particularly the semi-circular canals, often lead to misregistration, despite the usage of multi-resolution registration.

A promising alternative tool is machine learning algorithms based on deep neural networks (DNN, or deep learning). Recently, an automated 2D measurement of hydrops ratio using a three-layer convolutional neural network (CNN) based segmentation (32) and a deep learning algorithm for fully automated 3D segmentation of the inner ear (33) were proposed. However, to the best of our knowledge, these algorithms are not accessible to the public at large.

This work proposes an open-source approach for inner ear TFS segmentation based on deep learning and using a specialized V-Net architecture (IE-Vnet) that will be made available to the scientific community. The discussion includes a comprehensive comparison of the currently available deep learning algorithms for 3D volumetric inner ear segmentation. In addition, we aimed to investigate the following questions:

(i) Is the training of the IE-Vnet on semi-manual, atlas-based pre-segmentations of inner ear TFS possible from a large cohort with comparatively little manual segmentation effort?
(ii) Is the IE-Vnet able to generalize across domain shift differences in MRI scanner hardware and sequence settings, or patient pathology without significant loss of segmentation accuracy, given appropriate augmentation techniques during training?

2. MATERIALS AND METHODS

2.1. Setting and Institutional Review Board Approval

This work was conducted at the interdisciplinary German Center for Vertigo and Balance Disorders (DSGZ) and the Neurology Department of the Munich University Hospital (LMU) between 2015 and 2019. This study used previously published datasets (10, 27, 30, 34, 35). Institutional Review Board approval was obtained before the initiation of the study (no. 094-10 and no. 641-15). All participants provided informed oral and written consent in accordance with the Declaration of Helsinki before inclusion in the study. The inclusion criterion was age between 18 and 80 years. The exclusion criteria were other (than vestibular) neurological or psychiatric disorders, as well as any MR-related contraindications (36), poor image quality, or missing MR sequences.

2.2. Datasets and Cohorts

The study included five different real-life datasets, denoted as D1–D5. Dataset 1 (D1, training dataset) was used to train the deep neural network model. Datasets 2–5 (D2–D5, test datasets) were used to investigate the model's out-of-sample performance due to MR scanner, MR sequence, or cohort and pathology. A detailed description of the domain differences between D1 and D2-5 is given in **Table 1**.

Abbreviations: ±, Standard deviation; 2D, Two-dimensional; 3D, Three-dimensional; ANTS, Advanced Normalization Toolkit; aSCC, anterior semi-circular canal; D1, Dataset 1, Training dataset; D2, Dataset 2, Test dataset; D3, Dataset 3, Test dataset; D4, Dataset 4, Test dataset; D5, Dataset 5, Test dataset; DL, Deep learning; ELH, Endolymphatic hydrops; ELS, Endolymphatic space; FLAIR, Fluid-attenuated inversion recovery; FH, Full-head; FHT, Full-head template; FOV, Field-of-view; GBCA, Gadolinium-based contrast agent; Gd, Gadolinium; GRAPPA, Generalized auto-calibrating partially parallel acquisition; HC, Healthy control; hSCC, horizontal semi-circular canal; IET, Inner ear template; IE-Vnet, Inner ear dedicated deep learning model based on a V-Net architecture; iMRI, Delayed intravenous gadolinium-enhanced MRI of the inner ear; iv, Intravenous; L, Left; MRI, Magnetic resonance imaging; n, Number; OTB, Optimal Template Building; PLS, Perlymphatic space; pSCC, posterior semi-circular canal; QC, Quality-control (led); R, Right; ROI, Region-of-interest; SCC, Semi-circular canal; SQ, Semi-quantitative; SPACE, Sampling perfection with application-optimized contrasts by using different flip angle evolutions; SyN, Symmetric Normalization; TFS, Total fluid space.

TABLE 1 | Domain differences between training (D1) and test (D2-D5) datasets.

	MR scanner	# Channels	ELH	Vestibulocochlear syndrome	Domain difference
D1	Skyra	20	Yes/No	Yes	No
D2	Skyra	20	No	No	ELH, pathology
D3	Skyra	20	Yes	Yes	No
D4	Verio	32	Unknown, but improbable	No	Scanner, coil, site, ELH, pathology
D5	Verio	32	Unknown, but possible	Yes	Scanner, coil, site

Test datasets with various properties were included to examine the robustness of the network's segmentation performance toward domain shift. This shift was caused either by changes in population (endolymphatic hydrops present or not, determined by an ELH grade ≥ 1; pathologies present or not), or by changes in the imaging hardware and sequence parameters (scanner model, number of channels in the head RF coil), or both.

2.2.1. Training Dataset D1

D1 included 358 ears of 179 consecutive patients (102 female= 56.9%; aged 19–80 years, mean age 52.2 ± 15.7 years) with peripheral vestibulocochlear syndromes that underwent iMRI for exclusion or verification of ELH (51 without ELH, 49 with unilateral ELH, 79 with bilateral ELH). Vestibulocochlear syndromes comprised Meniere's disease (n = 78), vestibular migraine (n = 69), acute unilateral vestibulopathy (n = 14), vestibular paroxysmia (n = 11), bilateral vestibulopathy (n = 5), and benign paroxysmal positional vertigo (n = 2). Patients were clinically diagnosed according to the respective international guidelines, such as the brny Society (www.jvr_web.org/ICVD.html or https://www.baranysociety.nl) when diagnosing vestibular migraine (37, 38), Menires disease (39), vestibular paroxysmia (40), bilateral vestibulopathy (41), acute unilateral vestibulopathy/vestibular neuritis (42) and benign paroxysmal positional vertigo (43). A detailed description of the diagnostic work-up of all cohorts can be found in the **Supplementary Material**.

2.2.2. Test Dataset D2 and D3

In comparison to D1, these test datasets have the same acquisition parameters (D2, D3) but differences in population (D2). **D2** included 20 ears of 10 consecutive Department of Neurology inpatients (7 female= 70%; aged 24–45 years, mean age 33.1 ± 6.7 years) without symptoms or underlying pathologies of the peripheral and central audio-vestibular system that underwent MRI with a contrast agent as part of their diagnostic workup and agreed to undergo iMRI sequences after 4 h without any indication of ELH. Patients were admitted into the clinic due to movement disorders (n = 3), epilepsy (n = 2), trigeminal neuralgia (n = 2), viral meningitis (n = 1), subdural hematoma (n = 1), and decompensated esophoria (n = 1). D2 underwent audio-vestibular testing confirmed the soundness of their peripheral end organs. **D3** included 20 ears of 10 consecutive patients (6 female= 60%; aged 20–58 years, mean age 37.8 ± 13.6 years) with peripheral vestibulocochlear syndromes that underwent iMRI for verification of ELH (7 with unilateral ELH, 3 with bilateral ELH). Pathologies comprehended patients with Meniere's disease (n = 3), vestibular migraine (n = 3), acute unilateral vestibulopathy (n = 2), vestibular paroxysmia (n = 1), and bilateral vestibulopathy (n = 1).

2.2.3. Test Dataset D4 and D5

In comparison to D1, these datasets differ regarding MR acquisition parameters (D4, D5) and population (D4). **D4** included 20 ears of 10 consecutive healthy controls (HC; 7 female= 70%; aged 25–52 years, mean age 36.6 ± 9.1 years). **D5** included 20 ears of 10 consecutive patients (4 female= 40%; aged 27–44 years, mean age 37.5 ± 5.6 years) with bilateral vestibulopathy. Measured MR sequences in D4 and D5 only distinguished between TFS within the entire inner ears bony labyrinth from the surrounding petrosal bone structure, but not between ELS and PLS within the TFS. The existence of an ELH cannot be excluded, but is unlikely in D4 and possible in D5.

2.3. MR Imaging Data Acquisition

2.3.1. Datasets D1-3

Four hours after intravenous injection of a standard dose (0.1 mmol/kg body weight) of Gadobutrol (Gadovist®, Bayer, Leverkusen, Germany), MR imaging data was acquired in a whole-body 3 Tesla MR scanner (Magnetom Skyra, Siemens Healthcare, Erlangen, Germany) with a 20-channel head coil. Head movements were minimalized in all three axes using a head positioning system for MRI (Crania Adult 01, Pearl Technology AG, Schlieren, Switzerland). A 3D-FLAIR (fluid-attenuated inversion recovery) sequence was used to differentiate ELS from PLS within TFS, and a spin-echo 3D-SPACE (three-dimensional sampling perfection with application-optimized contrasts by using different flip angle evolutions) sequence to delineate the TFS from the surrounding bone. ELH was classified on 3D-FLAIR images as enlarged negative-signal spaces within TFS, according to a previously reported convention (8, 10). The 3D-FLAIR had the following parameters: TE 134 ms, TR 6,000 ms, TI 2240 ms, FA 180°, FOV 160 × 160 mm^2, 36 slices, base resolution 320, averages 1, acceleration factor of 2 using a parallel imaging technique with a generalized auto-calibrating partially parallel acquisition (GRAPPA) algorithm, slice thickness 0.5 mm, 0.5 × 0.5 × 0.5 mm^3 spatial resolution.

The spin-echo 3D-SPACE sequence had the following parameters: TE 133 ms, TR 1000 ms, FA 100°, FOV 192 × 192 mm^2, 56 slices, base resolution 384, averages 4, acceleration factor of 2 using GRAPPA algorithm, 0.5 mm slice thickness, 0.5 × 0.5 × 0.5 mm^3 spatial resolution. Further structural sequences included a T2-weighted sequence (TE 89 ms, TR 4,540 ms, FOV 250 × 250 mm^2, 42 slices, base resolution 364, averages 1, acceleration factor of 2 using GRAPPA algorithm, slice thickness 3 mm, voxel size $0.7\times\ 0.7 \times 3\ mm^3$) and a T1-weighted magnetization-prepared rapid gradient echo (MP-RAGE) sequence with an isotropic spatial resolution of $1.0 \times 1.0 \times 1.0\ mm^3$ (TE 4.37 ms, TR 2,100 ms, FOV $256 \times 256\ mm^2$, 160 slices).

2.3.2. Datasets D4-5

MR imaging data were acquired in a whole-body 3.0 Tesla MR scanner (Magnetom Verio, Siemens Healthcare, Erlangen, Germany) with a 32-channel head coil. Head movements were minimalized in all three axes using a head positioning system for MRI (Crania Adult 01, Pearl Technology AG, Schlieren, Switzerland). A spin-echo 2D-SPACE sequence was used to delineate the bony labyrinth (TR 1,000 ms, TE 138 ms, FA 110°, FOV $180 \times 180\ mm^2$, 60 slices, base resolution 384, averages 2, slice thickness 0.5 mm, $0.5 \times 0.5 \times 0.5\ mm^3$ spatial resolution). Further structural sequences included a T2-weighted sequence (TE 94 ms, TR 4,000 ms, FOV $230 \times 230\ mm^2$, 40 slices, base resolution 364, averages 1, acceleration factor 2 using GRAPPA algorithm, slice thickness 3 mm, voxel size $0.7\times\ 0.7 \times 3\ mm^3$) and a T1-weighted magnetization-prepared rapid gradient echo (MP-RAGE) sequence with a field-of-view of 256 mm and an isotropic spatial resolution of $1.0\times\ 1.0 \times 1.0\ mm^3$ (TE 4.37 ms, TR 2,100 ms, 160 slices).

2.4. Creation of Ground Truth Using Atlas-Based Segmentation

The ground-truth (or gold standard) segmentation for D1-5 was created using the T2 and SPACE MRI volumes in a semi-manual process, with the assistance of automatic, atlas-based segmentation. 2D- or 3D-SPACE MRI volumes served as input to the IE-Vnet model. A flowchart of the (semi-)manual ground-truth segmentation can be viewed in **Figure 1**. **Figure 2** depicts an exemplary T2 volume along with a ground-truth segmentation mask. First, two custom templates and atlases were created from scratch, specifically for automated pre-segmentation of the inner ear. Then, registrations were performed using linear affine and non-linear Symmetric Normalization [SyN, (44)] as well as Optimal Template Building [OTB, (45)], which are part of the Advanced Normalization Toolkit (ANTs)[1]. Also, all subjects T1, T2 and FLAIR volumes were spatially co-aligned with the SPACE volume via intra-subject rigid registration.

The first atlas localized the inner ears inside full-head (FH) or limited FOV (field-of-view) MRI scans. To this end, a full-head template (FHT) was created from T2 volumes using ANTs OTB, and the inner ear structures' central location was annotated with a single landmark for each side, respectively. Finally, FHT plus annotations, i.e., the full-head atlas, were non-linearly registered to all subjects' volumes. Thus, left and right inner ears could be located in all participants's heads.

The second atlas enabled automatic pre-segmentation of the inner ear. Therefore, inner ear localization landmarks were transferred from the FH T2-FLAIR scans to the narrow FOV SPACE scans. Here, inner ears were cropped using a $4 \times 3 \times 2$ cm region-of-interest (ROI) that contained the entire inner ear

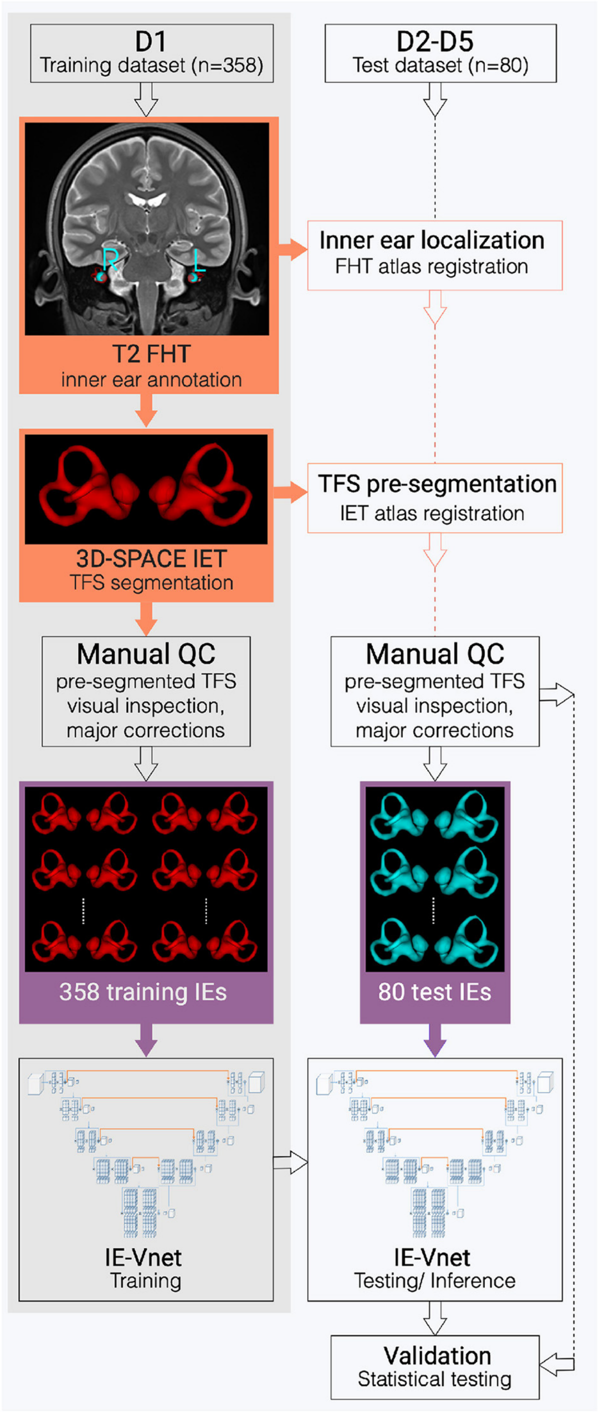

FIGURE 1 | Flowchart of the inner ear's auto-segmentation. Auto-segmentation of the inner ear (IE) involved data preparation and manual ground-truth annotation of the IEs total fluid space (TFS) masks in training (D1, grey shading) and test (D2-D5, white shading) datasets. First, pre-segmentations (orange boxes) were obtained in D1-D5 via a custom-built full-head template (FHT) and an inner-ear template (IET). Then, manual quality control (QC), followed by manual refinement of IE segmentations (purple boxes), trained and examined the IE-Vnet model. Finally, its predictions were validated under various forms of domain shift in the test datasets D2-D5 (cf. **Table 1**).

---

[1] ANTs open-source code and binaries: https://stnava.github.io/ANTs/.

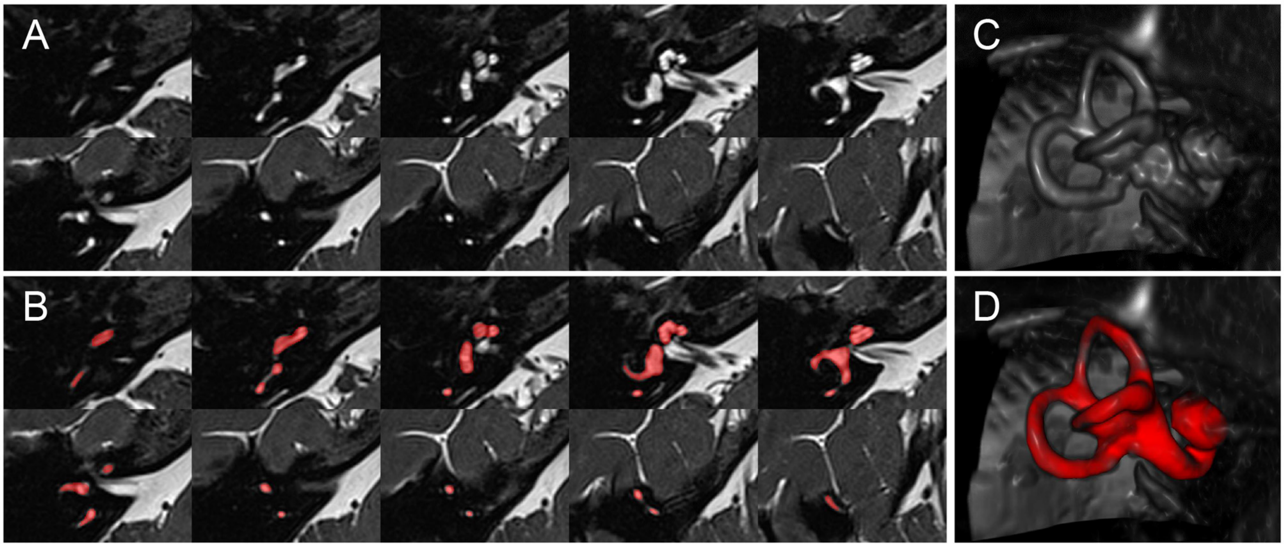

FIGURE 2 | Inner ear MR example case. Depiction of an exemplary SPACE volume along with its ground-truth segmentation masks. **(A)** Depiction of ten axial slices from the SPACE MRI sequence volume, through the right inner ear, from caudal to cranial, covering a range of 12.4 mm (~ 1.4 mm slice distance). **(B)** Like **(A)**, but with the manually segmented total fluid space (TFS) mask (colored in red). **(C)** Volume rendering of the right inner ear ROI, which serves as input to the IE-Vnet model. **(D)** Like **(C)**, but the manually segmented TFS surface overlaid in red.

structure and a sufficient margin of 5–10 mm to all sides to account for slight localization errors. Inside the ROI, SPACE voxel intensities were resampled at 0.2 mm isotropic resolution (i.e., 200 × 150 × 100 voxels). All ROI cubes were geometrically centered to the origin ($[0, 0, 0]$) coordinate. At the origin, right-sided inner ears were re-oriented onto the left inner ears through horizontal flipping. A single inner ear template (IET) using ANTs OTB was computed from this uni-directed set of inner ears. This template was annotated with manual segmentation of the total fluid space (TFS), first by intensity thresholding with Otsu's method (46), followed by manual refinement with various 3D mask editing tools "Segment Editor Module", mainly 3D brush, eraser, and scissor tool in 3D Slicer [2] (47).

All inner ears in training (D1) and testing (D2-5) were pre-segmented using two atlas registrations; first, an inner ear localization with the FHT, followed by TFS segmentation with the IET. Then, an automatic refinement step was performed post-registration by intersecting an Otsu-thresholded mask with a 0.5 mm dilated atlas mask to account for patient-wise shape- and intensity- variations. Despite this automatic refinement, every automatic segmentation needed to be quality-controlled (QC) and corrected for mistakes in an additional manual process. Two different QC and correction strategies were implemented in the training dataset (D1) and test datasets (D2–D5) to balance the amount of manual annotation effort and the TFS masks criticality. The automatic segmentation underwent a visual QC check in each of the 358 training inner ears (D1). Inner ear localization worked very robustly, without any inner ears being missed or mislocalized. In contrast, the atlas-based segmentation was not as robust, with severe mis-segmentations (e.g., partially incomplete or entirely missed semi-circular canals or cochlear turns) in 64 out of 358 training inner ear ROIs (17.9%). These were manually refined before network training, while the remaining 302 inner ears were used for training, even if minor visual errors in the atlas auto-segmentations were present. In contrast, atlas-segmentation in the test datasets (D2–D5) was not only visually inspected, but all 80 inner ears were thoroughly error-corrected and manually refined with the aforementioned 3D Slicer mask editing tools. Manual refinement of a single inner ear, for an experienced annotator familiar with the 3D Slicer user interface, took on the order of 5–15 min.

The pre-processing steps necessary for inner ear segmentation in new MRI volumes are limited to localizing the left and right inner ear. This can be achieved automatically using a full-head registration (performed in this work) and requires no manual interaction. Alternatively, the inner ears can also be manually localized using landmark annotation. Depending on the workstation hardware and registration parametrization, a fully automatic inner ear ROI localization can be performed in 1–2 min. However, a manual localization is much faster and requires two clicks, which can be performed in seconds.

2.5. IE-Vnet Neural Network Architecture and Training

2.5.1. Architecture and Loss Function

The deep learning architectures for volumetric 3D segmentation were based on a V-Net model (48), which is a variant of the 3D U-Net family of architectures (49). The basic idea of these fully convolutional architectures is to extract hierarchical image features using learnable convolutional filters at an increasingly

---

[2] 3D Slicer open-source code and binaries: https://www.slicer.org/.

coarse resolution and image representation. The down-sampling and up-sampling operations are achieved via pooling/un-pooling operations (49) or forward/transpose convolutions (48). In this work, the network was designed as a variant of a V-Net architecture, with four down-sampling levels, with $[16, 32, 64, 128, 256]$ 3D-convolutional filters at each level (kernel size: $3 \times 3 \times 3$ voxels), and with residual blocks spreading two convolutional layers each within each level. Each convolutional layer is followed by Instance Normalization (50), channel-wise random dropout ($p = 0.5$), and non-linear activation with Parametrized Rectified Linear Units (PReLU) (51). The loss function used for training was the Dice loss (48). The recently published cross-institutional and open-source deep learning framework "Medical Open Network for AI" (MONAI) (52)[3] was used to implement the network, pre-processing, augmentation and optimization. **Figure 3** visualizes the architecture.

2.5.2. Pre-processing and Augmentation Scheme

All volumes in D1–D5 were pre-processed with simple spatial padding to a volume size $[208, 160, 112]$, and intensity scaling to the range $[0 \ldots 1]$. The dataset D1 was split into 90% training data ($N = 161$ subjects, 322 inner ears) and 10% validation data ($N = 18$ subjects, 36 inner ears). Random image augmentation was used to enlarge the training set size artificially, since fully convolutional segmentation networks require large amounts of training data for robust and accurate prediction. Augmentation steps included random contrast adjustment (gamma range: $[0.3, \ldots 1.5]$, probability of occurrence $p_o = 0.9$), addition of random Gaussian noise ($\mu = 0, \sigma = 1.0, p_o = 0.5$), random horizontal flipping ($p_o = 0.5$), and random affine-elastic transformation ($p_o = 0.75$; 3D translation: 15% of ROI dimensions; 3D rotation: 20°; scaling: ±15%; grid deformation: magnitude range $[5 \ldots 100]$, sigma range: $[5 \ldots 8]$).

2.5.3. Optimization

Adam stochastic optimization algorithm (53) at a learning rate of $3e - 4$ was used to train the network weights.

2.6. Validation Parameters

Segmentation accuracy was quantified using spatial overlap indexes, such as Dice overlap coefficient (54, 55), Hausdorff distance (56, 57), and mean surface distance (58).

Localized performance issues within the inner ear were visually assessed using a semi-quantitative five-point Likert-type response scale (59, 60). Therefore, the level of agreement in the segmentation outcome of the cochlea, sacculus, utriculus, the anterior semi-circular canal (aSCC), posterior SCC (pSCC), and horizontal SCC (hSCC), respectively, were quantified using the following categories: 5-Strongly agree (no structure missing, no false-positive segmentation, clean contour), 4-Agree (no structure missing, no false-positive segmentation, ≤ 1 unclean contour), 3-Neither agree nor disagree, (no structure missing, ≤ 1 false-positive segmentation, > 1 unclean contour), 2-Disagree (≤ 1 missing structure, > 1 false-positive segmentation, clean or unclean contour), and 1-Strongly disagree (> 1 missing structure, > 1 false-positive segmentation, clean or unclean contour).

2.7. Statistical Testing

Normal distribution of Dice overlap measures across datasets was determined using Shapiro and Wilk testing (61) and homoskedastic across datasets was determined using Bartlett and Fowler testing (62) before statistical analysis. Consequently non-parametric testing was further applied. Given their ordinal nature (63), non-parametric testing was also applied to the Likert-type expert ratings.

Statistical hypothesis tests were then performed to investigate two questions: First, the sidedness of the network was checked, i.e., whether there was a statistically significant difference in segmentation accuracy (Dice overlap coefficients, Likert ratings) between left and right inner ears. To this end, a non-parametric Wilcoxon signed-rank test was applied to the Dice, and Likert outcomes, paired between the left and right inner ears of each test subject. Second, the null-hypothesis was verified, i.e., that the Dice overlap median outcomes of the four test datasets D2-D5 were equal. The purpose of this was to investigate the generalization capability of the network, i.e., whether a shift in population or imaging parameters or both (cf. **Table 1**) led to a measurable deterioration of segmentation performance. To this end, a non-parametric Kruskal-Wallis test for independent samples was employed with the concatenated left and right Dice and Likert outcomes as the dependent variable and the test set indicator (D2–D5) as the independent variable. *Post-hoc*, a non-parametric tests [Mann-Whitney U (64)] between Dice and Likert outcomes was performed in all pairs of test datasets D2–D5. All statistical analyses were applied using the open-source libraries Scipy Stats (65), Statsmodels (66), and Pingouin (67). Values are presented as means ± standard deviations.

3. RESULTS

Results are presented separately for the training and testing stage, followed by statistical comparisons.

3.1. Training Results

Figure 4 shows the evolution of Dice loss for model training and the corresponding Dice metric on the withheld validation set. The maximum validation Dice overlap metric of 0.944 was obtained at epoch 113, and this best-performing model was saved for forwarding inference on the withheld test datasets D2-D5 (cf. Sections 3.2, 3.3), as well as for open-source dissemination. Notably, the loss curve showed a steady convergence toward the minimum obtained at the final iteration. Simultaneously, the validation metric showed a steady convergence without any signs of overfitting throughout the entire optimization procedure. The total training time took around 11 h on a consumer-level workstation (AMD Ryzen Threadripper 1950X 8-core CPU, 32 GB RAM, Nvidia 1080 Ti GPU).

3.2. Test Results

The total inference time for 80 samples was 15.2 s, i.e., on average 0.19 s ± 0.047 s for each cropped and up-sampled

---

[3] Project MONAI documentation and code: https://monai.io/.

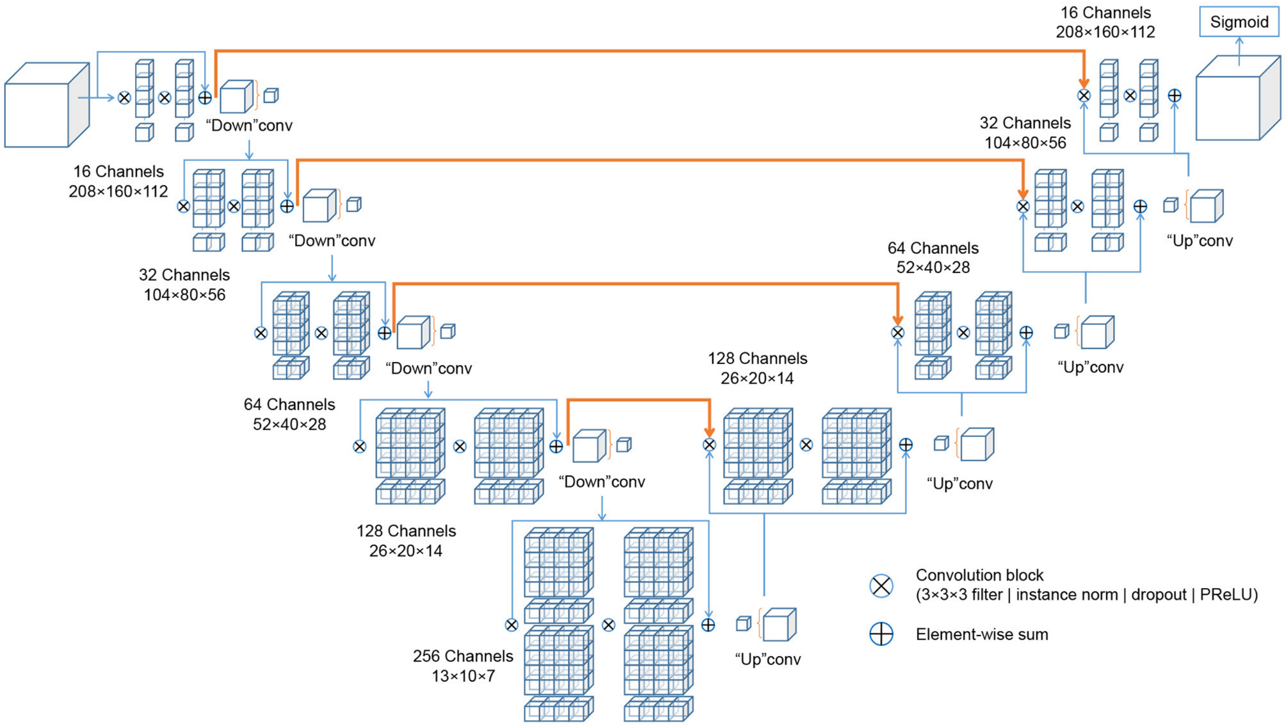

FIGURE 3 | Schematic representation of the IE-Vnet architecture. The IE-Vnet architecture is designed as a variant of a V-Net architecture with four down-sampling levels, [16, 32, 64, 128, 256] 3D-convolutional filters at each level (kernel size: 3 × 3 × 3 voxels), and with residual blocks spreading two convolutional layers each within each level. Each convolutional layer is followed by Instance Normalization (50), channel-wise random dropout ($p = 0.5$), and non-linear activation with Parametrized Rectified Linear Units (PReLU) (51). The convolutions aim to extract features from the data and, at the end of each stage, reduce its resolution by using appropriate stride. The left part of the network consists of a compression path, while the right part decompresses the signal until its original size is reached. A more detailed description can be found in Milletari et al. (48).

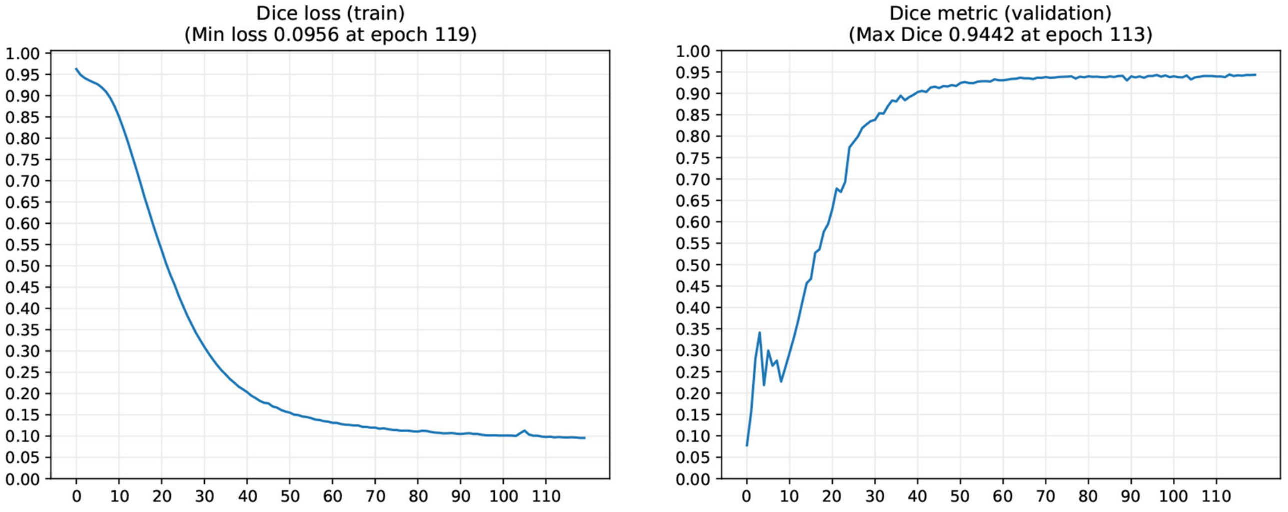

FIGURE 4 | IE-Vnet training loss and validation metrics. IE-Vnet training loss **(left graphic)** and validation **(right graphic)** metrics were observed during 120 epochs of training. In addition, the maximum validation Dice overlap metric of 0.944 was obtained at epoch 113. Notably, the loss curve showed a steady convergence toward the minimum obtained at the final iteration. At the same time, the validation metric showed a steady convergence without any signs of overfitting throughout the entire optimization procedure.

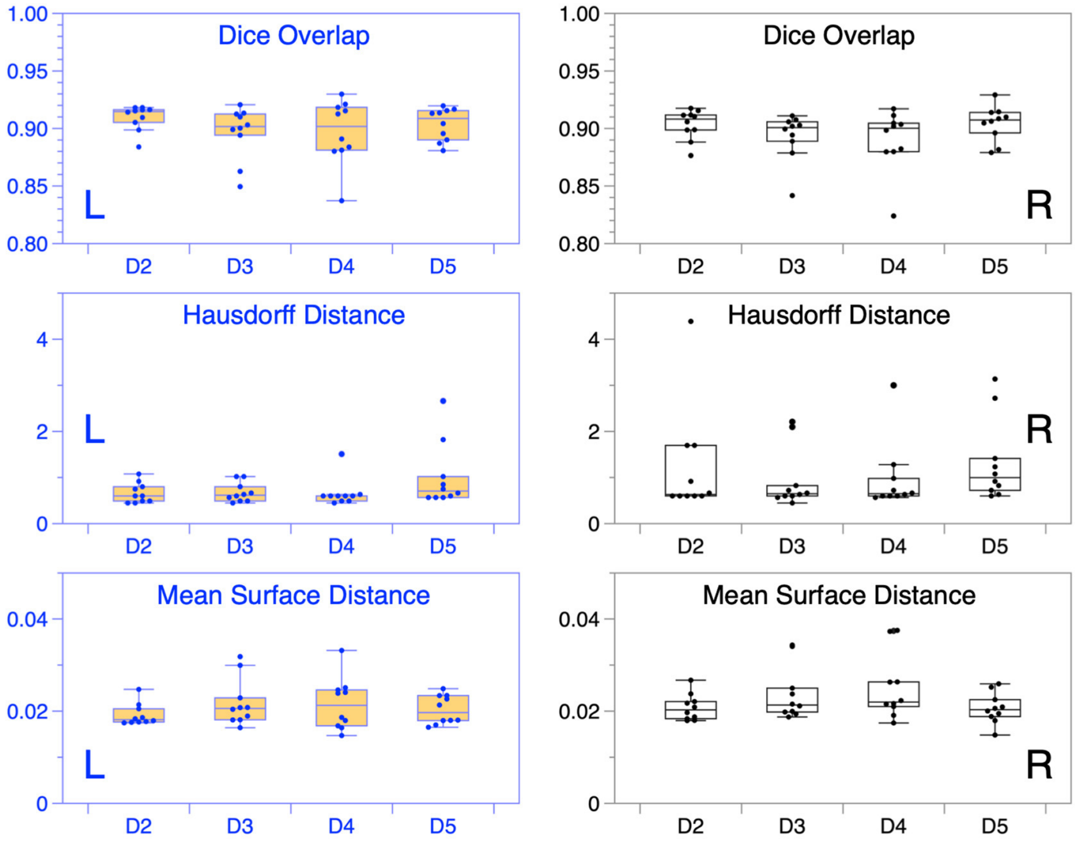

FIGURE 5 | IE-Vnet segmentation quality control. Alignment between ground-truth and prediction in the four test datasets D2-D5 (20 IE each, 80 IE altogether) was measured by the quantitative metrics of Dice overlap coefficient **(upper row)**, Hausdorff maximum surface distance **(middle row)**, and average surface distance **(lower row)**. Results of left ears (blue) are depicted on the left (L), while results of the right ears (black) are shown on the right (R). In most cases across D2-5, congruence between model prediction and manual ground-truth was high.

inner ear volume at 0.2 mm isotropic resolution (i.e., 200 × 150 × 100 voxels). The agreement of TFS segmentation between manual ground-truth and the networks prediction was quantified by three metrics: Dice overlap coefficient "Dice", maximum Hausdorff surface distance "HDmax", mean surface distance "SDmean", along with five-point Likert-type response scale "LS". These metrics are illustrated with boxplots in **Figure 5**, and summarized numerically in **Table 2**.

Several points are noteworthy. On average, across all left and right inner ears and in all four test datasets, the Dice overlap coefficient showed a mean value of 0.900 ± 0.020, the Hausdorff maximum surface distance a mean value of 0.93 ± 0.71 mm), and the mean surface distance a mean value of 0.022 ± 0.005 mm). Thus, the segmentation performance seems quantitatively consistent across the test datasets D2–D5 (cf. **Figure 5** and **Table 2A**), which was further confirmed by statistical analyses (cf. Section 3.3). The mean Likert scales of the inner ear structures were altogether consistently high (4.913 ± 0.337) across both inner ears and in all four test datasets. However, depending on the location, shape and intricacy of the separate inner ear structures, Likert scores consistently differed in performance success (cf. **Table 2B**) with the most robust results in the vestibulum (sacculus: 4.988 ± 0.112, utriculus: 5.000 ± 0.000), intermediate results in cochlea (4.925 ± 0.265) and posterior SCC (4.888 ± 0.477), and least robust results in the anterior (4.813 ± 0.576) and horizontal SCC (4.863 ± 0.590). The mentioned pattern can be verified in the several outliers, in particular in the Hausdorff distance values in both right and left inner ears. Two cases with outlier Hausdorff distances on the order on 3 mm and above are presented in **Figures 6C,D**. Visual inspection reveals that these comparatively high surface errors stem either from challenging cases, which were also difficult in manual ground truth segmentation in the horizontal and posterior SCC (panel D), or minor prediction artifacts in the anterior SCC such as isolated blobs, rather than gross mis-segmentations (panel C). Such artifacts could be filtered away through minor post-processing like connected-components filters. In most cases, it is noteworthy that surface congruence between model prediction and manual ground truth was very high, with mean surface distances on the order on 0.02 mm, and with very few cases of surface distances above 0.03 mm. This is also reflected in the form of visual agreement

TABLE 2 | IE-Vnet segmentation results on four test datasets D2-D5 (20 inner ears each) compared to manual ground-truth.

Dataset	D2		D3		D4		D5	
	Mean	SD	Mean	SD	Mean	SD	Mean	SD
(A) Accuracy								
Dice	0.906	0.012	0.895	0.021	0.904	0.014	0.894	0.026
HDmax	0.949	0.862	0.804	0.476	1.170	0.774	0.811	0.565
SDmean	0.020	0.003	0.023	0.005	0.021	0.003	0.023	0.006
(B) Performance								
Cochlea	4.950	0.224	4.900	0.308	4.900	0.308	0.950	0.224
Sacculus	5.000	0.000	5.000	0.000	4.950	0.224	5.000	0.000
Utriculus	5.000	0.000	5.000	0.000	5.000	0.000	5.000	0.000
aSCC	4.800	0.616	4.800	0.616	4.900	0.308	4.750	0.716
pSCC	4.900	0.447	4.900	0.447	4.850	0.671	4.900	0.308
hSCC	4.950	0.224	4.850	0.671	4.850	0.671	4.800	0.696

Segmentation accuracy (A) was measured by the quantitative metrics of Dice overlap coefficient ("Dice"), Hausdorff maximum surface distance ("HDmax," in [mm]), and average surface distance ("SDmean," in [mm]). Localized performance (B) issues within the inner ear were assessed using a semi-quantitative five-point Likert-type response scale for the cochlea, sacculus, utriculus, the anterior semi-circular canal (aSCC), posterior SCC (pSCC), and horizontal SCC (hSCC) respectively. A detailed description of the used categories can be found in Section 2.6.

between ground truth and prediction, as visible in two cases in **Figures 6A,B**.

3.3. Impact of Side and Domain Shift

We investigated whether the IE-Vnet segmentation model is affected by a side bias and whether its segmentation performance is affected by variance of the population or imaging parameters (cf. **Table 1**). The first test was performed in a paired manner between Dice overlap measures in the left and right inner ears for all 40 test subjects (D2–D5). This analysis yielded no significant difference between sides (two-sided Wilcoxon signed-rank test: $p = 0.061$; normality rejected, Shapiro-Wilk test: $p < 0.001$). Further, we examined whether differences in image acquisition led to domain shifts across the four test datasets that impacted our model's segmentation performance. This test yielded no significant difference between Dice overlap outcomes across datasets D2–D5 (Kruskal-Wallis test: $p = 0.146$; homoscedasticity rejected, Bartlett test: $p < 0.01$). Further, the pair-wise *post-hoc* tests between datasets D2-D5 yielded no significant differences in Dice overlaps (Mann-Whitney U, all BH-FDR corrected p-values at $p > 0.20$). Equivalent results were obtained for qualitative expert ratings of segmentation results upon visual inspection. No significant differences in Likert scale ratings were found across any of the rated regions (cochlea, sacculus, utriculus, anterior, posterior, and horizontal SCC), neither between sides (Wilcoxon signed-rank test, all p-values above $p = 0.162$), nor between group-medians across D2–D5 (Kruskal-Wallis test: all p-values above $p = 0.392$), nor pair-wise across D2–D5 (*post-hoc*, Mann-Whitney U, all BH-FDR corrected p-values at $p > 0.860$).

4. DISCUSSION

The current work proposes a novel inner ear TFS segmentation approach using a dedicated deep learning (DL) model based on a V-Net architecture (IE-Vnet). A variant of a V-Net deep convolutional neural network architecture was trained to perform segmentation inference on inner ear volumes. During training, various image augmentation techniques were used to account for expected variations in out-of-sample datasets, such as image contrast and intensity, noise, or affine/deformable distortions of geometry. The training dataset was constructed through atlas-based pre-segmentations with comparatively minor manual correction and segmentation effort (aim i). As a result, the inferred IE-Vnet segmentations on four testing datasets were free from side bias and robust to various domain shift sources, such as MRI scanner hardware and sequences and patient pathology (aim ii). Compared to atlas-based segmentation, the novel model was roughly 2,000 times faster and managed to avoid gross mis-segmentations in more than 20% of test cases, especially in high-volume datasets. In the following, IE-Vnet, compared to currently available neural network algorithms used for MR inner ear segmentation, its technical and clinical implications, methodical limitations, and future work will be discussed.

4.1. Technical Implications

4.1.1. Accuracy of Segmentation

The average Dice values during testing (0.900) are noticeably lower when compared to training (0.944). This effect can be attributed to the fact that the TFS ground-truth regions were manually refined in every test sample with considerably more effort than the training set. Nevertheless, these indicate accurate segmentation (31), especially in structures like the semi-circular canals, where the Dice metric is known to degrade quickly for small regions or regions with fine-grained protrusions (68). Furthermore, the overall low surface distance of 0.02 mm can be attributed to the fact that the volumes were bi-cubically up-sampled to a resolution of 0.2 mm before inference. Therefore,

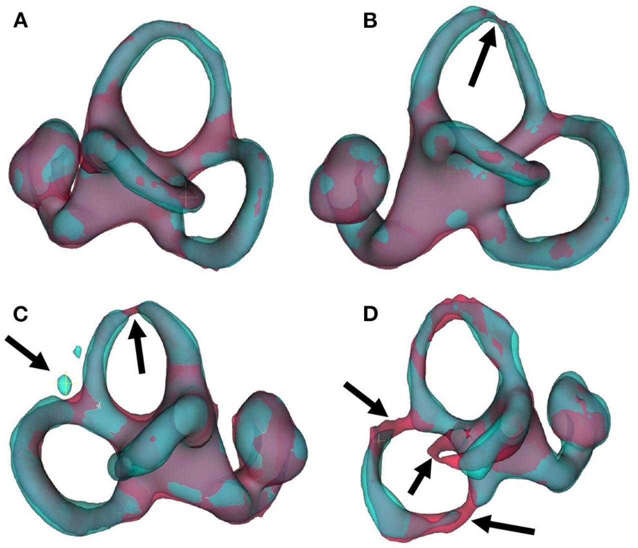

FIGURE 6 | IE-Vnet 3D segmentation predictions visualized. Visualization of 3D segmentations predicted by the IE-Vnet model (color: cyan), overlaid onto manual ground-truth 3D surface contours (color: red). **(A)** Exemplary case of a highly accurate segmentation Dice > 0.92, Hausdorff maximum surface distance < 0.5 mm, mean surface distance < 0.02 mm, 5/5 Likert scale (LS) for cochlea, sacculus, utriculus, anterior, posterior and horizontal SCC. Manual ground-truth and prediction are in high agreement over the entire surface. **(B)** Another example of a highly accurate segmentation. The arrow denotes a location with hypo-intense semi-circular canal voxels, as marked manually in red, and the model prediction predicts a thinning at the same location. LS was 5/5 for cochlea, sacculus, utriculus, anterior, posterior and horizontal SCC. **(C)** An exemplary case of an overall accurate segmentation, but with a high Hausdorff surface distance of > 4 mm. LS was 5/5 for cochlea, sacculus, utriculus, posterior and horizontal SCC, and 2/5 for anterior SCC. Visual inspection reveals two isolated blobs, which could be removed with simple post-processing, such as connected components analysis and removal of small islands. **(D)** A failure case. Notably, manual ground-truth creation in this sample was challenging as well. LS was 5/5 for utriculus and anterior SCC, 4/5 for cochlea and sacculus, 2/5 for horizontal SCC, and 1/5 for posterior SCC. Low-contrast and high noise in SPACE sequences, with further potential challenges like motion artifacts, can lead to irregular ground-truth contours (left arrow) or unusually thin semi-circular canal segments (middle and right arrow). In such cases, model predictions may result in in-contiguous semi-circular canals and noisy surface contours.

the manual ground-truths predicted outer surfaces are smooth and consistent even in the presence of fine-grained details.

4.1.2. Generalization

The validation metric showed a steady convergence without any signs of overfitting throughout the entire optimization procedure that points to a well-parameterized network and data augmentation scheme. Furthermore, the results from our statistical analyses on Dice overlap in both inner ears imply the models freedom from side bias. Further, Dice overlap comparisons (group- and pair-wise) across the four testing datasets show no measurable difference in segmentation performance, indicating that the trained network is robust to variations in scanner hardware, image sequence parameters, and population characteristics. When discussing generalization, it is important to also consider whether quantitative metrics are sufficient to obtain trustworthy and interpretable results. A recent study (69) on chest X-ray classification for computer-aided diagnosis of COVID-19 cases has shown that it is vital to incorporate expert validation into the validation of results. Otherwise, it is possible that AI models learn to classify disease statuses based on confounding factors, rather than based on true pathology image content. In particular, image segmentation suffers less from the danger of spurious correlations than image classification: the segmentation output can be overlaid with the source image, and the model predictions become inherently interpretable. However, apart from quantitative metrics like Dice overlap score, or Hausdorff surface distance, a model validation can benefit from additional, expert-based qualitative ratings of the segmentation result. Hence, a differentiated Likert scale rating for the different inner ear structures (cochlea, sacculus, utriculus, anterior, posterior and horizontal semi-circular canal) was incorporated and obtained further insight into the model's performance. In particular, a performance pattern became evident in which, in decreasing order, the most robust results were found in the vestibulum (sacculus, utriculus), while cochlea and posterior SCC performed moderately well. Horizontal SCC and anterior SCC were most susceptible to segmentation errors. Notably, the lack of statistically significant differences in Likert ratings confirms that our model generalizes well. Ideally, these results should be corroborated in further prospective studies and larger cohorts.

4.1.3. Inference Speed Compared to Atlas

On average, the segmentation of a single volume with IE-Vnet took 0.19 ± 0.047 s, including volume loading and pre-processing, and 0.093 s for inference alone. The average segmentation time for inner ears was 377.0 ± 36.9 s using deformable registration. In total, the segmentation was about 2,000 times faster than a state-of-the-art atlas-based method. However, atlas registration is computed on the CPU, while the inference is fully GPU accelerated; hence the comparison is not entirely fair. It is worth noting that GPU-accelerated deformable registration libraries were introduced recently with speedups in the order of 10–100 times (70). Moreover, deep models for deformable (71) and diffeomorphic (72) image registration were recently proposed, allowing for registration times comparable to those of our model. However, deep models for registration are trained with dataset sizes in the order of a few thousand sample volumes (71, 72). Furthermore, atlas-based registration was less robust than IE-Vnet segmentation, as all test dataset volumes required manual correction after atlas pre-segmentation. Hence, our IE-Vnet model was not only trained on TFS contours obtained from registration. Instead, our segmentation model learned patient-wise adaptations, including individual threshold-based refinements and entire manual corrections of atlas auto-segmentations. Patient-specific prediction of the TFS contour, along with the fast inference in the order of milliseconds, makes deep convolutional network models like IE-Vnet attractive for large-scale studies in clinical and neuroscientific imaging-based studies of the inner ear.

4.1.4. Robustness Compared to Atlas

Atlas-based auto-segmentation in our datasets led to severe mis-segmentations (e.g., incomplete or missing semi-circular canals or cochlear turns), which occurred in 17.9% of cases in the training dataset (D1) and 22% of all cases in the test datasets (D2-5), and almost all cases in D2-5 required minor manual corrections along the entire TFS surface. Therefore, the actual speedup is probably much higher regarding automated post-processing or manual refinement steps necessary to fix atlas segmentation failures. The exact reason for the high rate of atlas mis-segmentations is unclear. It cannot be excluded that a better parameterization of the deformable registration could improve the success ratio. As mentioned, the very thin and, at times, low-contrast semi-circular canals would remain a challenge for atlas registration.

4.2. Comparison to Currently Available Neural Network Algorithms for MR Inner Ear Segmentation

In recent years, deep learning has revolutionized medical image analysis, particularly segmentation (73). Among an ever-growing number of architectures and approaches proposed for volumetric segmentation, two of the most popular and successful methods (74, 75) are 3D U-Net (49) and the previously proposed V-Net (48). In addition, the latest published suggestions for inner ear segmentation can also be seen in this development- whether for CT (76–78) or MRI (32, 33). In the following, currently available neural network algorithms used for MR inner ear (IE) segmentation will be compared (see **Table 3** for an overview).

To the best of our knowledge, there are two machine learning MR IE segmentation proposals to date. First, Cho et al. (32) developed an automated measurement of 2D cochlea and vestibulum hydrops ratio from iMRI using CNN-based segmentation. Its primary difference is its usage of 2D data and focused usability on ELH area ratios in cochlea and vestibule. This tool should prove helpful to make ELH classifications (4, 5, 8, 9) more objective and comparable for clinical radiologists during the diagnostic assessment. For research purposes, ELH classification and 2D- or 3D- quantification methods were reliable and valuable for diagnosing endolymphatic hydrops (25). However, the reliability increases from ELH classification to 2D- and again to 3D-quantification methods (10). A model for complete 3D segmentation of TFS, including semi-circular canals (SCC), not only enables 3D volumetric analyses but gives it a substantially wider application area, e.g., IE surgical planning.

Second, Vaidyanathan et al. (33) recently suggested a fully automated segmentation of the inner ears TFS based on deep learning similar to our current approach. There are many overlaps in methodology and application, e.g., a similar network architecture. In the following, it will be referred to as IE-Unet. Compared to IE-Vnet, IE-Unet does not need to localize the inner ears in a separate pre-processing step. On the other hand, IE-Vnet operates at a more than twice higher resolution (0.2 mm isotropic vs. 0.45 mm), which leads to smoother surface boundaries of the output segmentation and can better deal with partial volume effects due to low voxel resolution in MRI. Notably, both solutions follow a similar approach to the same problem (IE MR TFS segmentation), which highlights their relevance and value compared to the method of Cho et al., whose usability is limited to the hydrops ratio in cochlea and vestibulum. Most importantly, though, both IE-Vnet and IE-Unet are highly complementary, making both trained models highly valuable. Therefore, we are choosing to publish our pre-trained model and accompanying code for training and inference open-source replication in other centers and alleviate similar studies in the community.

4.3. Clinical Implications

Deep learning models for medical image analysis have reached a maturity (74) that makes them relevant for further clinical and research-based investigations of the inner ear in the neuro-otological and vestibular domain. Once released, the proposed inner ear TFS segmentation approach using a dedicated deep learning (DL) model based on a V-Net architecture (IE-Vnet) has the potential to become a core tool for high-volume trans-institutional studies in vestibulocochlear research, such as on the endolymphatic hydrops (ELH).

IE-Vnet bridges the current gap existing for available automatic 3D ELS quantification methods. In particular, its input can be seamlessly combined with a previously published open-source pipeline for automatic iMRI ELS segmentation (27) via the TOMAAT module (81) in 3DSlicer (82).

4.4. Limitations and Future Work

There are methodical limitations in the current study that need to be considered in interpreting the data. One limitation of IE-Vnet in its current form is its reliance on a pre-localization and cropping of a cubical inner ear ROI obtained via deformable registration of the FHT and a transfer of the inner ear annotations. Their computational time was not considered in the discussion since both IE-Vnet, and the IET atlas-segmentation assume a previous localization and ROI cropping of the inner ear. The pre-processing steps are limited to localizing the left and right inner ear in the present work. This can be achieved fully automatically using a full-head registration and requires no manual interaction (other than, e.g., a post-registration visual inspection of whether the cropped ROI indeed contains the inner ear). In the current study, inner ear localization was successful for all 100% of inner ears. This can be achieved fully automatically using a full-head registration and requires no manual interaction (other than e.g., a post-registration visual inspection whether the cropped ROI indeed contains the inner ear). In this study, inner ear localization was successful for all 100% of inner ears. Given that IE-Vnet is trained to be robust toward a localization uncertainty of ∼1 cm (cf. augmentations in Section 2.5.2) this registration can be parametrized at a reasonably low resolution (e.g., deformation fields at 5 mm resolution). Consequently, in our study, inner ear localization via deformable registration was comparatively fast and took 25 s for both inner ears of each subject on a commodity laptop with 4a CPU. Alternatively, the inner ears can also be manually localized using landmark annotation. Depending on the workstation hardware and registration parametrization, a

TABLE 3 | Overview of MR IE deep learning segmentation algorithms in comparison.

	IE-Vnet	**IE-Unet**	**INHEARIT**
Machine learning technique	Deep learning	Deep learning	Deep learning
Network structure	3D Vnet (48)	3D Unet (49)	2D CNN based on VGG-19 (79)
Input	T2-weighted sequences	T2-weighted sequences	Hydrops-Mi2 (80)
Output	3D TFS segmentation	3D TFS segmentation	2D hydrops ratio
Output resolution	0.2 x 0.2 x 0.2 mm^3	0.45 x 0.45 x 0.45 mm^3	0.5 x 0.5 mm^2
(A) Training and testing parameters			
Ground truth	Semi-manual atlas-based segmentation	Manual segmentation	Manual segmentation
Training dataset	**Mono-centric (n=179)**	**Mono-centric (n=944)**	**Mono-centric (n=124)**
Features	*3T, multi-scanner, multi-scale*	*1.5T, 3T, multi-vendor, multi-scale*	*3T, 1 scanner, 1 scale*
Participants	*Vestibular pathologies and HC*	*IE pathologies*	*MD, VM, VN*
Test dataset	**Mono-centric (n=80)**	**Multi-(n=3)-centric (n=276)**	***5-fold cross validation of Training dataset***
Features	*3T, multi-scanner, multi-scale*	*1.5T, 3T, multi-vendor, multi-scale*	
Participants	*Vestibular pathologies and HC*	*IE pathologies*	*see above*
(B) Model performance			
Accuracy (Dice)	0.90 ± 0.02	0.87 (CI 0.87-0.88)	0.83 ± 0.04
Robustness	**100% in test sets D2-5**	**98.3% in test centers B-D**	**n.r.**
To artifacts	*n.a.*	*Yes*	*n.r.*
To outliers	*Yes*	*Yes*	*n.r.*
To noise	*Yes*	*Yes*	*n.r.*
Speed (localization/segmentation)	25s / 0.19 s	n.r. / 6.5 s	n.r. / within 1 s
Ability to segment diseased IE	Yes	Yes	Yes
Full automatization	Yes	Yes	Yes
Manual intervention needed	IE localization	Data preparation	No
Data availability	No	No	No
Model availability	Yes	No	No
Source availability	Yes	No	No

In the following the current study is referred to as "IE-Vnet." The approach of Vaidyanathan et al. (33) is referred to as "IE-Unet." Cho et al. (32) called their approach "INHEARIT" and are referred to as such. INHEARIT offers an automatic 2D area ELH (endolymphatic hydrops) ratio segmentation customized to the needs of a clinical radiologist, while IE-Vnet and IE-Unet enable 3D volumetric TFS segmentation with broad usability. The comparison considers a) parameters of the training and testing of the models, as well as their b) performance. IE-Vnet and Unet represent a similar approach to the same problem and can be complementary. However, while Unet offers a large dataset, IE-Vnet operates at a more than twice higher resolution, and its pre-trained model and accompanying codebase will be published open-source. CI, confidence interval 95%; ELH, Endolymphatic hydrops; HC, Healthy controls; Hydrops-Mi2, HYbriD of Reversed image Of Positive endolymph signal and native image of positive perilymph Signal- Multiplied with heavily T2-weighted MR cisternography; IDL, idiopathic hearing loss; IE, inner ear; INHEARIT, INner ear Hydrops Estimation via ARtificial InTelligence; MD, Morbus Mnire; MRC, MR cisternography; n.a., not analyzed; n.r., not reported; TFS, Total fluid space; VM, Vestibular migraine; VN, Vestibular neuritis.

fully automatic inner ear ROI localization could be performed in 1–2 min. A manual localization is much faster and requires two clicks, which can be performed in the order of seconds. However, it would be attractive to incorporate this step into the deep learning architecture itself, either via a cascaded setup of two networks (83), one for ROI localization and one for segmentation (IE-Vnet), or via a sliding-window inference approach (84). Both approaches are exciting avenues for future work. Another issue is that rare cases with strong artifacts can still lead to mis-segmentations (e.g., **Figure 6D**). However, such cases are statistically rare (long-tail problem) and challenging to solve. Instead, prior knowledge of the shape and topology of the inner ears TFS could be incorporated into the regularization model, e.g., through statistical shape models (85, 86).

5. CONCLUSION

The current work proposes a novel volumetric MR image segmentation approach for the inner ears total fluid space (TFS) using a dedicated deep learning (DL) model based on V-Net architecture (IE-Vnet). IE-Vnet demonstrated high accuracy, speedy prediction times, and robustness toward domain shifts. Furthermore, its output can be seamlessly combined with a previously published open-source pipeline for automatic iMRI ELS segmentation. Taken together, IE-Vnet has the potential to become a core tool for high-volume trans-institutional studies of the inner ear in vestibular research and will also be released as a free and open-source toolkit.

DATA AVAILABILITY STATEMENT

The original contributions presented in the study are included in the article's **Supplementary Material**, further inquiries can be directed to the corresponding authors.

ETHICS STATEMENT

The studies involving human participants were reviewed and approved by Ethics Commission of the medical faculty of the Ludwig-Maximilians-Universität, Munich, Germany. The patients/participants provided their written informed consent to participate in this study.

AUTHOR CONTRIBUTIONS

S-AA and JF: conception, design of the study, analysis of the data, drafting the manuscript, and providing funding. GV: acquisition and analysis of the data. MD: conception and design of the study, drafting the manuscript, and providing funding. VK: conception, design of the study, acquisition, analysis of the data, drafting the manuscript, and providing funding. All authors contributed to the article and approved the submitted version.

FUNDING

This work was partially funded by the German Foundation of Neurology (Deutsche Stiftung Neurologie, DSN), Verein zur Förderung von Wissenschaft und Forschung an der Medizinischen Fakultät der LMU (Association for the Promotion of Science and Research at the LMU Medical Faculty), and the German Federal Ministry of Education and Research (BMBF) via the German Center for Vertigo and Balance Disorders (DSGZ, Grant No. 01 EO 0901).

ACKNOWLEDGMENTS

We thank B. Ertl-Wagner and O. Dietrich for insightful discussions and their unwavering support during this project, and K. Göttlinger for copy-editing the script.

SUPPLEMENTARY MATERIAL

The Supplementary Material for this article can be found online at: https://www.frontiersin.org/articles/10.3389/fneur.2022.663200/full#supplementary-material

Datasets D1-5: Measurement of the Auditory, Semicircular Canal, and Otolith Functions

Diagnostic work-up included a careful neurological (e.g., history-taking, clinical examination), and neuro-orthoptic assessment with, e.g., Frenzel goggles, fundus photography, adjustments of the subjective visual vertical (SVV), video-oculography (VOG) during caloric stimulation and head-impulse test (HIT), as well as pure tone audiometry (PTA). A tilt of the SVV is a sensitive sign of a graviceptive vestibular tone imbalance. SVV was assessed when sitting in an upright position in front of a half-spherical dome with the head fixed on a chin rest (87). A mean deviation of > 2.5 from the true vertical was considered a pathological tilt of SVV (87). The impairment of vestibulo-ocular reflex (VOR) in higher frequencies was measured by using high-frame-rate VOG with EyeSeeCam ((88), EyeSeeTech, Munich, Germany). A median gain during head impulses < 0.6 (eye velocity in °/s divided by head velocity in °/s) was considered a pathological VOR (89). Furthermore, horizontal semicircular canal responsiveness in lower frequencies was assessed by caloric testing with VOG. This was done for both ears with 30°C cold and 44° C warm water. Vestibular paresis was defined as >25% asymmetry between the right- and left-sided responses (90).

REFERENCES

1. Strupp M, Brandt T, Dieterich M. *Vertigo and Dizziness: Common Complaints. 3rd Edn*. London: Springer (2022).
2. Brandt T, Dieterich M. The dizzy patient: don't forget disorders of the central vestibular system. *Nat Rev Neurol*. (2017) 13:352–62. doi: 10.1038/nrneurol.2017.58
3. Pyykkö I, Zou J, Gürkov R, Naganawa S, Nakashima T. Imaging of temporal bone. In: Lea J, Pothier D, editors. *Advances in Oto-Rhino-Laryngology, vol. 82*. S. Karger AG (2019). p. 12–31. Available online at: https://www.karger.com/Article/FullText/490268.
4. Nakashima T, Naganawa S, Pyykko I, Gibson WPR, Sone M, Nakata S, et al. Grading of endolymphatic hydrops using magnetic resonance imaging. *Acta Otolaryngol Suppl*. (2009) 560:5–8. doi: 10.1080/00016480902729827
5. Gürkov R, Flatz W, Louza J, Strupp M, Ertl-Wagner B, Krause E. In vivo visualized endolymphatic hydrops and inner ear functions in patients with electrocochleographically confirmed Ménière's disease. *Otol Neurotol*. (2012) 33:1040–5. doi: 10.1097/MAO.0b013e31825d9a95
6. Baráth K, Schuknecht B, Naldi AM, Schrepfer T, Bockisch CJ, Hegemann SCA. Detection and grading of endolymphatic hydrops in Menière disease using MR imaging. *AJNR Am J Neuroradiol*. (2014) 35:1387–92. doi: 10.3174/ajnr.A3856
7. Attyé A, Eliezer M, Boudiaf N, Tropres I, Chechin D, Schmerber S, et al. MRI of endolymphatic hydrops in patients with Meniere's disease: a case-controlled study with a simplified classification based on saccular morphology. *Eur Radiol*. (2017) 27:3138–46. doi: 10.1007/s00330-016-4701-z
8. Kirsch V, Becker-Bense S, Berman A, Kierig E, Ertl-Wagner B, Dieterich M. Transient endolymphatic hydrops after an attack of vestibular migraine: a longitudinal single case study. *J Neurol*. (2018) 265:51–3. doi: 10.1007/s00415-018-8870-3
9. Bernaerts A, Vanspauwen R, Blaivie C, van Dinther J, Zarowski A, Wuyts FL, et al. The value of four stage vestibular hydrops grading and asymmetric perilymphatic enhancement in the diagnosis of Menière's disease on MRI. *Neuroradiology*. (2019) 61:421–9. doi: 10.1007/s00234-019-02155-7
10. Boegle R, Gerb J, Kierig E, Becker-Bense S, Ertl-Wagner B, Dieterich M, et al. Intravenous delayed gadolinium-enhanced MR imaging of the endolymphatic space: a methodological comparative study. *Front Neurol*. (2021) 12:647296. doi: 10.3389/fneur.2021.647296
11. Naganawa S, Kanou M, Ohashi T, Kuno K, Sone M. Simple estimation of the endolymphatic volume ratio after intravenous administration of a single-dose of gadolinium contrast. *Magn Reson Med Sci*. (2016) 15:379–85. doi: 10.2463/mrms.mp.2015-0175
12. Yang S, Zhu H, Zhu B, Wang H, Chen Z, Wu Y, et al. Correlations between the degree of endolymphatic hydrops and symptoms and audiological test

results in patients with menière's disease: a reevaluation. *Otol Neurotol*. (2018) 39:351–6. doi: 10.1097/MAO.0000000000001675

13. Inui H, Sakamoto T, Ito T, Kitahara T. Volumetric measurements of the inner ear in patients with Meniere's disease using three-dimensional magnetic resonance imaging. *Acta Otolaryngol*. (2016) 136:888–93. doi: 10.3109/00016489.2016.1168940
14. Ito T, Inui H, Miyasaka T, Shiozaki T, Matsuyama S, Yamanaka T, et al. Three-Dimensional magnetic resonance imaging reveals the relationship between the control of vertigo and decreases in endolymphatic hydrops after endolymphatic sac drainage with steroids for meniere's disease. *Front Neurol*. (2019) 10:46. doi: 10.3389/fneur.2019.00046
15. Naganawa S, Kawai H, Taoka T, Sone M. Improved HYDROPS: imaging of endolymphatic hydrops after intravenous administration of gadolinium. *Magn Reson Med Sci*. (2017) 16:357–61. doi: 10.2463/mrms.tn.2016-0126
16. Ohashi T, Naganawa S, Takeuchi A, Katagiri T, Kuno K. Quantification of endolymphatic space volume after intravenous administration of a single dose of gadolinium-based contrast agent: 3D-real inversion recovery versus HYDROPS-Mi2. *Magn Reson Med Sci*. (2019) 19:119–24. doi: 10.2463/mrms.mp.2019-0013
17. Naganawa S, Nakamichi R, Ichikawa K, Kawamura M, Kawai H, Yoshida T, et al. MR imaging of endolymphatic hydrops: utility of iHYDROPS-Mi2 combined with deep learning reconstruction denoising. *Magn Reson Med Sci*. (2020) 20:272–9. doi: 10.2463/mrms.mp.2020-0082
18. Nakashima T, Pyykkö I, Arroll MA, Casselbrant ML, Foster CA, Manzoor NF, et al. Meniere's disease. *Nat Rev Dis Primers*. (2016) 2:16028. doi: 10.1038/nrdp.2016.28
19. Bakker CJ, Bhagwandien R, Moerland MA, Ramos LM. Simulation of susceptibility artifacts in 2D and 3D Fourier transform spin-echo and gradient-echo magnetic resonance imaging. *Magn Reson Imaging*. (1994) 12:767–74. doi: 10.1016/0730-725X(94)92201-2
20. Naganawa S, Yamakawa K, Fukatsu H, Ishigaki T, Nakashima T, Sugimoto H, et al. High-resolution T2-weighted MR imaging of the inner ear using a long echo-train-length 3D fast spin-echo sequence. *Eur Radiol*. (1996) 6:369–74. doi: 10.1007/BF00180615
21. Ito T, Naganawa S, Fukatsu H, Ishiguchi T, Ishigaki T, Kobayashi M, et al. High-resolution MR images of inner ear internal anatomy using a local gradient coil at 1.5 Tesla: correlation with histological specimen. *Radiat Med*. (1999) 17:343–7.
22. Naganawa S, Yamazaki M, Kawai H, Bokura K, Sone M, Nakashima T. Imaging of endolymphatic and perilymphatic fluid at 3T after intratympanic administration of gadolinium-diethylene-triamine pentaacetic acid. *Magn Reson Med Sci*. (2012) 29:7. doi: 10.3174/ajnr.A0894
23. Naganawa S, Yamazaki M, Kawai H, Bokura K, Sone M, Nakashima T. Imaging of ménière's disease after intravenous administration of single-dose gadodiamide: utility of subtraction images with different inversion time. *Magn Reson Med Sci*. (2012) 11:7. doi: 10.2463/mrms.11.213
24. Gürkov R, Berman A, Dietrich O, Flatz W, Jerin C, Krause E, et al. MR volumetric assessment of endolymphatic hydrops. *Eur Radiol*. (2015) 25:585–595. doi: 10.1007/s00330-014-3414-4
25. Homann G, Vieth V, Weiss D, Nikolaou K, Heindel W, Notohamiprodjo M, et al. Semi-quantitative vs. volumetric determination of endolymphatic space in Menière's disease using endolymphatic hydrops 3T-HR-MRI after intravenous gadolinium injection. *PLoS ONE*. (2015) 10:e0120357. doi: 10.1371/journal.pone.0120357
26. Kirsch V, Ertl-Wagner B, Berman A, Gerb J, Dieterich M, Becker-Bense S. High-resolution MRI of the inner ear enables syndrome differentiation and specific treatment of cerebellar downbeat nystagmus and secondary endolymphatic hydrops in a postoperative ELST patient. *J Neurol*. (2018) 265:48–50. doi: 10.1007/s00415-018-8858-z
27. Gerb J, Ahmadi SA, Kierig E, Ertl-Wagner B, Dieterich M, Kirsch V. VOLT: a novel open-source pipeline for automatic segmentation of endolymphatic space in inner ear MRI. *J Neurol*. (2020) 267:185–96. doi: 10.1007/s00415-020-10062-8
28. Oh SY, Dieterich M, Lee BN, Boegle R, Kang JJ, Lee NR, et al. Endolymphatic hydrops in patients with vestibular migraine and concurrent Meniere's disease. *Front Neurol*. (2021) 12:594481. doi: 10.3389/fneur.2021.594481
29. Ahmadi SA, Raiser TM, Ru¨hl RM, Flanagin VL, zu Eulenburg P. IE-Map: a novel *in-vivo* atlas and template of the human inner ear. *Sci Rep*. (2021) 11:3293. doi: 10.1038/s41598-021-82716-0
30. Kirsch V, Nejatbakhshesfahani F, Ahmadi SA, Dieterich M, Ertl-Wagner B. A probabilistic atlas of the human inner ear's bony labyrinth enables reliable atlas-based segmentation of the total fluid space. *J Neurol*. (2019) 266:52–61. doi: 10.1007/s00415-019-09488-6
31. Klein A, Andersson J, Ardekani BA, Ashburner J, Avants B, Chiang MC, et al. Evaluation of 14 nonlinear deformation algorithms applied to human brain MRI registration. *Neuroimage*. (2009) 46:786–802. doi: 10.1016/j.neuroimage.2008.12.037
32. Cho YS, Cho K, Park CJ, Chung MJ, Kim JH, Kim K, et al. Automated measurement of hydrops ratio from MRI in patients with Ménière's disease using CNN-based segmentation. *Sci Rep*. (2020) 10:7003. doi: 10.1038/s41598-020-63887-8
33. Vaidyanathan A, van der Lubbe MFJA, Leijenaar RTH, van Hoof M, Zerka F, Miraglio B, et al. Deep learning for the fully automated segmentation of the inner ear on MRI. *Sci Rep*. (2021) 11:2885. doi: 10.1038/s41598-021-82289-y
34. Kirsch V, Keeser D, Hergenroeder T, Erat O, Ertl-Wagner B, Brandt T, et al. Structural and functional connectivity mapping of the vestibular circuitry from human brainstem to cortex. *Brain Struct Funct*. (2016) 221:1291–1308. doi: 10.1007/s00429-014-0971-x
35. Kirsch V, Boegle R, Keeser D, Kierig E, Ertl-Wagner B, Brandt T, et al. Handedness-dependent functional organizational patterns within the bilateral vestibular cortical network revealed by fMRI connectivity based parcellation. *Neuroimage*. (2018) 178:224–37. doi: 10.1016/j.neuroimage.2018.05.018
36. Dill T. Contraindications to magnetic resonance imaging. *Heart*. (2008) 94:943–8. doi: 10.1136/hrt.2007.125039
37. Lempert T, Olesen J, Furman J, Waterston J, Seemungal B, Carey J, et al. Vestibular migraine: diagnostic criteria. *J Vestib Res*. (2012) 22:167–72. doi: 10.3233/VES-2012-0453
38. Dieterich M, Obermann M, Celebisoy N. Vestibular migraine: the most frequent entity of episodic vertigo. *J Neurol*. (2016) 263:82–9. doi: 10.1007/s00415-015-7905-2
39. Lopez-Escamez JA, Carey J, Chung WH, Goebel JA, Magnusson M, Mandalà M, et al. Diagnostic criteria for Méenièe's disease. *J Vestib Res*. (2015) 25:1–7. doi: 10.3233/VES-150549
40. Strupp M, Lopez-Escamez JA, Kim JS, Straumann D, Jen JC, Carey J, et al. Vestibular paroxysmia: diagnostic criteria. *J Vestib Res*. (2016) 26:409–15. doi: 10.3233/VES-160589
41. Strupp M, Kim JS, Murofushi T, Straumann D, Jen JC, Rosengren SM, et al. Bilateral vestibulopathy: diagnostic criteria consensus document of the classification committee of the bārāny society. *J Vestib Res*. (2017) 27:177–89. doi: 10.3233/VES-170619
42. Strupp M, Brandt T. Vestibular neuritis. *Seminars Neurol*. (2009) 29:509–19. doi: 10.1055/s-0029-1241040
43. von Brevern M, Bertholon P, Brandt T, Fife T, Imai T, Nuti D, et al. Benign paroxysmal positional vertigo: diagnostic criteria consensus document of the committee for the classification of vestibular disorders of the bárány society. *Acta Otorrinolaringol Espanola*. (2017) 68:349–60. doi: 10.1016/j.otorri.2017.02.007
44. Avants BB, Epstein CL, Grossman M, Gee JC. Symmetric diffeomorphic image registration with cross-correlation: evaluating automated labeling of elderly and neurodegenerative brain. *Med Image Anal*. (2008) 12:26–41. doi: 10.1016/j.media.2007.06.004
45. Avants BB, Yushkevich P, Pluta J, Minkoff D, Korczykowski M, Detre J, et al. The optimal template effect in hippocampus studies of diseased populations. *Neuroimage*. (2010) 49:2457–66. doi: 10.1016/j.neuroimage.2009.09.062
46. Otsu N. A threshold selection method from gray level histograms. *IEEE Trans Syst Man Cybern*. (1979) 9:62–6. doi: 10.1109/TSMC.1979.4310076
47. Kikinis R, Pieper SD, Vosburgh KG. 3D Slicer: a platform for subject-specific image analysis, visualization, and clinical support. In: Jolesz FA. editor. *Intraoperative Imaging and Image-Guided Therapy*. New York, NY: Springer New York (2014). p. 277–89.
48. Milletari F, Navab N, Ahmadi SA. V-Net: fully convolutional neural networks for volumetric medical image segmentation. In: *2016 Fourth International Conference on 3D Vision (3DV)*. Stanford, CA: IEEE (2016). p. 565–71.

49. Çiçek O, Abdulkadir A, Lienkamp SS, Brox T, Ronneberger O. 3D U-net: learning dense volumetric segmentation from sparse annotation. In: Ourselin S, Joskowicz L, Sabuncu MR, Unal G, Wells W, editors. *Medical Image Computing and Computer-Assisted Intervention-MICCAI 2016. Vol. 9901 of Lecture Notes in Computer Science*. Athens, Greece: Springer International Publishing (2016). p. 424–32.
50. Ulyanov D, Vedaldi A, Lempitsky V. Instance normalization: the missing ingredient for fast stylization. *arXiv:160708022 [cs]*. (2017) ArXiv: 1607.08022.
51. He K, Zhang X, Ren S, Sun J. Delving deep into rectifiers: surpassing human-level performance on imagenet classification. In: *2015 IEEE International Conference on Computer Vision (ICCV)*. Santiago: IEEE (2015). p. 1026–34.
52. Ma N, Wenqi Li, Brown R, Yiheng Wang, Behrooz, Gorman B, et al. *Project-MONAI/MONAI: Medical Open Network for AI in Medicine and Deep Learning in Healthcare Imaging: v0.5.3*. Zenodo (2021). Available online at: https://zenodo.org/record/4323058.
53. Kingma DP, Ba J. Adam: a method for stochastic optimization. In: *3rd International Conference for Learning Representations (ICLR)*. San Diego, CA (2015). Availalble online at: https://arxiv.org/abs/1412.6980
54. Dice LR. Measures of the amount of ecologic association between species. *Ecology*. (1945) 26:297–302. doi: 10.2307/1932409
55. Kh Z, Sk W, A B, Cm T, Mr K, Sj H, et al. Statistical validation of image segmentation quality based on a spatial overlap index. *Acad Radiol*. (2004) 11:178–89. doi: 10.1016/S1076-6332(03)00671-8
56. Huttenlocher DP, Klanderman GA, Rucklidge WA. Comparing images using the hausdorff distance. *IEEE Trans Pattern Anal Mach Intell*. (1993) 15:850–63. doi: 10.1109/34.232073
57. Taha AA, Hanbury A. An efficient algorithm for calculating the exact hausdorff distance. *IEEE Trans Pattern Anal Mach Intell*. (2015) 37:2153–63. doi: 10.1109/TPAMI.2015.2408351
58. Maurer CR, Qi R, Raghavan V. A linear time algorithm for computing exact Euclidean distance transforms of binary images in arbitrary dimensions. *IEEE Trans Pattern Anal Mach Intell*. (2003) 25:265–70. doi: 10.1109/TPAMI.2003.1177156
59. Likert R. A technique for the measurement of attitudes. (1932) *Arch Psychol*. 140:55. doi: 10.2307/297087
60. Jebb AT, Ng V, Tay L. A review of key likert scale development advances: 1995–2019. *Front Psychol*. (2021) 12:637547. doi: 10.3389/fpsyg.2021.637547
61. Shapiro SS, Wilk MB. An analysis of variance test for normality (complete samples). *Biometrika*. (1965) 52:591. doi: 10.2307/2333709
62. Bartlett MS, Fowler RH. Properties of sufficiency and statistical tests. *Proc R Soc Lond A Math Phys Sci*. (1937) 160:268–82. doi: 10.1098/rspa.1937.0109
63. Mircioiu C, Atkinson J. A comparison of parametric and non-parametric methods applied to a likert scale. *Pharmacy*. (2017) 5:26. doi: 10.3390/pharmacy5020026
64. Mann HB, Whitney DR. On a test of whether one of two random variables is stochastically larger than the other. *Ann Math Stat*. (1947) 18:50–60. doi: 10.1214/aoms/1177730491
65. Virtanen P, Gommers R, Oliphant TE, Haberland M, Reddy T, Cournapeau D, et al. SciPy 1.0: fundamental algorithms for scientific computing in python. *Nat Methods*. (2020) 17:261–72. doi: 10.1038/s41592-020-0772-5
66. Seabold S, Perktold J. Statsmodels: econometric and statistical modeling with python. In: *9th Python in Science Conference*. San Diego, CA (2010). p. 92–6.
67. Vallat R. Pingouin: statistics in Python. *J Open Source Softw*. (2018) 3:1026. doi: 10.21105/joss.01026
68. Crum WR, Camara O, Hill DLG. Generalized overlap measures for evaluation and validation in medical image analysis. *IEEE Trans Med Imaging*. (2006) 25:1451–61. doi: 10.1109/TMI.2006.880587
69. DeGrave AJ, Janizek JD, Lee SI. AI for radiographic COVID-19 detection selects shortcuts over signal. *Nat Mach Intell*. (2021) 3:610–9. doi: 10.1038/s42256-021-00338-7
70. Wu J, Tang X. A large deformation diffeomorphic framework for fast brain image registration via parallel computing and optimization. *Neuroinformatics*. (2020) 18:251–66. doi: 10.1007/s12021-019-09 438-7
71. Dalca AV, Balakrishnan G, Guttag J, Sabuncu MR. Unsupervised learning for fast probabilistic diffeomorphic registration. In: *Medical Image Computing and Computer Assisted Intervention – MICCAI 2018. vol. 11070*. Granada: Springer International Publishing (2018). p. 729–38.
72. Dalca AV, Balakrishnan G, Guttag J, Sabuncu MR. Unsupervised learning of probabilistic diffeomorphic registration for images and surfaces. *Med Image Anal*. (2019) 57:226–36. doi: 10.1016/j.media.2019.07.006
73. Litjens G, Kooi T, Bejnordi BE, Setio AAA, Ciompi F, Ghafoorian M, et al. A survey on deep learning in medical image analysis. *Med Image Anal*. (2017) 42:60–88. doi: 10.1016/j.media.2017.07.005
74. Hesamian MH, Jia W, He X, Kennedy P. Deep learning techniques for medical image segmentation: achievements and challenges. *J Digit Imaging*. (2019) 32:582–96. doi: 10.1007/s10278-019-00227-x
75. Lei T, Wang R, Wan Y, Du X, Meng H, Nandi AK. Medical image segmentation using deep learning: a survey. *arXiv:200913120*. (2020).
76. Heutink F. Multi-Scale deep learning framework for cochlea localization, segmentation and analysis on clinical ultra-high-resolution CT images. *Comput Methods Progr Biomed*. (2020) 191:105387. doi: 10.1016/j.cmpb.2020.105387
77. Hussain R, Lalande A, Girum KB, Guigou C, Bozorg Grayeli A. Automatic segmentation of inner ear on CT-scan using auto-context convolutional neural network. *Sci Rep*. (2021) 11:4406. doi: 10.1038/s41598-021-83955-x
78. Nikan S, Osch KV, Bartling M, Allen DG, Rohani SA, Connors B, et al. PWD-3DNet: a deep learning-based fully-automated segmentation of multiple structures on temporal bone CT scans. *IEEE Trans Image Process*. (2021) 30:15. doi: 10.1109/TIP.2020.3038363
79. Simonyan K, Zisserman A. Very deep convolutional networks for large-scale image recognition. *arXiv:14091556 [cs*]. (2015).
80. Naganawa S, Yamazaki M, Kawai H, Bokura K, Sone M, Nakashima T. Imaging of Ménière's disease after intravenous administration of single-dose gadodiamide: utility of multiplication of MR cisternography and HYDROPS image. *Magn Reson Med Sci*. (2013) 12:63–8. doi: 10.2463/mrms.2012-0027
81. Milletari F, Frei J, Aboulatta M, Vivar G, Ahmadi SA. Cloud deployment of high-resolution medical image analysis with TOMAAT. *IEEE J Biomed Health Inform*. (2019) 23:969–77. doi: 10.1109/JBHI.2018.2885214
82. Fedorov A, Beichel R, Kalpathy-Cramer J, Finet J, Fillion-Robin JC, Pujol S, et al. 3D slicer as an image computing platform for the quantitative imaging network. *Magn Reson Imaging*. (2012). 30:1323–41. doi: 10.1016/j.mri.2012.05.001
83. Christ PF, Elshaer MEA, Ettlinger F, Tatavarty S, Bickel M, Bilic P, et al. Automatic liver and lesion segmentation in CT using cascaded fully convolutional neural networks and 3D conditional random fields. In: *Medical Image Computing and Computer-Assisted Intervention – MICCAI 2016. vol. 9901*. Athens: Springer International Publishing (2016). p. 415–23.
84. Chen X, Girshick R, He K, Dollar P. TensorMask: a foundation for dense object segmentation. In: *2019 IEEE/CVF International Conference on Computer Vision (ICCV)*. (2019). p. 2061–9.
85. Ahmadi SA, Baust M, Karamalis A, Plate A, Boetzel K, Klein T, et al. Midbrain segmentation in transcranial 3D ultrasound for parkinson diagnosis. In: Fichtinger G, Martel A, Peters T, editors. *Medical Image Computing and Computer-Assisted Intervention – MICCAI 2011 Lecture Notes in Computer Science*. Berlin; Heidelberg: Springer (2011). p. 362–9.
86. Gutiãrrez-Becker B, Sarasua I, Wachinger C. Discriminative and generative models for anatomical shape analysis on point clouds with deep neural networks. *Med Image Anal*. (2021) 67:101852. doi: 10.1016/j.media.2020.101852
87. Dieterich M, Brandt T. Ocular torsion and tilt of subjective visual vertical are sensitive brainstem signs. *Ann Neurol*. (1993) 33:292–9. doi: 10.1002/ana.410330311
88. Schneider E, Villgrattner T, Vockeroth J, Bartl K, Kohlbecher S, Bardins S, et al. EyeSeeCam: an eye movement-driven head camera for the examination of natural visual exploration. *Ann N Y Acad Sci*. (2009) 1164:461–7. doi: 10.1111/j.1749-6632.2009.03858.x
89. Halmagyi GM, Curthoys IS. A clinical sign of canal paresis. *Arch Neurol*. (1988) 45:737–739. doi: 10.1001/archneur.1988.00520310043015
90. Jongkees LB, Maas JP, Philipszoon AJ. Clinical nystagmography. A detailed study of electro-nystagmography in 341 patients with vertigo. *Practica Otorhinolaryngol*. (1962) 24:65–93. doi: 10.1159/000274383

Conflict of Interest: S-AA was employed by NVIDIA GmbH.

The remaining authors declare that the research was conducted in the absence of any commercial orfinancial relationships that could be construed as a potential conflict of interest.

Advantages of publishing in Frontiers

OPEN ACCESS
Articles are free to read for greatest visibility and readership

FAST PUBLICATION
Around 90 days from submission to decision

HIGH QUALITY PEER-REVIEW
Rigorous, collaborative, and constructive peer-review

TRANSPARENT PEER-REVIEW
Editors and reviewers acknowledged by name on published articles

Frontiers
Avenue du Tribunal-Fédéral 34
1005 Lausanne | Switzerland

Visit us: www.frontiersin.org
Contact us: frontiersin.org/about/contact

REPRODUCIBILITY OF RESEARCH
Support open data and methods to enhance research reproducibility

DIGITAL PUBLISHING
Articles designed for optimal readership across devices

FOLLOW US
@frontiersin

IMPACT METRICS
Advanced article metrics track visibility across digital media

EXTENSIVE PROMOTION
Marketing and promotion of impactful research

LOOP RESEARCH NETWORK
Our network increases your article's readership